Search for Supersymmetric particles in e^+e^- collisions at LEP

Gobinda Majumder

Tata Institute of Fundamental Research

Mumbai 400 005

1997

Search for Supersymmetric particles in e^+e^- collisions at LEP

Gobinda Majumder

Tata Institute of Fundamental Research
Mumbai 400 005

A Thesis submitted to the

University of Mumbai

for the degree of
Doctor of Philosophy in Physics

November, 1997

To my parents and my elder brother

Acknowledgement

I gratefully acknowledge the excellent guidance of my thesis supervisor Prof. S.N. Ganguli, during the past five years.

I also thank other faculty members of our group, Prof. A. Gurtu, Prof. T. Aziz, Dr. R. Raghavan, Dr. K. Sudhakar and Dr. K. Mazumdar for their assistance and suggestions regarding my analysis. Suggestions from Prof. V.S. Narasimham and Prof. N.K. Mondal are also thankfully acknowledged. I thank P.V. Deshpande for his efforts towards maintaining our group's computing system in good shape.

I thank the European Organisation for Nuclear Research, which provided me local hospitality at Geneva to work in a charming and exciting research environment. I thank the LEP accelerator group, who provide the stable e^+e^- *beams for high energy research.*

I acknowledge the cooperation help of all the members of L3 collaboration. I thank all the members of new particle group in L3, in particular to A. kunin, M. Pieri, S. Rosier, A. Favara, S. Mele and M. Felcini, who helped me to complete my analysis. I acknowledge many help from R. Clare and D. Stickland for solving L3 software related problem. Thanks to M. Hafeez, R. Khan and P. Marchesini for their help in solving all kinds of computing problems in L3.

I would like to thank all my colleagues in our group. In various stages of my work S. Mangla, S. Sarkar, S. Dutta, M. Maity, T. Moulik, S. Bhattacharya, S. Banerjee and N. Raja helped me as much as they could.

I would also like to thank Sandeep Ghosh, without whose useful suggestions the thesis would not have come to its present form.

I express my gratitude to Dr. A. Bhadra, whose help and encouragement has been a source and strength throughout my career.

Dr. S. Raychaudhury's help in making me understand the basics of SUSY theory is gratefully acknowledged.

Finally, I would like to mention the name of Prof. S. Banerjee, who guided me at almost each and every step of my analysis. Without his help I could not have finished this work within the stipulated time.

Contents

Synopsis **(v)**

List of Figures **(xvi)**

List of Tables **(xix)**

1 Introduction **1**

2 Theoretical Overview **3**

2.1 The Standard Model (SM) 3

2.2 Why go Beyond the Standard Model ? 4

2.2.1 The fine-tuning Problem 5

2.3 Supersymmetry (SUSY) 6

2.3.1 The Minimal Supersymmetric Standard Model (MSSM) 6

2.3.2 Lagrangian of the Minimal Supersymmetric Standard Model 8

2.3.3 Supersymmetry Breaking 9

2.3.3.1 The Higgs Sector and Electroweak Symmetry Breaking . . . 10

2.3.3.2 The Chargino Sector 11

2.3.3.3 The Neutralino Sector 11

2.3.3.4 The Squark and Slepton Sector 12

2.3.4 R-Parity 14

2.3.5 Constraints on Free Parameters from GUT Motivation 15

2.3.6 Experimental Constraints on Supersymmetric Mass Spectra 18

2.3.6.1 Results from HERA 19

2.3.6.2 Results from Tevatron 19

2.3.6.3 Results from LEP1 19

2.3.6.4 Indirect Constraints 19

3 The Large Electron Positron Collider **23**

3.1 LEP Run at the Z-peak (LEP 1) 25

3.2 LEP Run Beyond the Z-peak (LEP 2) 26

3.2.1 Superconducting RF Cavity 27
3.2.2 Bunch Train Mode 27
3.2.3 LEP Injection Energy 28
3.2.4 Change in LEP Optics 29
3.2.5 Ramping and Squeezing of the Beam 30
3.3 Calibration of LEP 2 Beam Energy 30

4 The L3 Detector **32**
4.1 Central Tracking System 33
4.1.1 Silicon Microvertex Detector 33
4.1.2 Time Expansion Chamber 35
4.1.3 Plastic Scintillating Fibre 37
4.1.4 Central Z Chamber 37
4.1.5 Precision of Central Tracking System 37
4.2 Electromagnetic Calorimeter 37
4.2.1 The Barrel and Endcap Electromagnetic Calorimeter 37
4.2.2 Forward Tracking Chamber 39
4.2.3 Active Lead Ring 39
4.2.4 Lead-Scintillating Fibre Calorimeter 41
4.3 Scintillation Counter 42
4.4 Hadron Calorimeter 43
4.4.1 Barrel Hadron Calorimeter 43
4.4.2 Endcap Hadron Calorimeter 44
4.4.3 Muon Filter 45
4.4.4 Energy and Angular Resolution of Hadron Calorimeter 46
4.5 Muon Chamber 46
4.5.1 P-Chamber 46
4.5.2 Z-Chamber 47
4.5.3 Forward Backward Muon Chamber 49
4.5.4 Resistive Plate Counter 49
4.6 Luminosity Monitor 51
4.7 Very Short Angle Tagger 52
4.8 L3 Magnet 53
4.9 Off-line Energy Calibration (G-Factors) 54
4.10 L3 Detector Resolution 54

5 L3 Trigger System **55**
5.1 Level 1 Trigger 55
5.1.1 Energy Trigger 56

5.1.2 Muon Trigger . . . 59
5.1.3 TEC Trigger . . . 59
5.1.4 Scintillator Trigger . . . 60
5.2 Level 2 Trigger . . . 61
5.3 Level 3 Trigger . . . 62

6 L3 Detector Simulation and Event Reconstruction 64
6.1 Monte Carlo Simulation . . . 64
6.1.1 Event Generation . . . 64
6.1.2 Detector Simulation . . . 68
6.2 Event Reconstruction . . . 69

7 Strategy for Selection of SUSY Events 71
7.1 Lepton Identifications . . . 72
7.1.1 Track Identification . . . 72
7.1.2 Electron Identification . . . 74
7.1.3 Muon Identification . . . 76
7.1.4 Tau Identification . . . 77
7.2 Kinematic Variables . . . 77
7.3 Choice of Selection Cuts . . . 84
7.3.1 Preselections . . . 85
7.3.2 Multidimensional Optimisation Procedure for Final Selection . . . 85
7.4 Selection Criteria and Efficiencies . . . 88
7.4.1 Selection Criteria at $\sqrt{s}$ = 130 - 136 GeV . . . 88
7.4.2 Selection Criteria at $\sqrt{s}$ = 161 GeV . . . 89
7.4.3 Selection Criteria at $\sqrt{s}$ = 172 GeV . . . 89
7.5 Error Estimation . . . 100
7.5.1 Statistical Error . . . 100
7.5.2 Systematic Uncertainties . . . 100

8 Experimental Data 103
8.1 LEP Run and L3 Data Collection . . . 103
8.2 Reconstruction of Data to the Search Level . . . 104
8.3 Searches for SUSY Signal in Data . . . 105
8.3.1 Searches at $\sqrt{s}$ = 130 - 136 GeV . . . 105
8.3.2 Searches at $\sqrt{s}$ = 161 – 172 GeV . . . 114
8.4 Conclusion . . . 118

9 Interpretation of Search Results in the MSSM Framework 119
9.1 Upper Bounds on Production Cross Sections . . . 119

9.2 Exclusion Plots using Data of $\sqrt{s}$ = 130 - 136 GeV 120
9.3 Exclusion Plots using Data of $\sqrt{s}$ = 161 – 172 GeV 121
9.3.1 Parametrisation of Selection Efficiencies 122
9.3.2 Upper Bound on Production Cross Sections at $\sqrt{s}$ = 161 – 172 GeV 122
9.3.3 Exclusion of Parameter Space and SUSY Particle Mass Plane 125
9.4 Summary 125

10 Summary and Outlook **130**

A Production and Decay Formulae of Selectron **132**
A.1 $e^+ + e^- \to \tilde{e}_i^+ + \tilde{e}_j^-$ 132
A.2 $\tilde{e}_i^\pm \to e^\pm \ + \ \tilde{\chi}_k^\circ$ 134

B Upper Limits of Signal Events **135**

C Fitted Values of the Parametrisation of Selection Efficiencies **136**

D Combination of two Luminosities for $\tilde{\ell}^+\tilde{\ell}^-$ Limits **137**

References **138**

List of Publications **(a)**

Synopsis

Title of the Thesis	:	Search for Supersymmetric particles
	:	in e^+e^- collisions at LEP.
Name of the Candidate	:	Gobinda Majumder
Registration No.	:	TIFR−58 dated 04.08.94
Degree	:	Doctor of Philosophy
Subject	:	Physics
Thesis Supervisor	:	Prof. S.N. Ganguli
Institution	:	Tata Institute of Fundamental Research.

The Large Electron Positron (LEP) Collider at CERN, Geneva, is in operation since 1989 to study the properties of Z° and $W^\pm$ bosons, which are the mediators of the weak interaction in the Standard Model (SM) [1] and search for new physics. ALEPH, DELPHI, L3 and OPAL are the four detectors, which are used to study the above mentioned physics. The experimental high energy physics group of TIFR is a member of the L3 collaboration.

The SM is a unified model of strong, electromagnetic and weak interactions. These interactions are mediated by the exchange of spin 1 gauge bosons. Particles acquire their masses through the Higgs mechanism requiring a neutral scalar particle called Higgs boson. At present the SM is extraordinarily successful in explaining the experimental data. However, there are several drawbacks. One of the main drawbacks is the hierarchy problem i.e., the mass of the Higgs bosons acquires the highest mass scale of the theory. Supersymmetric [2] theory is one way to solve the hierarchy problem.

Supersymmetry (SUSY) invokes a symmetry between fermions and bosons. SUSY associates superpartners to all known SM particles which have the same quantum numbers except spin which differ by $\frac{1}{2}$. The simplest supersymmetric generalisation of Standard Model is the Minimal Supersymmetric Standard Model (MSSM). This theory needs two complex Higgs doublets to give masses to **up**- and **down**-type quarks and the Higgs sector is therefore enlarged with 5 physical Higgs bosons. Particles and fields are embedded inside the superfields and are shown in table 1.

Superfield	spin 1	spin 1/2	spin 0
Gauge	Photon Gluons $W^\pm$, Z	Photino Gluinos Gauginos	
Higgs		Higgsinos	Higgs Bosons
Fermion		Fermions	Sfermions

Table 1: Particle and field content in MSSM model.

This thesis describes the search for SUSY particles decaying via leptonic mode using the L3 detector. The experimental data were collected during the years 1995 and 1996 at centre of mass energies ($\sqrt{s}$) ranging from 130 to 172 GeV.

SUSY introduces a multiplicative quantum number called **R-Parity**, which is defined as $\mathbf{R} = (-1)^{3(B-L)+2S}$ (R-parity is +1 for all SM particles and −1 for all superpartners), where B = baryon number, L = lepton number and S = spin of the particle. Conservation of R-parity implies: (a) supersymmetric particles are created in pairs from SM particles and (b) the Lightest Supersymmetric Particle (LSP) is stable and elusive to detectors. The latter leads to a generic signal for R-Parity conserving SUSY theories as missing energy in the detector.

Exact supersymmetry predicts superpartners of the SM particles to have the same mass. Since we have not yet been able to see the superparticles, supersymmetry must be a broken symmetry.

The physical mass eigenstates of the SUSY particles are :

Charginos ($\tilde{\chi}^{\pm}_{1,2}$) **:** These are Dirac fermions which are mixture of charged higgsinos ($\tilde{\mathrm{h}}^{\pm}$) and winos ($\tilde{\mathrm{w}}^{\pm}$).

Neutralinos ($\tilde{\chi}^{\circ}_{1,2,3,4}$) **:** These are Majorana fermions which are mixture of neutral higgsinos ($\tilde{\mathrm{h}}^{\circ}_{1,2}$), zino ($\tilde{\mathrm{z}}^{\circ}$) and photino ($\tilde{\gamma}$).

Sfermions ($\tilde{\mathrm{f}}_{1,2}$) **:** Scalar particles which are combinations of left and right handed sfermions except $\tilde{\nu}_L$ which is only left handed.

Gluinos ($\tilde{g}$) **:** Supersymmetric partners of gluons.

Grand Unified Theory (GUT) motivated MSSM assumes mass unifications at a very high energy scale of $\sim 10^{16}$ GeV. It is economic from experimental point of view since it has only 5 unknown parameters :

$\mathbf{m}_{1/2}$: Common gaugino mass at the GUT scale
$\mathbf{m}_{\circ}$: Common scalar mass at the GUT scale
$\mathbf{A}_{\circ}$: Common trilinear interaction term
$\mathbf{t}an\,\beta$: Ratio of vacuum expectation values of two Higgs doublets
μ : Higgsino mixing parameter

Renormalisation group evolution of these parameters gives all the relevant sparticle masses and couplings at the weak scale.

Feynman diagrams for slepton production are shown in figure 1. Similarly Charginos are produced through s- and t-channel diagrams mediated by γ^*/Z^* and $\tilde{\nu}$ respectively; neutralino through the s-, t- and u-channels mediated by Z^*, $\tilde{\mathrm{e}}_{L,R}$ and $\tilde{\mathrm{e}}_{L,R}$ respectively. Some examples of SUSY particles decay modes are: ($\tilde{\ell}^{\pm} \rightarrow \ell^{\pm}\tilde{\chi}^{\circ}_i$, $\tilde{\chi}^{\pm}_i\nu$, $W^{*\pm}\tilde{\nu}$ etc.), ($\tilde{\chi}^{\pm}_i \rightarrow W^{*\pm}\tilde{\chi}^{\circ}_j$, $\ell^{\pm}\tilde{\nu}$, $\tilde{\ell}^{\pm}\nu$ etc.), ($\tilde{\chi}^{\circ}_i \rightarrow Z^*\tilde{\chi}^{\circ}_j$, $\tilde{\chi}^{\pm}_j W^{*\mp}$, $\ell^{\pm}\tilde{\ell}^{\mp}$ etc.). Decay branching ratios to different channels depend on the SUSY parameters.

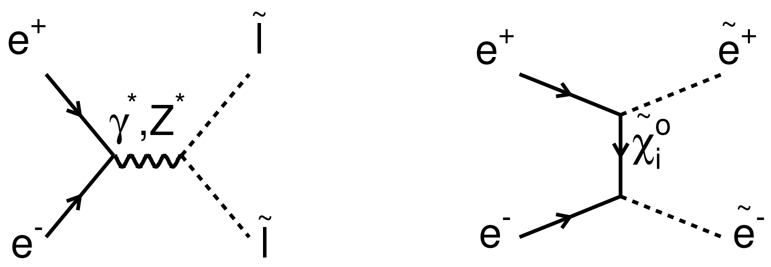

Figure 1: Feynman diagrams for slepton ($\tilde{\ell}$) production.

Aim : This thesis describes the search for the supersymmetric particles e.g., sleptons ($\tilde{\ell}$), chargino ($\tilde{\chi}_1^{\pm}$) and neutralino ($\tilde{\chi}_2^{\circ}$). In this work we have considered R-Parity conservation and $\tilde{\chi}_1^{\circ}$ is taken as the LSP. Lower limits on the mass of $\tilde{\ell}$ and $\tilde{\chi}_1^{\pm}$ have been set to $\leq$ 45GeV ($\approx$ $\mathrm{M_Z}/2$) from the searches at LEP 1 [3] with $\sqrt{\mathrm{s}}$ around M_Z. We have studied the production and decay of right handed slepton ($\tilde{\ell}_R$) and chargino ($\tilde{\chi}_1^{\pm}$) from 45 GeV to the kinematic limit of the production (86 GeV).

Expected production cross-section : In the mass range of our search the expected production cross sections of chargino ($\tilde{\chi}_1^{+}\tilde{\chi}_1^{-}$) and neutralino ($\tilde{\chi}_1^{\circ}\tilde{\chi}_2^{\circ}$) could be as high as 10 pb and 20 pb respectively whereas this is less than 5.0 pb and 0.8 pb for right handed selectrons and smuons (or stau) respectively.

Expected SM Background : Basic backgrounds due to SM processes are : (a) γ^*/Z^* exchange in $\mathrm{e^+e^-}$ interactions leading to $\mathrm{f\bar{f}}$, (b) two photon processes in $\mathrm{e^+e^-} \rightarrow \mathrm{e^+e^-f\bar{f}}$ and (c) four fermion final states in $\mathrm{e^+e^-} \rightarrow f\bar{f}f'\bar{f}'$, where the contributions are from ZZ, WW, Zee, Weν and Z$\nu\bar{\nu}$ channels. Overall cross section from these processes is $\sim$ 10 nb. Most of the backgrounds are from the first two process. Cross section for four fermion processes is only 3$-$15 pb within the energy range $\sqrt{\mathrm{s}}$ = 130$-$172 GeV. But the events from the four fermion final states have almost the same signature as SUSY signals and hence this gives rise to an irreducible background to SUSY signals. To get a reasonable signal to background ratio one needs to suppress the background by several orders of magnitude. Since different SM processes are dominant at different $\sqrt{\mathrm{s}}$, selection criteria have to be designed for each $\sqrt{\mathrm{s}}$ separately.

L3 detector and Lepton identification : L3 detector composed of central tracking detector (TEC), electro-magnetic calorimeter (ECAL), hadron calorimeter (HCAL) and muon chamber (MUCH). We identify electron from the shower pattern of calorimetric energy deposit and association of a track in the TEC. Muons are identified as a track in the muon chamber with an associated track in the TEC and 'minimum ionising particle' signal in calorimeters. Taus are identified through their decay products e.g., electron, muon or hadronic shower in the calorimeter with a small opening angle associated with a few ($\leq$ 3) tracks in TEC. Leptons are identified with high efficiency and high purity over a wide range of energy from 2 GeV to beam energy.

Monte Carlo (MC) Simulation : The response of the detector to various physics processes has been simulated using Monte Carlo technique. Events corresponding to SUSY signals and to the SM processes are generated in two steps. In the first step the particles are generated using the basic physics processes under study e.g., SUSY signals are generated using generator, SUSYGEN [4]. In the second step the generated particles are traced through the detector material and the response of each active detector component is simulated. These simulated data are reconstructed using the standard L3 reconstruction program, which is used also for the real data. These simulated events are used also to distinguish SUSY signals from SM processes and to calculate selection efficiencies.

Characteristics of the expected SUSY signal : SUSY signals in our searching mode have the following properties: two leptons (electrons, muons or τ jets) with large acoplanarity, small visible energy, large missing transverse momentum and very little energy in the forward direction. Acoplanarity is defined as: $\pi - |\phi_2 - \phi_1|$, where $\phi_{1,2}$ are the azimuthal angles of two leptons. With the help of these and other kinematic variables e.g., multiplicity in TEC and in calorimeters, missing energy direction, visible and invisible mass of the event, energy deposited in different subdetector etc., we try to distinguish SUSY signals from the SM backgrounds.

Preselection : First level selection has been done on the basis of the following event topologies: two acoplanar leptons, low multiplicity, small visible energy, very small energy in the hadronic calorimeter, closeness of the tracks to the interaction vertex, missing energy vector within the detector accepted region etc. This reduces the SM background by two order of magnitude while the SUSY signals are reduced only by a few percent. This preselection allows us to have a close look at the remaining SM backgrounds which are reasonably similar to the SUSY signals.

Final Selection : We have used an objective approach to choose the cut parameters for the final selection using the Monte Carlo samples for signal and background. We have carried out a multidimensional optimisation procedure which takes into account the correlation between the variables used in the final selection.

Optimisation is done by the minimisation of the sensitivity function, which is related to the average Poisson upper limit of the signals and the signal efficiency [5]. The sensitivity function is defined as $\sum_{n=0}^{\infty} K_n P_b(n)/\varepsilon$, where K_n is the 95% CL Poisson upper limit on the average number of signal events from n observed events with background of b events and $P_b(n)$ is the Poisson probability for observing n events with background of b events. ε is the overall signal efficiency.

Simulation results : Selection efficiencies of different SUSY particles at $\sqrt{\mathrm{s}}$ = 130$-$136 GeV depend mainly on the mass difference, ΔM (= $\mathrm{M}_{SUSY} - \mathrm{M}_{LSP}$) and almost independent of M_{SUSY}, where M_{SUSY} is the mass of the SUSY particle and M_{LSP} is the mass of the LSP. For $\Delta\mathrm{M} \geq 10$ GeV, the efficiencies are nearly constant ($\sim 70\,\%$ for $\mathrm{e}^+\mathrm{e}^- \rightarrow \tilde{\mathrm{e}}^+\,\tilde{\mathrm{e}}^-$ and 60 % for $\mathrm{e}^+\mathrm{e}^- \rightarrow \tilde{\mu}^+\,\tilde{\mu}^-$), whereas for low Δ M the efficiencies decrease with Δ M because of poor leptonic identification of the low energy lepton.

The selection efficiencies at $\sqrt{\mathrm{s}} = 161 - 172$ GeV have strong dependence on ΔM and they have also a weak dependence on the mass of the sparticle [6]. Efficiencies increase with ΔM and reach the maximum for $\Delta\mathrm{M} \sim 25-35$ GeV and thereafter they decrease. Typical efficiencies for that region are 70 %, 60 %, 40 %, 55 % and 45 % for $\mathrm{e}^+\mathrm{e}^- \rightarrow \tilde{\mathrm{e}}^+\,\tilde{\mathrm{e}}^-$,

$e^+e^- \rightarrow \tilde{\mu}^+\tilde{\mu}^-$, $e^+e^- \rightarrow \tilde{\tau}^+\tilde{\tau}^-$, $e^+e^- \rightarrow \tilde{\chi}_1^+\tilde{\chi}_1^-$ and $e^+e^- \rightarrow \tilde{\chi}_1^\circ\tilde{\chi}_2^\circ$ channels respectively.

Systematic errors : Statistical errors for the above efficiencies vary from 1 % to 5 % for different mass points. Systematic errors due to the detector resolution ($\sim$ 1.3 % and 2.9 % for $\tilde{e}^+\tilde{e}^-$ and $\tilde{\mu}^+\tilde{\mu}^-$ respectively), trigger efficiency ($\sim$ 0.3 % and 1.0 % for $\tilde{e}^+\tilde{e}^-$ and $\tilde{\mu}^+\tilde{\mu}^-$ respectively) and luminosity measurement (0.65 %) have been estimated.

Data Sample : We use data collected by the L3 experiment in the years 1995 and 1996 at $\sqrt{s}$ ranging from 130 − 172 GeV. Integrated luminosities, recorded number of events and the events passed after preselection are shown in table 2.

$\sqrt{s}$ (GeV)	Integrated luminosity (pb^{-1})	Events recorded $\times 10^5$	Events after preselection
130−136	5.1	4.5	30
161	10.1	7.7	69
170−172	10.0	9.0	69

Table 2: Luminosity and data used in this search.

Comparison with Monte Carlo : We have chosen events (both from real data and SM processes) with two identified leptons to compare the data with Monte Carlo events from SM physics processes after normalising to proper luminosities. There is a good agreement between data and MC (figure 2) suggesting that the kinematic variables are well measured and the detector effects as well as the SM physics process are also well understood.

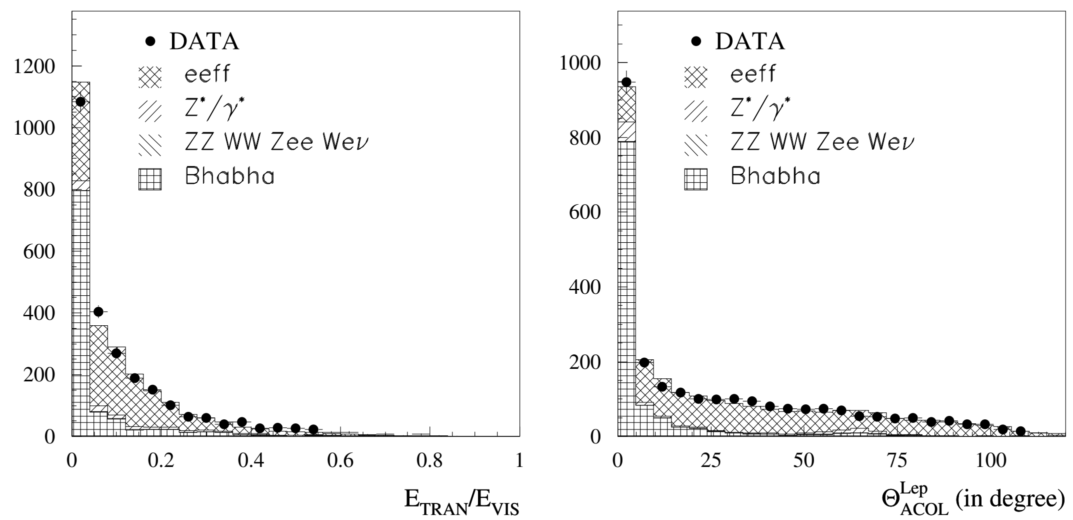

Figure 2: (a) Normalised transverse energy imbalance and (b) acolinearity angle between the lepton pair measured at $\sqrt{s}$ = 172 GeV compared with the expectations from the standard background processes.

Results : At $\sqrt{s}$ = 130–136 GeV, we do not have any candidate event for $\tilde{e}^+\tilde{e}^-$ and $\tilde{\mu}^+\tilde{\mu}^-$ processes and the background from SM processes is negligible. There is one candidate event in $\tilde{\tau}^+\tilde{\tau}^-$ channel, whereas we expect 0.8 event from the Standard Model processes in the data sample of 5.1 pb^{-1}.

At $\sqrt{s}$ = 161–172 GeV, no event passed through the selection criteria for $\tilde{e}^+\tilde{e}^-$ and $\tilde{\mu}^+\tilde{\mu}^-$ processes. However, there are two candidate events at $\sqrt{s}$ = 172 GeV, one for $\tilde{\tau}^+\tilde{\tau}^-$ and the other for $\tilde{\chi}_1^+\tilde{\chi}_1^-$ channel. We expect 2.8 events from the Standard Model processes in the data sample equivalent to integrated luminosity of 20.1 pb^{-1}.

The observed events are compatible with the expected number of events from the SM physics. We therefore conclude that we have not seen any new physics beyond the SM.

Limits on production cross section of SUSY particles : Efficiencies for the given set of mass points are parametrised in terms of M_{SUSY} and ΔM from the measured efficiencies at a few points in $\mathrm{M_{SUSY}}$ vs $M_{\tilde{\chi}_1^0}$ plane. The 95% CL upper bounds on the production cross sections for $\tilde{e}_R$, $\tilde{\mu}_R$, $\tilde{\tau}_1$ and similar bounds on the cross section times branching ratio of $\tilde{\chi}^{\pm} \rightarrow e/\mu$ in $\tilde{\chi}_1^+\tilde{\chi}_1^-$ have been determined from the number of observed and background events using Poisson statistics after folding in the selection, trigger efficiencies and the integrated luminosities. These are shown in figure 3.

Interpretation in the MSSM framework : The excluded cross section for the slepton searches can be interpreted in the framework of MSSM by comparing them with the expected cross sections at different sets of parameter values. The excluded cross section for the process $e^+e^- \rightarrow \tilde{\tau}^+\tilde{\tau}^-$ does not add to the existing LEP 1 limit. The results for the processes $e^+e^- \rightarrow \tilde{e}^+\tilde{e}^-$ and $e^+e^- \rightarrow \tilde{\mu}^+\tilde{\mu}^-$ at $\sqrt{s}$ = 161 GeV and 172 GeV have been used to exclude part of the parameter space. Using the combined data of $\sqrt{s}$ = 161 GeV and 172 GeV, lower limit on right handed scalar electron mass has been determined to be 69 GeV. This is tested for a wide range of $\tan\beta$ and μ. As an example figure 4 shows the 95 % CL exclusion region in the $M_{\tilde{\ell}_R}$ vs $M_{\tilde{\chi}_1^0}$ mass plane for $\tan\beta = 1.2$ and $\mu = -200$ GeV.

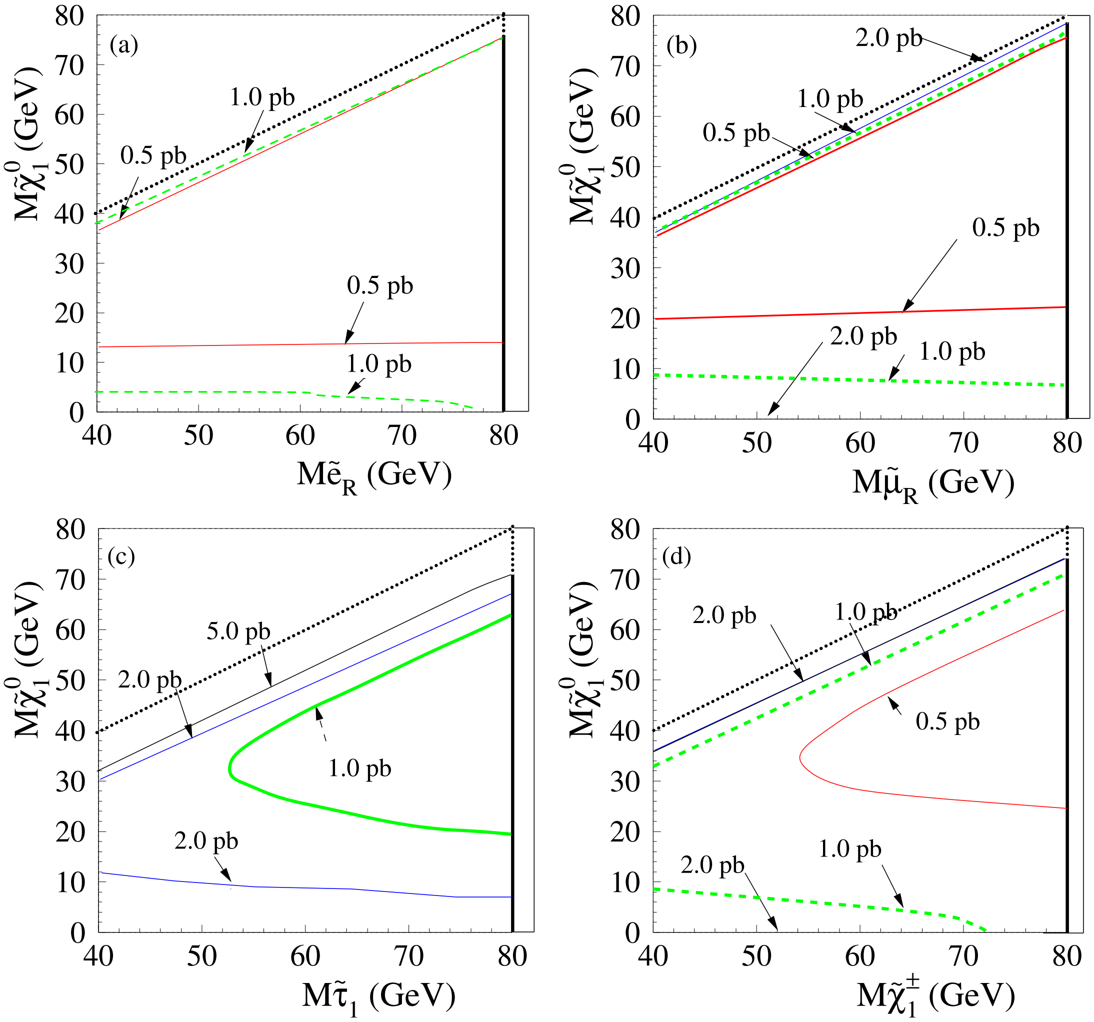

Figure 3: 95% CL contours of upper bounds on cross sections for the processes (a) $e^+e^- \to \tilde{e}_R^+\tilde{e}_R^-$, (b) $e^+e^- \to \tilde{\mu}_R^+\tilde{\mu}_R^-$, (c) $e^+e^- \to \tilde{\tau}_1^+\tilde{\tau}_1^-$ as a function of slepton and neutralino masses. (d) 95% CL contours of upper bounds on cross section times branching ratio for the process $e^+e^- \to \tilde{\chi}_1^+\tilde{\chi}_1^-$ at $\sqrt{s} = 161$ GeV as a function of the chargino and neutralino masses. Dotted lines imply $M_{SUSY} = M_{\tilde{\chi}_1^0}$ and the deep solid lines to the kinematic limit.

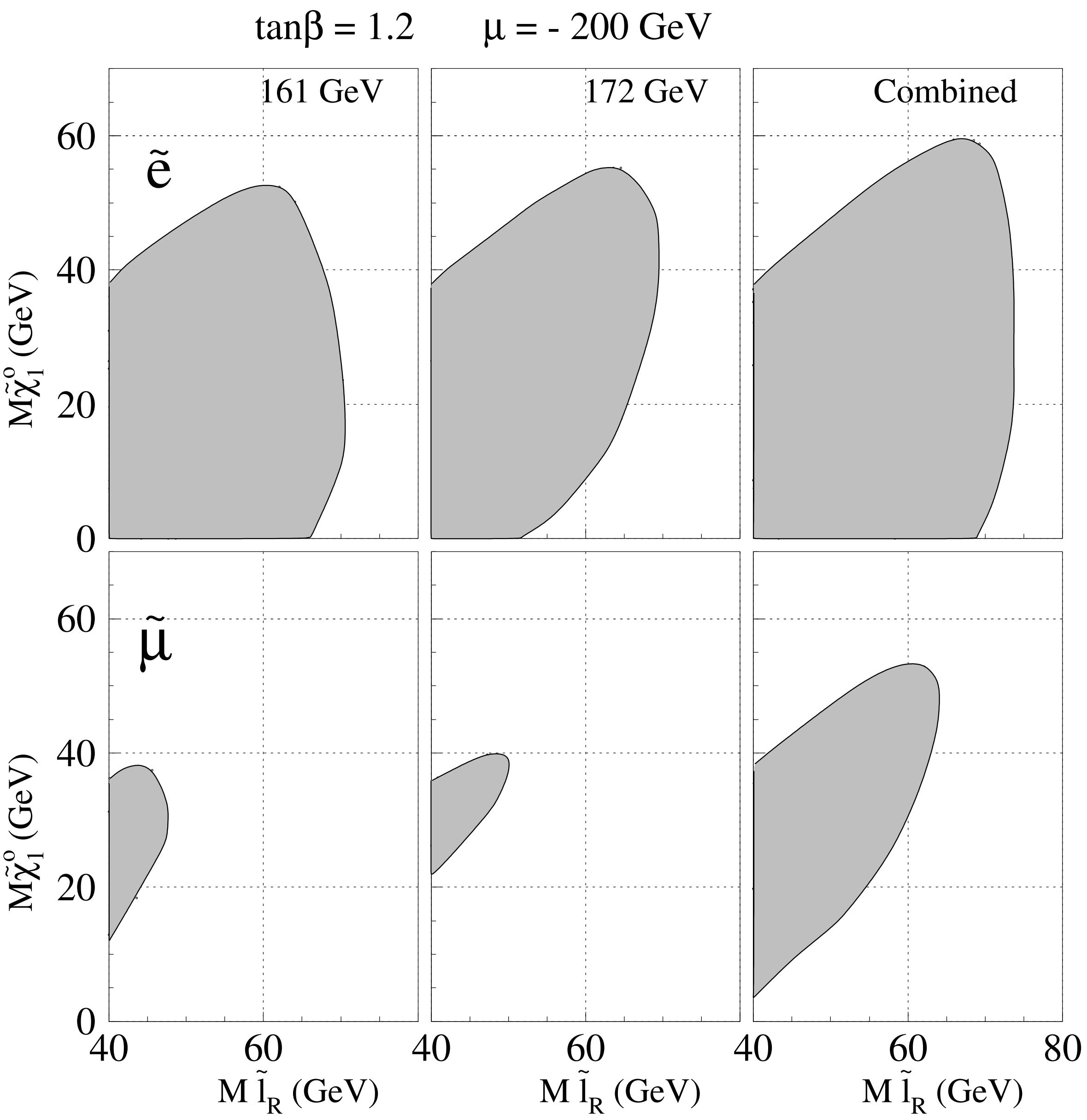

Figure 4: 95% CL exclusion region in $M_{\tilde{\ell}_R} - M_{\tilde{\chi}_1^\circ}$ plane using the combined data for the processes $e^+e^- \rightarrow \tilde{e}_R^+\tilde{e}_R^-$ and $e^+e^- \rightarrow \tilde{\mu}_R^+\tilde{\mu}_R^-$.

Reference

[1] S. L. Glashow, Nuclear Physics **22** (1961) 579;
S. Weinberg, Physical Review Letters **19** (1967) 1264;
A. Salam, in Proceedings of the 8th Nobel Symposium, ed. N. Svartholm, (Almquist and Wiksell, Slockholm, 1968)

[2] Y. Gollfand and E. Likhrman, JETP Lett. **13** 323(1971); D. Volkov and V. Akulov Physics Letters **B** 46, 109(1973); J. Wess and B. Zumino, Nuclear Physics **B** 70, 39(1974).

[3] ALEPH Collaboration, D. Decamp *et al.*, Physics Letters **B** 236 (1990) 86;
ALEPH Collaboration, D. Decamp *et al.*, Physics Letters **B** 244 (1990) 541;
ALEPH Collaboration, D. Decamp *et al.*, Physics Reports 216 (1992) 253;
DELPHI Collaboration, P, Abreu *et al.*, Physics Letters **B** 247 (1990) 157 ;
OPAL Collaboration, K. Ahmet *et al.*, Physics Letters **B** 240 (1990) 261;
OPAL Collaboration, K. Ahmet *et al.*, Physics Letters **B** 248 (1990) 211;
L3 Collaboration, B. Aveda *et al.*, Physics Letters **B** 233 (1989) 530;
L3 Collaboration, M. Acciarri *et al.*, Physics Letters **B** 350 (1995) 109.

[4] S. Katsanevas, in the LEP200 workshop report, CERN 96/01 (1996).

[5] L3 Collaboration, M. Acciarri *et al.*, Physics Letters **B** 377 (1996) 289.

[6] S. Banerjee *et al.*, L3 Internal note 2111, 1996.

Statement Required Under Ordinance 0.770

I hereby state that the work presented in this thesis has not been submitted to this or any other university for Ph.D or any other degree.

Statement Required Under Ordinance 0.771

Statement No. 1 regarding new facts:

This is the first time SUSY particles were searched in these high energy ranges and in a very clean e^+e^- collider environment. Lower limit on right handed scalar electron mass has been determined to be 69 GeV.

Statement No. 2 regarding author's contribution in joint work:

The L3 experiment is a large collaborative effort comprising of around 500 physicists from about 50 institutes/laboratories all over the world. Many individuals have contributed significantly towards the successful joint venture in the fields of detector design, building and maintenance as well as software development, both online and off-line, without which this work would not have been realized. The scientists and engineers of the CERN accelerator divisions contributed towards the excellent performances of the LEP collider over the years. I have carried out these analyses under the supervision of Prof. SN Ganguli.

The major contributions of the author in this study are :

- Lepton identification over a wide range of energy from 2 GeV to 86 GeV.
- Choice of different kinematic variables to identify SUSY signals from the standard model background.
- Determination of selection efficiencies and systematic errors in the data analysis.
- Parametrisation of efficiencies in terms of M_{SUSY} and $M_{\tilde{\chi}^0_1}$.
- Limits on the production cross section of scalar leptons.
- Determination of lower limit on masses of scalar leptons.

Signature of the Candidate *Signature of the Supervisor*

List of Figures

2.1 Loops contribution to the self energy of the Higgs boson 6
2.2 Sfermion loops contribution to the Higgs self energy 7
2.3 Chargino production and decay diagrams 12
2.4 Neutralino production and decay diagrams 13
2.5 Slepton production and decay diagrams 14
2.6 Evolution of coupling constants and SUSY particle masses 17
2.7 $\tilde{e}^+_R\tilde{e}^-_R$ production cross section at $\sqrt{s} = 161.3$ GeV 18
2.8 Results from HERA (H1) 20
2.9 Exclusion plots from Tevatron data 21
2.10 Loop diagrams for b $\rightarrow$ s γ process 22

3.1 The LEP collider at CERN 24
3.2 LEP injection scheme 25

4.1 L3 detector 34
4.2 Silicon Microvertex Detector... 35
4.3 Time Expansion Chamber.. 36
4.4 Momentum resolution in central tracking system 38
4.5 BGO crystal and L3 electromagnetic calorimeter. 40
4.6 Energy and position resolution of barrel BGO calorimeter. 40
4.7 Upgraded forward tagger of the L3 41
4.8 Lead-scintillating fibre calorimeter 42
4.9 R-Z view of hadron calorimeter 44
4.10 Wire grouping for the HCAL barrel 45
4.11 R-Φ view of an octant of precision chamber 47
4.12 Sagitta measurement in P chamber 48
4.13 Two layers of drift cells in muon Z-chamber 48
4.14 Forward backward muon chamber of L3 50
4.15 Drift chamber in F/B MUCH 50
4.16 Muon momentum resolution 51
4.17 A Bhabha event in the luminosity monitor 52

4.18 Schematic view of the VSAT ... 53
4.19 XY-view of two VSAT boxes ... 53
4.20 L3 detector resolution ... 54

5.1 L3 online trigger system ... 56
5.2 L3 calorimeter segmentation for trigger signals ... 57

6.1 L3 event reconstruction data flow ... 70

7.1 Particle identification in L3 detector ... 73
7.2 Track in central tracking system ... 74
7.3 EM shower shape variables ... 75
7.4 DCA of track and Φ extrapolation ... 75
7.5 Muon in L3 detector ... 76
7.6 Tau as a narrow hadronic jets ... 77
7.7 Kinematic variables : ETTT and θ_{acop} ... 80
7.8 Kinematic variables : E_{30° and $\sin\theta_{\mathrm{miss}}$ ... 81
7.9 Kinematic variables : $\not{E}^{\mathrm{b}}_{60^\circ}$ and $\not{E}^{\perp}_{25^\circ}$ ... 81
7.10 Signal vs backgrounds : $\mathrm{M_{Vis}}/\sqrt{\mathrm{s}}$, $\mathrm{E_{TRAN}}$, $[\mathrm{E}_\perp^{\ell_1} + \mathrm{E}_\perp^{\ell_2}]/\mathrm{E_{vis}}$ and ETTT ... 82
7.11 Signal vs backgrounds : $\mathrm{E_{electron(1)}}/\mathrm{E_b}$, $\theta^{\mathrm{lep}}_{\mathrm{acop}}$ $\mathrm{M_{Invis}}/\sqrt{\mathrm{s}}$ and $\sin\theta_{\mathrm{miss}}$ ... 83
7.12 Production cross sections of the Standard Model processes ... 87
7.13 Slepton efficiencies at $\sqrt{\mathrm{s}}$ = 130 - 136 GeV ... 90
7.14 SM backgrounds at $\sqrt{\mathrm{s}}$ = 130 - 136 GeV ... 91
7.15 Selection efficiencies at $\sqrt{\mathrm{s}}$ = 161 GeV ... 94
7.16 Trigger efficiencies at $\sqrt{\mathrm{s}}$ = 161 GeV ... 95
7.17 Overall efficiencies at $\sqrt{\mathrm{s}}$ = 161 GeV ... 96
7.18 Residual SM backgrounds at $\sqrt{\mathrm{s}}$ = 161 GeV ... 97
7.19 Combined efficiencies at $\sqrt{\mathrm{s}}$ = 172 GeV ... 98
7.20 Residual SM backgrounds at $\sqrt{\mathrm{s}}$ = 172 GeV ... 99

8.1 Comparison of data and SM Monte Carlo at $\sqrt{\mathrm{s}}$ = 130 GeV ... 106
8.2 Comparison of data and SM Monte Carlo at $\sqrt{\mathrm{s}}$ = 130 GeV ... 107
8.3 Comparison of data and SM Monte Carlo at $\sqrt{\mathrm{s}}$ = 161 GeV ... 108
8.4 Comparison of data and SM Monte Carlo at $\sqrt{\mathrm{s}}$ = 172 GeV ... 109
8.5 Comparison of data and SM Monte Carlo at $\sqrt{\mathrm{s}}$ = 172 GeV ... 110
8.6 Comparison of data and SM Monte Carlo at $\sqrt{\mathrm{s}}$ = 172 GeV ... 111
8.7 Comparison of data and SM Monte Carlo at $\sqrt{\mathrm{s}}$ = 172 GeV ... 112
8.8 The candidate event in the $\mathrm{e^+e^-} \to \tilde{\tau}^+\tilde{\tau}^-$ channel at $\sqrt{\mathrm{s}}$ = 136 GeV ... 113
8.9 $\mathrm{e^+e^-} \to \tilde{\chi}_1^+\tilde{\chi}_1^-$ candidate event at $\sqrt{\mathrm{s}}$ = 172 GeV ... 116
8.10 $\mathrm{e^+e^-} \to \tilde{\tau}^+\tilde{\tau}^-$ candidate event at $\sqrt{\mathrm{s}}$ = 172 GeV ... 117

9.1 95 % CL exclusion plot at $\sqrt{s}$ = 130 - 136 GeV 121
9.2 Parametrisation of efficiencies at $\sqrt{s}$ = 161 GeV 123
9.3 Parametrisation of efficiencies at $\sqrt{s}$ = 172 GeV 124
9.4 Upper bounds on cross sections for sleptons 126
9.5 Exclusion plots from $\tilde{e}_R$ and $\tilde{\mu}_R$ searches 127
9.6 Exclusion plots in SUSY particles mass plane 128
9.7 Exclusion plots in SUSY parameter space 129

B.1 Poisson upper limit on signal events 135

D.1 Ratio of $\tilde{\ell}^+\tilde{\ell}^-$ production at $\sqrt{s}$ = 161 GeV and 172 GeV 137

List of Tables

2.1 SM gauge groups and gauge fields 3
2.2 List of fermionic weak eigenstates and their quantum numbers 4
2.3 Chiral Superfields of the MSSM 7
2.4 Vector Superfields of the MSSM 7

3.1 Radio frequency cavity used at different $\sqrt{s}$ 27
3.2 Comparison of beam properties with 8 and 12 bunches per beam 28
3.3 Uncertainty on LEP 2 beam energy calibration 31

4.1 Properties of BGO crystal 38

5.1 Level 1 energy trigger 59
5.2 Level 1 muon trigger 60

7.1 Criteria of a track to identify leptons 73
7.2 Electron selection criteria 76
7.3 Muon selection criteria 77
7.4 Selection of hadronic jets in tau decay 78
7.5 Loose cuts to study the kinematic variables 80
7.6 Loose cuts for SUSY selection 85
7.7 Cross sections of the Standard Model processes at three $\sqrt{s}$ 86
7.8 Slepton pair selection at $\sqrt{s}$ = 130 - 136 GeV 88
7.9 Improved slepton selection criteria at $\sqrt{s}$ = 136 GeV 89
7.10 $e^+e^- \to \tilde{e}^+\tilde{e}^-$ and $e^+e^- \to \tilde{\mu}^+\tilde{\mu}^-$ selection at $\sqrt{s}$ = 161 GeV 92
7.11 $e^+e^- \to \tilde{\chi}_1^+\tilde{\chi}_1^-$ and $e^+e^- \to \tilde{\tau}^+\tilde{\tau}^-$ selection at $\sqrt{s}$ = 161 GeV 92
7.12 Effect of different cuts at $\sqrt{s}$ = 161 GeV 93
7.13 $e^+e^- \to \tilde{e}^+\tilde{e}^-$ and $e^+e^- \to \tilde{\mu}^+\tilde{\mu}^-$ selection at $\sqrt{s}$ = 172 GeV 93
7.14 $e^+e^- \to \tilde{\chi}_1^+\tilde{\chi}_1^-$ and $e^+e^- \to \tilde{\tau}^+\tilde{\tau}^-$ selection at $\sqrt{s}$ = 172 GeV 97
7.15 Effect of different cuts at $\sqrt{s}$ = 172 GeV 99

8.1 Status of LEP run and L3 data taking at $\sqrt{s}$ = 130 – 172 GeV 104
8.2 Characteristics of the candidate event at $\sqrt{s}$ = 136 GeV 114

8.3 Observed and expected number of events at $\sqrt{s}$ = 130 - 136 GeV 114
8.4 Characteristics of the candidate events at $\sqrt{s}$ = 172 GeV 115
8.5 Observed and expected number of events at $\sqrt{s}$ = 161 – 172 GeV 115

C.1 Fitted values of parametrisation of selection efficiencies 136

Chapter 1

Introduction

CERN's Large Electron Positron Collider (LEP) is designed for precision test of the Standard Model (SM) as well as to search for new physics beyond the SM. Out of several theoretical models, Supersymmetric theory is the most favourite model to overcome the shortcomings of the SM. Tevatron, HERA, LEP 1 (in the first phase, LEP ran at the centre of mass energies ($\sqrt{s}$) around Z-peak ($M_Z = 91.187$ GeV) from September 1989 to October 1995) searched for supersymmetric particles and consequently constrained certain parameters of the model. Charged scalar leptons and charginos have been ruled out by LEP 1 upto a mass of $\approx \frac{M_Z}{2}$.

Since November 1995, LEP collider has been running beyond the Z-peak (LEP 2). With the increase of $\sqrt{s}$, particles of higher masses beyond $\frac{M_Z}{2}$ became kinematically accessible. In November 1995 LEP ran at $\sqrt{s} = 130$ - 136 GeV and in 1996 it was operated with the $\sqrt{s}$ ranging between 161 GeV and 172 GeV. Searches have been carried out for new physics within the framework of Grand Unified Theory (GUT) motivated Minimal Supersymmetric Standard Model (MSSM). The searches looked for right handed scalar leptons ($\tilde{\ell}_R$) and chargino ($\tilde{\chi}_1^{\pm}$), in the leptonic decay mode from $\approx M_Z/2$ to the kinematic limit of production.

A brief outline of the thesis is given below :

Chapter 2 discusses the SM, its successes and drawbacks and the role of supersymmetry in overcoming the problems in the SM. It also describes the GUT motivated MSSM model, its free parameters, constraints from previous experimental results and theoretical calculations.

Chapter 3 describes the LEP collider. The chain of accelerators preceding the LEP and the upgradation needed to go from the $\sqrt{s} \sim M_Z/2$ to 172 GeV are also discussed.

Chapter 4 presents a description of the L3 detector, structure and motivation to design different subdetectors and their performances.

Chapter 5 describes online trigger criteria for the detector.

Chapter 6 describes the Monte Carlo (MC) simulation of physics events. It also describes reconstruction of MC events as well as the L3 data events from the recorded digitised detector responses.

Chapter 7 gives in detail the selection procedure : identification of leptons, choice of kinematic variables to distinguish the SUSY signals from the SM (background) processes, various distributions for both signals and backgrounds, preselections, multidimensional optimisation procedure for the final selection of SUSY signals, results of the selection procedure using the MC samples for different $\sqrt{s}$ and error calculations.

Chapter 8 describes briefly LEP runs and L3 data collections during the years 1995 and 1996 and the searches for supersymmetric particles.

Chapter 9 interprets the search results from these high energy runs. Lack of evidence of new physics gives an upper limit of production cross section of charged scalar leptons which decay to ordinary charged leptons and neutralinos, mass limit on right handed selectron ($\tilde{e}_R$) and various exclusion plots in the framework of MSSM.

Chapter 10 summarises the main results of the work and future possibility of such searches.

The main contribution of the author in this thesis are as follows : (i) in the choice of kinematic variables to distinguish the SUSY signals from the SM backgrounds and the set up of the selection criteria for SUSY searches (*chapter 7*), (ii) search of the SUSY particles from the L3 data recorded in the years 1995 and 1996 (*chapter 8*) and (iii) estimation of the upper limits on the production cross sections of the scalar leptons and various exclusion plots in the SUSY parameter space (*chapter 9*).

Chapter 2

Theoretical Overview

2.1 The Standard Model (SM)

The Standard Model [1], is a model of fundamental interactions which explains almost all the existing results of High Energy experiments.

The SM is based on a nonabelian gauge theory and consists of an unified theory of weak and electromagnetic interactions, known as the *Glashaw-Salam-Weinberg* (GSW) theory and a theory of strong interactions, *Quantum Chromodynamics* (QCD).

The Lagrangian of this model is constructed to be invariant under an $\mathrm{SU(3)_C} \times \mathrm{SU(2)_L} \times \mathrm{U(1)_Y}$ gauge transformation, where $\mathrm{SU(3)_C}$, $\mathrm{SU(2)_L}$, and $\mathrm{U(1)_Y}$ are the transformation groups corresponding to quantum numbers called colour, weak isospin and weak hypercharge respectively. Details of these groups are given in table 2.1.

Interaction	Group	Generator	Gauge fields	Field strength
Strong	$\mathrm{SU(3)_C}$	$\frac{1}{2}\lambda_\mathrm{a}(\mathrm{a} = 1,2..,8)$	$g^a_\mu(a = 1,2,..,8)$	g_s
Electro –	$SU(2)_L$	$\frac{1}{2}\sigma_i(i = 1,2,3)$	$W^i_\mu(i = 1,2,3)$	g
Weak	$U(1)_Y$	$\frac{1}{2}Y$	B_μ	g'

Table 2.1: SM gauge groups and gauge fields : λ_a are the Gell-Mann matrices and σ_i are the Pauli spin matrices.

Gauge fields are vector fields and gauge invariance requires the gauge bosons to be massless.

The known basic constituents of matter are fermions (spin 1/2) : (a) leptons, which are freely propagating particles and (b) quarks, which are 'confined' objects, always bound to other quarks (and antiquarks). Charged leptons take part in electromagnetic and weak interactions and neutral leptons only in weak interactions, while quarks take part in strong as well as in electroweak interactions. A list of fermionic weak eigenstates in SM and their basic quantum numbers is given in table 2.2.

Families	Generation 1st	2nd	3rd	T_3	Y	Q
Leptons	$\begin{pmatrix} \nu_e \\ e \end{pmatrix}_L$	$\begin{pmatrix} \nu_\mu \\ \mu \end{pmatrix}_L$	$\begin{pmatrix} \nu_\tau \\ \tau \end{pmatrix}_L$	$+1/2$ $-1/2$	-1 -1	0 -1
	e_R	μ_R	τ_R	0	-2	-1
Quarks	$\begin{pmatrix} u \\ d \end{pmatrix}_L$	$\begin{pmatrix} c \\ s \end{pmatrix}_L$	$\begin{pmatrix} t \\ b \end{pmatrix}_L$	$+1/2$ $-1/2$	$+1/3$ $+1/3$	$+2/3$ $-1/3$
	u_R	c_R	t_R	0	$+4/3$	$+2/3$
	d_R	s_R	b_R	0	$-2/3$	$-1/3$

Table 2.2: List of fermionic weak eigenstates and their quantum numbers : T_3, Y and Q are the Weak Isospin, Hypercharge and electric charge respectively.

The SM Lagrangian provides massless fermions and gauge bosons. But the charged leptons, quarks and also weak vector bosons (Z and $W^{\pm}$) are massive. To generate the masses of the weak gauge bosons Z and $W^{\pm}$ one needs to add a complex doublet scalar fields to the SM. The scalar potential may then be arranged to have a spontaneous symmetry breaking (where the choice of an unique physical ground state leads to a Lagrangian which is not gauge invariant). The fields may then be reparametrised so that three out of four degrees of freedom of the doublet give non zero values of mass of $W^{\pm}$ (M_W) and mass of Z (M_Z). The scalar degrees of freedom thus become the longitudinal polarisations of massive vector bosons. This is called the Higgs mechanism. One remaining degree of freedom of the doublet corresponds to the existence of a massive neutral scalar particle. This is the *Higgs* boson. Gauge boson masses are related to the Higgs vacuum expectation value denoted by v ($\sim$ 246 GeV).

The Higgs boson mass can be written as $m_H = \lambda v$, where λ is a constant appearing in the Higgs potential with an unknown value; the mass is therefore unknown as well. Experimentally its mass is excluded upto 70.7 GeV [2] with the current data.

The Higgs mechanism also provides mass to all fermions, expressed as $m_f = \lambda_f v$, where λ_f is the so-called Yukawa coupling of the species f to the scalar Higgs boson.

2.2 Why go Beyond the Standard Model ?

The Standard Model has been experimentally verified except the detection of the Higgs boson, which may be too heavy to be accessible to experiments at the currently available energies. Then why has so much time and energy been devoted to looking for signatures of *new physics* beyond the SM ? The answer is that the SM is a combination of some theoretical assumptions and several phenomenological inputs, as a result the model can not be the ultimate theory of fundamental interactions (there are in all 19 free parameters in this model). So, physicists have tried to make models which address some of the untouched problems in the SM. In the same time all these models have to reproduce the SM results which have been verified as well as predict correctly the experimental results which are not well explained by the SM (e.g., $\sin^2\theta_{\rm eff}^{\rm lept}$($\rm A_{LR}$ [3]), $\rm A_{FB}^{0,\,b}$ [4]). Usually these theories predict new particles and/or new couplings which may be used to test the model.

Some of the unanswered theoretical questions in the SM are :

- Why are the left handed fermions SU(2) doublets and right handed ones SU(2) singlets ?
- Why are there three colours ? Why is there replication among fermion families, but not in the scalar sector ? Why are there just three fermion generations ?
- Why do the fermion masses, Cabibbo-Kobayashi-Maskawa (CKM) angles and the weak mixing angle have the values they do ?
- Why do the quarks participate in the strong interactions, but leptons do not ?

There are a few experimental results which do not match well with the SM predictions e.g., (a) the solar and atmospheric neutrino puzzles [5], (b) Excess of events at very high x and $\rm Q^2$ in the ep collisions at HERA [6], (c) the $\rm e^+e^-$ Collider results as mentioned above etc. Apart from the non-discovery of the Higgs boson which may be just a matter of Higgs being too heavy and perhaps the solar and atmospheric neutrino problems, none of these are serious drawback at the moment.

2.2.1 The fine-tuning Problem

A more serious drawback in the SM is the high mass of the Higgs bosons due to the bosonic and/or fermionic loop corrections. Let us consider the fermionic loop. The contribution to the Higgs mass from fermion loops, as shown in figure 2.1, due to the two-point function of the SM Higgs field, is given by [7]

$$\delta m_{_H} = -\,2N(f)\lambda_f^2\int_{m_f}^{\Lambda}\frac{d^4k}{(2\pi)^4}\left[\frac{1}{k^2-m_f^2}+\frac{2m_f^2}{(k^2-m_f^2)^2}\right] \tag{2.1}$$

where N(f) is the multiplicity (summation over colour factor) and $\lambda_{\rm f}$ is the $\rm Hf\bar{f}$ coupling. The first term of the above equation is *quadratically* divergent ! If we replace the cut-off scale Λ by M_{Planck} (Planck scale energy), the resulting correction would be some 30 orders of magnitude larger than the physical Higgs boson mass which is expected to be $\leq$ 1 TeV (to preserve unitarity of WW scattering amplitudes [8]). There is no symmetry in the

SM that protects the Higgs mass in the way that the photon and the fermion masses are protected by gauge and chiral symmetries respectively. One would then need *fine tuning* to cancel a very large mass due to loop corrections. Moreover the fine tuning would have to be done afresh in different orders of perturbation theory. This is the technical aspect of *hierarchy problem*; scalar masses are driven to be close to the highest mass scale of the theory.

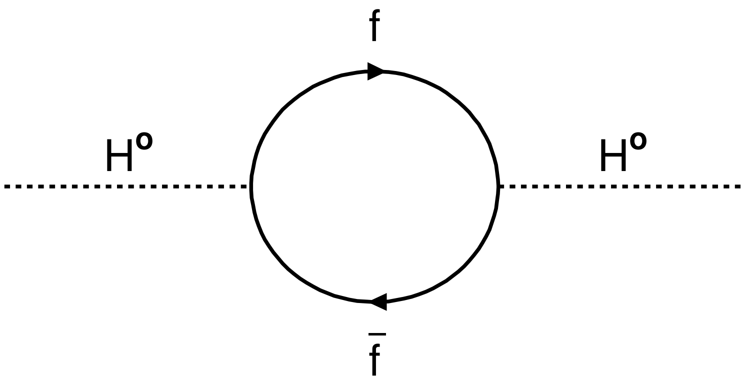

Figure 2.1: A fermion anti-fermion loops which contribute to the self energy of the Higgs boson in the Standard Model.

2.3 Supersymmetry (SUSY)

Supersymmetric field theories are able to solve the fine tuning problem. Supersymmetry (SUSY) [9] is a novel type of symmetry that mixes bosonic degrees of freedom with the fermionic degrees of freedom and vice versa. Thus in SUSY each fermion has a bosonic partner and vice versa. For each particle which contributes to a Feynman loop diagram (figure 2.1), there exits a second loop (figure 2.2) which is also quadratically divergent. The fermion loops have a factor of (-1) compared to the bosonic loops, thus all loop graphs cancel for exact supersymmetry. In exact supersymmetry, the masses of the supersymmetric partners are equal to the masses of the SM particles. It has been shown that the divergence cancellation holds to all orders of perturbation theory. These are called non-renormalisation theorems. Even when exact supersymmetry is broken and the masses are different, the dangerous quadratic divergence still cancel.

2.3.1 The Minimal Supersymmetric Standard Model (MSSM)

The simplest supersymmetric generalisation of the Standard Model is the Minimal Supersymmetric Standard Model (MSSM). It is a supersymmetric theory based on the standard $\mathrm{SU(3)_C \times SU(2)_L \times U(1)_Y}$ gauge group with electroweak symmetry spontaneously

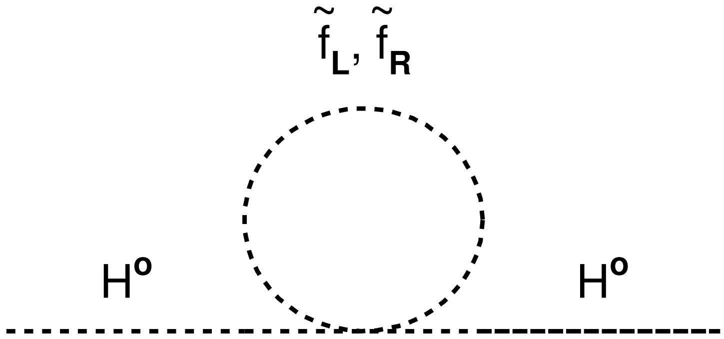

Figure 2.2: Sfermion loops contribution to the Higgs self energy.

broken via vacuum expectation values of *two* different Higgs doublets. The particle content of the MSSM is shown in tables 2.3 and 2.4. The theory requires two different Higgs doublets for the following reasons :

- A model with a single Higgs doublet superfield has nonvanishing gauge anomalies arising from fermion triangle diagrams.
- Superpotential does not allow introduction of the Hermitian conjugate of a Higgs superfield (or of any other chiral superfield). So to give masses to both **up**- and **down**-type quarks, one needs two Higgs doublets.

Superfield	$SU(3)_C$	$SU(2)_L$	$U(1)_Y$	Particle content
$\hat{Q}$	3	2	$\frac{1}{3}$	$(\mathrm{u}_L, \mathrm{d}_L), (\tilde{\mathrm{u}}_L, \tilde{\mathrm{d}}_L)$
$\hat{U}^c$	$\bar{3}$	1	-$\frac{4}{3}$	$\bar{\mathrm{u}}_R, \tilde{\mathrm{u}}^*_R$
$\hat{D}^c$	$\bar{3}$	1	$\frac{2}{3}$	$\bar{\mathrm{d}}_R, \tilde{\mathrm{d}}^*_R$
$\hat{L}$	1	2	-1	$(\nu_L, \mathrm{e}_L), (\tilde{\nu}_L, \tilde{\mathrm{e}}_L)$
$\hat{E}^c$	1	1	2	$\bar{\mathrm{e}}_R, \tilde{\mathrm{e}}^*_R$
$\hat{H}_1$	1	2	-1	$(\mathrm{H}_1^\circ, \mathrm{H}_1^-)$, $(\tilde{\mathrm{h}}_1^\circ, \tilde{\mathrm{h}}_1^-)$
$\hat{H}_2$	1	2	1	$(\mathrm{H}_2^+, \mathrm{H}_2^\circ)$, $(\tilde{\mathrm{h}}_2^+, \tilde{\mathrm{h}}_2^\circ)$

Table 2.3: Chiral Superfields of the MSSM.

Superfield	$SU(3)_C$	$SU(2)_L$	$U(1)_Y$	Particle content
$\hat{G}^a$	8	1	0	$g,\ \tilde{g}$
$\hat{W}^i$	1	3	0	$W_i, \tilde{w}_i$
$\hat{B}$	1	1	0	$B,\ \tilde{b}$

Table 2.4: Vector Superfields of the MSSM.

2.3.2 Lagrangian of the Minimal Supersymmetric Standard Model

Having specified the superfields of the theory, the next step is to construct the supersymmetric Lagrangian. There is very little freedom in the allowed interactions between the ordinary particles and their superpartners. Kinematic part of the Lagrangian for the global supersymmetry can be written in four-component spinor notation [14]

$$\mathcal{L}_{\mathrm{KE}} = \sum_{\mathrm{i}} \left\{ (\mathrm{D}_\mu \, \mathrm{S_i})^\dagger \, (\mathrm{D}^\mu \, \mathrm{S_i}) + \mathrm{i} \, \bar{\psi}_{\mathrm{i}} \, \gamma^\mu \, \mathrm{D}_\mu \, \psi_{\mathrm{i}} \right\} + \sum_{\mathrm{A}} \left\{ -\frac{1}{4} \mathrm{F}^{\mathrm{A}}_{\mu\nu} \, \mathrm{F}^{\mu\nu\,\mathrm{A}} + \frac{\mathrm{i}}{2} \bar{\lambda}_{\mathrm{A}} \, \gamma^\mu \, \mathrm{D}_\mu \, \lambda_{\mathrm{A}} \right\} \quad (2.2)$$

where D_μ is the $\mathrm{SU(3)_C \times SU(2)_L \times U(1)_Y}$ gauge covariant derivative, γ^μ are Dirac 4-matrices, ψ_{i} and $\mathrm{S_i}$ are the fermion fields of the SM and those of their superpartners, $F^A_{\mu\nu}$ is the Yang-Mills gauge field and λ_A is the Majorana gaugino superpartner of the corresponding gauge boson. The summation $\sum_i$ is over all fermion fields of the SM, their scalar partners and the 2 Higgs doublets with their fermion partners. The summation $\sum_A$ is over the $\mathrm{SU(3)_C}$, $\mathrm{SU(2)_L}$ and $\mathrm{U(1)_Y}$ gauge fields with their partners, Majorana fermions called *gauginos*.

The interaction between the chiral superfields of table 2.3, the gauginos and the gauge fields of table 2.4 are completely specified by the gauge symmetries and by the supersymmetry, as are the quadratic interactions of the scalar,

$$\mathcal{L}_{\mathrm{int}} = -\sqrt{2} \sum_{\mathrm{i,A}} g_{\mathrm{A}} \left(\mathrm{S_i^\dagger T^A} \bar{\psi}_{\mathrm{i\,L}} \, \lambda_{\mathrm{A}} + \mathrm{h.c.} \right) - \frac{1}{2} \sum_{\mathrm{A}} \left(\sum_{\mathrm{i}} g_{\mathrm{A}} \, \mathrm{S_i^\dagger T^A S_i} + \xi_{\mathrm{A}} \right)^2 \quad (2.3)$$

where $\mathrm{T^A}$ is the group generator in the appropriate representation, g_A is the relevant gauge coupling constant and ξ_{A} are constants which can be non-zero only for $\mathrm{U(1)_Y}$ gauge group factors.

The only freedom in constructing the supersymmetric Lagrangian (once the superfields and gauge symmetries are chosen) is contained in a function called the Superpotential (W). Superpotential gives rise to both the scalar potential and the Yukawa interactions of the fermions with the scalars [15],

$$\mathcal{L}_{\mathrm{W}} = -\sum_{\mathrm{i}} |\mathrm{F_i}|^2 - \frac{1}{2} \sum_{\mathrm{ij}} \left[\bar{\psi}_{\mathrm{i\,L}} \mathrm{A_{ij}} \, \psi_{\mathrm{j}} + \mathrm{h.c.} \right] \quad (2.4)$$

where $\mathrm{F_i} = \left. \frac{\partial \mathrm{W}}{\partial \hat{\mathrm{z}}_{\mathrm{i}}} \right|_{\hat{\mathrm{z}}_{\mathrm{i}} \to \mathrm{z_i}}$, $\mathrm{A_{ij}} = \left. \frac{\partial^2 \, \mathrm{W}}{\partial \hat{\mathrm{z}}_{\mathrm{i}} \, \partial \hat{\mathrm{z}}_{\mathrm{j}}} \right|_{\hat{\mathrm{z}} \to \mathrm{z}}$

and z_i is the scalar component of the chiral superfield $\hat{z}_i$. The usual approach is to write the most general $\mathrm{SU(3)_C \times SU(2)_L \times U(1)_Y}$ invariant superpotential with arbitrary coefficients for the interactions,

$$\begin{aligned} W = \; & \mu\, \varepsilon_{\alpha\beta}\, \hat{H}_1^\alpha\, \hat{H}_2^\beta + \varepsilon_{\alpha\beta} \left[h^l_{ij}\, \hat{H}_1^\alpha\, \hat{L}_i^\beta\, \hat{E}_j^c + h^d_{ij}\, \hat{H}_1^\alpha\, \hat{Q}_i^\beta\, \hat{D}_j^c + h^u_{ij}\, \hat{H}_2^\alpha\, \hat{Q}_i^\beta\, \hat{U}_j^c \right] \\ & + \varepsilon_{\alpha\beta} \left[\lambda_{ijk}\, \hat{L}_i^\alpha\, \hat{L}_j^\beta\, \hat{E}_k^c + \lambda'_{ijk}\, \hat{L}_i^\alpha\, \hat{Q}_j^\beta\, \hat{D}_k^c \right] + \lambda''_{ijk} \hat{U}_i^c\, \hat{D}_j^c\, \hat{D}_k^c \end{aligned} \tag{2.5}$$

where α, β are $SU(2)$ indices and i, j, k are the generation indices, μ is the Higgs mass parameter (often called as supersymmetric Higgsino mixing parameter), h_{ij}'s are co-efficients of scalar potential terms and λ_{ijk}'s are the co-efficients of Yukawa interaction terms. λ_{ijk} is antisymmetric with respect to the first two indices, while λ''_{ijk} is antisymmetric under the interchange of the last two. A bi-linear term $\hat{\mathrm{L}}\,\hat{\mathrm{H}}_2$ can also be included in the superpotential, but this can be rotated away by redefinition of the fields.

2.3.3 Supersymmetry Breaking

Exact symmetry predicts that superpartners have the same mass as their SM partners. However, no experimental evidence for the supersymmetric particle spectrum exists at present. This requires the supersymmetric partners to have a much larger mass than their SM counterparts. Thus, supersymmetry must be a broken symmetry. It is typically assumed that the SUSY breaking occurs at a very high scale. In the absence of an understanding of the origin of supersymmetry-breaking, it is parametrised by incorporating soft supersymmetry breaking terms consistent with the SM symmetries. 'Soft' means that they do not lead to quadratic divergence in the scalar self-energies. These terms have been classified by Girardello and Grisaru [16]. For the MSSM they consist of

- Gaugino mass terms $-\frac{1}{2}\mathrm{M}_\ell\, \bar{\lambda}_\ell\, \lambda_\ell$, where ℓ is labels of gaugino groups
- Scalar mass terms $-\mathrm{m}^2_{\phi_\mathrm{i}} \mid \phi_\mathrm{i} \mid^2$,
- Bilinear terms $-\mathrm{B}_\mathrm{ij}\, \phi_\mathrm{i}\, \phi_\mathrm{j}$ + h.c. and
- Trilinear scalar interactions $-\mathrm{A}_\mathrm{ijk}\, \phi_\mathrm{i}\, \phi_\mathrm{j}\, \phi_\mathrm{k}$ + h.c.

The complete set of soft SUSY breaking terms in the MSSM is given by the Lagrangian [16, 20],

$$\begin{aligned} -\mathcal{L}_{soft} = \; & \varepsilon_{\alpha\beta} \left(A^u_{ij}\, H_2^\alpha\, Q_i^\beta\, U_j^c + A^d_{ij}\, H_1^\alpha\, Q_i^\beta\, D_j^c + A^l_{ij}\, H_1^\alpha\, L_i^\beta\, E_j^c + h.c. \right) \\ & + (m^2_Q)_{ij}\, Q_i^\dagger\, Q_j + (m^2_u)_{ij}\, (U_i^c)^\dagger\, U_j^c + (m^2_d)_{ij}\, (D_i^c)^\dagger\, D_j^c \\ & + (m^2_L)_{ij}\, (L_i^c)^\dagger\, L_j^c + (m^2_e)_{ij}\, (E_i^c)^\dagger\, E_j^c + \frac{1}{2} \left(M_1\, \bar{\tilde{b}}\, \tilde{b} + M_2\, \bar{\tilde{w}}\, \tilde{w} + M_3\, \bar{\tilde{g}}\, \tilde{g} \right) \\ & + m_1^2 \mid H_1 \mid^2 + m_2^2 \mid H_2 \mid^2 + \left(B\mu\, \varepsilon_{\alpha\beta}\, H_1^\alpha\, H_2^\beta + h.c. \right) \end{aligned} \tag{2.6}$$

This Lagrangian has arbitrary square masses for the scalars (m^2_Q, m^2_u, m^2_d, m^2_L, m^2_e, m^2_1 and m^2_2) and gauginos (M^2_1, M^2_2 and M^2_3) and also arbitrary tri-linear (A^u, A^d and A^l) and bi-linear (B) mixing terms. $\mathcal{L}_{soft}$ has clearly broken the supersymmetry since the SUSY partners of the ordinary particles have been given arbitrary masses. This has come at the expense of introducing a large number of unknown parameters (more than 50!).

2.3.3.1 The Higgs Sector and Electroweak Symmetry Breaking

The scalar potential involving Higgs bosons is [17]

$$\begin{aligned} V_H = & \left(|\,\mu\,|^2 + m_1^2\right)|H_1|^2 + \left(|\,\mu\,|^2 + m_2^2\right)|H_2|^2 + B\,\mu\left(\varepsilon_{\alpha\beta}\,H_1^\alpha\,H_2^\beta + h.c.\right) \\ & + \frac{g^2 + g'^2}{8}\left(|H_1|^2 - |H_2|^2\right)^2 + \frac{1}{2}g^2\,|H_1^\dagger\,H_2\,|^2 \end{aligned} \tag{2.7}$$

So the Higgs potential of the SUSY model can be seen to depend on three independent parameters $((|\,\mu\,|^2 + \mathrm{m}_1^2)\,,\ (|\,\mu\,|^2 + \mathrm{m}_2^2)\,,\ \mathrm{B}\,\mu)$, where B is a new mass parameter. Clearly $B\mu = 0$ implies unbroken SUSY. For the broken symmetry parameters must satisfy the relation

$$2\,(B\,\mu)^2 > \left(|\,\mu\,|^2 + m_1^2\right)\left(|\,\mu\,|^2 + m_2^2\right) \tag{2.8}$$

We assume that these conditions are met. When the symmetry is spontaneously broken the neutral components of the Higgs doublets get vacuum expectation values

$$\langle H_1^\circ \rangle \equiv v_1 \quad \text{and} \quad \langle H_2^\circ \rangle \equiv v_2$$

When the electroweak symmetry is broken, the W and Z gauge bosons get masses which are fixed by v_1 and v_2 e.g.,

$$M_W^2 = \frac{g^2}{2}\left(v_1^2 + v_2^2\right)$$

After the symmetry-breaking and the Higgs mechanism are allowed to operate, three out of eight degrees of freedom are absorbed by $W^\pm$ and Z bosons to get their longitudinal polarisations, leaving five degrees of freedom, a charged Higgs boson ($H^\pm$), a CP-odd neutral Higgs boson (A) and two CP-even neutral Higgs bosons (h and H).

After fixing $(v_1^2 + v_2^2)$ with the W mass, the Higgs sector can be described by two additional parameters. The usual choice is $tan\,\beta \equiv v_2/v_1$ and M_A, the mass of pseudoscalar Higgs boson, the masses of other scalars being [18]

$$\begin{aligned} M_{h,H}^2 &= \frac{1}{2}\left[M_A^2 + M_Z^2 \pm \left\{(M_A^2 + M_Z^2)^2 - 4\,M_A^2\,M_Z^2\,cos^2(2\,\beta)\right\}^{1/2}\right] \\ M_{H^\pm} &= M_W^2 + M_A^2 \end{aligned} \tag{2.9}$$

Equation 2.9 predicts $\mathrm{M_h} \leq \mathrm{M_Z}$ but radiative corrections [19] have increased the bound upto about 130 GeV.

2.3.3.2 The Chargino Sector

The spin $\frac{1}{2}$ partners of the $W^{\pm}$ bosons, called Winos ($\tilde{w}^{\pm}$) and the spin $\frac{1}{2}$ partners of the charged Higgs bosons, called Higgsinos ($\tilde{h}^{\pm}$) have the same quantum numbers and hence can mix. The physical mass eigenstates $\tilde{\chi}^{\pm}_{1,2}$, are linear combinations formed by diagonalizing the mass matrix and are usually called *charginos*. In the $\tilde{w}^{\pm} - \tilde{h}^{\pm}$ basis the chargino mass matrix is

$$M_{\tilde{\chi}^{\pm}} = \begin{pmatrix} M_2 & \sqrt{2}\, M_W \, sin\beta \\ \sqrt{2}\, M_W \, cos\beta & \mu \end{pmatrix} \tag{2.10}$$

The masses are then

$$M^2_{\tilde{\chi}^{\pm}_{1,2}} = \frac{1}{2}\left\{ M_2^2 + 2M_W^2 + \mu^2 \mp \left[\left(M_2^2 - \mu^2\right)^2 + 4M_W^2 \, cos^2 2\beta + 4M_W^2 \left(M_2^2 + \mu^2 + 2\,\mu M_2 \, sin\, 2\,\beta\right)\right]^{1/2} \right\} \tag{2.11}$$

and are extremely sensitive to the values of M_2, μ and $\tan\beta$.

By convention $\tilde{\chi}^{\pm}_1$ is the lighter chargino. Production and decay mechanisms [10] at an e^+e^- collider are shown in figure 2.3. The main $\tilde{\chi}^{\pm}_1$ decay mode is $\tilde{\chi}^{\pm}_1 \rightarrow \tilde{\chi}^{\circ}_1 \, W^{\pm *}$. Other two decay modes are specific to accidental features of the spectrum, such as the existence of a scalar charged lepton or scalar neutrino lighter than the chargino, in which case the decay modes $\tilde{\chi}^{\pm}_1 \rightarrow \tilde{\ell}\, \nu_L$ or $\tilde{\chi}^{\pm}_1 \rightarrow \ell\, \tilde{\nu}_L$ would have branching ratio close to 1. Chargino can decay to the lighter Higgs too, if kinematically allowed. In these searches only the first decay mode has been chosen, assuming that sfermions and the lightest Higgs boson are all heavier than the chargino.

2.3.3.3 The Neutralino Sector

In the neutral fermion sector, the neutral fermion partners of the B and W^3 gauge bosons, $\tilde{b}$ and $\tilde{w}^3$, can mix with the neutral fermion partners of the Higgs bosons, $\tilde{h}^{\circ}_1$ and $\tilde{h}^{\circ}_2$. Hence the physical states, neutralinos ($\tilde{\chi}^{\circ}_i$), are found by diagonalizing the 4×4 mass matrix,

$$M_{\tilde{\chi}^{\circ}_i} = \begin{pmatrix} M_1 & 0 & -M_Z \, cos\beta \, s_w & M_Z \, sin\beta \, s_w \\ 0 & M_2 & M_Z \, cos\beta \, c_w & -M_Z \, sin\beta \, c_w \\ -M_Z \, cos\beta \, s_w & M_Z \, cos\beta \, c_w & 0 & -\mu \\ M_Z \, sin\beta \, s_w & -M_Z \, sin\beta \, c_w & -\mu & 0 \end{pmatrix} \tag{2.12}$$

where $c_w = cos\theta_W$ and $s_w = sin\theta_W$

Matrix elements are calculated in $\tilde{b}$, $\tilde{w}^3$, $\tilde{h}^{\circ}_1$ and $\tilde{h}^{\circ}_2$ basis. By convention $M_{\tilde{\chi}^{\circ}_1} < M_{\tilde{\chi}^{\circ}_2} < M_{\tilde{\chi}^{\circ}_3} < M_{\tilde{\chi}^{\circ}_4}$ and physical mass must be positive. This can be achieved by a chiral rotation of the neutralino fields. Physics involving neutralinos depends on M_1, M_2, μ and $\tan\beta$.

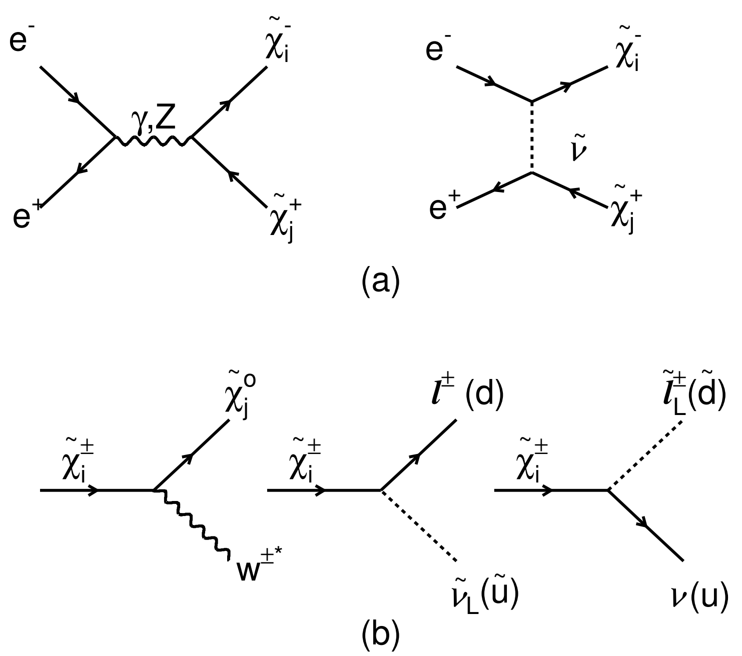

Figure 2.3: Feynman diagrams for chargino **(a)** Production and **(b)** Decay processes (ℓ, u and d imply charged lepton, up-type quark and down-type quark respectively).

The lightest neutralino $\tilde{\chi}_1^\circ$, is usually assumed to be the LSP (cosmological considerations [11] rule out an LSP with charge or colour, leaving only the lightest neutralino and the sneutrinos as possible LSP's). Production (at an e^+e^- collider) and decay mechanisms [12] are shown in figure 2.4. First decay mode has been used for these analyses.

2.3.3.4 The Squark and Slepton Sector

The left handed $SU(2)_L$ quark and lepton doublets have scalar partners

$$\tilde{Q} = \begin{pmatrix} \tilde{u}_L \\ \tilde{d}_L \end{pmatrix} \quad \text{and} \quad \tilde{L} = \begin{pmatrix} \tilde{\nu}_L \\ \tilde{e}_L \end{pmatrix}$$

Similarly the right handed quarks (u_R, d_R) have scalar partners denoted by $\tilde{u}_R$, $\tilde{d}_R$ and right handed electron (e_R) has a scalar partner $\tilde{e}_R$. The mass degeneracy is split by the soft mass terms of equation 2.6. Tri-linear (A) terms allow the scalar partners of left- and right-handed fermions to mix to form mass eigenstates. In the quark sector, the mixing between the scalar partners of left- and right-handed quark, is given by the mass squared matrix

$$M^2_{(\tilde{u},\tilde{d})} = \begin{pmatrix} \tilde{m}_Q^2 + m_{(u,d)}^2 + M_Z^2\left(T_3 - Q_{(u,d)}\sin^2\theta_W\right)\cos 2\beta & m_{(u,d)}\left(A^{(u,d)} - \mu\left(\cot\beta, \tan\beta\right)\right) \\ m_{(u,d)}\left(A^{(u,d)} - \mu\left(\cot\beta, \tan\beta\right)\right) & \tilde{m}_{(u,d)}^2 + m_{(u,d)}^2 + M_Z^2\, Q_{(u,d)}\sin^2\theta_W\cos 2\beta \end{pmatrix} \quad (2.13)$$

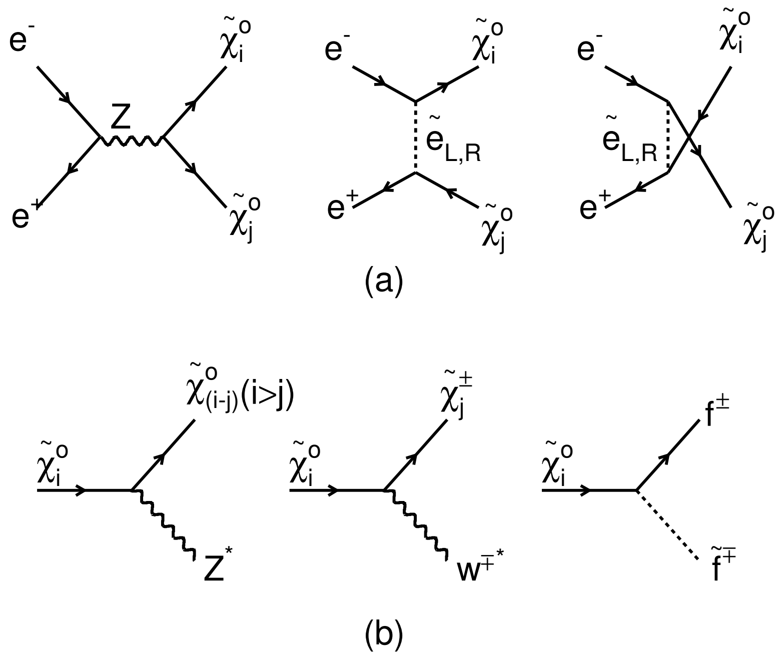

Figure 2.4: Feynman diagrams for neutralino (**a**) Production and (**b**) Decay processes.

Similarly for the charged lepton sector

$$M^2_{\tilde{\ell}} = \begin{pmatrix} \tilde{m}^2_L + m^2_\ell - M^2_Z \left(\frac{1}{2} - \sin^2\theta_W\right) cos2\beta & m_\ell \left(A^\ell - \mu \, tan\,\beta\right) \\ m_\ell \left(A^\ell - \mu \, tan\,\beta\right) & \tilde{m}^2_\ell + m^2_\ell - M^2_Z \sin^2\theta_W \, cos2\beta \end{pmatrix} \tag{2.14}$$

The mixing effects are proportional to the relevant fermion masses and hence will be largest in the third generation. For the others, neglecting mixing the diagonal L- and R-type sfermion masses are given by

$$\begin{aligned} M^2_{\tilde{f}_L} &= \tilde{m}^2_{Q,L} + m^2_f + M^2_Z \left(\mathrm{T}_3 - Q_f \sin^2\theta_W\right) cos\,2\beta \\ M^2_{\tilde{f}_R} &= \tilde{m}^2_f + m^2_f + M^2_Z \, Q_f \sin^2\theta_W \, cos\,2\beta \end{aligned} \tag{2.15}$$

The coupling of the sfermions to gauge bosons and fermions are completely fixed by gauge invariance, with no free parameters. A few examples of the couplings are [14]:

$$\begin{aligned} \gamma^\mu \, \tilde{f}_{L,R}(p) \, \tilde{f}^*_{L,R}(p') &: \; - ieQ_f \, (p+p')^\mu \\ W^{\mu-} \, \tilde{f}_L(p) \, \tilde{f}'^*_L(p') &: \; - \frac{ig}{\sqrt{2}} \, (p+p')^\mu \\ Z^\mu \, \tilde{f}_{L,R}(p) \, \tilde{f}^*_{L,R}(p') &: \; - \frac{ig}{cos\,\theta_W} \left[\mathrm{T}_3 - Q_f \sin^2\theta_W\right] (p+p')^\mu \\ \tilde{\gamma} \, \mathrm{f} \, \tilde{f}_{L,R} &: \; \mp \frac{ieQ_f}{\sqrt{2}} \, (1 \pm \gamma_5) \end{aligned} \tag{2.16}$$

Production of sleptons from e^+e^- interactions and their decay modes [13] are shown in figure 2.5 (explicit calculations are given in appendix A). $\tilde{\ell} \rightarrow \ell\tilde{\chi}_1^\circ$ is the main decay mode that is used for searches of sleptons in this thesis because this decay mode is expected to be dominant in most of the parameter space.

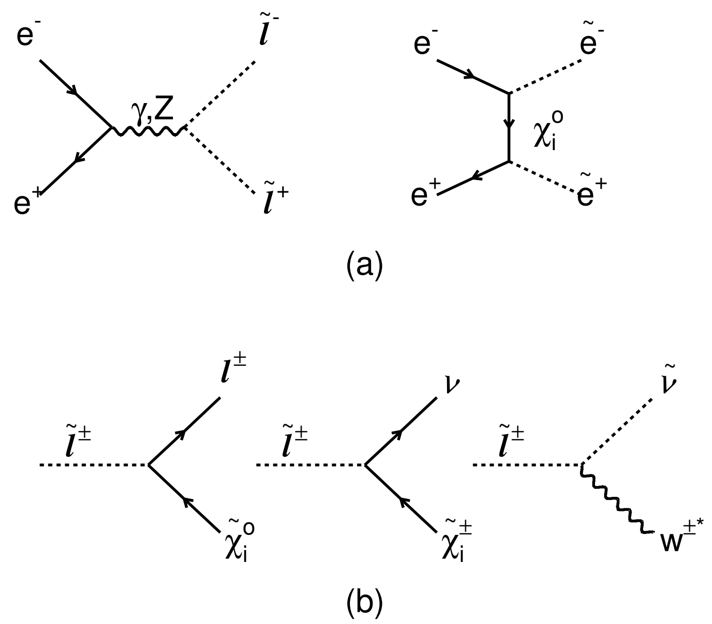

Figure 2.5: Feynman diagrams for slepton **(a)** Production and **(b)** Decay processes.

2.3.4 R-Parity

The terms in the second line of equation 2.5 with couplings λ_{ijk}, λ'_{ijk}, λ''_{ijk} contribute to lepton- and baryon-number violating interactions and can lead to proton decay at tree level through the exchange of the scalar partner of the down quark. These interactions are severely restricted by experimental data [20, 21].

There are several approaches to solve this problem. The simplest way is to make the coefficients λ_{ijk}, λ'_{ijk}, λ''_{ijk} small enough to avoid the contradiction with experimental limits e.g., $n - \bar{n}$ oscillation, neutrinoless double beta decay, $e - \mu - \tau$ universality, $\nu_\mu - e$ scattering, ν_μ deep-inelastic scattering etc., [22]. Another way is to make either the lepton number violating interactions λ_{ijk}, λ'_{ijk} or the baryon number violating interactions λ''_{ijk} to be zero, which would forbid proton decay.

A more elegant strategy is to require that all of these undesirable lepton and baryon number violating terms are forbidden by a symmetry. This symmetry is called **R-parity**. It leads to conservation of a multiplicative quantum number defined as $\mathbf{R} = (-1)^{\mathbf{3(B-L)+2S}}$, where B, L and S represent baryon number, lepton number and spin of the particle [23]. R is thus +1 for all standard model (SM) particles and −1 for all super-partners.

Consequences of **R-parity** conservation are :

- SUSY partners can only be pair produced from Standard Model particles.
- The lightest SUSY particle (LSP) is stable.
- The LSP will interact very weakly with ordinary particles (through the exchange of a heavy virtual SUSY particle).
- Thus, a generic signal of this theory is missing energy from the non-observed LSP.

R-Parity conservation is assumed in these analyses. Consequently one of the main criteria of these searches is missing energy ($\not{E}$) and missing transverse momentum ($\not{p}_T$) .

2.3.5 Constraints on Free Parameters from GUT Motivation

Apart from the 19 free parameters of the Standard Model, the MSSM consists of the following additional free parameters :

- Squarks masses (spin 0) : $(\tilde{u}_L, \tilde{d}_L)$, $\tilde{u}_R$, $\tilde{d}_R$, $(\tilde{c}_L, \tilde{s}_L)$, $\tilde{c}_R$, $\tilde{s}_R$, $(\tilde{t}_L, \tilde{b}_L)$, $\tilde{t}_R$, $\tilde{b}_R$
- Sleptons masses (spin 0) :$(\tilde{\nu}_{e_L}, \tilde{e}_L)$, $\tilde{e}_R$, $(\tilde{\nu}_{\mu_L}, \tilde{\mu}_L)$, $\tilde{\mu}_R$, $(\tilde{\nu}_{\tau_L}, \tilde{\tau}_L)$, $\tilde{\tau}_R$
- Gaugino masses (spin $\frac{1}{2}$) : M_1, M_2, M_3
- Trilinear couplings : A^u, A^d, A^c, A^s, A^t, A^b, A^e, A^μ, A^τ
- Higgs sector (spin 0) : μ

Other parameters of the Higgs sector are given in terms of M_A and $tan\,\beta$ which replace the higgs mass and the vacuum expectation value in the SM. In this list, it is assumed that there is no flavour-mixing in the squark sector. One may have many mixing angles and phases.

An independent value for each one of the above masses and couplings leads to a proliferation of new parameters, making phenomenological analysis almost impossible. It is useful to assume a higher symmetry, broken at some ultrahigh scale, which relates these parameters. An especially appealing and economic class of models is based on minimal supergravity (SUGRA), where it is assumed that the $SU(3)_C \times SU(2)_L \times U(1)_Y$ Gauge couplings unify at some ultrahigh energy $M_{GUT} \sim 10^{16}$ GeV.

$$\sqrt{\frac{5}{3}}g_1(M_{GUT}) \;=\; g_2(M_{GUT}) \;=\; g_3(M_{GUT}) \;=\; g_{GUT}$$

where the factor 5/3 comes from the difference between the GUT normalisation and the usual SM normalisation of the *hypercharge* generator. In SUGRA models, supersymmetry is a local symmetry at some ultrahigh scale close to M_{Planck} and the supersymmetry-breaking corresponds to a Higgs Mechanism in a so-called hidden sector, composed only of particles and masses of this high scale. This spontaneous breaking of supersymmetry is communicated to the visible sector, essentially the MSSM (plus a gravitino) through gravitational interactions, which, being universal, do not distinguish between flavours. Thus, at $\mathrm{M_{GUT}}$, there are only a few independent SUSY parameters [14, 24].

- A common gaugino mass ($m_{1/2}$).
- A common scalar mass ($m_\circ$).
- A common trilinear interaction (A) and
- The bilinear coupling (B).

The various MSSM masses and couplings have to be evolved (as shown in figure 2.6) [25] from the common value at M_{GUT} to the electroweak scale. This generally involves solving coupled differential equations, with the values of the four GUT-scale parameters as boundary conditions.

At lowest order, gaugino masses are scaled in the same way as the corresponding squared coupling constants,

$$M_i(M_W) \;=\; m_{1/2}\frac{g_i^2(M_W)}{g^2_{_{GUT}}}$$

yielding

$$M_1 \;=\; \frac{5}{3}\, tan^2\,\theta_\mathrm{W}\, M_2 \;=\; \frac{5}{3}\,\frac{\alpha_{em}}{\alpha_s\, cos^2\,\theta_\mathrm{W}}\, M_3$$

After a solution of the corresponding renormalisation group equations for $\alpha_{_\mathrm{GUT}} = \frac{1}{24.3}$, $\mathrm{M_{GUT}} = 2.0 \times 10^{16}$ GeV, $\sin^2\theta_\mathrm{W} = 0.2324$ and A(GUT) = 0, one finds the numerical formulae for squark and slepton square masses [26] as

$$\begin{aligned}
M^2_{\tilde{\mathrm{e}}_L}(\mathrm{M_Z}) &= m_\circ^2 + 0.52\, m_{1/2}^2 + 0.27\,\mathrm{M_Z^2}\cos 2\beta\\
M^2_{\tilde{\nu}_L}(\mathrm{M_Z}) &= m_\circ^2 + 0.52\, m_{1/2}^2 + 0.50\,\mathrm{M_Z^2}\cos 2\beta\\
M^2_{\tilde{\mathrm{e}}_R}(\mathrm{M_Z}) &= m_\circ^2 + 0.15\, m_{1/2}^2 + 0.23\,\mathrm{M_Z^2}\cos 2\beta\\
M^2_{\tilde{\mathrm{u}}_L}(\mathrm{M_Z}) &= m_\circ^2 + 6.50\, m_{1/2}^2 + 0.35\,\mathrm{M_Z^2}\cos 2\beta\\
M^2_{\tilde{\mathrm{d}}_L}(\mathrm{M_Z}) &= m_\circ^2 + 6.50\, m_{1/2}^2 - 0.42\,\mathrm{M_Z^2}\cos 2\beta\\
M^2_{\tilde{\mathrm{u}}_R}(\mathrm{M_Z}) &= m_\circ^2 + 6.10\, m_{1/2}^2 + 0.15\,\mathrm{M_Z^2}\cos 2\beta\\
M^2_{\tilde{\mathrm{d}}_R}(\mathrm{M_Z}) &= m_\circ^2 + 6.00\, m_{1/2}^2 - 0.07\,\mathrm{M_Z^2}\cos 2\beta\\
M^2_{\tilde{\mathrm{b}}_R}(\mathrm{M_Z}) &= M^2_{\tilde{\mathrm{d}}_R}(\mathrm{M_Z})\\
M^2_{\tilde{\mathrm{b}}_L}(\mathrm{M_Z}) &= M^2_{\tilde{\mathrm{d}}_L}(\mathrm{M_Z}) - 0.49\, m_\circ^2 - 1.21\, m_{1/2}^2\\
M^2_{\tilde{\mathrm{t}}_R}(\mathrm{M_Z}) &= M^2_{\tilde{\mathrm{u}}_R}(\mathrm{M_Z}) + m_t^2 - 0.99\, m_\circ^2 - 2.42\, m_{1/2}^2\\
M^2_{\tilde{\mathrm{t}}_L}(\mathrm{M_Z}) &= M^2_{\tilde{\mathrm{d}}_L}(\mathrm{M_Z}) + m_t^2 - 0.49\, m_\circ^2 - 1.21\, m_{1/2}^2
\end{aligned} \tag{2.17}$$

coefficients of $\mathrm{M_Z^2}\cos 2\beta$ are $(\mathrm{T_3} - Q_f \sin^2\theta_\mathrm{W})$ for the corresponding fermions.

After mixing the eigenstates of the stop mass squared matrix are

$$M^2_{\tilde{t}_{1,2}}(\mathrm{M_Z}) = \frac{1}{2}\left[0.5\,m_\circ^2 + 9.1\,m_{1/2}^2 + 2\,m_t^2 + 0.5\,M_Z^2\,cos\,2\beta\right] \\ \mp \frac{1}{2}\left[\left(1.5\,m_{1/2}^2 + 0.5\,m_\circ^2 + 0.2\,M_z^2\,cos\,2\beta\right)^2 + 4\,m_t^2\,\left(A^t - \mu\,cot\,\beta\right)^2\right]^{1/2} \quad (2.18)$$

The electroweak symmetry breaking constraint allows one to eliminate bi-linear coupling B in favour of $tan\,\beta$ and also adjust the magnitude (but not the sign) of the μ parameter to get the measured Z boson mass. Thus various SUSY parameters, masses and mixing are then determined in terms of the parameter set

$$m_\circ,\ m_{1/2},\ \tan\beta,\ A \text{ and } sign(\mu)$$

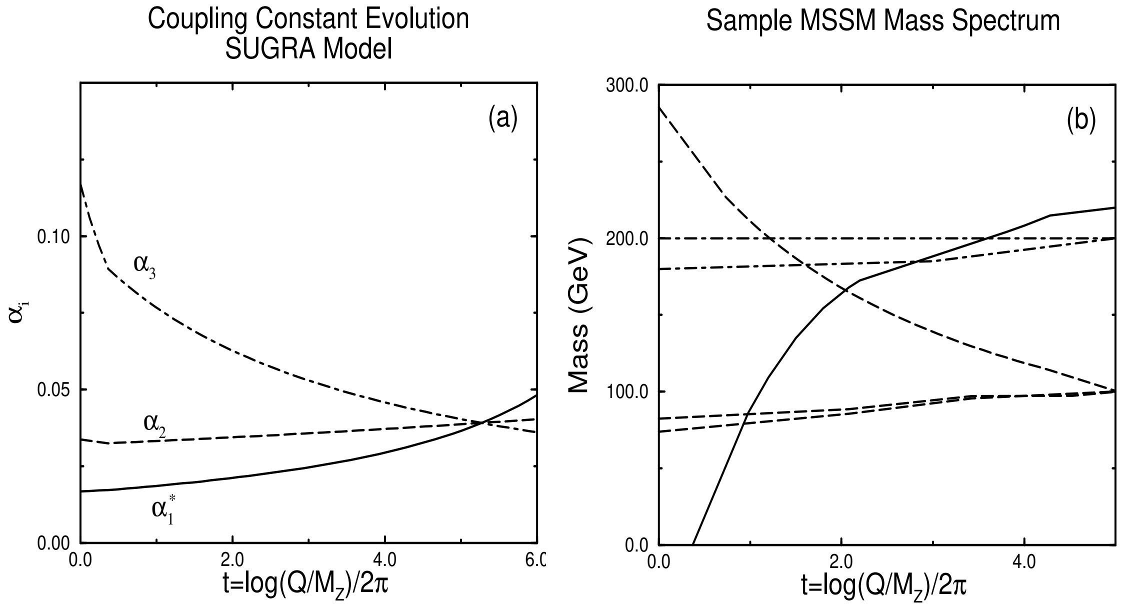

Figure 2.6: Evolution of (a) coupling constants ($\alpha_1^* \equiv 5/3\,\alpha_1$) and (b) SUSY particle masses for a given set of parameter (at the unified scale, $\mathrm{m_\circ} = 200\,\mathrm{GeV}$, $\mathrm{m_{1/2}} = 100\,\mathrm{GeV}$, $\mu = 100\,\mathrm{GeV}$ and $\mathrm{A_i} = 0$). The solid line is the lightest neutral Higgs boson mass. The dashed lines are the gaugino masses (the largest is the gluino) and the dot-dashed lines are typical slepton masses [14].

Searches to be described in the thesis are based on slightly loose constraint (in a constrained MSSM) model, where instead of $sign(\mu)$, μ is an independent variable like the other four. In this framework, typical production cross-sections of right-handed selectron pair ($\tilde{\mathrm{e}}_R^+\tilde{\mathrm{e}}_R^-$) at $\sqrt{\mathrm{s}} = 161.3$ GeV are shown in the figure 2.7.

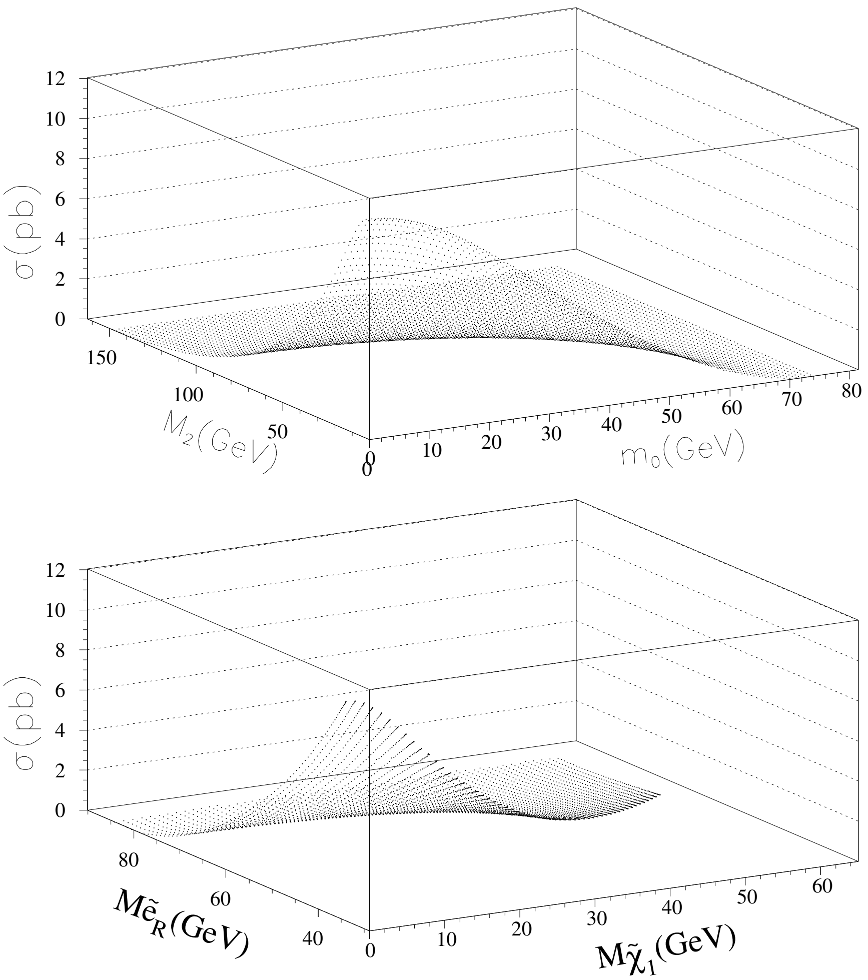

Figure 2.7: $\tilde{e}^+_R\tilde{e}^-_R$ production cross section at $\sqrt{s} = 161.3$ GeV are shown in (Top) M_2 and $m_\circ$ plane and (Bottom) $M_{\tilde{e}_R}$ and $m_{\tilde{\chi}^\circ_1}$ plane (for $\tan\beta = 2.0$, $\mu = -200.$ and A = 0).

2.3.6 Experimental Constraints on Supersymmetric Mass Spectra

No direct experimental evidence for supersymmetry has been found. Many searches for SUSY particles have recently been performed by the LEP1, HERA and Tevatron experiments. Negative results of the these searches improved the existing limits on masses and couplings and these are summarised below :

2.3.6.1 Results from HERA

Within the MSSM with conserved *R-parity*, **H1** experiment at HERA searched for $\tilde{\mathrm{e}}\,\tilde{\mathrm{q}}$ pairs using their dominant decay modes into the LSP ($\tilde{\chi}_1^\circ$) [27]. No signal was found and exclusion limits of 95% confidence level were derived for the parameters $\mathrm{M}_{\tilde{\mathrm{e}}}$, $\mathrm{M}_{\tilde{\mathrm{q}}}$, M_2 and $\tan\beta$ as shown in figure 2.8.

2.3.6.2 Results from Tevatron

Searches for the production of lowest mass chargino and second neutralino ($\bar{p}\,p \rightarrow \tilde{\chi}_1^\pm + \tilde{\chi}_2^\circ$) have been made at the Tevatron. The cleanest channels for this search are the purely leptonic decay channels, where the signature would be three leptons plus missing transverse energy $\not{E}_T$. Both D∅ and CDF experiments at tevatron have carried out searches in the following four channels : eee, $ee\mu$, $e\mu\mu$, $\mu\mu\mu$ [28]. Exclusion curves obtained from the negative results of these searches are shown in figure 2.9.

2.3.6.3 Results from LEP1

All the four experiments at LEP have searched [29] for $\tilde{\ell}$, $\tilde{\chi}_1^\pm$, $\tilde{\chi}_2^\circ$ in the decay modes $(\mathrm{e^+e^-} \rightarrow \tilde{\ell}^+\,\tilde{\ell}^- \rightarrow \ell\,\ell\,\tilde{\chi}_1^\circ\,\tilde{\chi}_1^\circ)$, $(\mathrm{e^+e^-} \rightarrow \tilde{\chi}_\mathrm{i}^+\,\tilde{\chi}_\mathrm{j}^- \rightarrow \tilde{\chi}_1^\circ\,\tilde{\chi}_1^\circ\,W^{+*}\,W^{-*})$ and
$(\mathrm{e^+e^-} \rightarrow \tilde{\chi}_1^\circ\,\tilde{\chi}_2^\circ \rightarrow \tilde{\chi}_1^\circ\,\tilde{\chi}_1^\circ\,Z^*$ (or $\mathrm{e^+e^-} \rightarrow \tilde{\chi}_2^\circ\,\tilde{\chi}_2^\circ \rightarrow \tilde{\chi}_1^\circ\,\tilde{\chi}_1^\circ\,\mathrm{Z^*\,Z^*}$)). There were no excess of events compared to the SM background in any of the search channels. Consequently masses of $\tilde{\mathrm{e}}$, $\tilde{\mu}$, and $\tilde{\tau}$ had been excluded upto 43.5 GeV, 42.6 GeV and 40.4 GeV respectively and the results are roughly independent of neutralino mass. For chargino sector, a pure wino of mass less than 45.5 GeV and a pure higgsino with mass less than 44.5 GeV are excluded; these results are also independent of neutralino mass up to 28 GeV. Upper limits of (a few) $\times 10^{-4}$ on the Br ($Z \rightarrow \tilde{\chi}_1^\circ\,\tilde{\chi}_2^\circ$ (or $\tilde{\chi}_2^\circ\,\tilde{\chi}_2^\circ$)) were obtained in a model independent way for the range of neutralino masses ($\approx\ M_Z/2$) accessible at LEP 1 energies.

2.3.6.4 Indirect Constraints

There are also indirect constraints on masses of supersymmetric particles. Few of them are described below :

- Anomalous magnetic moment of muon ($\Delta\, a_\mu \sim cos\,\theta_\mathrm{W}\, sin\,\theta_\mathrm{W}\, m_\mu\,(M_{\tilde{\mu}_R} - M_{\tilde{\mu}_L})/M_x^3$, where M_x is the mass of the SUSY particle in the triangular loop), which is constrained to $-2\times10^{-8} < \Delta\, a_\mu < 2.6\times10^{-8}$ with 95 % CL [30] predicted $M_{\tilde{\mu}_L} \approx M_{\tilde{\mu}_R}$.
- The effects of the SUSY particles (except Higgs bosons) at the electroweak scale are suppressed by powers of M_W^2/M_{SUSY}^2, where M_{SUSY} is the relevant SUSY particle

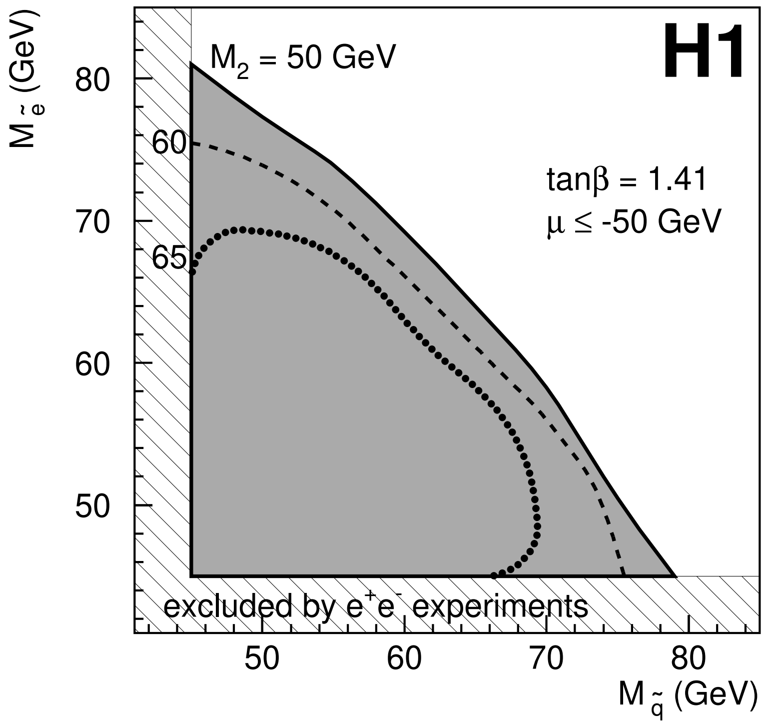

Exclusion limits at 95% confidence level in the $\mathrm{M}_{\tilde{\mathrm{q}}}$ vs $\mathrm{M}_{\tilde{\mathrm{e}}}$ plane for different values of M_2 (dash line for $M_2 = 60$ and dot line for $M_2 = 65$ GeV) and $\mu \leq$ -50 GeV, $\tan\beta = 1.41$.

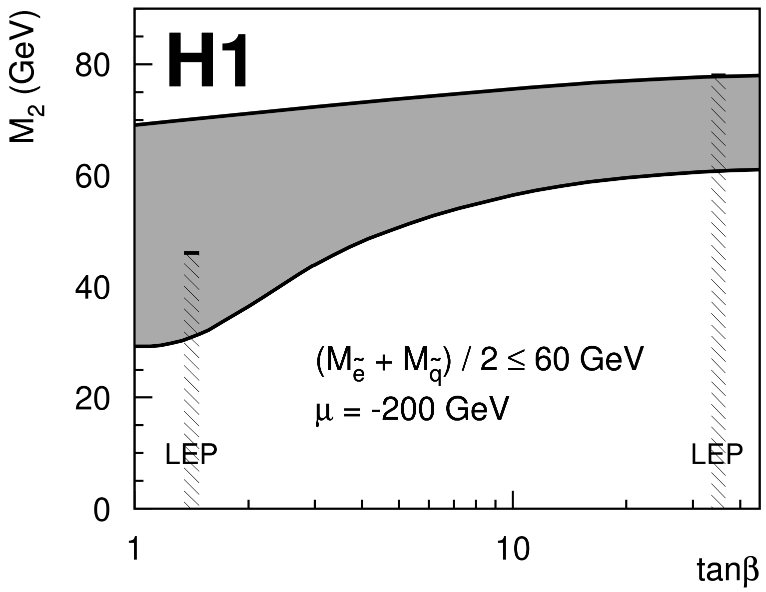

Excluded region at 95% CL for M_2 as a function of $\tan\beta$ for $(\mathrm{M}_{\tilde{\mathrm{e}}} + \mathrm{M}_{\tilde{\mathrm{q}}})/2 \leq$ 60 GeV and $\mu =$ -200 GeV (shaded area). The two hatched symbols show the upper limits on M_2 obtained for $tan\,\beta = 1.41$ and 35 from e^+e^- collisions at LEP for $\sqrt{s} = 130$ - 136 GeV.

Figure 2.8: Exclusion plots from HERA (H1).

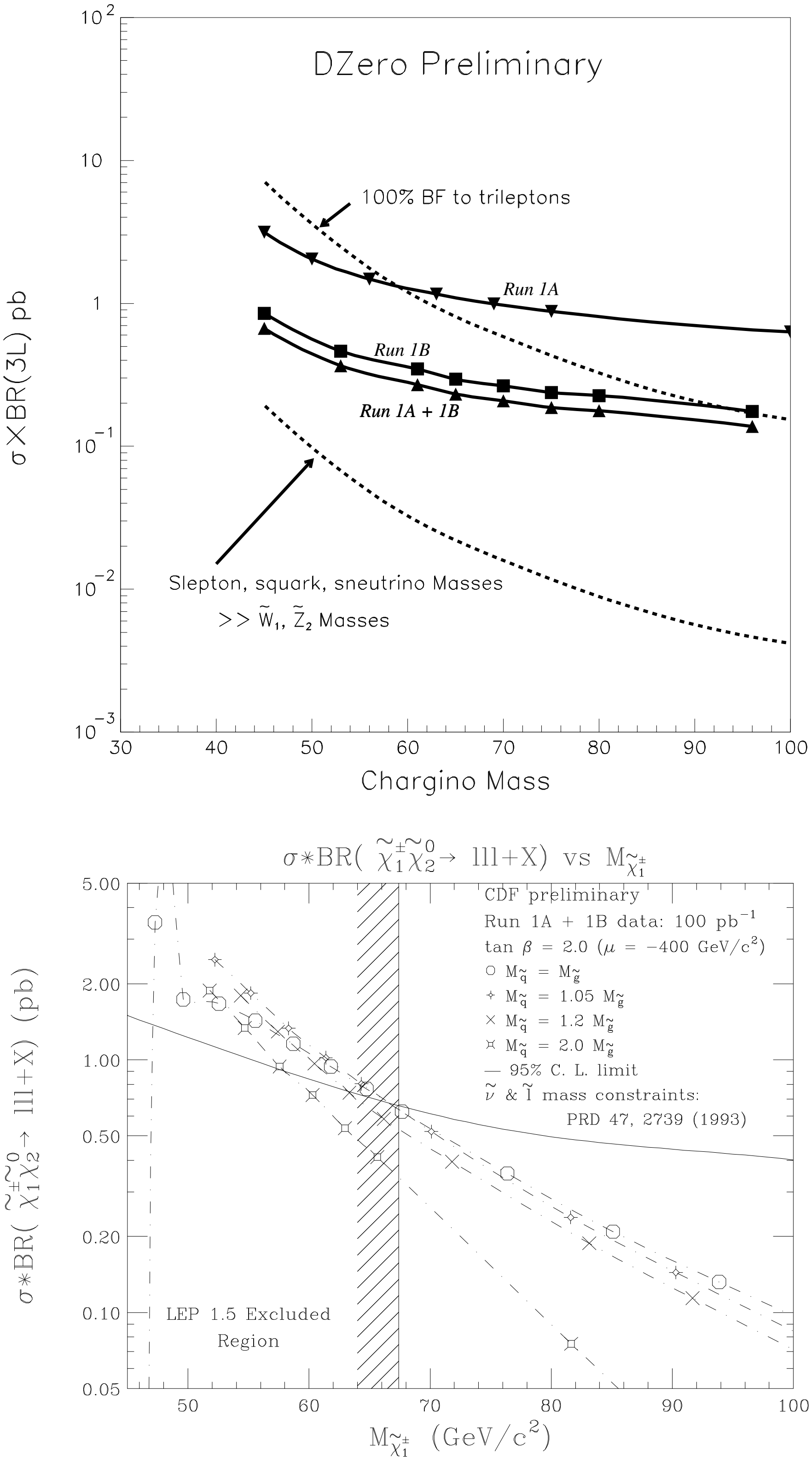

Figure 2.9: Exclusion plots from Tevatron data.

mass; so the SUSY particles give negligible contribution to electro-weak data. Attempts have been made to do a global fit to the electroweak data and fix the SUSY mass spectra. The fit result prefer either a small $tan\,\beta$ (~ 2) or relatively high $tan\,\beta$ (~ 30).

- An important indirect limit on SUSY parameters comes from the flavour changing neutral current processes like mixing of $\bar{K}^{\circ}$-K° and $\bar{B}^{\circ}$-B°. Off-diagonal elements in the squared mass matrix (equation 2.13) favour for more mixing due to non degenerate mass splitting. Consequence of non observation of the effects of SUSY spectra in these mixing is that some of the flavour off-diagonal entries in the squark mass squared matrices have to be an order of magnitude lower than the diagonal ones [31].

- Several indirect limits are coming from the effects of SUSY particles in rare decay processes. Contribution of SUSY particles in the loop diagrams can affect rare decay processes like B and K decays. The most restrictive one is coming from the CLEO result of the inclusive decay $B \rightarrow X_s\gamma$ [32]

$$Br\,(B \rightarrow X_s\gamma) = (2.32 \pm 0.67) \times 10^{-4}$$

which is very sensitive to loops contribution due to SUSY particles. All the loops diagrams are shown in figure 2.10, where 'u' and 'd' refer to **up**- and **down**-type quarks. The contribution from $t\,H^{\pm}$ loops always adds constructively and for large

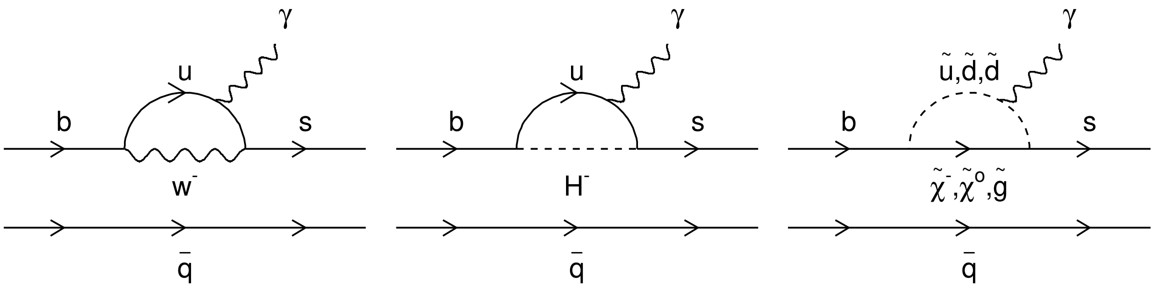

Figure 2.10: Loop diagrams for $b \rightarrow s\gamma$ process.

tan β, $\tilde{q}$-$\tilde{\chi}^{\pm}$ contribution completely dominates over others. Constraints from the CLEO result to the parameter space are very strong and large region for $\mu < 0$ and for large $tan\,\beta$ are excluded [33].

Chapter 3

The Large Electron Positron Collider

The CERN's Large Electron Positron Collider (LEP) is an e^+e^- accelerator and storage ring of circumference 26.7 km, designed to operate at a Centre of Mass Energy (CME) of 80 to 200 GeV. The LEP accelerator ring, as shown in figure 3.1, is situated in an underground tunnel with an average diameter 4 m and of varying depth, from a minimum 50 m to a maximum of 150 m and has an inclination of 1.4 %. It consists of eight bending sections of length 2840 m each with a radius of curvature 3300 m and eight straight sections of length 490 m each. Each of the eight bending sectors consists of 31 standard cells of length 79.11 m comprised of magnets in the following order: a defocussing quadrupole, a vertical orbit corrector, a group of six bending dipoles, a focussing sextupole, a focussing quadrupole, a horizontal orbit corrector, a second group of six bending dipoles, and finally a defocussing sextupole. The magnetic systems focus the electron and positron beams in the ideal orbit during the ramping and storage. The middle of the alternate four straight sectors are equipped with four detectors ALEPH (IP4) [34], DELPHI (IP8) [35], L3 (IP2) [36] and OPAL (IP6) [37], where IP in the parenthesis stands for interaction point of e^+ and e^- beams.

The LEP storage ring is the last accelerator in a chain of five (figure 3.2), each of which accelerates the same electrons and positrons generated by an electron gun and the positron converter. Electrons from the gun are accelerated through a LINAC to 200 MeV. Part of the beam is deviated towards a tungsten target to produce the positrons through bremsstrahlung followed by pair production. A second LINAC is used to accelerate them upto 600 MeV and the electrons and positrons are then accumulated in a 600 MeV Electron-Positron Accumulator (EPA). EPA condenses the beams into bunches through synchrotron radiation damping. The CERN Proton Synchrotron (PS) accelerates them upto 3.5 GeV and then injects them into the CERN Super Proton Synchrotron (SPS) which operates as a 22 GeV electron-positron injector to LEP. Electron and positron bunches are accelerated separately in PS and also in SPS. In LEP, particles are accelerated simultaneously to the desired energy.

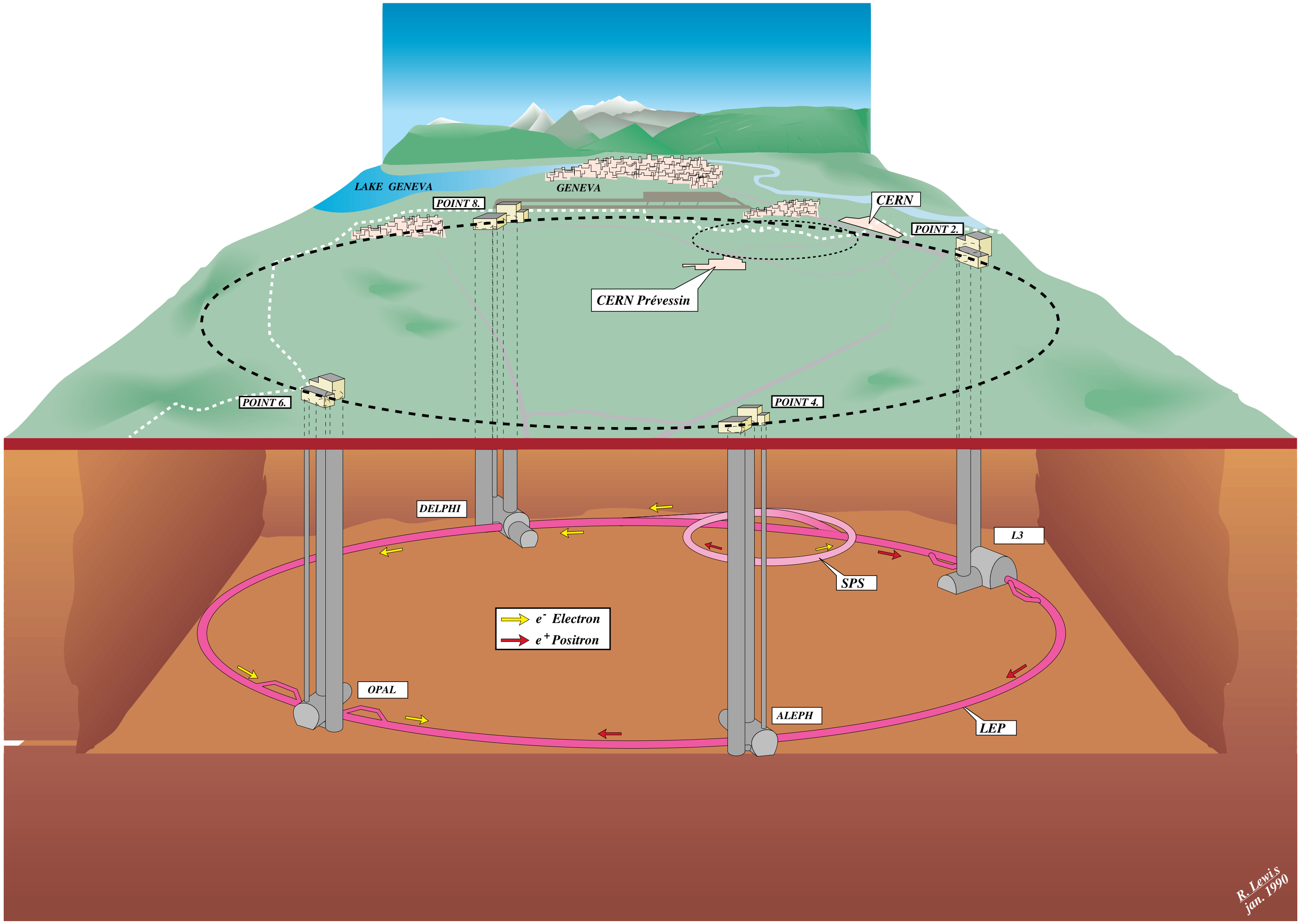

Figure 3.1: The LEP collider at CERN.

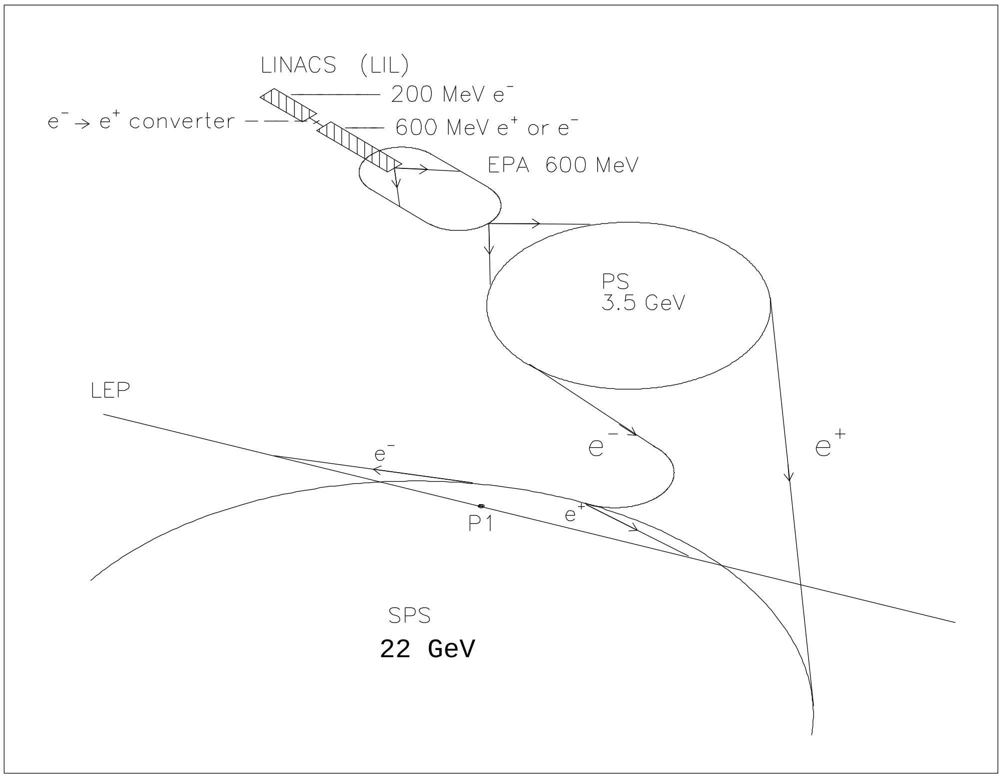

Figure 3.2: LEP injection scheme.

The design of a particle collider gives priority to two most fundamental parameters, beam energy range and the luminosity ($\mathcal{L}$). The beam energy range must be sufficient to achieve the desired physics within the kinematic limit and the luminosity must also be sufficient for a reasonable rate of observations of such physics events. For a head-on collision, the luminosity at any collision point is defined as

$$\mathcal{L} = \frac{N_e\, N_p\, k_b\, f_{rev}}{4\,\pi\,\sigma_x\,\sigma_y} \tag{3.1}$$

where $\mathrm{N_e}$ ($\mathrm{N_p}$) is the number of electrons (positrons) per bunch, $\mathrm{k_b}$ is the number of bunches per beam, $\mathrm{f_{rev}}$ is the revolution frequency and $\sigma_\mathrm{x}\,\sigma_\mathrm{y}$ is the cross section of the bunches in the transverse plane. Typical values of these quantities are : $\mathrm{N_e} \sim \mathrm{N_p} \sim 10^{11} - 10^{12}$, $\mathrm{f_{rev}} \sim 11.235\,\mathrm{KHz}$, $\mathrm{k_b} = 4$ or 8, $\sigma_\mathrm{x} \sim 150\,\mu$m and $\sigma_\mathrm{y} \sim 15\,\mu$m.

3.1 LEP Run at the Z-peak (LEP 1)

From September '89 to October '95 LEP ran around Z-peak ($\sqrt{\mathrm{s}} \sim \mathrm{M_Z}$). Design luminosity at these energies was $1.7\times 10^{31}\ \mathrm{cm^{-2}\,s^{-1}}$. The accelerator system consists of 128 five-cell Radio Frequency (RF) copper cavities powered by 16 one MW klystrons, which are symmetrically placed on both side of interaction points IP2 and IP6. With the introduction of *pretzel* scheme [38] two cavities nearest to the arcs had to be removed at each side of both points, bringing the total number of cavities to 120.

The operating frequency of the RF cavity is 352.21 MHz which corresponds to 31320 times the revolution frequency of the beam circulating in LEP. At Z-peak, beam energy loss is $\sim$ 120 MeV per revolution due to synchrotron radiation and this energy is compensated by the RF cavities. Upto middle of 1992, LEP ran with 4×4 bunch mode. At each possible interaction points (eight) four electrostatic separators (each of which is 4 m long and produces a vertical electric field of 2 MV/m between the plates separated by 11 cm) could separate the electron and positron beam by 40 standard deviations of the vertical beam size (σ_y). The separators are powered in all eight possible collision points during injection, accumulation and energy ramping. Just before the physics data taking, the separators in the experimental collision points are switched off to allow collisions. The luminosity is tuned by beam-beam tuneshift and is much below the design value. The *pretzel* scheme, which uses 8 bunches per beam with lower bunch current was introduced to increase the luminosity and a set of eight horizontal separators was installed for this scheme. Luminosity achieved in 1994 for a stable run was 1.17×10^{31} cm^{-2} s^{-1}.

The LEP energy has been calibrated using the following procedures :

- The Flux loop [39],
- The Field Display [40, 41],
- Proton beam run [41] and
- Resonance Depolarization [42, 43]

The last one was able to give the best absolute precision, $\frac{\sigma_E}{E} \sim 1.5 \times 10^{-5}$.

3.2 LEP Run Beyond the Z-peak (LEP 2)

The main motivation of LEP 2 run is to measure the mass of W boson (M_W), with a precision of $\sim$ 35 MeV and also to search for new physics beyond the SM. To achieve these targets the LEP machine had to be upgraded from the earlier configuration, e.g., the beam energy needs to be doubled, luminosity should be $\sim 7.0\times 10^{31}$ cm^{-2} s^{-1} to get total integrated luminosity $\sim$ 500 pb^{-1} in three years. In November 1995 LEP energy went above the Z-peak ($\sqrt{s}$ = 130 - 136 GeV) and in 1996 it ran at $\sqrt{s} = 161 - 172$ GeV. Mainly the following upgradations have been done to achieve the above mentioned energy and luminosity.

- Increase of LEP beam energy (superconducting cavity)
- Increase of bunch current (bunch train mode)
- Increase in LEP injection energy (SPS)
- Change in the beam optics

3.2.1 Superconducting RF Cavity

Beam energy loss due to synchrotron radiation increases as the 4th power of beam energy, e.g., it increases from $\sim$ 120 MeV/per beam/per turn at $\sqrt{s} = M_Z$ to 1.228 GeV and 1.600 GeV at $\sqrt{s} = 161$ GeV and 172 GeV respectively. Existing RF copper cavities of LEP 1 are unable to compensate the huge amount of energy loss.

The original energy upgrading programme consisted of the addition of 192 superconducting (SC) cavities of active length 17 m (32 at the interaction points IP2 and IP6 each and 64 each at points IP4 and IP8) to the existing 120 Cu cavities. 160 were made with the Cu/Nb technology with a design gradient of 6 MV/m and the 32 others were made out of solid Nb with a gradient of 5 MV/m.

The July 1996 start-up saw the number of SC cavities installed in LEP rise from 64 to 144 and by the October 1996 the number of SC cavities had been increased to 176. Number of RF cavities used in three higher $\sqrt{s}$ and the Z run are shown in table 3.1.

$\sqrt{s}$ (GeV)	# of Cu cavity	# of SC cavity
M_Z	120	-
130-136	120	64
161	86	144
172	52	176

Table 3.1: Radio frequency cavity used at different $\sqrt{s}$.

In the 1996/97 shut down period, the following upupgradation was done.

- IP2: remove 34 Cu cavities and install 32 Nb/Cu cavities
- IP4: install 16 Nb/Cu cavities
- IP8: install 16 Nb/Cu cavities

After this shut down the total maximum 'operational' RF voltage is 2490 MV, allowing an 'operational' beam energy of 94.1 GeV.

Shutdown 97/98 :

IP6: remove 34 Cu cavities and install another 32 Nb/Cu cavities. After this shut down the total maximum 'operational' RF voltage is expected to be 2884 MV, allowing an 'operational' beam energy of 96.2 GeV.

3.2.2 Bunch Train Mode

The final constraint for the total beam current is the available RF power. However, various instabilities limit the bunch currents even further.

One such constraint is due to the Transverse Mode Coupling Instability (TMCI) or the fast head-tail instability which is presently well modelled. For a bunch length of 10 mm the maximum bunch current that can be accumulated with 4 bunches per beam before TMCI is reached are 890 μA for the 90°/60° optics and 980 μA for the 108°/90° optics.

One way to increase the beam current is to increase the number of bunches. Two schemes were tested for this scenario : *Pretzel* scheme and *bunch train* scheme [44]. Experimental evidence indicates that the bunch current is limited in the Pretzel scheme due to horizontal beam-beam encounters in mid-arc where the momentum dispersion is maximum. The 'bunch train with head-on collision' does not suffer from this limitation.

In the original proposal [45] a scheme with 7 bunches per train was envisaged. A stricter upper limit of 750 ns has been imposed by the LEP detectors on the total length of a bunch train. Due to the magnetic configuration around each experimental interaction region and the resulting minimum distance from the IP to the first separator, the minimum inter-bunch spacing is around 87 $\lambda_{\rm RF}$ (74.2 m or 247.5 ns), thereby limiting the number of bunches in a train to four. In 1995 the operation of LEP with 4 trains with 4 bunches per beam proved to be very difficult. Operating with 12 bunches per beam gives less luminosity compared to 8 bunches per beam. Test results are shown in table 3.2.

Optics	$\mathrm{I_b}$		k [1]		$\mathcal{L}$	
	mA	lim			10^{31} cm^{-2} s^{-1}	
$\beta_{\rm x}$(m)			1.25	1.5	1.25	1.5
108/90						
8×8	0.68	TMCI	0.040	0.020	8.6	8.6
12×12	0.54	tot. cur.	0.026	0.013	6.8	6.8

Table 3.2: Currents, coupling and luminosity for $\mathrm{E_b}$ = 80.5 GeV, $\mathrm{I_{tot}} \leq$ 13 mA using 8 or 12 bunches per beam for two values of horizontal beta function ($\beta_{\rm x}$) in the interaction point.

As the number of bunches in a train is limited to two, bunch spacing may change from 87 λ_{RF}. It turned out that only three spacings 118, 168 and 174 λ_{RF} are compatible with the requirement of Beam Orbit Monitoring (BOM) system. The 1996 run was performed with 118 λ_{RF} and the same spacing has been retained for 1997.

3.2.3 LEP Injection Energy

During 1995 the injection energy of LEP was increased from 20 GeV to 22 GeV, with a corresponding increase in the maximum bunch current that can be accumulated and it

[1]beam-beam tune shift coupling parameter, k, is the ratio between vertical and horizontal emittance. Emittance is defined as the product between the rms beam size and the rms angular spread in the beam.

gave the expected 10 % increase in the single bunch current. The various factors which can limit the injection energy are summarised below :

• RF voltage : The available RF voltage in the SPS is 43 MV and the required RF voltage for accelerating electrons in the SPS for different energies are shown in the adjacent table. Comparison between the presently available and required RF voltage indicates that the maximum possible momentum for leptons in SPS is 23 GeV.

Momentum (GeV)	Voltage (MV)
20	24
22	35
23	42
24	50

• The SPS main magnetic cycle : In the main magnetic cycle for the SPS (main bending magnets and quadrupoles) the lepton cycles are separated by 1.2 s. At the end of each cycle the magnets are magnetised with a current corresponding to 23.5 GeV. Hence, a maximum beam momentum upto 23.5 GeV has no repercussions on the cycle lengths nor on the magnetic history.

• Synchrotron radiation : The acceptable radiation dose, received by the magnetic coils due to the synchrotron radiation should not exceed the dose induced by the protons, being 10^6 rad/year [46]. The yearly radiation dose due to the synchrotron radiation inside the SPS magnet coils is shown as a function of electron beam energies.

Energy (GeV)	Dose (rad/yr)
20	6.6×10^4
22	2.0×10^5
23	4.6×10^5
24	1.0×10^6

Thus with the maximum RF voltage available, the SPS can deliver e^+/e^- beams of 23 GeV to LEP without any additional investments. But looking at the repercussions of RF cavity trips in the SPS, the SPS e^+/e^- beam has been operating at 22 GeV.

3.2.4 Change in LEP Optics

The LEP 1 layout of the insertion magnets is not adequate to achieve the LEP 2 energies. Apart from the necessity to install new superconducting cavities near IP2 and IP6, the insertion layouts in IP4 and IP8 required entire modifications.

During the 95/96 shut-down period the last pair of new superconducting low emittance quadrupoles were installed at IP4. The three other experimental interaction points had already been equipped with these stronger magnets in previous shut-down period.

Three optics were considered for the high energy runs : $90°/60°$ optics gives the best performance followed closely by the $108°/90°$ lattice and then by $108°/60°$ lattice. The $108°/90°$ lattice gives much more luminosity than the $108°/60°$ optics due to the difference in average vertical beta function in the arc and therefore is recommended for further development. During the 1996 LEP run the optics used was mainly $90°/60°$.

It was well proven that $90°/60°$ lattice seems adequate for high energy. However during the 96 run, use of $108°/90°$ lattice maximised the energy and therefore is recommended for further development. Finally a $90°/90°$ optics, which has already been used in LEP is also being investigated for future runs.

3.2.5 Ramping and Squeezing of the Beam

The 96 start-up scheme consists of injecting at 22 GeV, ramping to 44 GeV, squeezing and then ramping to the final energy. It takes 17.5 minutes to reach 80 GeV, even without stopping. The present ramp rate of 67.5 MeV/s is 1/8 th of the original LEP design.

3.3 Calibration of LEP 2 Beam Energy

In the framework of the LEP energy calibration, a total of 16 Nuclear Magnetic Resonance (NMR) probes [47] as well as 10 temperature probes have now been installed on the dipoles in the LEP tunnel. The NMR field display installation in the LEP dipole reference magnet has been updated for the increased LEP energy. LEP energy calibration could be done using these procedures :

- The Flux loop
- The NMR probe
- Mϕller scattering [48]
- Resonance Depolarization (RD)

Among the above procedures, Mϕller scattering has not been tested so far. The resonance depolarisation method, which relies on the transverse polarisation of beam, is found to be the most reliable one to measure the beam energy at LEP 1. But it is not possible to perform RD calibration at LEP 2 beam energies because the asymptotic transverse polarisation is negligible. The expression for asymptotic polarisation is given by :

$$P_\infty = \frac{8}{5\sqrt{3}} \frac{1}{1 + \tau_{ST}/\tau_d}$$

where $(1/\tau_d)$ is the rate of depolarisation and $(1/\tau_{ST})$ is the Sokolov-Ternov self polarisation of the beam. Although the self polarisation rate increases as E^5, the depolarization effects due to resonances driven by machine imperfections also increase rapidly with energy. The simplest model of resonant depolarization foresees $\tau_{ST}/\tau_d \approx \nu_s^2$, where $\nu_s = a\gamma$ is the energy dependent spin tune and

$$P_\infty = \frac{92.8\%}{1 + b\, E_{beam}^2}$$

The values of 'b' found experimentally on LEP are 3.1×10^{-4} at $E_{beam} = 44.74$ GeV and 3.3×10^{-3} at $E_{beam} = 50.04$ GeV. There is almost no polarisation beyond $E_{beam} = 60$ GeV.

Finally the following steps have been adopted to carry out the calibration of beam energy at LEP 2 :

• Precise energy calibration was performed with resonant depolarisation method at $E_{beam} = 50$ GeV, where the transverse polarisation was measured to be 5 %.

• Extrapolation to the higher energy is done using the flux loop to provide a calibration of nonlinearity of the ensemble of the LEP dipoles and a set of NMR probes for a precise measurement of the local magnetic field in a sample of LEP magnets. Total uncertainty on LEP energy calibration in the year 1996 is given in table 3.3.

		$\sigma(E_{beam})$ in MeV	
		$\sqrt{s} = 80.5$ GeV	$\sqrt{s} = 86.0$ GeV
Energy scale error :			
	Polarisation systematic	1	1
	e^+e^- energy difference	2	2
	Fill-by-fill normalisation	10	5
	Extrapolation from 50 GeV	24	29
	Orbit correction	1	1
Variation within fill :			
	Tide model	1	1
	NMR/temperature model	2	2
IP specific :			
	Dispersion	1	5
	RF	5	5
Total		27	30

Table 3.3: Uncertainty on LEP 2 beam energy calibration $[\sigma(E_{beam})]$: main uncertainty comes due to the extrapolation of beam energy from 50 GeV to 80.5–86.0 GeV.

The overall error estimate for 1996 was 27 MeV at 80.5 GeV and 30 MeV at 86.0 GeV.

Chapter 4

The L3 Detector

The L3 detector [36, 49–54] (shown in figure 4.1) is designed to study e^+e^- interactions at LEP in the Centre of Mass Energy range $80-200$ GeV with emphasis on high resolution 4-momenta measurements of electrons, photons, muons and hadronic jets. The detector is installed at the second interaction point of the LEP collider. The entire detector is surrounded with a large solenoidal magnet providing an uniform magnetic field of 0.5 Tesla and toroidal field for the forward backward muon chamber. The detector is $\sim$ 17 m long and has a diameter $\approx$ 16 m. The choice of low fields in a large volume is to optimise the muon momentum resolution. The L3 detector consists of following components :

- Central tracking system : To measure the momenta and sign of charge of all charged particles and to determine the position of primary and secondary vertices.
- Electromagnetic calorimeter : To measure the energy and direction of electrons and photons with a high degree of accuracy (energy resolution is 5 % at 100 MeV and better than 1 % above 2 GeV).
- Scintillation counters : For an independent trigger system.
- hadron calorimeter (HCAL) : To absorb all the hadronic shower and measure the energy and direction of hadrons.
- Muon chamber : To measure the sagitta of muon tracks to provide $\Delta p/p < 1.5\,\%$ at $p = 50$ GeV.
- Luminosity (LUMI) monitor : To measure the luminosity delivered by LEP.
- Very short angle tagger (VSAT) : To tag two photon collisions.
- Solenoidal and toroidal magnets.

All the subdetectors except the muon chambers are located inside a support tube (ST). The part of the ST inside the magnet (14.1 m long) is made of nonmagnetic stainless steel. The remaining portion is made of carbon steel. Dimensions of the support tube are, 32 m length, 4.45 m outer diameter, 0.05 m thickness which is equivalent to 0.52 interaction length (λ_{int}). It has a flange support at each end to transmit the load to the ground. Each flange rests on two servo-controlled mechanical jacks to allow continuous alignment of the ST with respect to the LEP beam.

A right handed coordinate system is used in L3. Its origin is at the centre of the detector, the positive z-axis points along the direction of the electron beam and positive x-axis points towards the centre of the LEP ring.

4.1 Central Tracking System

4.1.1 Silicon Microvertex Detector

At the beginning of 1991, the radius of the LEP beam pipe at its four detector points was reduced from 8.0 cm to 5.5 cm. L3 decided to take advantage of this newly acquired space by installing a silicon microvertex detector (SMD) to upgrade the central tracking capability.

The SMD consists of two cylindrical layers at 6 cm and 8 cm radii from the beam line covering the entire 360° in azimuthal angle (ϕ) and a region $22^\circ - 158^\circ$ in θ coverage [54] as shown in figure 4.2. It is mounted on a 1 m long cylindrical tube split lengthwise into two symmetric halves. The tube is made from a laminate of 3 mm thick nomex honeycomb core glued between 315 μm thick aluminium carbon fibre skins. Each layer consists of 12 modules, the inner ones being partially overlapping ($\approx 10\,\%$) to allow alignment with the track, the outer ones do not overlap but have a 2° stereo rotation with respect to the inner ones to resolve pattern recognition ambiguities.

Each half ladder is in turn built from two electrically and mechanically joined double sided silicon sensors, a special low-mass kapton cable attached to one side of sensor pair and a front-end readout electronics. The sensors are built from an n-doped silicon crystal, with high resistivity ($\rho_{\mathrm{n}} > 4\mathrm{K}\Omega$-cm) and a thickness of 300 μm. The junction side is divided into 1537 p^+ strips, with a pitch of 25 μm, while the ohmic side consists of 1409 n^- strips, with a pitch of 50 μm. The active area of the sensor is $7.04 \times 3.84\,\mathrm{cm}^2$. The p and n side are used for R-Φ and z coordinate measurement respectively. The sensors are read out with a pitch of 50 μm on the R-Φ side and 150/200 μm in the central/forward region on the z side. Total number of readout channels is 73728. The whole SMD is quite transparent, 1.2 % of radiation length ($\mathrm{X}_\circ$) at normal incidence, including 2 measuring layers and supporting structure.

The readout frequency is $\sim$ 400 KHz, with a total readout time of 3.9 ms for the 1536 channels of one daisy chain. The dead time introduced is negligible, despite the fact that the SMD alone has a number of channels which is equivalent to the rest of the L3 detector.

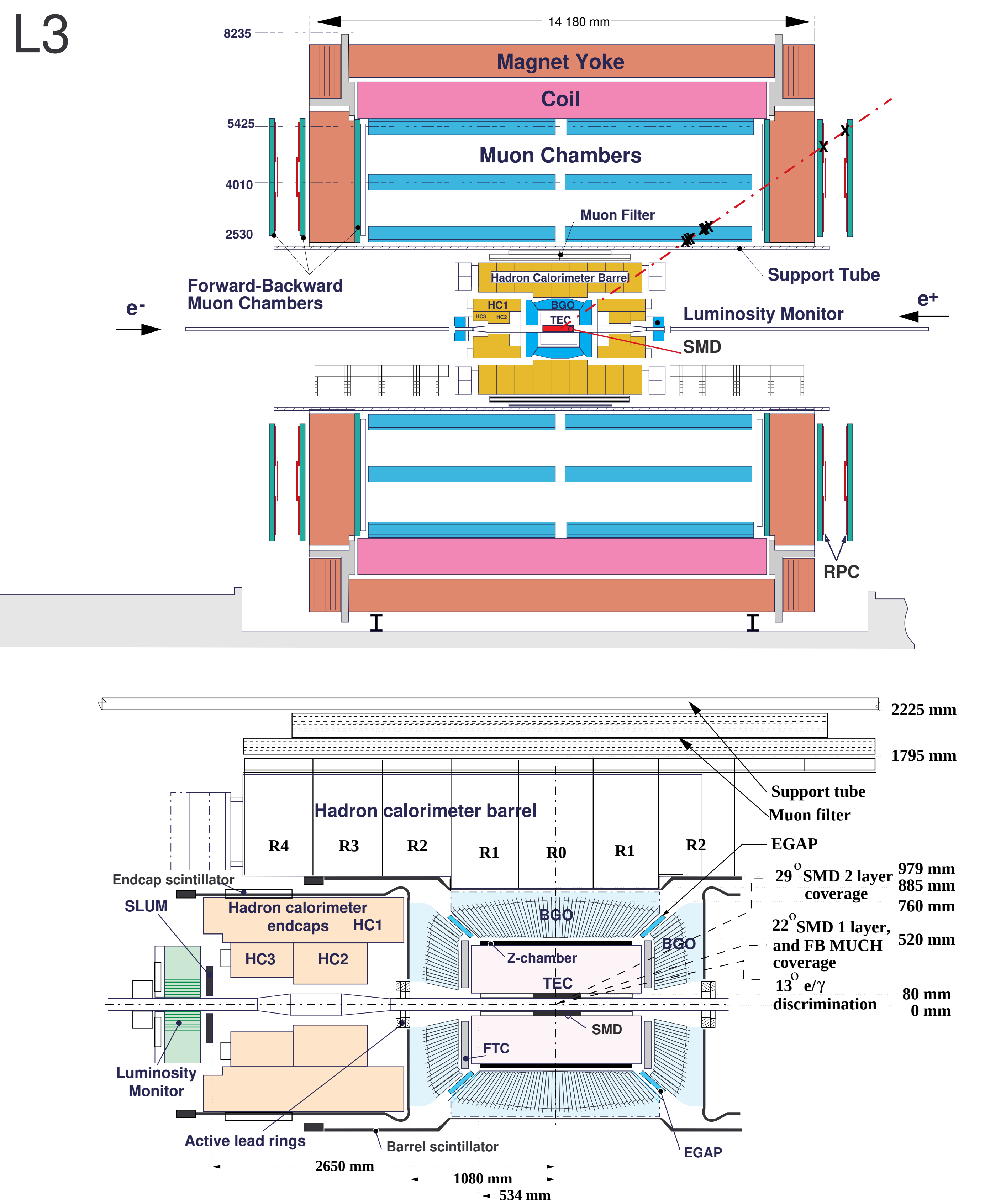

Figure 4.1: L3 detector.

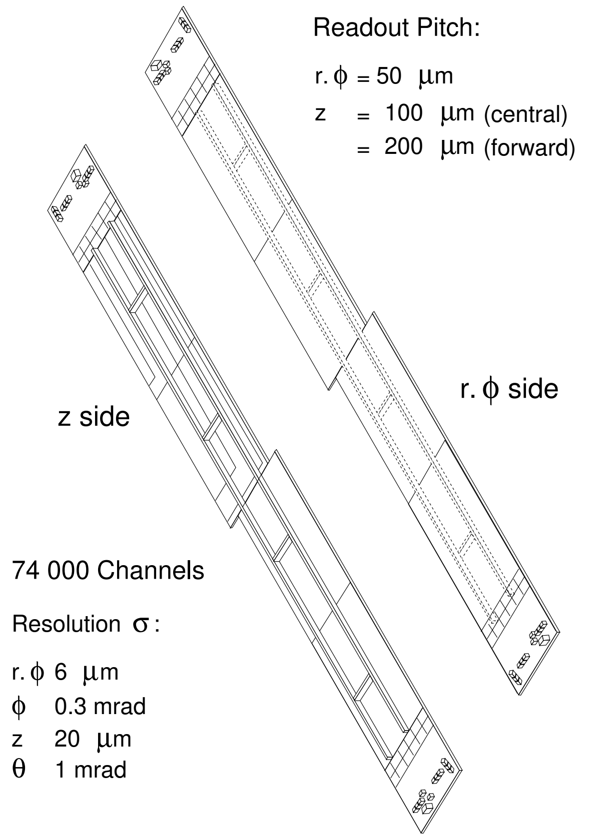

(a) View of SMD ladder both in z side in R-Φ side.

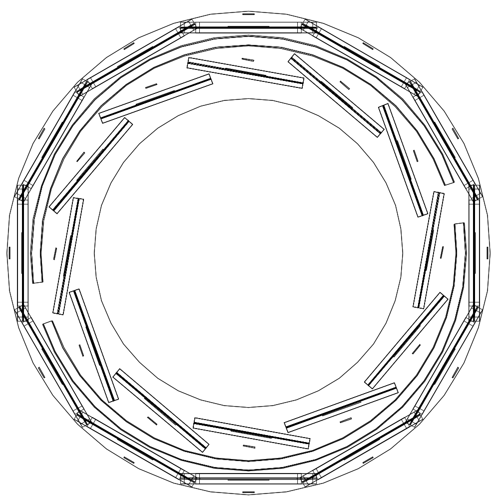

(b) R-Φ view of SMD in L3 detector.

Figure 4.2: Silicon Microvertex Detector.

4.1.2 Time Expansion Chamber

The Time Expansion Chamber (TEC) [55] consists of two concentric cylindrical drift chambers using common end plates. It is operated in 'time expansion' mode (shown in figure 4.3(a)) by having the high field amplification region near the sense wire plane well separated from the low drift field region using an additional grid wire plane as shown in figure 4.3(b). The wires of length 982 mm are aligned parallel to the beam line. The anode wire planes are arranged radially forming 12 inner and 24 outer ϕ sectors as shown in figure 4.3(a). The sectors are separated from each other by the cathode planes. The TEC operates with a low diffusion 80 % CO_2 and 20 % isobutane gas mixture at a pressure of 1.2 bar (abs) and a low drift velocity 5.96 μm/ns at an electric field of 900 V/cm. The drift velocity v_d has linear dependence on the electric field (E), temperature (T), gas pressure (P) and isobutane content (f) ($v_{\rm drift} \propto ({\rm ET/P}){\rm f}$). Furthermore this gas has a very small Lorentz angle (2.35°).

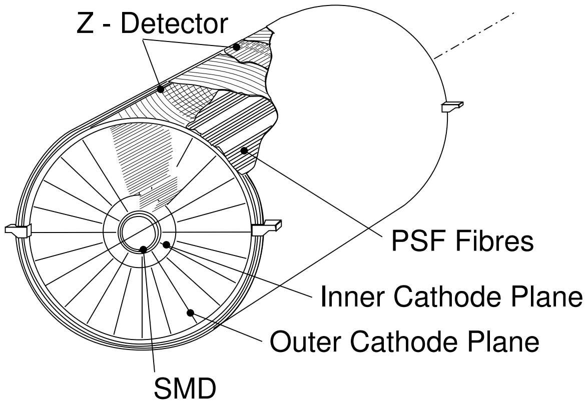

(a) Perspective view of the central tracking detector.

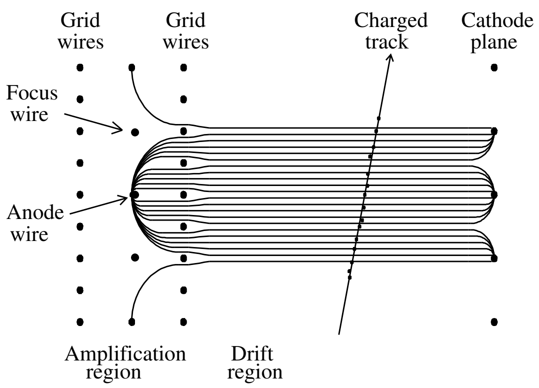

(b) Drift and amplification region of TEC.

Figure 4.3: Time Expansion Chamber.

The inner sector of TEC has 6 standard wires and 2 charge division (CD) wires, while the outer sector has 31 standard, 14 left-right ambiguity (LR) and 9 charge division (CD) wires allowing for a maximum of 62 coordinate measurements for a single track.

Track momenta are calculated from the bending of the tracks in the R-Φ plane. Total lever arm for momentum measurement in TEC is 31.7 cm. For polar angle (θ) below 42° the number of wires available for track identification reduces linearly with $\tan\theta$ ($\mathrm{dn}/\mathrm{d}(\tan\theta) \approx 91$). Tracks with $\theta > 13^\circ$ can be reconstructed so that one is able to distinguish between charged and neutral particles.

The left-right ambiguity can be resolved by matching the tracks between the inner and the outer sectors. In addition a group of five grid wires on either side of 14 anodes in each outer sector is connected to a preamplifier via capacitor. The signals are then fed into a differential amplifier. The polarity of the output signal, corresponding to asymmetry of the avalanche at the anode [56] is used to determine the side of the incoming drift electrons.

Gold plated tungsten anode wires (of 20 μm diameter) measure the Z-coordinates of the tracks through charge division, down to polar angles of 18°.

The single wire efficiency is defined as the number of hits effectively used in the fit of a track over all possible hits for this track. It is found to be 93 % for R-Φ measurement and 78 % for charge division wires.

4.1.3 Plastic Scintillating Fibre

The Plastic Scintillating Fibre (PSF) [55] system is used to calibrate the drift velocity in TEC. The outer surface of each TEC is wrapped with a ribbon of PSF. Each ribbon has 143 optically isolated fibres with a cross section of $0.55 \times 1.0\,\mathrm{mm}^2$ and a length of 1.3 m. The drift velocity, determined from the average drift time of each anode wire and the corresponding PSF position, is measured with an accuracy of 0.1 %.

4.1.4 Central Z Chamber

The Z chamber [55] consists of two cylindrical proportional chambers with cathode strip readout, covering the outer cylinder of TEC. It has an effective length of 1.07 m, an outer diameter of 0.98 m and a thickness of 21.5 mm, which is equivalent to $0.013\,\mathrm{X}_\circ$. It is filled with the same gas mixture as used in TEC. The four layers of cathode planes (u, v, w and z layers) are made of kapton foil carrying copper strips of 4.45 mm pitch which form an angle of -69°, 90°, 69°, and 90° with respect to the beam direction.

4.1.5 Precision of Central Tracking System

Single wire resolution of TEC is 50 μm in the bending plane and double track resolution is 450 μm. This leads to a resolution in the measurement of transverse momentum as $\sigma(\mathrm{p_T})/\mathrm{p_T}^2 = 0.02\,(\mathrm{GeV})^{-1}$. In the non-bending plane, z coordinates are measured by Z chamber which has single track resolution of 300 μm and double track resolution of 7 mm.

SMD improves the tracking device by providing,

- Intrinsic resolution of 6 μm on the R-Φ coordinate, 20 μm in z corresponding to $\Delta\,\phi = 0.3$ mrad and $\Delta\,\theta = 1.0$ mrad.
- Resolution on distance of closest approach (DCA) of $\sim$ 50 μm.
- Resolution on $\mathrm{p_T}$ at 45 GeV of 47 % (1.7 times better than TEC only). The global $\mathrm{p_T}$ resolution is shown in figure 4.4.
- efficiency (ϵ) = 99.9 % for the ϕ layers and ϵ = 99.3 % for the z layers.

4.2 Electromagnetic Calorimeter

4.2.1 The Barrel and Endcap Electromagnetic Calorimeter

The barrel and endcaps of the electromagnetic (EM) calorimeter are made of Bismuth Germanium Oxide (BGO) crystals. The choice of BGO as the material for EM calorimeter

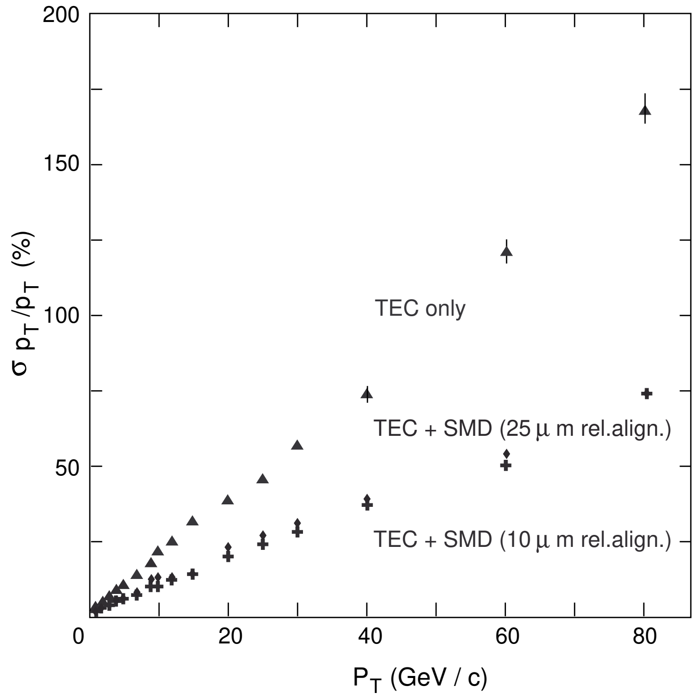

Figure 4.4: Momentum resolution in central tracking system.

is due to it high stopping power (short radiation length) for photons and electrons and large interaction length (λ_{int}) for hadrons. Furthermore it has low afterglow and is non-hygroscopic. Characteristics of BGO crystal are shown in table 4.1.

Density (g/cm^3)	7.13	Radiation length (cm)	1.12
Interaction length (cm)	22	Moliere radius (cm)	2.4
Refractive index	2.15	λ_{peak} (nm)	480
Temperature coefficient %/° C	-1.55	Photon yield (γ/MeV)	$\approx$ 8000
Radiation hardness (Gy)	10	Decay time (ns)	300

Table 4.1: Properties of BGO crystal.

The EM calorimeter consists of 10734 BGO crystals (7680 for barrel and 3054 for endcaps). Each BGO crystals is 24 cm long and is a truncated pyramid of about 2×2 cm^2 at the front face and 2.6×2.6 cm^2 to 2.9×2.9 cm^2 at the back faces according to the position (θ) of the crystals (figure 4.5(a)). The polished crystals are coated with a thin layer ($\approx$ 50 μm) of high reflectivity paint to ensure nearly uniform light collection efficiency. Two silicon photodiodes of dimensions 1.5 cm^2 detect the scintillation light from the rear face of the crystals. They are insensitive to the magnetic field and have a quantum efficiency of $\sim$ 70 %.

The barrel part of the EM calorimeter is divided into two half cylinders along z. The barrel calorimeter covers a θ-range of 42.3° to 137.7°. The inner radius of the barrel is

52 cm. Each half barrel consists of 24 rings along the polar angle θ and each ring contains 160 crystals over the entire azimuthal (ϕ) range. There are 24 different shapes of crystals corresponding to different polar angles.

The endcaps (EC) are made of two symmetric parts, with 1527 BGO crystals giving a polar angle coverage of $9.9^\circ < \theta, (180^\circ - \theta) < 36.8^\circ$. Endcaps contain 17 different shapes of crystals. Each EC is split into two halves separated by a vertical plane.

All θ slices point towards the interaction point while ϕ slices are tilted by 10 mrad to avoid cracks. All the cracks in the barrel result to a loss of 0.35 % in solid angle.

The calorimeter was calibrated using electrons of energies 0.18, 2, 10 and 50 GeV with an accuracy better than 1 %. The energy resolution has been found to be $\approx$ 5 % at 100 MeV and about 1.4 % at high energies. The impact point has been determined using the centre of gravity method. The position resolution is $\approx$ 1 mm corresponding to angular resolution of $\approx$ 2 mrad for EM showers at 45 GeV.

The detector is continuously calibrated with

- Bhabha events
- Radio frequency quadrupole [57]
- Cosmic muon [58]
- Xenon lamp [59]

Energy and position resolutions from beam test as well as from LEP data are shown in figure 4.6.

4.2.2 Forward Tracking Chamber

In front of each of the endcap BGO calorimeter four drift chambers (with a gas mixture of 38.5 % ethane and 61.5 % Ar) have been installed to measure the position and the direction of charged particles with spatial resolution better than 200 μm, and angular resolution better than 10 mrad.

4.2.3 Active Lead Ring

The Active Lead Ring (ALR) [50] covers the entire azimuthal angle and the coverage of polar angle is $3.9^\circ < \theta, (180^\circ - \theta) < 8.7^\circ$ in the gap between the forward BGO calorimeters and the luminosity monitors. It is located at 108 cm $< |z| <$ 118.4 cm. Each unit consists of five scintillator layers of 10 mm thick alternating with lead converters for a total length of 22 $X_\circ$. Three scintillator layers (P1, P2, P3) have a segmentation in the azimuthal angle (16 ϕ-scintillators) and remaining two (T1, T2) have a segmentation in

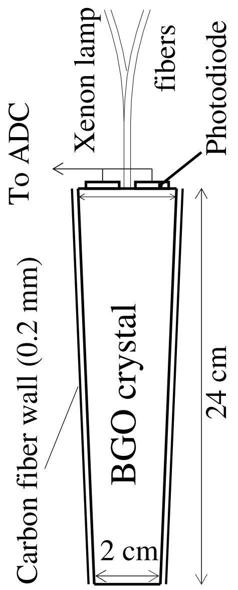

(a) A barrel BGO crystal.

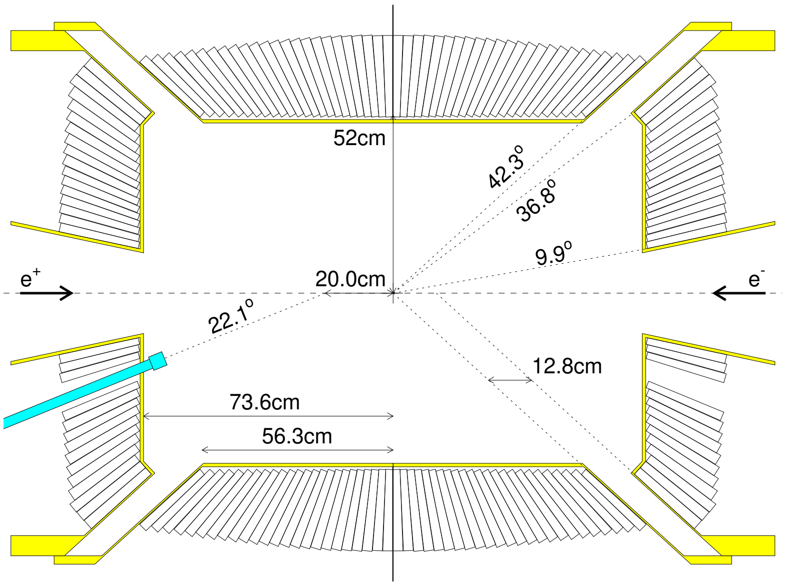

(b) Longitudinal view of BGO detector.

Figure 4.5: BGO crystal and L3 electromagnetic calorimeter.

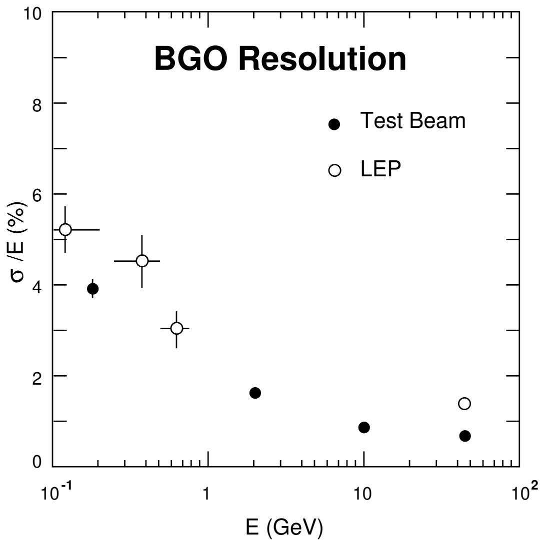

(a) Energy resolution of BGO calorimeter.

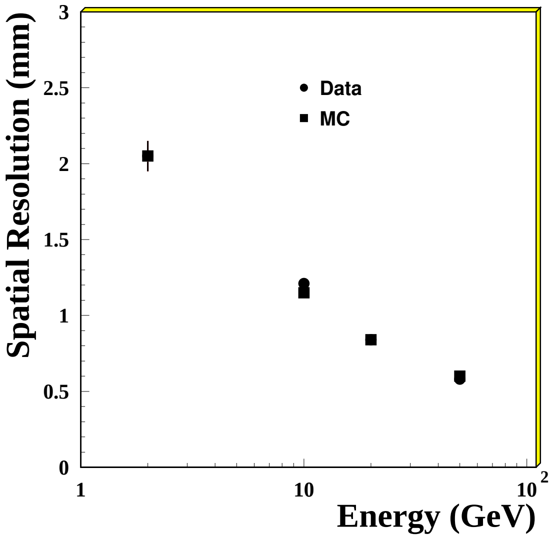

(b) Position resolution of BGO calorimeter.

Figure 4.6: Energy and position resolution of barrel BGO calorimeter.

the polar angle (5 θ-scintillators) as shown in figure 4.7. θ layers and ϕ layers are tilted by 7.5° with respect to each other. Thickness of each lead converter has been optimised to get the best **e/h** response. The scintillators are read out at their outer edge by silicon PIN photodiodes of dimensions $10 \times 20\,\mathrm{mm}^2$.

The resulting resolutions for electromagnetic showers are $\Delta\,E/E\ =\ 15\,\%$, $\Delta\,\theta\ =\ 0.45°$, $\Delta\,\phi\ =\ 2.7°$ at 45 GeV . The polar angle information of ALR is efficiently used to trigger the two photon events.

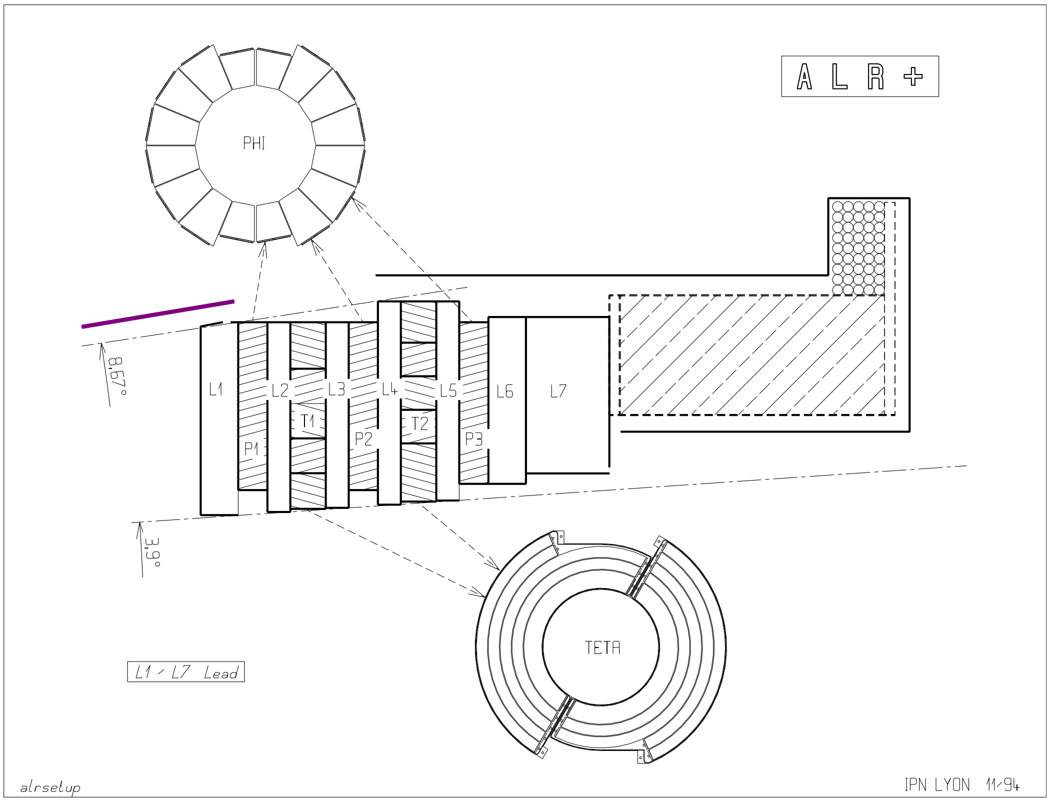

Figure 4.7: R-Φ view of the scintillator layers for a module of the upgraded ALR. Layers P1, P2 and P3 are ϕ-scintillators while layers T1 and T2 are θ-scintillators and L1 to L7 are lead converters [50].

4.2.4 Lead-Scintillating Fibre Calorimeter

During the 1995/96 shutdown period, the gap between barrel and endcap EM calorimeters has been filled with lead-scintillating fibre calorimeter (EGAP). Each gap is filled up with 24 modules of trapezoidal blocks. They are placed side by side to fit in the gap (shown in figure 4.8). The gap between the modules is tilted by about 25 mrad with respect to the interaction vertex to avoid loss of particles in the cracks.

The ratio in volume between the lead and the fibres is 4:1, giving $X_\circ = 0.72$ cm, in order to ensure a sufficient shower containment ($21\,X_\circ$).

From the test beam study one obtains the energy resolution as :

$$\frac{\sigma(\mathrm{E})}{\mathrm{E}} = \left(2.3 + \frac{11.6}{\sqrt{\mathrm{E(GeV)}}}\right)\,\%$$

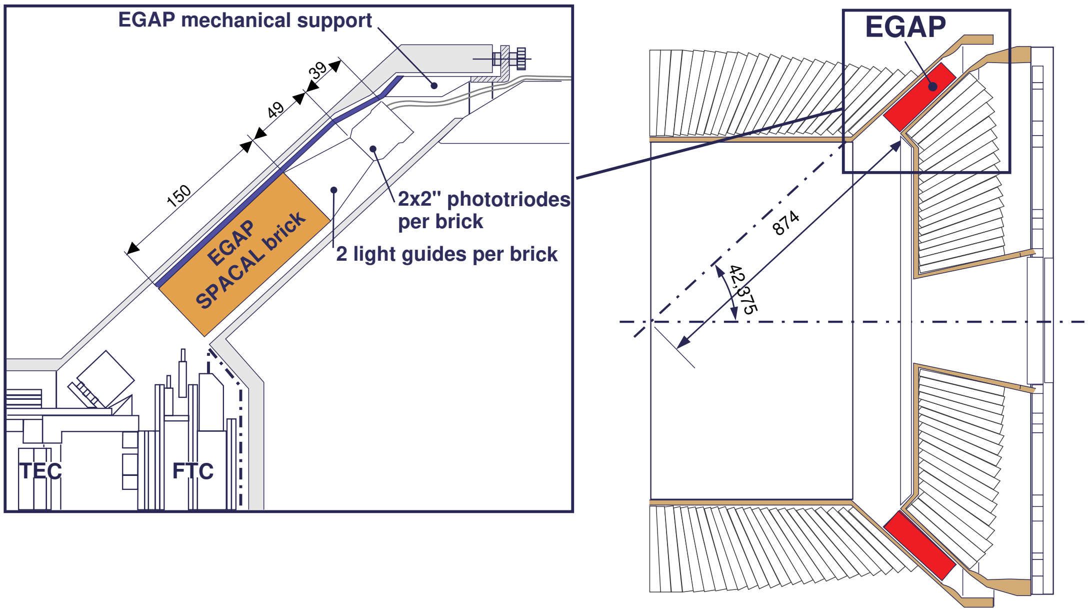

Figure 4.8: Lead-scintillating fibre calorimeter (EGAP).

4.3 Scintillation Counter

The scintillation counters measure the time of the particles passing through the detector with respect to the beam crossing time. The barrel part consists of 30 plastic scintillation paddles of length 2.9 m and thickness 1 cm. Both ends of the paddles are connected by light-guides to photomultipliers. In the R-Z plane the counters follow the shape of the hadron calorimeter and have a radial distance of 886 mm for $|z| < 800$ mm and 979 mm for 800 mm $< |z| < 1000$ mm from the beam axis. Polar angle coverage of the barrel counters is $34^\circ < \theta < 146^\circ$ ($|\cos\theta| < 0.83$).

The endcap scintillation counter system [60] consists of 16 counters located between the BGO and the HCAL endcaps on either side of the interaction point. Counters are made out of 3 plates of 5 mm thick plastic scintillator. The light from each plate is collected by 10 wave-length shifting fibres of diameter 1 mm glued into grooves of 1.5 mm $\times$ 1.5 mm. 30 fibres per counter-end are connected into an optical connector at the outside edge of the counters. A flexible guide (30 fibres, 17 mm long) connects the counters to the photo tubes which are situated outside the hadron barrel. The counters have an inner (outer) radius of 230 mm (746 mm). They are screwed to the shielding of the BGO endcaps. Middle of 2nd scintillator plate is located at a distance of z = $\pm$ 1132.5 mm from the nominal interaction point. This results into a polar angle coverage of $11.5^\circ < \theta < 34.1^\circ$ ($0.83 < |\cos\theta| < 0.98$).

A time resolution of 460 ps has been achieved from the dimuon events in barrel part and 1.9 ns in endcap. The efficiency of the scintillator hit for muon pair events is larger than 99 % [61].

4.4 Hadron Calorimeter

The barrel and endcap hadron calorimeters [62] are fine sampling calorimeters made of proportional chambers (80 % Ar + 20 % CO_2 mixture) interleaved with uranium plates as passive medium. Each chamber is made of a plane of brass (Cu : Zn = 63 : 37) tubes with 0.3 mm thick walls and 5 mm $\times$ 10 mm inner dimensions. In barrel part, the lengths of the tubes range from 347 mm to 605 mm depending upon the position of the chamber inside HCAL module. The chambers are shielded on both sides against uranium irradiation by 0.7 mm thick brass plates. The uranium layers are 5 mm (10 mm) thick for the fine (coarse) sampling part of the detector. Choice of uranium absorber was made because of its short interaction length, λ_{int} ($\approx$ 11 cm). R-Z view of half of the HCAL is shown in figure 4.9.

4.4.1 Barrel Hadron Calorimeter

The barrel hadron calorimeter has a modular structure consisting with 9 rings (along z-axis) of 16 modules (in ϕ) each and provides a complete coverage in azimuthal angle and a polar angle coverage of $37^\circ < \theta < 143^\circ$. The innermost ring is centred at the interaction vertex and is flanked on either side by one ring of long modules followed by three rings of short modules. The 4.725 m long barrel part has an outer radius of 1.795 m and inner radius of 0.886 m for the inner three rings and 0.979 m for the outer rings. Long (short) modules contain 60 (53) planes of proportional chambers and 53 (51) uranium plates.

The wires in each module are grouped to form readout towers. The segmentation is 9 in ϕ and also 9 in z; 10 segmentation in the radial direction for long modules, whereas 8 for short modules. The granularity decreases with radial distance as shown in figure 4.10.

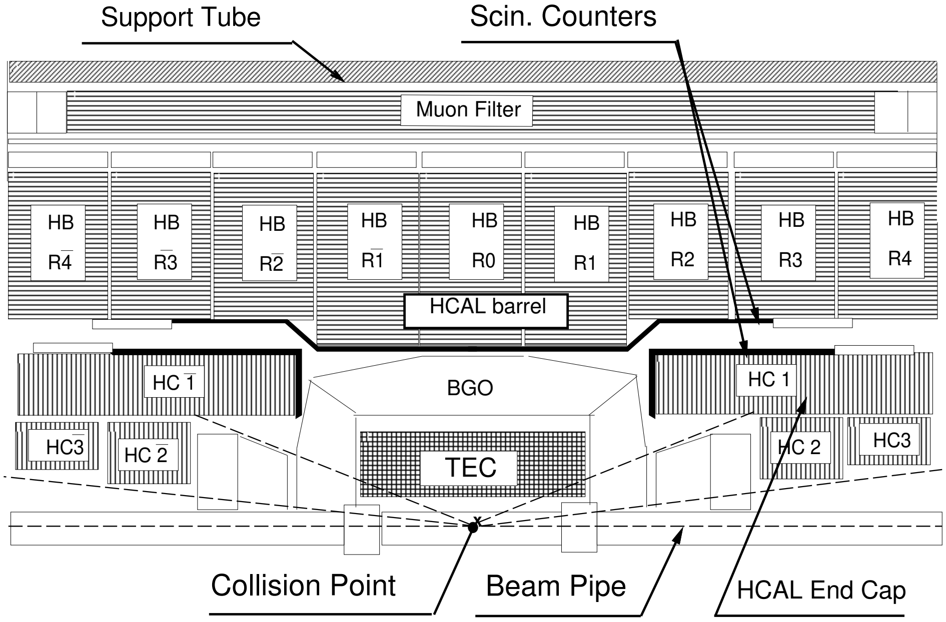

Figure 4.9: R-Z view of hadron calorimeter.

Typically, each tower covers $\Delta\theta = 2.5°$, $\Delta\phi = 2.5°$. The number of wires in each tower depends on the position of the tower and ranges from 3 to 28. The total number of charge sensitive readout channels from all 371764 wires of 7968 proportional wire chambers is 23040.

4.4.2 Endcap Hadron Calorimeter

The endcaps of the hadron calorimeter cover the polar angle regions $5.5° < \theta, (180° - \theta) < 23°$ over a full azimuthal angle. Angular regions $23° < \theta, (180° - \theta) < 37°$ covered by the combination of barrel and endcap. The solid angle covered by the endcaps extends the coverage of the HCAL to 99.5 % of 4π. Each endcap consists of three separate rings: an outer ring (HC1) and two inner rings (HC2 and HC3). Within a half-ring, odd numbered layers consists of four chambers (U-layers), each covering an interval $\Delta\phi = 45°$. Even numbered layers (V-layers with 3 full chambers and two half chambers) are rotated by $\Delta\phi = 22.5°$ with respect to the odd numbered ones. This stereo angle between successive layers allows measurement of the coordinate ϕ orthogonal to θ.

The 54140 wires of 2284 individual forward chambers are grouped into 3960 tower signals.

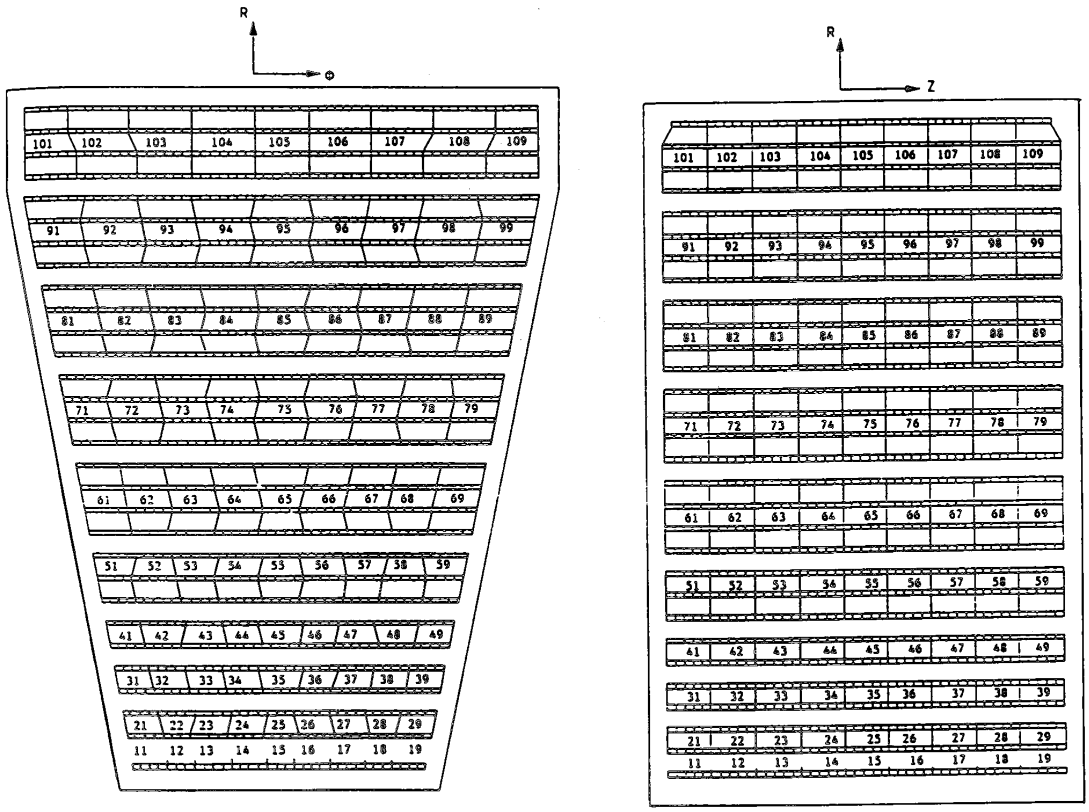

Figure 4.10: Wire grouping for the long module of HCAL barrel; left view : Φ projection and right view : Z projection.

4.4.3 Muon Filter

A muon filter [63] octant is 4 m long, 1.39 m wide and 0.21 m thick. It consists of six brass absorber plates, 1.0 cm thick each, interleaved with five layers of brass proportional chamber using 80 % Ar + 20 % CO_2 mixture. On the top of the outer layer, there are five additional 1.5 cm thick brass plates of different widths, assembled in a trapezoid shape to match the support tube circular shape. Muon filter provides on the average one λ_{int} to the hadron calorimeter.

Inner four layers of proportional chambers contain 16 chambers and the outer one consists 14 chambers. Each chamber is 4 m long and is made up of a comblike brass profile with eight tubes, equipped with a resistive anode wire along the tube axis. Total number of read-out channel is 9984.

4.4.4 Energy and Angular Resolution of Hadron Calorimeter

- Hadron calorimeter provides 2.5° angular resolution for hadronic jets and the energy resolution is

$$\frac{\Delta\,\mathrm{E}}{\mathrm{E}} = \left(5 + \frac{55}{\sqrt{\mathrm{E}\,(\mathrm{GeV})}}\right)\,\%$$

- The amount of material traversed by a particle originating at the interaction point varies between 6 to 7 nuclear interaction length (λ_{int}).

4.5 Muon Chamber

The muon chamber [64] consists of a barrel muon chamber (P-chambers and Z-chambers) and forward backward muon chambers on either side of the interaction point.

The barrel muon detector (figure 4.1) consists of two ferris wheels (symmetric under z-reflection), each having eight independent octants. Each octant consists of five precision P-chambers : two chambers (MO $\approx$ $6 \times 2.3\,m^2$) in the outer layer, two chambers (MM $\approx$ $6 \times 1.7\,m^2$) in the middle layer and one inner (MI $\approx$ $6 \times 2.2\,m^2$) chamber. They measure track coordinate in the bending plane to measure the momentum of the charged particles. In addition, the top and bottom of the MI and MO chambers are covered by six drift chambers (Z-chamber) to measure z-coordinate along the beam. Polar angle coverage with all three layers of P chambers is $44^\circ < \theta < 136^\circ$ and the corresponding solid angle coverage is 64 % of 4π. The two inner layers cover $35^\circ < \theta < 145^\circ$ (76 % of 4π solid angle).

4.5.1 P-Chamber

Each of the P-chambers contains about 320 signal wires and a total of 3000 wires as shown in figure 4.11 (including field shape, cathode and guard wires). With a gas mixture of 61.5 % Ar and 38.5 % C_2H_6, the P-chambers are operated in drift mode. Single wire resolution varies from 110 μm to 250 μm depending upon the distance from the wire plane and the slope of the track. Prime consideration is given to the accuracy of the sagitta (S $= (s_2 - \frac{s_1+s_3}{2})$ as shown in figure 4.12) determination, because momentum resolution is directly proportional to the error on sagitta measurement

$$\Delta\,S = \left[\left(\frac{\epsilon_1}{2}\right)^2 + \epsilon_2^2 + \left(\frac{\epsilon_3}{2}\right)^2\right]^{1/2}$$

where ϵ_i is the resolution of layer i. For a better momentum measurement, each of the MI and MO chambers have 16 signal wires while MM chamber has 24 signal wires to measure coordinates along a track in the bending plane.

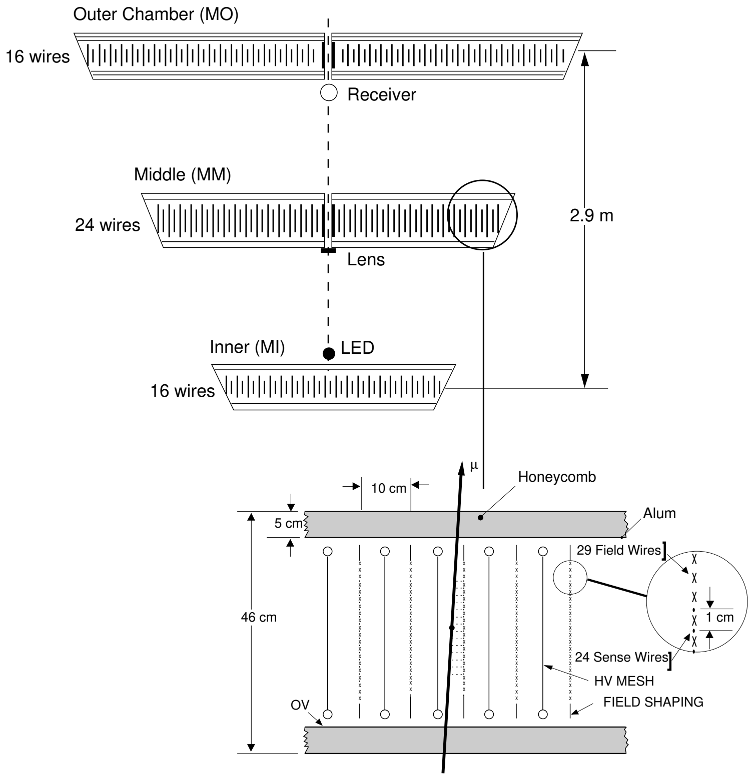

Figure 4.11: Muon chamber : R-Φ view of an octant of precision chamber.

The resolution in the measurement of sagitta (consequently the transverse momentum) depends on,

- Intrinsic resolution of the chambers which is $\approx$ 60 μm
- Multiple scattering in the chambers which is $\approx$ 43 μm at 45 GeV
- Systematic error in the relative alignment which is $\approx$ 30 μm

Consequently, the resolution on transverse momentum is

$$\frac{\sigma(p_T)}{{p_T}^2} \approx 0.0005(\mathrm{GeV})^{-1}$$

4.5.2 Z-Chamber

The Z-chambers consist of two layers of drift cells offset by one half (shown in figure 4.13) cell with respect to each other to resolve left-right ambiguities. All the 96 Z chambers have dimensions of 6 m $\times$ 2 m. Each cell has two parallel aluminium I beam connected to -2.4 kV and one gold-plated molybdenum anode wire with 50 μm diameter at $+2.15$ kV in the centre. It uses gas mixture of 91.5 % Ar and 8.5 % CH_4. Position resolution of Z-chamber, is typically 500 μm.

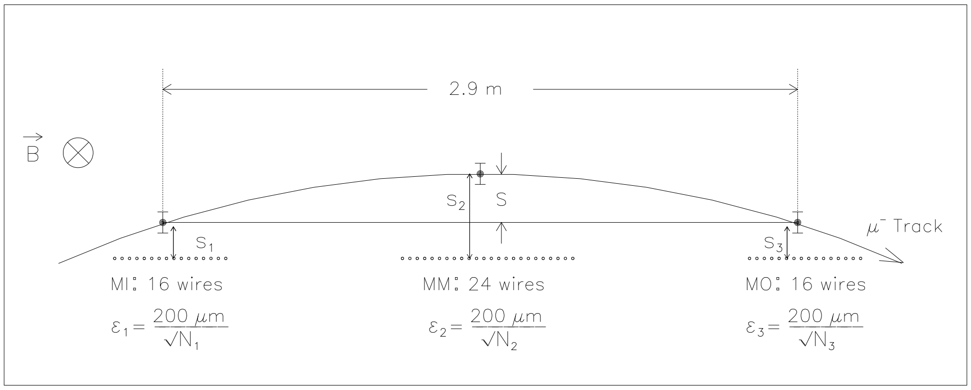

Figure 4.12: Muon chamber : Sagitta measurement in P chamber.

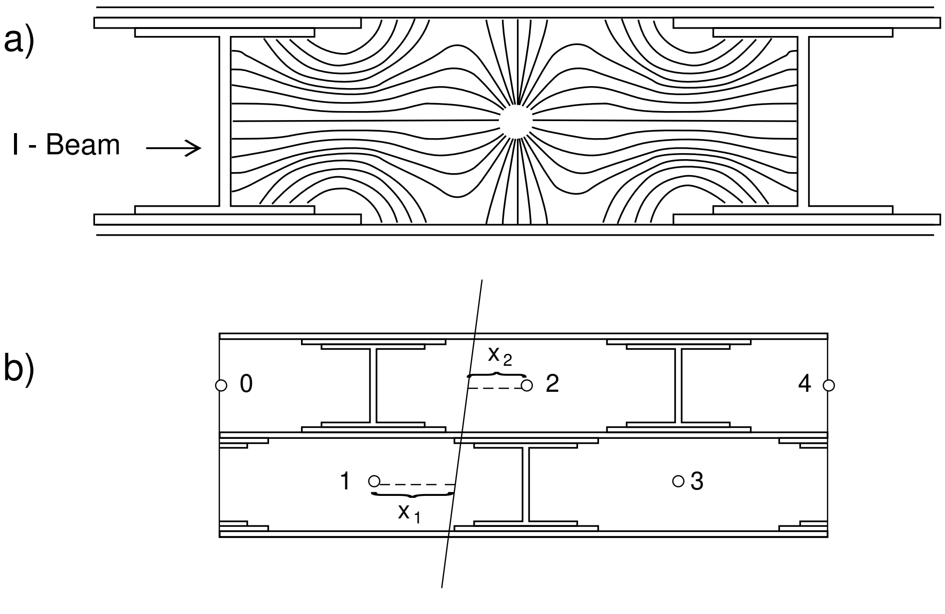

Figure 4.13: Drift cells in muon Z-chamber : a) field line inside the chamber and b) alignment of two layers.

4.5.3 Forward Backward Muon Chamber

The F/B muon chamber [52] consists of 96 precise drift chambers mounted in three layers (FI, FM and FO) on either side of the two magnet pole pieces, which are now toroidally magnetised (figure 4.14). Drift chamber uses the gas mixture of 86 % Ar, 10 % CO_2 and 4 % isobutane. All the chambers are of a trapezoidal shape. The bending coordinate is measured by X and W layers (x-z projection[1]) containing 19 and 18 cell each, with the orthogonal coordinate measured by the Y layer (y-z projection) containing 27 cells. They consist of three layers (Y, X, W) composed of a drift cell design as shown in figure 4.15. In the S-region ($36^\circ \leq \theta, (180^\circ - \theta) \leq 44^\circ$), the muons are analysed by measuring the helical bend in the solenoidal field with the drift chambers MI, MO and FI. In the T-region ($24^\circ \leq \theta, (180^\circ - \theta) \leq 36^\circ$) muons are deflected by the toroidal magnetic field and the coordinates are measured in the FI, FM and FO chambers. Y-layers mainly measure the polar angle deflection of tracks. The single wire resolution is $\approx 250\ \mu$m. Momentum resolution in S-region is 3 to 19 % at 45 GeV and in the T-region, it deteriorates to 30 % mainly due to multiple scattering in 1 metre thick magnetic doors.

4.5.4 Resistive Plate Counter

Trigger in the T-region of forward-backward muon chamber is provided by a system of Resistive Plate Counters (RPC) chosen for their fast time response and high efficiency.

Two layers of RPCs are assembled outside the magnetic door between the FM and the FO chambers as shown in figure 4.14. Every layer is divided into two independent units (Left and Right units) consisting of three RPCs (large, medium and small) of trapezoidal shape to fit the octagonal shape of L3. The middle unit is overlapped to the other two to avoid dead areas.

The sensitive volume of L3 RPC is a 2 mm thick gas gap between the electrodes operating in the limited streamer region under a uniform electric field of about 4 kV/mm. The gap is filled with a mixture of argon (58 %), isobutane (38 %) and freon (4 %).

RPC provides a space resolution of 7.7 mm, time resolution of 2.16 ns and a detection efficiency of about 99.5 %.

Expected muon momentum resolution as a function of polar angle is shown in figure 4.16.

[1]A local coordinate system is defined for each octant in which z coincides with electron beam direction, y points radially outward along the octant centreline

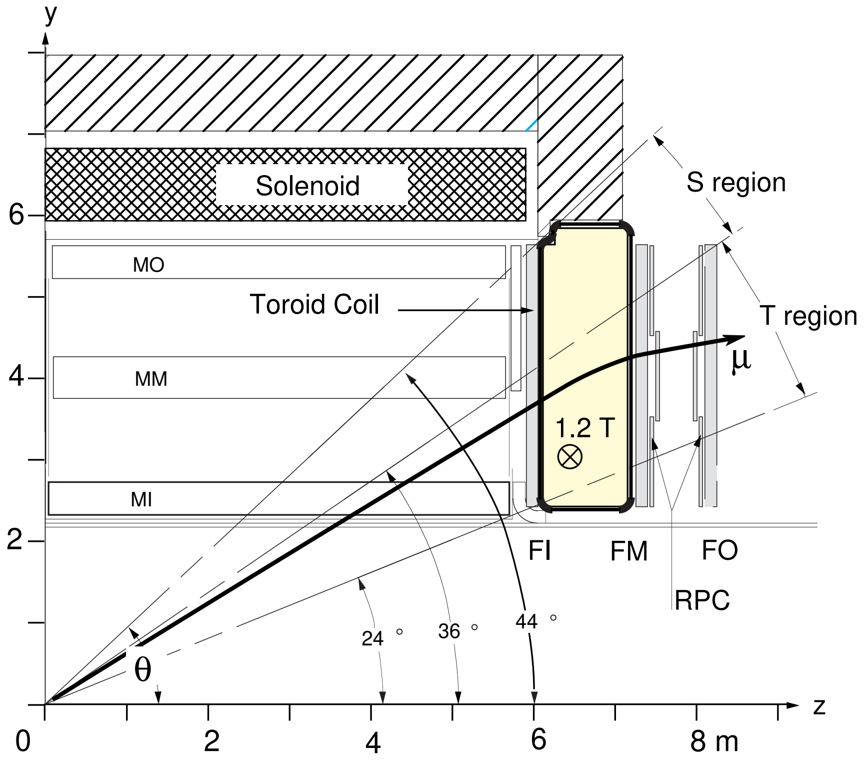

Figure 4.14: Side view of the forward backward muon chamber of L3 showing inner (FI), middle (FM) and outer (FO) drift chambers and RPC's for triggering. The two angular regions, solenoidal and toroidal are also indicated [52].

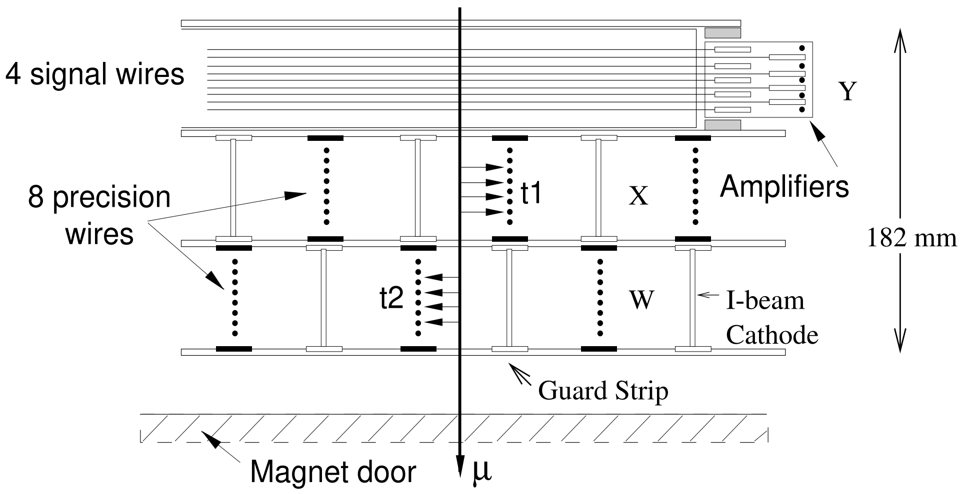

Figure 4.15: Drift chamber (in F/B MUCH) of three layers made of cells with 4 signal wires interspersed with five field wires and guard strips above and below the wire plane.

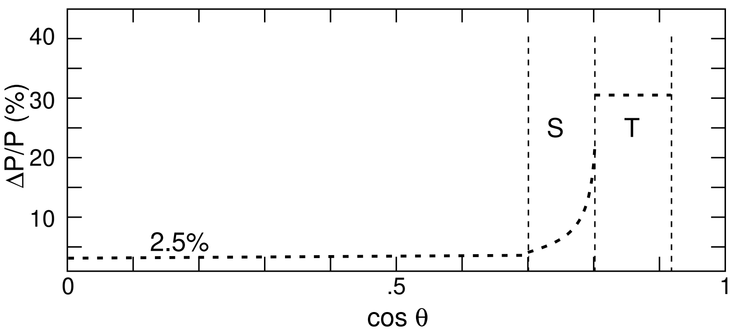

Figure 4.16: Muon momentum resolution (at 50 GeV) as a function of polar angle [52].

4.6 Luminosity Monitor

L3 luminosity monitor [66] consists of two detectors, situated at a distance 265 cm on either side the interaction vertex, as shown in figure 4.17. Each one consists of a calorimeter made of BGO crystals, which provides excellent energy resolution (2 % at 45 GeV) complemented by a tracker made of single sided silicon wafers which have intrinsic geometrical precision of about 1-2 μm. The luminosity monitor covers polar angle region 25 mrad $\leq \theta, (180° - \theta) \leq$ 70 mrad.

- **BGO calorimeter**

304 BGO crystals are situated at a distance $|z| =$ 273 cm from the interaction vertex with inner radius 68 mm and outer radius 192 mm. It consists of eight rings each covering 15 mm radially, parallel to beam pipe, having 16 azimuthal sectors of 22.5° each. The crystals are 26 cm long (24 $X_\circ$) and range in cross-section from 1.5×1.5 cm^2 to 1.5×3.0 cm^2.

- **Silicon strip detector**

Silicon strip detector (SLUM) is mounted in front of the BGO crystal at $|z| =$ 265 cm with inner radius 76 mm and outer radius 154 mm. On each side of the detector there are three layers: two layers of strips concentric with the beam axis (96 R wafers of three different pitches 64×0.5 mm, 16×1.875 mm and 16×1.0 mm) to measure the θ angle of the traversing particle and one layer of strips perpendicular to the beam axis (64 ϕ wafers of size 0.375°) to measure its ϕ angle. Each of the detector layer is built out of 16 silicon wafers which have an overlap of 1.5° in ϕ. The material in SLUM layers is equivalent to only 0.05 $X_\circ$.

With the combination of BGO crystal and SLUM, the absolute luminosity has been measured with an experimental precision of about 0.05 % at the Z peak and $\sim$ 0.6 % at high energy run. For the luminosity measurement events were selected with a tight fiducial volume on one side restricting the radial coordinate to 99.6 mm $<$ R $<$ 176.2 mm and restricting the azimuthal angle to $|90° - \phi| >$ 11.6° and $|270° - \phi| >$ 11.6° due to gaps in the detector. The loose fiducial volume on the opposite side is given by 92.8 mm $< \mathrm{R} < 183.8$ mm and $|90^\circ - \phi| > 4^\circ$ and $|270^\circ - \phi| > 4^\circ$.

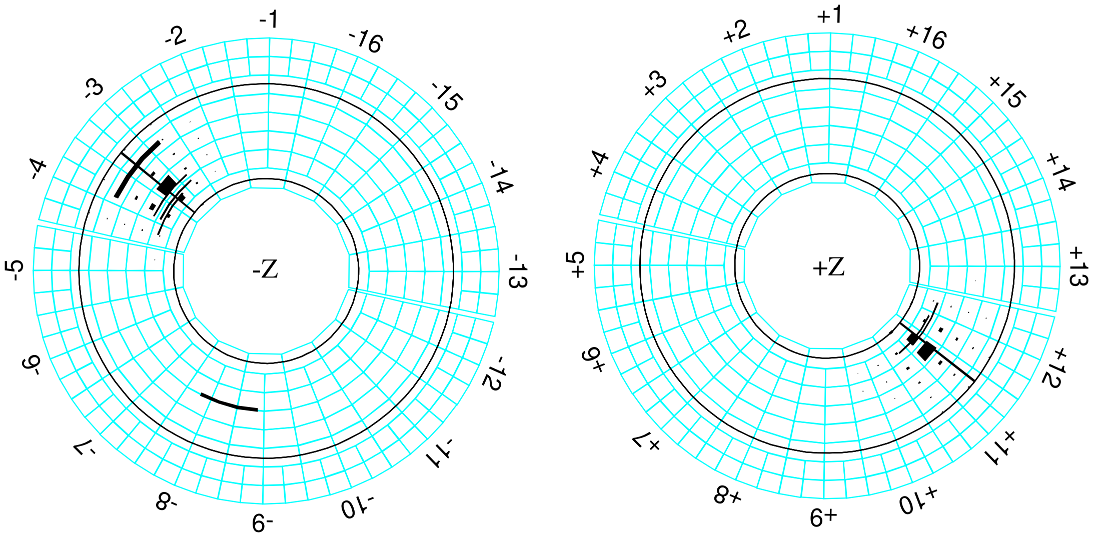

Figure 4.17: A Bhabha event in the luminosity monitor. Deep circular lines displayed the boundary of the silicon detector. The energy detected in the BGO is shown as squares, areas of which are proportional to the amount of energy deposited. The hits in the silicon detector are shown by highlighted line segments. Since they are located at different z positions, the silicon hit occurs at a somewhat smaller radius than the BGO impact points [66].

4.7 Very Short Angle Tagger

Very Short Angle Tagger (VSAT) [67] was installed during the 1995-96 shutdown to measure the electrons and photons at very small angle ($4.6\,\mathrm{mrad} < \theta, (180^\circ - \theta) < 10.2\,\mathrm{mrad}$). The detector consists of 4 boxes with 24 BGO crystals of size $9 \times 18 \times 220\,\mathrm{mm}^2$ each and they are positioned in the horizontal plane on each side of the beam pipe, behind the first quadrupole magnets as shown in figures 4.18 and 4.19. Each crystal has a photodiode for light collection and a LED to monitor the channel response. Resolutions of the detector are : $\Delta\,\mathrm{E}/\mathrm{E} = 5\,\%$, $\Delta\,\theta = 0.1$ mrad and $\Delta\,\phi = 40$ mrad for Bhabha events of energy 80.5 GeV.

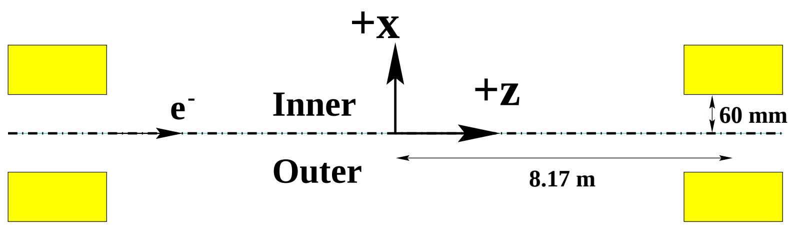

Figure 4.18: Schematic view of the VSAT boxes with the coordinates.

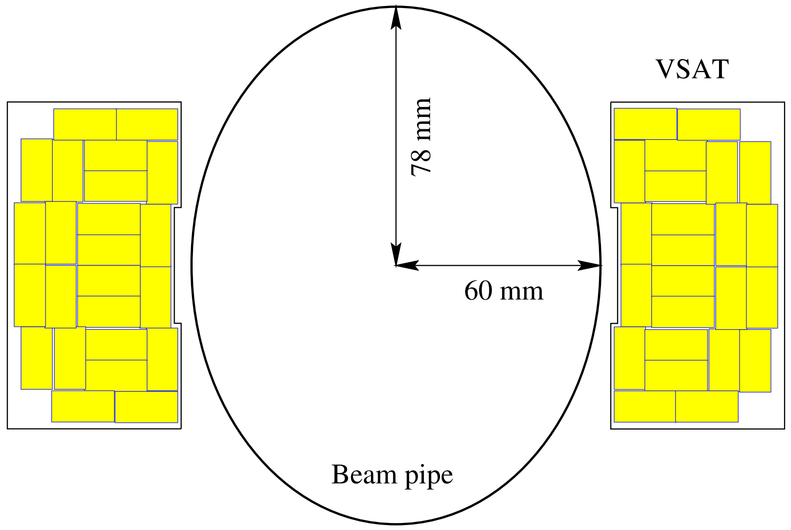

Figure 4.19: XY-view of two VSAT boxes.

4.8 L3 Magnet

All the subdetectors except the F/B muon chamber are kept inside a huge octagonal shaped solenoidal coil (of inner radius 5.93 m, total length 11.9 m and weight 1100 ton) which is surrounded by an iron yoke (made of soft iron with 5 % carbon content having outer radius of 7.9 m) and is closed at its ends by two iron doors (combined weight of the system is $\approx$ 7800 ton). An uniform solenoidal field of strength 0.5 Tesla along the positive z-direction is provided by 30 kA current (corresponding to power of 4.2 MW) through the coils.

Inside the support tube, magnetic field was mapped with Hall probes, whereas the remaining volume has been mapped with about thousand magnetoresistors. In addition, 5 NMR probes monitor the absolute value of the magnetic field.

A conductor made from hollowed aluminium with a cross section of 125×40 mm^2 was wound between the inner and outer radius of magnet door to provide a toroidal field. There are 36 turns per side. The coils are excited by 6.3 kA current with a 15 V voltage drop and gives a field of 1.2 Tesla along ϕ direction.

Fields are measured using induction coils and Hall plates. The field map was calculated with the h3-D program TOSCA [68].

4.9 Off-line Energy Calibration (G-Factors)

In accelerated based experiments, particles produced in interactions are detected using various subdetector, e.g., tracking chambers, calorimeters, muon chambers etc. Information from the subdetectors are related to the energy, momentum and identity of the particles produced. Since large and complicated detectors like the L3 detector contain dead materials and gaps, the visible energy in the detector can not be related to the energy of the particles or the events simply through the calibration of the detector components. Hence an off-line energy calibration factors (so called G-Factors) are used to relate the visible energy of particles and the total event in the detector to the actual energy. In the L3 detector the energy of the particles and the total event are obtained from calorimeters and muon chambers.

Energy from different part of L3 detector, $\mathrm{E_i}$ can be related to the energy of the event as

$$\mathrm{E_{event}} = \sum_{\mathrm{i}} \mathrm{G_i}\ \mathrm{E_i} + \sum_{\mu} |\mathrm{P}_{\mu}|$$

where $\mathrm{G_i}$ are the G-Factors corresponding to the subdetectors, more precisely a particular region of the subdetectors and P_μ are momenta of the muons from the muon chambers. Change in subdetector responses and the addition of new subdetectors in the L3 detector forced to have different G-Factors for different physics runs. G-Factors are also recalibrated according to the physics of interest.

4.10 L3 Detector Resolution

Global energy resolution of various particles are shown in figure 4.20 as a function of energy.

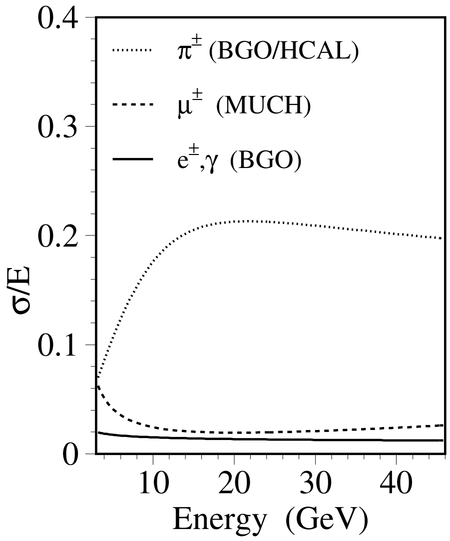

Figure 4.20: L3 detector resolution as a function of energy.

Chapter 5

L3 Trigger System

Trigger logic in any experiment is an integral part of the detector system to record a desired event. The L3 trigger system aims to record all interactions of physics interest and reject background events, e.g., beam-gas, beam-wall, cosmic muons etc. The beam crossing rate is 45 KHz for the four bunch operation of LEP. With luminosities of 10^{31} cm^{-2} s^{-1} standard physics processes can give rise to signal rate of $\sim$ 1 Hz. So one needs a trigger system which reduces the 45 KHz beam crossing rate to a few Hz of rate for recording on tapes. This is achieved using three levels of trigger to minimise the detector dead time. After a bunch crossing, each subdetector provides a coarse digitised data within a few μs (before next bunch crossing) to the level 1 and level 2 trigger system. For a bunch crossing satisfying level 1 triggers, all the subdetector signals are read out by front end electronics for a complete reconstruction of the event and information from Level 1 trigger logic goes to level 2. Level 3 trigger logic analyses the event with a complete reconstructed event information to store/reject it, if the event satisfying level 2. Figure 5.1 shows a schematic view of three levels of L3 online trigger system and their performances.

Some events are recorded on tape using random triggers (known as *beam-gate trigger* event) in order to study machine background and the noise level of the detector. The beam-gate trigger rate is restricted to 0.1 Hz. Also a small fraction of the events rejected by the level 2 and level 3 triggers are kept and recorded on tape. These events along with the trigger categories on which no rejection is applied, permit on-line and off-line checks of the level 3 decision performed.

5.1 Level 1 Trigger

The Level 1 has four triggers based on calorimeters (electromagnetic calorimeters (ECAL), barrel and endcap hadron calorimeters (HCAL), luminosity monitor (LUMI), active lead ring (ALR) and very short angle tagger (VSAT)), scintillation counters, muon

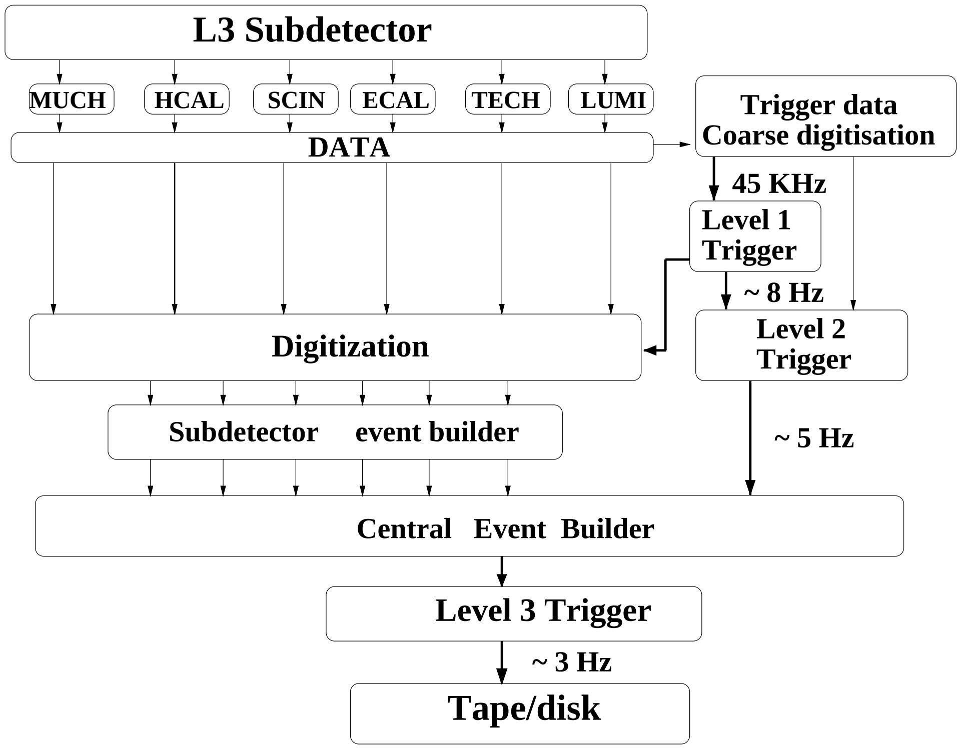

Figure 5.1: L3 online trigger system.

chambers and the TEC. Each subdetector is gated by the beam crossing signal and a decision is taken to accept or reject an event before the next beam crossing. Negative decision of level 1 trigger does not contribute to any dead time, because it clears the front end electronics before the next beam crossing. After a positive decision, the detector data are digitised and stored within 500 μs into multievent buffers and the system is made ready for the next trigger. Combined (logical .OR. of all trigger system) level 1 trigger rate is typically 8 Hz, corresponding to a dead time of 0.4 %. The system can however cope with a trigger rate upto 500 Hz with 25 % dead time. Individual trigger systems are described briefly in the following subsections.

5.1.1 Energy Trigger

This trigger selects events from the energy deposits in the calorimeters. It uses measurements from ECAL, HCAL, LUMI, ALR and VSAT.

ECAL : The 7680 crystals of the barrel provide 256 analog signals for the energy trigger, each corresponding to 30 crystals grouped together, to obtain an azimuthal segmentation (ϕ) of 32 segments and a polar segmentation (θ) of 8 segments. Endcaps consisting of 3054 crystals, provide additional 128 trigger signals with 4 polar segmentation and 32 azimuthal segmentation. Groupings are not uniform in endcap.

HCAL : The middle 7 rings of barrel are subdivided into an inner part A and an outer part B. Thickness of region A corresponds to one interaction length (λ_{int}). Two end rings do not have any A layer. Each endcap ring is subdivided into 16 ϕ segments and two layers of A and B. The layer A again corresponds to one λ_{int}. In total, A (B) has 16 ϕ and 11 (13) θ segments as shown in figure 5.2.

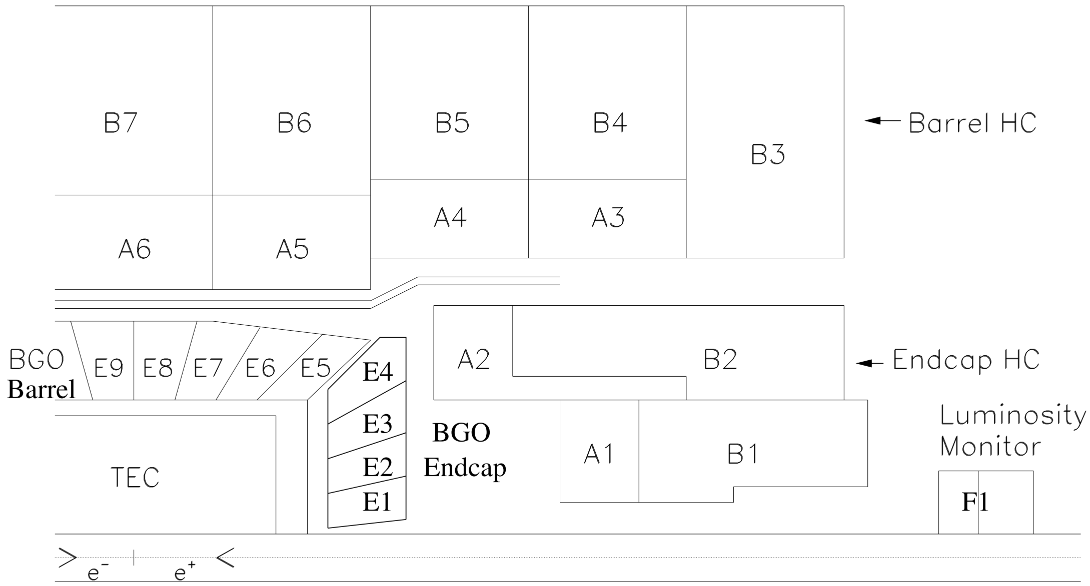

Figure 5.2: L3 calorimeter segmentation for trigger signals.

Part of the trigger information from the central tracking chamber is correlated with the energy trigger. The TEC trigger processor supplies 32 one-bit words to the energy trigger which are used by the cluster finder. Each bit indicates that atleast one track was found in a given ϕ-region corresponding to two electromagnetic trigger segments.

In total, the energy trigger processes 512 data words from the ECAL, 384 words from HCAL, 32 words from LUMI monitor and also uses 32 bits from the TEC trigger.

The following background processes are most critical to the level 1 energy trigger :

- Beam gas interaction,
- Uranium induced noise in the hadron calorimeter and
- Coherent electronic noise, mostly from the electromagnetic calorimeter.

To avoid triggering on background sources and at the same time keep energy threshold as low as possible, a series of different trigger conditions have been implemented [50, 70].

- *Total energy trigger :* The simplest trigger is based on the value of total energy detected by the two calorimeters, electromagnetic and hadron, ($E^{ecal+hcal}$). The total electromagnetic energy (E^{ecal}) is also computed to use in trigger with a lower threshold, since it has no uranium noise. Lower thresholds are also used by excluding the small angle regions ($18° \leq \theta \leq 162°$) for the total calorimetric energy and total ECAL energy ($E^{ecal+hcal}_{large\,angle}$, $E^{ecal}_{large\,angle}$). This reduces the effect of beam gas interactions.

- *Cluster trigger :* A trigger is defined for one or more clusters (localised energy deposit in a given θ and ϕ) in the angular range $18° < \theta < 162°$. A lower threshold is used when a track in TEC points to one such cluster.

- *Single photon trigger:* The trigger is designed to detect events of the type $Z° \rightarrow \nu\bar{\nu}\gamma$. This requires a low energy cluster in the barrel ECAL (the endcap electromagnetic calorimeter is not considered for the photon because the background from processes $e^+e^- \rightarrow e^+e^- \gamma$ becomes dominant in that region) with the additional requirement that there must be very little energy elsewhere in the electromagnetic calorimeter.

- *Hit counting trigger :* If any given trigger element records energy above a threshold depending on the calorimeter type and the polar angle, one associates a hit to that element. If the number of hits exceeds 2 within the angular region $18° < \theta < 162°$, the event is accepted by the trigger.

- *Luminosity trigger :* Each of the luminosity monitor provides 16 signals to the energy trigger corresponding to a segmentation in ϕ of 22.5°. A double tag trigger requires the total energies in the two luminosity monitors to exceed a threshold (different for each one), irrespective of their angular correlation. A single tag trigger requires a large deposit of energy in only one of the two luminosity monitors, also helps to monitor the on-line trigger efficiency.

- *ALR and VSAT trigger :* ALR trigger system is based on a set of 4 programmable 8 channel (energy threshold 300 MeV) comparators. The *.OR.* of the 32 channels gives (a) the single tag trigger (ST), (b) Bhabha trigger (BH) which is a coincidence between two opposite channels and (c) two photon trigger (GG) is due to signals in atleast one ALR channel and one track in TEC. To avoid a high trigger rate from ST and BH triggers, a 8-bit prescaler is implemented for a maximum rejection factor of 255. VSAT also has similar trigger logic. Since 1996 the ALR trigger is a combination of ALR and VSAT triggers.

The energy trigger thresholds are summarised in table 5.1. Energy trigger rate is $\sim$ 3 - 4 Hz and its efficiency for Z decays into electrons and hadrons is greater than 99.9 %.

Trigger type		Threshold (GeV)
Total Energy	E^{ecal}	25
	$E^{ecal+hcal}$	25
Large angle energy	E^{ecal}	8
	$E^{ecal+hcal}$	15
Cluster	Without TEC	6
	TEC & E^{ecal}	2.5
	TEC & E^{hcal}	2
Single photon	ECAL Barrel ($E_{clus}/E_{tot} > 0.8$)	1.
Single electron	TEC & Single tag	46.5
Hit	E^{ecal}, E^{hcal} (barrel)	2.5, 3
	E^{ecal}, E^{hcal} (endcap)	4, 5
Luminosity	Back to back	22.5
	Single tag prescaled by 40	46.5
	Double tag	38.5, 7.5
TEC + ALR	One TEC track & ALR energy	22.5

Table 5.1: Level 1 energy trigger.

5.1.2 Muon Trigger

The barrel muon trigger selects events with at least one particle which penetrates the muon chamber with transverse momentum greater than 1 GeV. It also requires a scintillation counter (SCNT) hit within 30 ns of the beam crossing time to remove the most dominant cosmic background. Muon in the forward-backward region are triggered by three different subdetectors: resistive plate chambers (RPC), endcap scintillators (ESCI) and F/B Muon Chambers (FB).

Trigger criteria [71] are summarised in table 5.2. Typical trigger rate is ~ 1 Hz with an efficiency greater than 99 %.

5.1.3 TEC Trigger

The TEC trigger [72] is used to select events with charged particles. TEC trigger can also be caused by background processes like beam-gas, synchrotron radiation and off momentum electrons. The rate of these background triggers decreases rapidly with the distance to the beam pipe. For this reason the inner chamber is not included in the trigger. Events are processed in three steps. Each step is carried out by a different set of electronics.

- *Segment divider (SD)* modules produce a hit pattern in the R-Φ projection using 14 left-right wires from each outer sector.
- *Track finder (TF)* modules receive the hit pattern information from the SD modules

Barrel Muon Trigger

Single Muon	2 out of 3 P-Chambers .AND. 3 out of 4 Z-Chambers .AND. 1 SCNT hit	
Dimuon	2 out of 3 P-Chambers .AND. 2 out of 4 Z-Chambers .AND. 1 SCNT hit	Acoplanarity [a] ± 2 (R-Z)

Forward Backward Muon Trigger

Single Muon	RPC .AND. [FI .AND. (FM U FO)] RPC .AND. ECSC ECSC .AND. [FI .AND. (FM U FO)]	
Dimuon	RPC .AND. RPC	± 4 (R-Z)
	RPC .AND. RPC	± 2 (R-Φ)
	RPC .AND. P_{track}	± 0 (R-Z)
	Barrel small angle .AND. ECSC	± 0
	RPC .AND. [FI*(FM U FO)]*ECSC	± 0 (R-Z)
	[FI*(FM U FO)] .AND. [FI*(FM U FO)]*ECSC	± 0 (R-Z)

Table 5.2: Level 1 muon trigger.

[a] Acoplanarity $= \pi - min\,(\,|\phi_2 - \phi_1\,|,\;\, 2\,\pi - |\phi_2 - \phi_1\,|\,)$

and search for track.

- *Track adder (TA)* modules are used to take the trigger decision based on the number of tracks ($0 < N_{track} < 48$), number of pairs of coplanar tracks (> 1, acoplanarity $< 60°$) transverse momentum of track ($p_T > 150 - 600$ MeV, depending on polar angle) etc.

The TEC trigger rate varies from 1 to 4 Hz depending on beam conditions. The efficiency of the trigger for a real Bhabha events is larger than 99.5 %.

5.1.4 Scintillator Trigger

Scintillator trigger [61, 73] is used to select high multiplicity events and to reject cosmic muons. A gate of 30 ns width is used to record hits in the scintillation counters. High multiplicity events are selected by requiring 5 hits spread over 90°. The rate of this trigger is typically 0.1 Hz with negligible background.

If an event has passed more than one trigger criteria out of the above four at level 1, it is automatically passed by level 2 and level 3 triggers, otherwise it is subjected through the trigger criteria of level 2 and level 3 as described in sections 5.2 and 5.3.

5.2 Level 2 Trigger

The inputs of the level 2 trigger [74] are : (a) the coarse data used in level 1, (b) the level 1 results and (c) information from combined clusters, jets etc., from calorimeters and loosely reconstructed tracks. Level 2 trigger is organised in terms of three independent parts comprising of energy trigger, TEC trigger and muon trigger.

- **The energy trigger** :

  Correlated noise is removed in level 1 by setting a threshold at 1 GeV. At the level 2, correlated noise is removed by setting a bias, which is computed for each event. This helps to reduce the noise level by a factor of 50 or so. Only the correlated hadronic deposits are added up to form the total hadronic energy measurement. Uranium noise activity, cosmic rays or events depositing energy only in the B layer of the hadron calorimeter are thus removed from the addition.

  The level 2 thresholds give rise to rejection $\sim 45\,\%$ of events selected by level 1 energy trigger. The analysis of large samples of e^+e^-, $\mu^+\mu^-$, $\tau^+\tau^-$ and $q\,\bar{q}$ final states demonstrates that this selection was achieved with 99.99 % selection efficiency.

- **The TEC trigger** :

  Most of the background contaminating the TEC trigger is induced by synchrotron radiation hitting the beam pipe. Such events are characterised by an excess of very low momentum tracks and tracks with origin different from interaction vertex.

  High momentum tracks from e^+e^- interactions are characterised by a sequence of hits in two adjacent anode wires. If the total number of such hits represents less than 20 % of the total number of hits measured in the event, or if more than 80 % of the recorded hits contribute to very low momentum tracks (< 70 MeV) the event is identified as beam-wall background and is rejected. TEC trigger needs at least one track having distance of closest approach (from the interaction vertex) less than 1 cm.

  The level 2 TEC trigger is able to reject nearly 80 % of the level 1 events. The efficiency of this trigger is 99.99 % based on a large sample of dimuon events.

- **The Muon trigger** :

  The level 2 muon trigger correlates the hits in the muon chamber and the scintillation counter. This leads to $\sim 70\,\%$ rejection of level 1 events with an inefficiency of 0.2 %, due to scintillator inefficiency.

The Level 2 trigger needs about 8 ms per event without incurring any additional dead time. For a positive level 2 signal the event builder collates the data for the entire event and transfers it to the level 3 trigger and the negative signal result resets of event builder memories. Depending on running condition and trigger type, a rejection factors of 45-80 % are obtained on the first level energy, muon and TEC triggers. Selection efficiencies greater than 99.95 % are obtained for Z events.

5.3 Level 3 Trigger

The level 3 trigger [75] performs a complete reconstruction of the event based on cluster reconstruction in the calorimeters, track reconstruction in the vertex chambers and in the muon chambers and the time of flight measured by the scintillator hodoscope. It takes $\sim$ 100 ms to analyse an event without inducing any additional dead time. If any error occurs in the processing of the event, like problem in decoding subdetector data, the event is accepted and an error flag is set to indicate a potential problem at the detector level. By using RISC processor addressed via fastbus, it is possible to accept up to 20 Hz as input rate without introducing any additional dead time to the system. Overall event writing rate is $\sim$ 2-3 Hz. Different trigger algorithms used in level trigger are described below :

- **The energy algorithm**:

  The channels which have energy below a threshold, (10 MeV for the BGO crystals and 50 MeV for the hadron calorimeter towers) are removed to eliminate most of the signals due to fluctuations of the electronic noise in the BGO and to uranium radioactivity in the HCAL.

  A cluster search is performed in the BGO calorimeter looking for contiguous regions of crystals around seeds of at least 50 MeV. The clusters with less than three crystals are not taken into account in the computation of the energy loss, but they are used to find coincidences with TEC tracks.

  A cluster search in the HCAL is performed in a very similar way to the BGO, requiring a starting cell with at least 500 MeV. In order to get rid of the uranium noise., the clusters which include only one tower or which have most of the energy (80 %) in the outer part (B layer) of the calorimeter are discarded.

  In the BGO barrel only ($42^\circ \leq \theta \leq 138^\circ$), a *single photon* is defined as the highest cluster which has more than two and less than 80 crystals.

- **The muon algorithm**:

  The level-3 trigger can further reduce the muon trigger rate applying a coincidence between the octant fired and the muon with the six scintillators infront of it.

  Moreover, taking advantage of the high resolution TDC used in the off-line analysis, a more stringent cut of $\pm$ 10 ns on the scintillation timing is also applied.

- **The TEC algorithm** :

  The level-3 TEC algorithm is made of four sequential steps :

  1. Pattern recognition in the vertex chamber,
  2. Evaluation of the multiplicity of the event,
  3. Correlation of the TEC tracks with the rest of the detector and
  4. TEC trigger decision.

The background fraction for all these triggers is typically 2-3 % with the 100 % efficiency for all the Z decay channel. This value is continuously checked on-line by looking at how many of these categories would have been rejected by level 3. A high rejection rate would indicate high level of noise.

On a positive level 3 result, the event, which has an average size of 34 kbytes (varies from 20 to 100 kbytes) is transferred to the online computer and written on tape.

The system has been designed to sustain an average rate of 10 Hz and a maximum peak rate of 50 Hz. However, the LEP machine gives very low background and these high rates are rarely experienced.

Chapter 6

L3 Detector Simulation and Event Reconstruction

6.1 Monte Carlo Simulation

Monte Carlo (MC) simulation is used to put the existing physics knowledge into the detector design and data analysis. It allows us to understand the response of the detector to physics processes and to estimate the systematic errors to a very precise level so that one can make both precision tests of known physics processes and searches for unknown new processes.

In L3, the MC simulation program generates events in two steps :

1. *Event generation*, where events are generated with a distribution according to the physics of interest and the results are stored as sets of 4-momenta, production vertices and particle types of all stable and unstable particles.

2. *Detector simulation*, where the generated particles are traced through the detailed representation of the detector and the response of each active element is simulated.

6.1.1 Event Generation

Various event generators are used to generate events for different physics processes. In these analyses, several generators have been used to describe the signal and background processes. The same table of particle properties (masses, widths, decay branching ratios etc.) has been used in all these generators. However, the radiative corrections are not the same for all the generators. The event generator SUSYGEN [76] has been used to generate the signal of SUSY events and the event generators BHAGENE3 [77]($e^+e^- \to e^+e^-$), KORALZ [78] ($e^+e^- \to \mu^+\mu^-$ and $e^+e^- \to \tau^+\tau^-$), KORALW [80] ($e^+e^- \to W^+W^-$), PYTHIA [81] ($e^+e^- \to q\bar{q}$, $e^+e^- \to Zee$, $e^+e^- \to Z/\gamma^* Z/\gamma^*$, $e^+e^- \to We\nu$ and

$e^+e^- \to e^+e^- q\,\bar{q}$), PHOJET [82] ($e^+e^- \to e^+e^- q\,\bar{q}$), DIAG36 [82] ($e^+e^- \to e^+e^- \ell^+\ell^-$), EXCALIBUR [83] ($e^+e^- \to f\,\bar{f}\,f'\,\bar{f}'$), GGG [84] ($e^+e^- \to \gamma\gamma$) for the different Standard Model processes. A brief description of different generators is given below :

1. **SUSYGEN** :

   SUSYGEN, based on the formalism of W. Bertl *et al* [10, 12, 13], is used for the production and decay of all MSSM sparticles in e^+e^- collisions. It takes into account cascade decays. It is interfaced to JETSET 7.4 [85] and includes initial state radiation. It has an option for both **R**-parity conserving decays and non-conserving decays.

   Assuming soft symmetry breaking at the GUT scale, all sparticle masses can be expressed in terms of 5 SUSY parameters and the SM parameters. The masses at electroweak scale are then determined by the well known Renormalisation Group (RG) equations. These SUSY parameters are

   $m_\circ$ $\equiv$ the common mass of the spin 0 squarks and sleptons,
   M_2 $\equiv$ the SU(2) gaugino mass parameter at electroweak (EW) scales,
   μ $\equiv$ the mixing parameter of the Higgs doublets,
   $tan\,\beta$ $\equiv$ the ratio of the vacuum expectation values of the two Higgs doublets and
   A $\equiv$ the trilinear coupling in the Higgs sector.

   Out of all the parameters $m_\circ$ is defined at the GUT scale, while the remainings are defined at the EW scale.

2. **BHAGENE3** :

   BHAGENE3 is used for wide angle bhabha scattering ($10^\circ < \theta_l < 170^\circ$) at centre of mass energies around and above the Z peak and also for μ-pair production in the region of Z peak. The generator includes complete one-loop electroweak corrections, leading two-loop effects from a heavy top quark which are of type $\alpha^2(m_t/m_Z)^4$ and QED corrections. Higher-order QED corrections are included in an improved soft photon approximation with exponentiation of initial state radiation. Multiple hard photon generation ($n_\gamma \leq 2\,(3)$ for initial (final) states) and $\mathcal{O}(\alpha)$ initial/final interference effects are also included. Events are generated in the full phase space of the final state taking care of explicit mass effects in the region of collinear mass singularities.

3. **KORALZ** :

   KORALZ is used to generate $\mu^+\mu^-$, $\nu\,\bar{\nu}$ and $\tau^+\tau^-$ pairs in e^+e^- interactions. It includes initial and final state bremsstrahlung corrections upto $\mathcal{O}(\alpha^2)$ (inclusive exponentiation, multiple QED hard bremsstrahlung from both initial and final states are included but no interference) and $\mathcal{O}(\alpha)$ electroweak corrections. Complete $\mathcal{O}(\alpha)$ QED corrections are included in the pure leptonic decay channels and for other decay channels an interface is provided to the PHOTOS [79] MC generator for approximate simulation of the QED corrections. It uses a software package TAUOLA [86], which provides more than twenty distinct τ^- decay modes : (a) leptonic decay modes $\tau^- \rightarrow \nu_\tau \bar{\nu}_e e^-(\gamma)$ and $\nu_\tau \bar{\nu}_\mu \mu^-(\gamma)$, (b) one meson modes, $\nu_\tau \pi^-$ and $\nu_\tau K^-$, (c) two-meson modes, $\nu_\tau \pi^- \pi^0$ and $\nu_\tau K^- \pi^0$, (d) three meson modes, $\nu_\tau \pi^- 2\pi^0$, $\nu_\tau 2\pi^- \pi^+$, $\nu_\tau K^+ K^- \pi^-$, $\nu_\tau \bar{K^0} K^0 \pi^-$, $\nu_\tau K^- \bar{K^0} \pi^0$, $\nu_\tau K^- 2\pi^0$, $\nu_\tau K^- \pi^- \pi^+$, $\nu_\tau K^0 \pi^0 \pi^-$ and $\nu_\tau \eta \pi^- \pi^0$, (e) four pion modes, $\nu_\tau \pi^- 3\pi^0$ and $\nu_\tau \pi^- \pi^- \pi^+ \pi^0$ (including the $w\pi^-$ contribution), (f) multipion modes, $\nu_\tau n \pi^{\pm,0}$ with $n > 4$ and finally the $\tau^- \rightarrow \nu_\tau \pi^- \pi^0 \gamma$ from the $w \rightarrow \pi\gamma$. Antiparticle (τ^+) also has the identical decay modes. The effect of longitudinal polarisations for the incoming $e^\pm$ and outgoing $\tau^\pm$ are also incorporated. Spin polarisation effects in τ decays are included except for multipion decays $\nu n \pi$ with $n > 4$. It is able to generate $\mu^+\mu^-$ and $\nu\bar{\nu}$ pair also. With some restrictions $u\bar{u}$, $d\bar{d}$, $c\bar{c}$, $s\bar{s}$ and $b\bar{b}$ final states can also be generated using this generator.

4. **KORALW** :

The Monte Carlo Program KORALW generates W^+W^- pair in e$^+$e$^-$ collision upto $\sqrt{s} \sim 200$ GeV. Main features of the generator are :

- Matrix element for W-pair production into four fermions (quarks and/or leptons) is used with proper treatment of W spin and finite W width.
- Multiple initial state radiation with finite transverse photon momenta are generated according to the Yennie-Frautschi-Suura MC technique [87]. A semi-analytical structure function based leading-logarithmic initial state radiation up to third order is also included in the distribution package. But a very simplified matrix element for QED photon emission is used.
- Decay of polarised τ lepton (decay product of W) is simulated in all possible channels, taking into account spin polarisation and QED bremsstrahlung, but there is no electroweak non-QCD correction.
- Quarks (decay products of W) are arranged into strings and fragmented into hadrons according to the LUND model using JETSET [85] with a simplified colour arrangement for four quark jets.
- Complete kinematics with exact four-momentum conservation is implemented for the entire production and decay processes.

5. **PYTHIA** :

The generator PYTHIA is used to generate a variety of high-energy physics events, e.g., multihadron final states in e$^+$e$^-$ collisions, two photon processes etc. In a process that contains coloured and/or charged object(s) in the initial or final state corrections due to gluon and/or photon radiation are incorporated. Both the parton shower (PS) and $\mathcal{O}(\alpha_s^2)$ matrix element (ME) options are used for radiations from quarks and gluons. *String fragmentation* model as well as independent fragmentation options are incorporated in the model. It includes all particles with their proper mass distributions and decay properties.

6. **PHOJET** :

   PHOJET is an event generator for minimum bias hadronic events in $p\,p$, $\gamma\,p$ and $\gamma\,\gamma$ interactions. The interaction is described by the Dual Parton Model (DPM) [88] in terms of Reggeon and Pomeron exchanges. At Born level, the photon-photon interactions are due to : (a) soft reggeon and pomeron exchange, (b) hard resolved photon-photon interaction, (c) single direct interactions and (d) double direct interactions. Produced partons are fragmented using the Lund fragmentation code JETSET.

7. **DIAG36** :

   DIAG36 is an event generator for the complete set of tree level QED diagrams (multiperipheral, bremsstrahlung, annihilation and conversion) for the process $e^+e^- \to e^+e^- f\,\bar{f}$, including all fermion masses. It can be used to generate events which cover the whole kinematically allowed phase-space or to generate events over a truncated phase space obtained by cuts applied for typical single- or double-tagged configurations.

8. **EXCALIBUR** :

   The Monte Carlo generator EXCALIBUR generates all four-fermion processes in e^+e^- interactions. Fermions are taken to be massless to allow a very fast evaluation of the matrix elements. 152 Feynman diagrams are incorporated in this generator for different channels. It incorporates the LL $\mathcal{O}(\alpha)$ and $\mathcal{O}(\alpha^2)$ initial state radiation, with exponentiation of the remaining soft-photon effects [83]. QCD corrections are implemented using the structure-function formalism [83].

9. **GGG** :

   It generates events with two or three γ's in e^+e^- collisions. It uses an analytic expression for the total annihilation cross section to the order α^3.

6.1.2 Detector Simulation

The L3 detector simulation program SIGEL3 is based on general purpose detector simulation package GEANT3 [89]. It provides a complete description of the L3 detector, including the details of each subdetector geometry down to the required level of accuracy ($\sim$ 10 - 100 μm) with all the properties of subdetector materials and magnetic field. Examples illustrating the complexity of this geometry are the hadron calorimeter, which consists of 425904 proportional brass tubes grouped into around 26K chambers, and the electromagnetic calorimeter, with 10734 BGO crystals of various shapes in a thin-walled carbon fiber structure etc. GEANT3 provides elaborate simulation of known physical processes and interaction of particles with matter such as decay, ionisation loss, multiple scattering, photoproduction, δ-ray production, bremsstrahlung and so on. For the complicated hadronic interaction processes GEANT3 uses a hadronic shower development package GHEISHA [90]. The response of the tracked particles in the active medium is simulated in detail. Electrons and photons are traced upto 100 KeV, muons and charged hadrons upto 1 MeV and neutrons upto 10 KeV. Test beam results of the calorimeters [?] are used to fine tune the parameters of the simulation package, e.g., the step size for particle tracking in all subdetectors, cut-off value for energy in different medium, saturation in light yield, electronic noise etc. All these reproduce not only the global energy response but also the energy and direction of individual particles or jets. Response and resolutions depend on the polar angle and the boundary regions of subdetectors.

Hits in the central tracking chamber (TEC) and in the muon chamber (MUCH) are simulated using the time-to-distance relation measured in the test beam data [91]. The effects of temperature, pressure, noise and cross-talk have been simulated. ADC and TDC informations are simulated in the scintillation counter taking care of light attenuation, time of flight of particles, time slewing due to varying pulse height etc. The effect of nonuniformity in light collection and electronic noise have been simulated in the electromagnetic calorimeter. In generating the signals in hadron calorimeter, the effect of uranium noise, gas saturation etc., have been introduced. L3 trigger criteria have been also simulated with realistic thresholds and their fluctuations to calculate the trigger efficiency from the MC events.

Deterioration of detector resolutions caused by the detector imperfections, e.g., the dead or noisy BGO crystals, defective towers in HCAL, disconnected sectors and inefficient wires in the TEC and MUCH vary with time during the data taking. In order to reproduce the data by the detector simulation, the time dependent detector response has been simulated in the MC event samples.

L3 data base system [92] stores all the information on the status and calibration of the detector for any given instant during the entire data taking period. During the reconstruction of simulated data, appropriate information can be retrieved from the database using the time and date attributed to the event to discard dead or noisy channels and apply appropriate calibration. This process is called *real detector Monte Carlo simulation.*

6.2 Event Reconstruction

The event reconstruction program REGEL3 [93] converts the raw digitised detector signals into physically meaningful observables, e.g., *Tracks* in the Central Tracking system, *Clusters* in the electromagnetic and hadron calorimeters, *Muons* in the MUCH (needs atleast one Z chamber and two P chambers hit), *Smallest Resolvable clusters* from the matching of ECAL and HCAL clusters, *Jets* (the combination of nearby clusters and muons etc., (detail in section 7.1)) which are used in physics analysis. Detector signals arising from the real e^+e^- interactions and the simulated data are reconstructed using the same L3 reconstructed program. The event reconstruction program tries to categorise the events according to different branch of physics processes using loose selection criteria. This helps to get a fast analysis.

Schematic view of data flow in L3 reconstruction program, starting from the detector signals to the objects used in physics analysis are shown in figure 6.1.

The reconstructed data are kept in three different formats according to decreasing size and increasing constraints.

- *Data Reconstruction* (DRE) Format: This format keeps (a) all raw detector informations like pulse heights of all ADC and TDC channels, (b) details of reconstructed objects of all individual channels, e.g., hits in the TEC and MUCH wires, energy deposits in calorimeters etc., and (c) all kinematic quantities of physically meaningful observables, e.g., cluster, bump, track, muon etc.
- *Data Summary* (DSU) Format : It keeps only the information (b) and (c) as described under DRE format. This format allows to re-reconstruct tracks, cluster etc., using database information.
- *Data Avanti* (DVN) Format : It keeps only the information (c). Reduced size of the events allows a quick analysis.

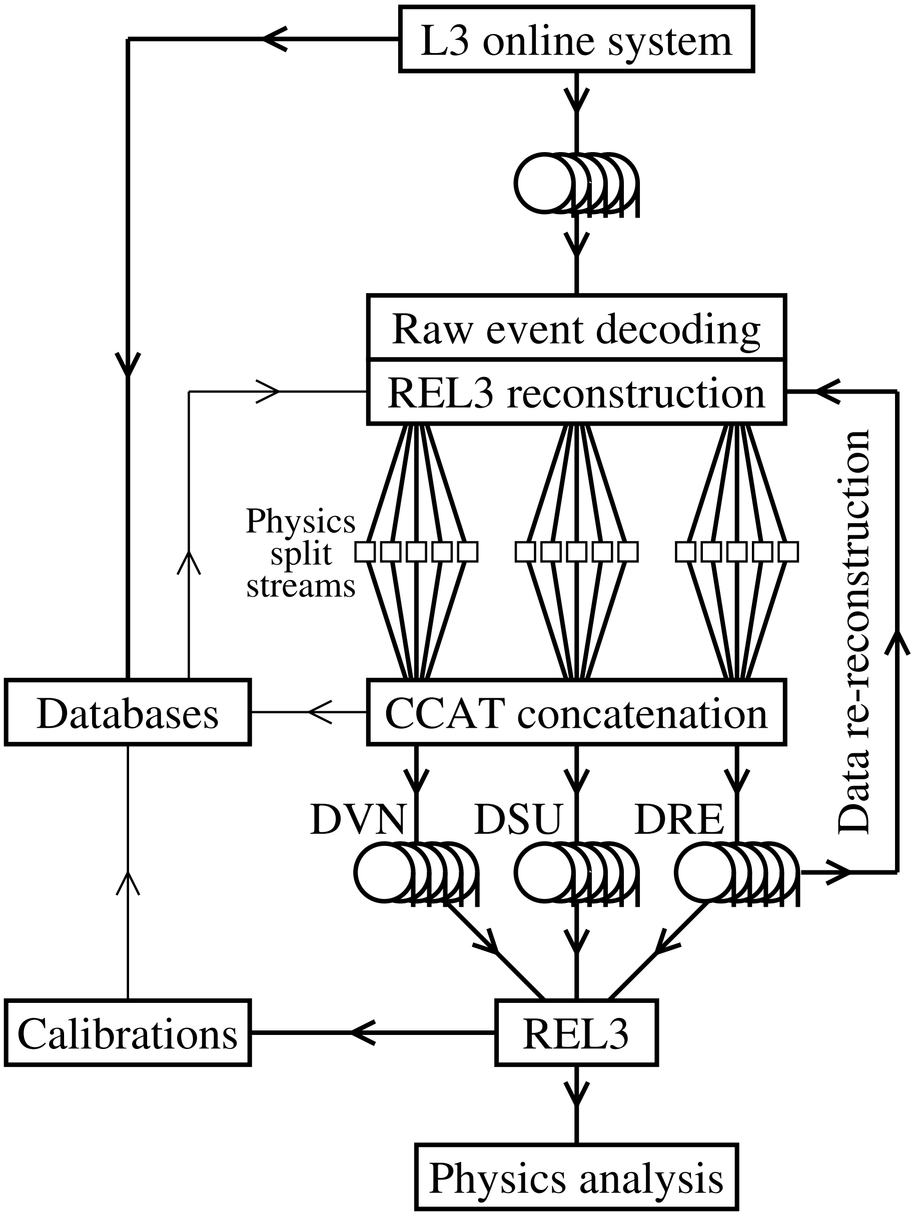

Figure 6.1: Flow of data in L3 reconstruction program from detector signals to the physics object.

Chapter 7

Strategy for Selection of SUSY Events

e^+e^- interactions in LEP collider give rise to final states through the Standard Model (SM) processes and may be there are new processes which can not be explained by the SM. To establish physics processes beyond the SM, one has to distinguish those events from the events coming through the SM processes. In these searches supersymmetry (SUSY) is assumed to be the physics beyond the SM.

Events from different physics processes have their own characteristics. Consequently they give rise to different types of signals in the subdetectors, e.g., $e^+e^- \rightarrow Z \rightarrow q\bar{q}$ process yields a large number of hadrons in the final state. This results in well balanced events i.e., within detector resolution, the vector sum of the three momenta of the final hadrons is zero and the energy sum of all the final state particles is equal to the centre of mass energy of the system. Events due to the process $e^+e^- \rightarrow Z \rightarrow \tau^+\tau^-$ can end up in one of the three possible channels : (1) events with two very narrow jets, (2) events with one narrow jet and one electron or muon, $e\,/\mu$ and (3) two charged leptons : $e\,e\,/\,e\,\mu\,/\,\mu\,\mu$. Though these events have large missing energy/momentum, the two jets are almost back to back.

On the other hand the SUSY processes which have been searched in these analyses :

- $e^+e^- \rightarrow \tilde{e}^+\tilde{e}^- \rightarrow e^+e^-\tilde{\chi}_1^\circ\tilde{\chi}_1^\circ$,
- $e^+e^- \rightarrow \tilde{\mu}^+\tilde{\mu}^- \rightarrow \mu^+\mu^-\tilde{\chi}_1^\circ\tilde{\chi}_1^\circ$,
- $e^+e^- \rightarrow \tilde{\tau}^+\tilde{\tau}^- \rightarrow \tau^+\tau^-\tilde{\chi}_1^\circ\tilde{\chi}_1^\circ$,
- $e^+e^- \rightarrow \tilde{\chi}_1^\circ\,\tilde{\chi}_2^\circ \rightarrow \ell^+\ell^-\tilde{\chi}_1^\circ\tilde{\chi}_1^\circ$

and • $e^+e^- \rightarrow \tilde{\chi}_1^+\,\tilde{\chi}_1^- \rightarrow \ell^+\ell'^-\,\nu\bar{\nu}'\,\tilde{\chi}_1^\circ\tilde{\chi}_1^\circ$

contain leptons and neutralinos in the final state. These events should have large missing energy, missing transverse momentum (section 2.3.4) and large acoplanarity of the leptons.

The following steps are taken to distinguish the SUSY signal events from the Standard Model background processes,

1. All particles in the final state are identified to the best capability so that the energy

is measured with the highest resolution.

2. A set of kinematic variables is chosen which can distinguish signals from background processes.
3. Cuts are chosen so as to obtain high selection efficiency for SUSY signal processes and efficient rejection of residual SM backgrounds.

Monte Carlo simulated events (chapter 6) are used to study selection criteria for SUSY signal events and the calculation of selection efficiencies.

The procedures to identify e, μ and τ are described in section 7.1. The kinematic variables used to distinguish SUSY signals from Standard Model processes are described in section 7.2. Selection procedures are given in section 7.3. Cut variables, selection efficiencies of SUSY events from the MC simulated events at $\sqrt{s}$ = 130-136 GeV, 161 GeV and 172 GeV are described in section 7.4 with systematic error estimation on efficiencies in section 7.5.

7.1 Lepton Identifications

The process of particle identification in the L3 detector have been illustrated in figure 7.1. Characteristics of different particles are:

γ	:	Electromagnetic (EM) bump without any associated track in central tracking system (CTS).
e	:	EM bump with an associated track in CTS.
μ	:	Track in muon chamber with associated *minimum ionising particle* (MIP) signals in calorimeters and CTS.
Hadrons	:	Collection of EM bumps and hadronic activity in hadron calorimeter within a certain cone.
τ	:	Narrow jets with a few charged tracks for hadronic decay else as an electron or muon.

The selection criteria of these particles are guided by the above general guide lines. But they critically depend on the type of physics under study because of difference in signal to noise ratio in these processes. The following subsections describe the particle identification criteria for these analyses presented in the thesis.

7.1.1 Track Identification

Due to ionisation loss all the charged particles deposit a fraction of its energy in the central tracking system and give rise to signals (hits) in TEC and SMD. One can reconstruct the trajectory of the particle from these hits. Particle identification can be assigned from (1) the rate of ionisation loss in the tracker (for low momentum particles) and (2)

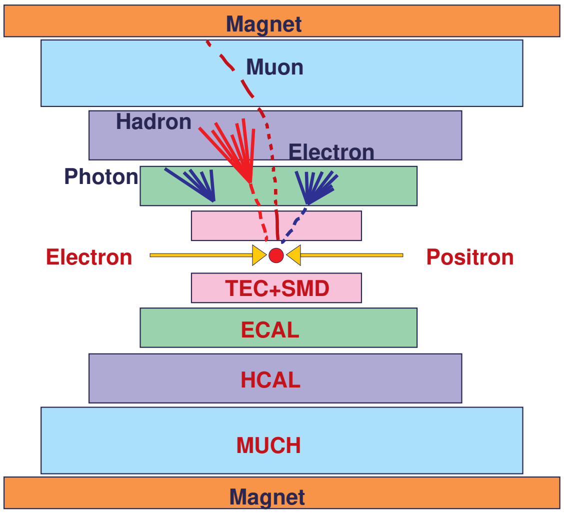

Figure 7.1: Particle identification in L3 detector.

characteristic association with signals in other subdetector. Electromagnetic bump in the electromagnetic calorimeter could be due to electron or photon. To distinguish electron from photon, the bump needs to be matched to a track found in the central tracking detector. To determine parameters of a muon, one needs to match signals in muon chamber with a track in central tracking system. Noise in the subdetector as well as possible bias in the reconstruction algorithms can sometimes produce a fake track candidate. One needs to eliminate such spurious tracks without losing genuine track candidates. This is achieved by selecting good tracks using TEC with a set of criteria as given in table 7.1.

• p_T	:	Transverse Momentum of track	$\geq$	50 MeV
• DCA	:	Distance of closest approach in R-Φ plane as shown in figure 7.4, the distance between X and O	$\leq$	10 mm
• HIT	:	Number of wires (out of 62) used for the track reconstruction	$\geq$	10
• SPAN	:	difference between the last and first wire numbers	$\geq$	15

Table 7.1: Criteria of a track to identify leptons.

Since the resolution of ϕ measurement of a track ($\Delta\phi \sim 0.3\,\mathrm{mrad}$) is much better than of θ measurement ($\Delta\theta \sim 1.0\,\mathrm{mrad}$), the matching between the track in TEC and the calorimetric clusters or muons is done in ϕ, keeping a loose constraint (10°) on space angle.

Mirror correction : Most of the wires in TEC cannot distinguish signals coming from the left or the right side. Consequently, the track reconstruction algorithm comes up with two solutions, one of which is correct (shown by the solid line OB in figure 7.2). The other solution, known as the *mirror* track (shown by the dashed line OA in figure 7.2) is eliminated by using (1) the information from 14 LR wires (which solves this ambiguity) in the outer TEC and (2) matching the track segments in inner and outer TEC. There are cases where the inner TEC information is missing due to inefficiencies and the information from LR wires becomes unreliable for tracks passing close to the cathode plane. The pattern recognition algorithm cannot resolve the *mirror* track problem in those cases.

One can solve this problem by searching the nearest calorimetric cluster or the muon to the track. This search is done both for the *true* track and its *mirror*. If there is at least a cluster or a muon which has $\Delta\phi \leq 50\,\mathrm{mrad}$ with respect to the *mirror* and if the minimum difference in the azimuthal angle satisfies $\Delta\phi_{mirror} < \Delta\phi_{true}$, then the *mirror* position (OA) is taken as the track position and consequently the relevant track characteristics are altered.

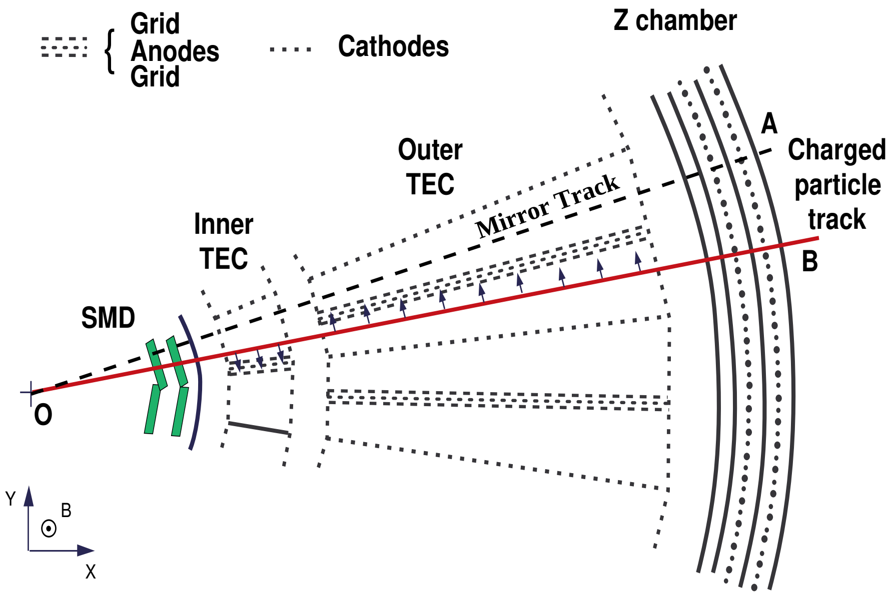

Figure 7.2: Track reconstruction in the SMD and the TEC. The *mirror* track is also shown.

7.1.2 Electron Identification

Electrons lose their energy through the development of electromagnetic (EM) shower. So an electron gives rise to a track in the central tracker and a narrow symmetric shower in the electromagnetic calorimeter. On the other hand, a photon does not give rise to a track, a hadron produces a much broader shower covering EM and hadron calorimeters and a muon deposits very small energy in the EM calorimeter confined to one or two crystals. So one can identify electron by demanding stringent criteria on the lateral shower profile, confinement of the shower in EM calorimeter and on the track association. One can also demand some isolation conditions on the electron candidates. The criteria for an electron are summarised in table 7.2. Some of the EM shower shape variables are shown in figure 7.3.

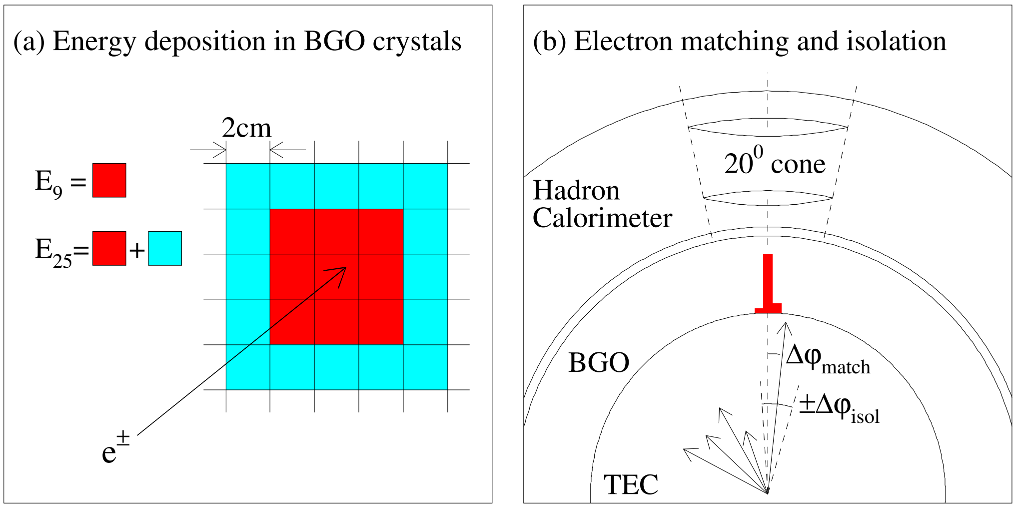

Figure 7.3: EM shower shape variables used to identify the EM bump.

The pattern recognition algorithm of the track calculates the azimuthal angle at the interaction point O as shown in figure 7.4. The azimuthal angle of an electromagnetic bump, ϕ_{bump}, on the other hand is computed by assuming a neutral particle traversing from the interaction point to the BGO front face. In the presence of 0.5 Tesla magnetic field, the trajectory gets bent and the azimuthal angle at the origin ϕ changes to ϕ' at the BGO front face. ϕ' can be calculated from ϕ and the measured track curvature, ρ, where ρ and p_T of the track and the magnetic field, B, are related by the expression $P_T\,(\mathrm{GeV}) = 0.3\,B\,(\mathrm{Tesla})\;\rho\,(\mathrm{metre})$. Matching is achieved using a cut on $\Delta\,\phi$ computed from the difference of ϕ' and ϕ_{bump}.

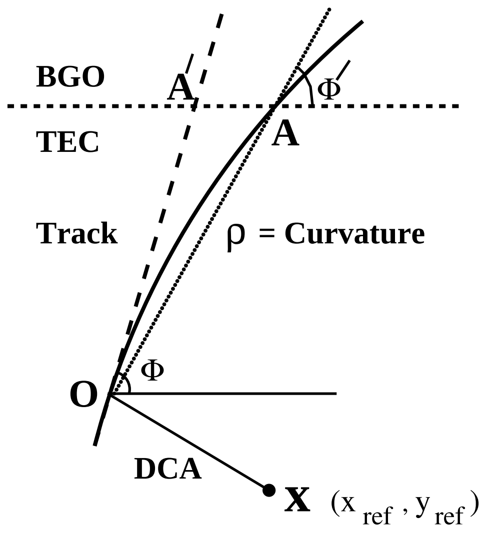

Figure 7.4: Distance of closest approach of the track from the reference point and extrapolation of azimuthal angle.

• E_e	:	Electron energy is estimated from the energy deposited in the central 9 BGO crystals with respect to the most energetic one (figure 7.3(a)) with the assumption that this energy comes from an electromagnetic shower	$\geq$	2.0 GeV
• E_9^c/E_{25}^c	:	Ratio of corrected energy of the bump calculated from the energy deposited in central 9 BGO crystal to central 25 BGO crystals with respect to most energetic one	$\geq$	0.95
• E_{HCAL}/E_{BGO}	:	Ratio of energies deposited in hadron calorimeter and BGO	$\leq$	0.1
• # of crystal	:	Number of BGO crystals in the bump	$\geq$	5
• E_{asso}	:	Energy associated within 10° half opening angle with respect to electron (figure 7.3(b))	$\leq$	5.0 GeV
• E_{asso}/E_e	:	Ratio of E_{asso} to electron energy	$\leq$	1.
• $\Delta\,\phi$	:	Difference in azimuthal angle of the EM bump and the closest TEC track	$\leq$	50 mrad
• χ^2	:	Chisquare of the shower shape fit to expected electromagnetic shower	$\leq$	5 (barrel) and
			$\leq$	10 (endcap)

Table 7.2: Electron selection criteria.

7.1.3 Muon Identification

Muons lose energy only through the ionisation loss. A good muon candidate is characterised by the track in muon chamber with an associated track in TEC and minimum ionising particle (MIP) signal in calorimeters, as shown in figure 7.5. Like electrons, muons should also be isolated from other clusters and tracks. Criteria for selecting a muon are given in table 7.3.

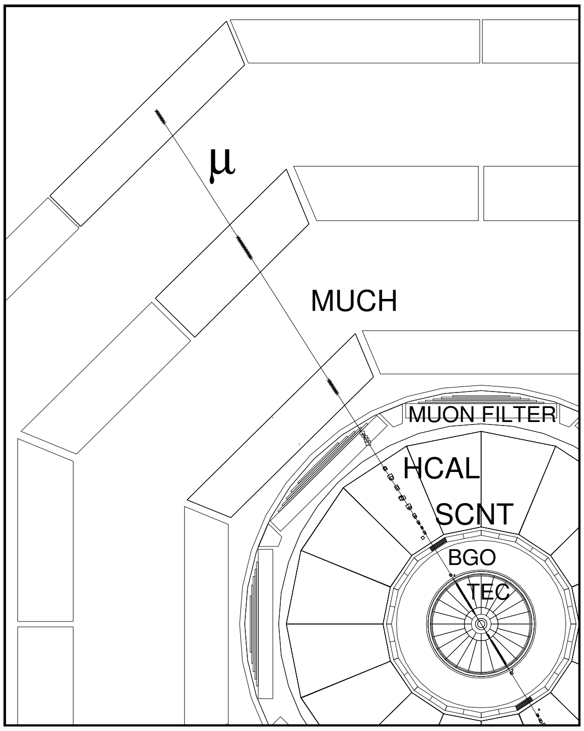

Figure 7.5: A muon in L3 Detector.

• E_μ	:	Energy of the muon	$\geq$	3.0 GeV
• DCA	:	Distance of closest approach of the muon track with respect to interaction vertex (both in R-Φ and R-Z plane)	$\leq$	200 mm
• E_{asso}	:	Energy associated within 5° to 10° half opening angle	$\leq$	5.0 GeV
• E_{assot}/E_μ	:	Ratio of associated energy within 10° half opening angle and muon energy	$\leq$	2.0
•$\Delta\,\phi$	:	Difference in azimuthal angle of the muon and the closest track	$\leq$	50 mrad

Table 7.3: Muon selection criteria.

7.1.4 Tau Identification

85 % of τ's decay to one charged particle and 15 % of the τ's decay to three charged particles. Branching ratio of τ to 5 or more charged particles is negligible ($<$ 0.5 %). Pure leptonic decay mode of τ is $\approx$ 17 % each for electron and muon. So a tau can be identified as an electron, muon or a hadronic jet with 1 or 3 charged tracks. Hadronic jets from tau decay are reconstructed with a cone algorithm, where an energetic charged track is taken as a source of the jets and the energy and direction of the jets are calculated using the vector sum of all clusters' and tracks' momenta within 10° cone of the track. A hadronic jet from a tau decay in L3 detector is shown in figure 7.6. The criteria for selection of such hadronic jet are given in table 7.4.

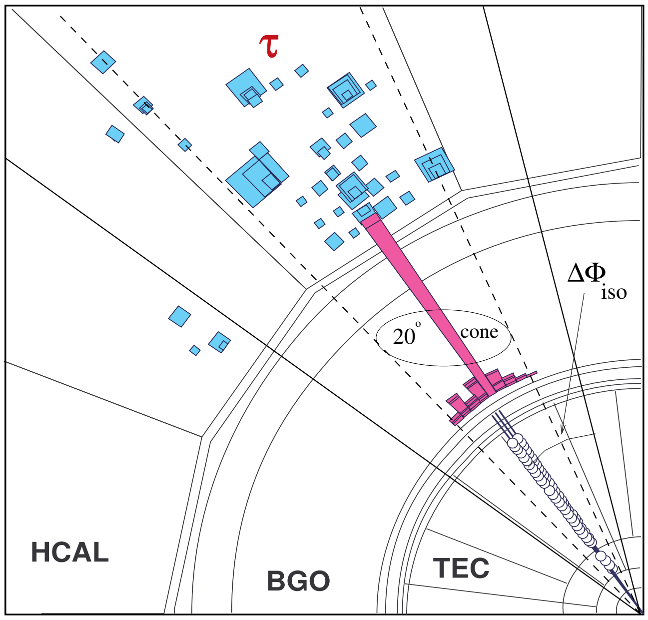

Figure 7.6: Tau as a narrow hadronic jets.

7.2 Kinematic Variables

Our study in this thesis is confined to supersymmetric particles decaying leptonically with the assumption that **R-parity** (section 2.3.4) is conserved. R-Parity conservation

• E_τ	:	Energy of the tau	$\geq$	2.0 GeV
• # Track	:	Number of TEC tracks within the jet	$\leq$	3
• # Cluster	:	Number of calorimetric clusters within the jet	$\leq$	8
• E_{asso}/E_τ	:	Ratio of energy associated within 10° to 20° cone and energy of the tau jet	$\leq$	1.0

Table 7.4: Criteria for selecting a hadronic jets in tau decay.

demands SUSY particles to be produced in pair and decay chains of a SUSY particle ends up with an odd number of lightest supersymmetric particles (LSP), which are stable. In this analysis lightest neutralino ($\tilde{\chi}_1^\circ$) is assumed to be the LSP. $\tilde{\chi}_1^\circ$ will not interact with the detector material and will be invisible like the neutrinos. So, SUSY signals in leptonic decay mode are associated with the following properties:

- Low multiplicity
- Small visible energy
- Large missing p_T
- Two leptons (electrons, muons or narrow jets) with large acoplanarity

Various *kinematic variables* [95] are required to distinguish SUSY signals from different types of Standard Model backgrounds using the above mentioned properties. Different variables discriminate different SM backgrounds from the expected SUSY signals. Description of all the kinematic variables used in the present analysis are given below.

Cluster : Calorimetric clusters are formed with energy greater than 100 MeV. Here cluster implies localised energy deposits in the calorimeters. A cluster may contain a single or more particles. Clusters found in the EGAP are not included in the count.

Track : Tracks in the event, which satisfy the following criteria (Span $\geq$ 30, Hit $\geq$ 20, DCA $\leq$ 10 mm, p_T $\geq$ 100 MeV etc. Cuts are optimised to reject tracks from beam-gas, beam-wall types of background and to accept tracks from true physics events).

E_{Vis} **:** Visible energy is the sum of the energies measured in the tracking chamber, BGO calorimeter, hadron calorimeter and in the muon chamber.

DCA_{min} **:** Minimum distance of closest approach (DCA) of all tracks in R-Φ plane. The good tracks are chosen using the criteria, Hit $\geq$ 15, p_T $\geq$ 100 MeV etc.

ETTT : Projected energy sum of two most energetic leptons in a direction perpendicular to their own thrust axis in R-Φ plane as illustrated in figure 7.7(a).

E_ℓ, θ_ℓ and ϕ_ℓ **:** Energy, the polar angle and the azimuthal angle of a lepton.

θ_{acop} **:** Acoplanarity angle (figure 7.7(b)) between the two most energetic leptons.

$\mathrm{E_{Lum}}$ **:** Total energy deposited in the luminosity monitor and in the Active Lead Ring (between 30 mrad to 162 mrad with respect to the beam pipe).

$\mathrm{E_{30^\circ}/E_{vis}}$ **:** Fractional energy deposit between 8.7° to 30° cone along the beam pipe as shown in figure 7.8(a).

$\sin\theta_{\mathrm{miss}}$ **: Sine** of the missing momentum direction as shown in figure 7.8(b).

$\mathrm{E_{vis}} - \mathrm{E}_{\ell_1} - \mathrm{E}_{\ell_2}$ **:** Energy of the event without the two most energetic leptons.

$[\mathrm{E}_\perp^{\ell_1} + \mathrm{E}_\perp^{\ell_2}]/\mathrm{E_{vis}}$ **:** Ratio of transverse energy of the two most energetic leptons to the visible energy.

$\not{E}^{\mathrm{b}}_{60^\circ}$ **:** Energy deposited in a 60° cone (space angle) opposite to the direction of the two most energetic leptons as shown in figure 7.9(a).

$\not{E}^{\perp}_{25^\circ}$ **:** Energy deposited in a 25° cone in R-Φ plane ($\Delta\,\Phi\,=\,25^\circ$) opposite to the direction of the vector sum of the two most energetic lepton momenta (figure 7.9(b)).

$\mathrm{E_{lepton(1)}}/E_b$ **:** Most energetic leptonic energy normalised to the beam energy.

$|\ \mathrm{T^{best}_{Scint}}\ |$ **:** Best scintillation timing with respect to the beam crossing time.

$\mathrm{E}_\perp$ **:** Total transverse energy imbalance of the event (in GeV).

$|\ \mathrm{E}_{||}\ |$ **:** Total longitudinal energy imbalance of the event (in GeV).

$\mathrm{M_{Vis}}/\sqrt{\mathrm{s}}$ **:** Ratio of visible mass and the centre of mass energy ($\mathrm{E_{CM}}$). Visible mass is defined as $\mathrm{M_{Vis}}\ =\ \sqrt{(\sum_i E_i)^2 - (\sum_i P_{ix})^2 - (\sum_i P_{iy})^2 - (\sum_i P_{iz})^2}$, where i run over all the tracks/clusters which are used to calculate visible energy.

$\mathrm{M_{Invis}}/\sqrt{\mathrm{s}}$ **:** Ratio of invisible mass and $\mathrm{E_{CM}}$. Invisible mass is defined as
$\mathrm{M_{Invis}}\ =\ \sqrt{(\sqrt{\mathrm{s}} - \sum_i E_i)^2 - (\sum_i P_{ix})^2 - (\sum_i P_{iy})^2 - (\sum_i P_{iz})^2}$.

$\mathrm{E_{Vis}}/\sqrt{\mathrm{s}}$ **:** Total visible energy normalised with respect to $\mathrm{E_{CM}}$.

$\mathrm{E_{BGO}/E_{Vis}}$ **:** Fraction of visible energy deposited in BGO.
$\mathrm{E_{Hcal}/E_{Vis}}$ **:** Fraction of visible energy deposited in HCAL.
$\mathrm{E_{Much}/E_{Vis}}$ **:** Fraction of visible energy of tracks as calculated from MUCH.

ϕ^ℓ_{123} **:** Sum of the three angles between three leptons (only when there are three identified leptons in the event) in R-Φ plane ($\Delta\phi_{12}\ +\ \Delta\phi_{23}\ +\ \Delta\phi_{31}$).

Distributions of some of the kinematic variables of the events which pass some loose selection cuts (as given in table 7.5; these cuts help mainly to remove non-physics and hadronic events) are shown in figures 7.10 and 7.11. From these figures it is clear that these kinematic variables have discriminating power to reject different types of SM processes from the SUSY signals.

# Tracks	$\geq$	1
# Tracks	$\leq$	6
$\mathrm{E_{Vis}}/\sqrt{\mathrm{s}}$	$\leq$	1.5
$\mathrm{E_{vis} - E_{\ell_1} - E_{\ell_2}}$	$\leq$	50 GeV
$\mid \mathrm{E}_{\parallel} \mid / \mathrm{E_{Vis}}$	$\leq$	0.8
$e + \mu + \tau$	$\geq$	2
$\mid \theta_l - \pi/2 \mid$	$\leq$	1.2 rad
$\mathrm{DCA_{min}}$	$\leq$	1 mm
$\mid \mathrm{T^{best}_{Scint}} \mid (\mu \geq 1)$	$\leq$	5 ns
$M_{ll'}$ [a]	$\geq$	5 GeV

[a]Invariant mass of two most energetic leptons.

Table 7.5: Loose cuts applied to the MC samples to study the kinematic variables for signals and background processes.

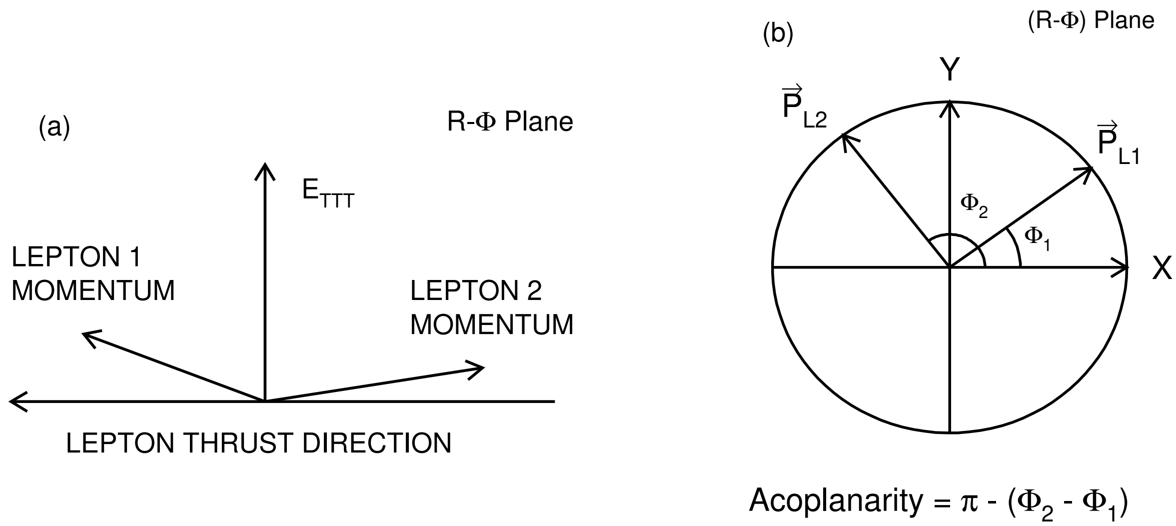

Figure 7.7: Kinematic variables : (a) ETTT : Projection of lepton momenta normal to the direction of their own thrust axis in the R-Φ plane and (b) Acoplanarity angle between two most energetic leptons.

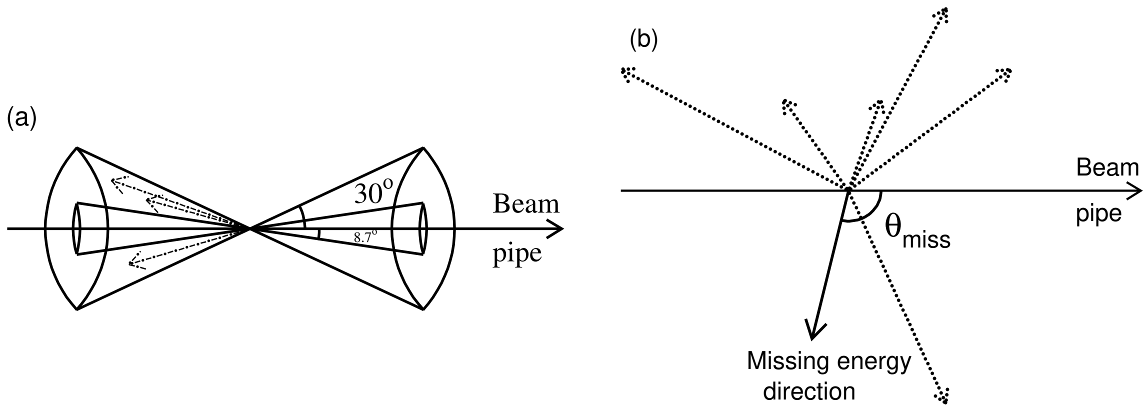

Figure 7.8: Kinematic variables : (a) Energy deposited in the forward direction of the detector (between 8.7° and 30° with respect to the beam direction) and (b) The angle of the missing momentum direction with respect to the beam direction.

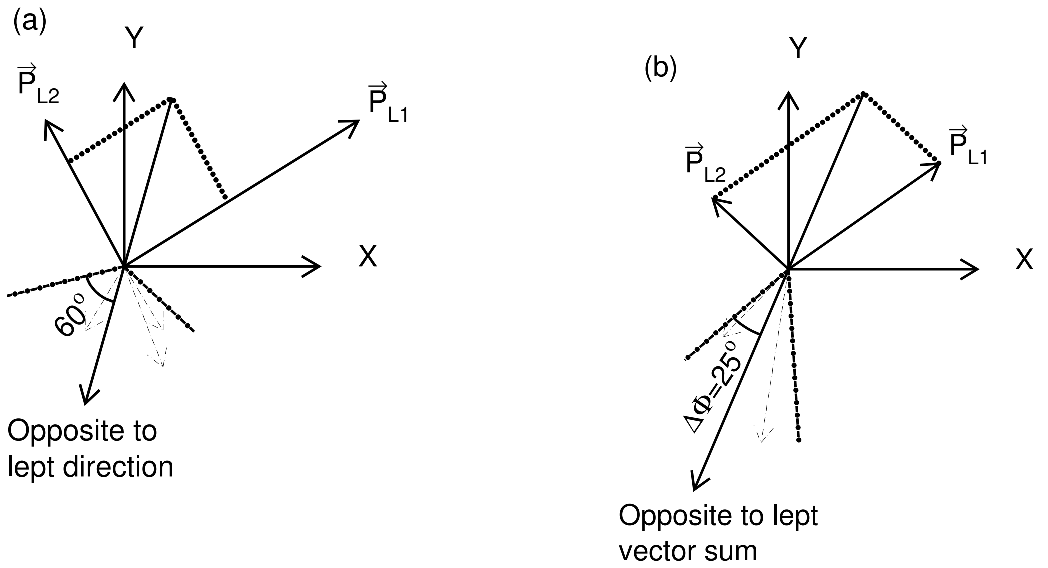

Figure 7.9: Kinematic variables : (a) Energy deposited within a 60° cone opposite to the two most energetic leptons as given by P_{L1} andP_{L2}. Thick dot-dashed lines indicate the boundary of the 60° cone and thin dot-dash lines with arrow show particles inside that boundary and (b) Energy deposited within $\Delta\,\Phi = 25°$ region opposite to the vector sum of two most energetic leptonic momenta.

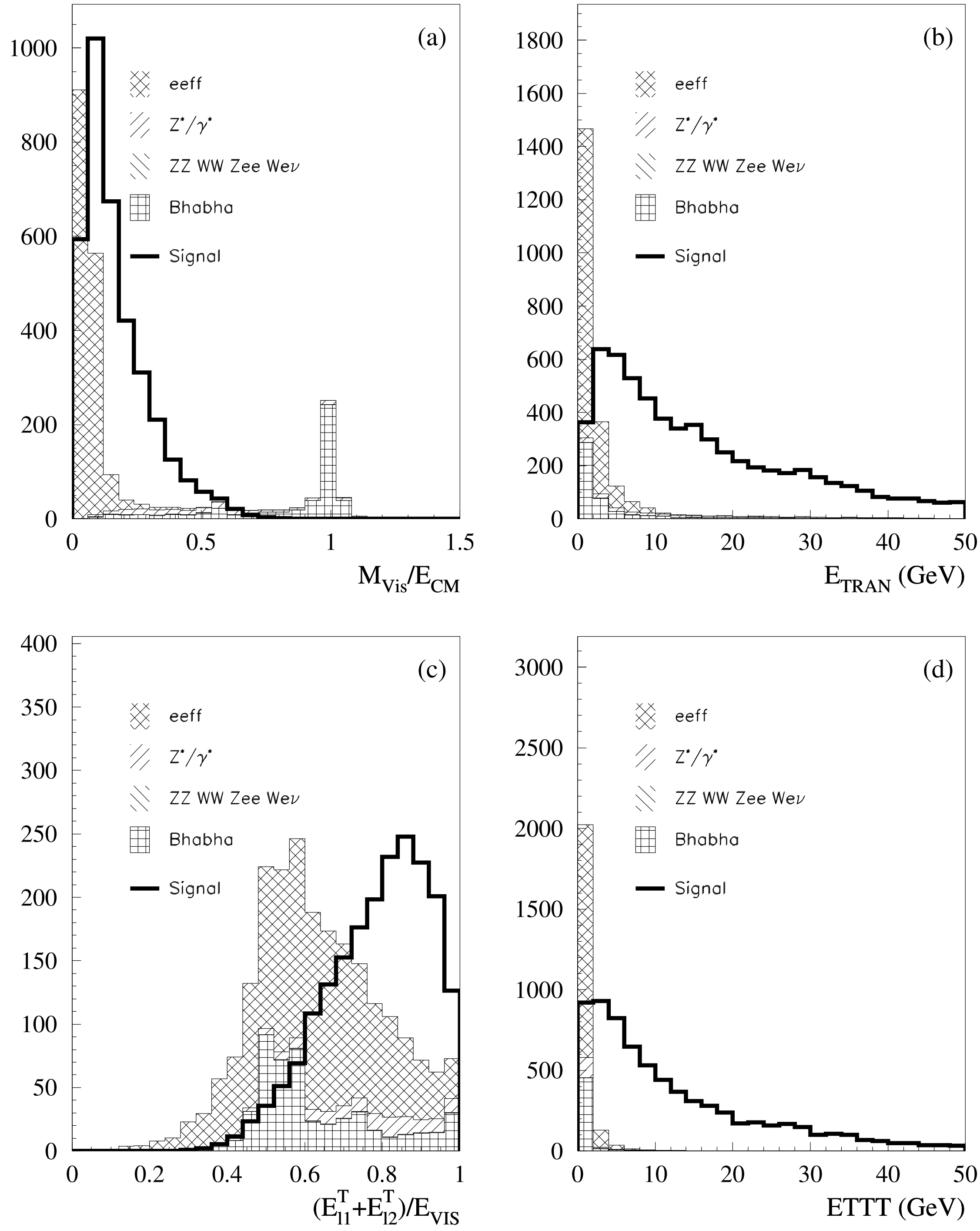

Figure 7.10: Distribution of kinematic variables at $\sqrt{s} = 161$ GeV, which are used to separate SUSY signals from the SM processes. Signal distributions (combination of $\tilde{e}^+\tilde{e}^-$, $\tilde{\mu}^+\tilde{\mu}^-$, $\tilde{\tau}^+\tilde{\tau}^-$ and $\tilde{\chi}_1^+\tilde{\chi}_1^-$ final states) are plotted with an arbitrary scale: (a) visible mass of the event normalised to the centre of mass energy, (b) transverse energy imbalance, (c) transverse energy of leptons normalised to visible energy and (d) projection of leptonic energies perpendicular to their own thrust axis in R-Φ plane .

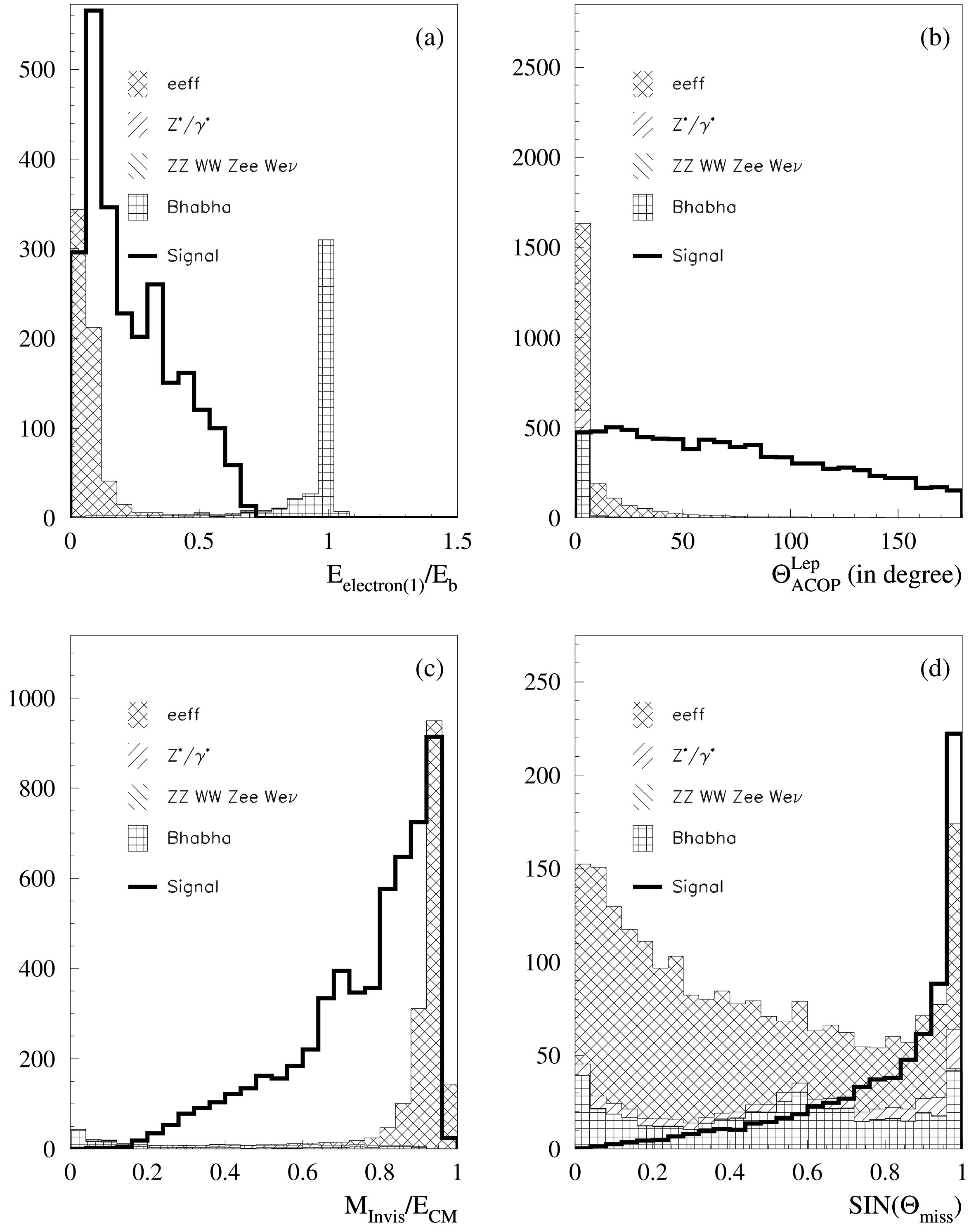

Figure 7.11: Distribution of kinematic variables for SUSY signal and SM background processes at 161 GeV : (a) ratio of energy of the most energetic lepton and beam energy, (b) acoplanarity of two leptons, (c) normalised invisible mass of the event normalised to the center of mass energy (d) **sine** of missing momentum direction.

7.3 Choice of Selection Cuts

Having all the kinematic variables in hand, one has to choose the optimum cut values of those variables to identify the SUSY signal events from the SM background events. Due to the finite resolution of the detector as well as the production and decay properties of both the SM and SUSY processes, they have overlaps in the distribution of the kinematic variables (as shown in figures 7.10 and 7.11). To prove the existence of SUSY, one needs a reasonable signal efficiencies; consequently these signals are contaminated by the SM events. So one has to optimise the cut values to get a better signal to background ratio, which will prove the existence of new physics or exclude the model.

Though all the R-Parity conserving SUSY signals have a generic signature of missing energy and missing transverse momentum, fraction of missing energy or other kinematic variables are not showing the same characteristics for all the SUSY processes which have been searched for. Distribution of kinematic variables depend on different SUSY channels and their decay mechanisms. Channel-wise optimisations of the cut values on the kinematic variables are needed to get a better signal to background ratio.

$\tilde{\mathrm{e}}$ and $\tilde{\mu}$ decay mainly through two body decay mode :

$$\begin{aligned} \tilde{\mathrm{e}} &\rightarrow e + \tilde{\chi}_1^\circ \\ \tilde{\mu} &\rightarrow \mu + \tilde{\chi}_1^\circ \end{aligned}$$

But $\tilde{\tau}$, $\tilde{\chi}_1^\pm$ and $\tilde{\chi}_2^\circ$ decay mainly into more than two stable particles. The decay modes are

$$\begin{aligned} \tilde{\tau} &\rightarrow \tau + \tilde{\chi}_1^\circ \\ \tilde{\chi}_1^\pm &\rightarrow W^{\pm^*} + \tilde{\chi}_1^\circ \\ \tilde{\chi}_2^\circ &\rightarrow Z^* + \tilde{\chi}_1^\circ \end{aligned}$$

where τ, $W^{\pm^*}$ and Z^* subsequently decay to stable particles.

Four independent sets of cuts have been used to select $\mathrm{e}^+\mathrm{e}^- \rightarrow \tilde{\mathrm{e}}^+\,\tilde{\mathrm{e}}^-$, $\mathrm{e}^+\mathrm{e}^- \rightarrow \tilde{\mu}^+\,\tilde{\mu}^-$, $\mathrm{e}^+\mathrm{e}^- \rightarrow \tilde{\tau}^+\,\tilde{\tau}^-$ and $\mathrm{e}^+\mathrm{e}^- \rightarrow \tilde{\chi}_1^+\,\tilde{\chi}_1^-$ processes. They correspond to events with two electrons, two muons, two τ's and two charged leptons (e or μ). For the process $\mathrm{e}^+\mathrm{e}^- \rightarrow \tilde{\chi}_1^+\,\tilde{\chi}_1^-$, where one $\tilde{\chi}_1^\pm$ decays to τ and the other decays to either e or μ or τ and the processes $\mathrm{e}^+\mathrm{e}^- \rightarrow \tilde{\chi}_1^\circ\,\tilde{\chi}_2^\circ$, where $\tilde{\chi}_2^\circ$ decays leptonically (e, μ or τ) one uses the same selection criteria as used for $\mathrm{e}^+\mathrm{e}^- \rightarrow \tilde{\tau}^+\,\tilde{\tau}^-$ selection.

Kinematics of the event, particularly the lepton energies vary with $\Delta\mathrm{M}$ ($= \mathrm{M}_{\mathrm{SUSY}} - \mathrm{M}_{\tilde{\chi}_1^\circ}$). The relative contribution of different SM processes also depend on the lepton energies. To get a better signal to background ratio, the event phase space has been divided into three parts according to the energy of the most energetic lepton and the set of cuts is optimised separately for these three parts.

7.3.1 Preselections

Some of the SM background processes are very different from SUSY signals in leptonic decay mode. Before going to the final optimisation procedure, very loose cuts on some kinematic variables were applied, which reduce the backgrounds by two orders of magnitude while the signals are reduced by only a few percents. This helps us to understand the characteristics of the remaining SM events, which have characteristics very similar to the SUSY signals. The cuts used for this preselection are summarised in table 7.6.

Global cuts					
$\theta_{\rm acop}$	$\geq$	0.05 rad	$[E_{\perp}^{\ell_1} + E_{\perp}^{\ell_2}]/E_{\rm vis}$	$\geq$	0.25
$DCA_{\rm min}$	$\leq$	1.0 mm	$E_{\rm Lum}/\sqrt{s}$	$\leq$	0.1
$\sin\theta_{\rm miss}$	$\geq$	0.14	$E_{\rm vis} - E_{\ell_1} - E_{\ell_2}$	$\leq$	50.0 GeV
$\not{E}_{25^\circ}^{\perp}$	$\leq$	10.0 GeV	$E_{\rm lepton(1)}/E_b$	$\leq$	0.9
$M_{\rm Vis}/\sqrt{s}$	$\leq$	0.75	# Tracks	$\geq$	1
ϕ_{123}^{ℓ}	$\leq$	6.1 rad	$\mid T_{\rm Scint}^{\rm best} \mid$	$\leq$	5 ns (# of μ ≥ 1)

Cuts for $e^+e^- \to \tilde{e}^+\tilde{e}^-$, $e^+e^- \to \tilde{\mu}^+\tilde{\mu}^-$ and $e^+e^- \to \tilde{\chi}_1^+\tilde{\chi}_1^-$ processes only					
# (e + μ)		1 to 3			
# Tracks	$\leq$	3		$=$	2 (e+μ= 1)
# Clusters	$\leq$	10	*ETTT*	$\geq$	2.0 GeV
# $\mu = 0$ ($e^+e^- \to \tilde{e}^+\tilde{e}^-$ process)			# e = 0 ($e^+e^- \to \tilde{\mu}^+\tilde{\mu}^-$ process)		

Cuts for $e^+e^- \to \tilde{\tau}^+\tilde{\tau}^-$ process only					
#(e + μ + τ)		2 to 3			
ETTT	$\geq$	1.5 GeV	# (Tracks + 2×(e+μ))	$\leq$	6

Table 7.6: Loose cuts for SUSY selection in leptonic decay mode.

7.3.2 Multidimensional Optimisation Procedure for Final Selection

All the kinematic variables, which have been used in the final selection are not independent. There are some correlation between some of these variables, e.g., $\theta_{\rm acop}$ and ETTT are related to each other through the azimuthal angle of the two leptons. To apply optimum cuts on these variables one should know the correlations between these variables. To avoid the explicit calculation of these correlations, multidimensional optimisation procedure has been used for the event selection. Correlations are implicitly taken into account in this procedure.

Optimisation is done by the minimisation of the sensitivity function, which is related to the average Poisson upper limit of the signals (without background subtraction) and the signal efficiency [96],

$$\frac{\sum_{n=0}^{\infty} K_n P_b(n)}{\varepsilon}$$

where K_n is the 95% CL Poisson upper limit on the average number of signal events with n observed events and an expected background of b events and $P_b(n)$ is the Poisson distribution for observing n events with an expected background of b events. ε is the overall signal efficiency. CERN Programme Library, MINUIT [97] has been used for the minimisation.

As shown in figure 7.12 and table 7.7 production cross sections of the SM processes vary with centre of mass energy ($\sqrt{s}$). At $\sqrt{s}$ = 130 GeV the production cross section of W^+W^-, $\sigma(e^+e^- \to W^+W^-)$, is small ($\sim$ 0.07 pb) compared to other SM processes and such events have negligible contribution to the total background. However, production cross sections are large at $\sqrt{s}$ = 161 GeV ($\approx$ 3.3 pb) and 172 GeV ($\approx$ 12.2 pb). Hence at these higher energies one needs very tight selection cuts to get a clean SUSY signal from this background process. Thus, different selection criteria have been used (i.e., cut parameters are separately optimised) for different $\sqrt{s}$.

Event types	Final state	σ (pb) at $\sqrt{s}$ =		
		130 GeV	161 GeV	172 GeV
Z/γ^*	e^+e^-	104 [1]	66	57
	$\mu^+\mu^-$	23	13	10
	$\tau^+\tau^-$	23	13	10
	$q\bar{q}$	326	146	121
Two photon ($e^+e^-f\bar{f}$)	$e^+e^-e^+e^-$	444 [2]	494	503
	$e^+e^-\mu^+\mu^-$	403	454	472
	$e^+e^-\tau^+\tau^-$	164	177	199
	$e^+e^-q\bar{q}$	13778	14276	14929
	$\gamma\gamma$	45 [3]	30	27
$f\bar{f}f'\bar{f}'$	WW	0.1	3.3	12.2
	$We\nu$	0.1	0.4	0.5
	$Z/\gamma^* Z/\gamma^*$	0.5	0.4	0.4
	Zee	2.1	2.5	2.7

Table 7.7: Typical production cross sections of the Standard Model processes at three different $\sqrt{s}$.

[1] $35° < \theta_{e^-(e^+)} < 145°$

[2] $M_{f\bar{f}} \geq 3$ GeV for f = e, μ and q and ≥ 4 GeV for f = τ and $10° < \theta_{f(\bar{f})} < 170°$

[3] $35° < \theta_\gamma < 145°$

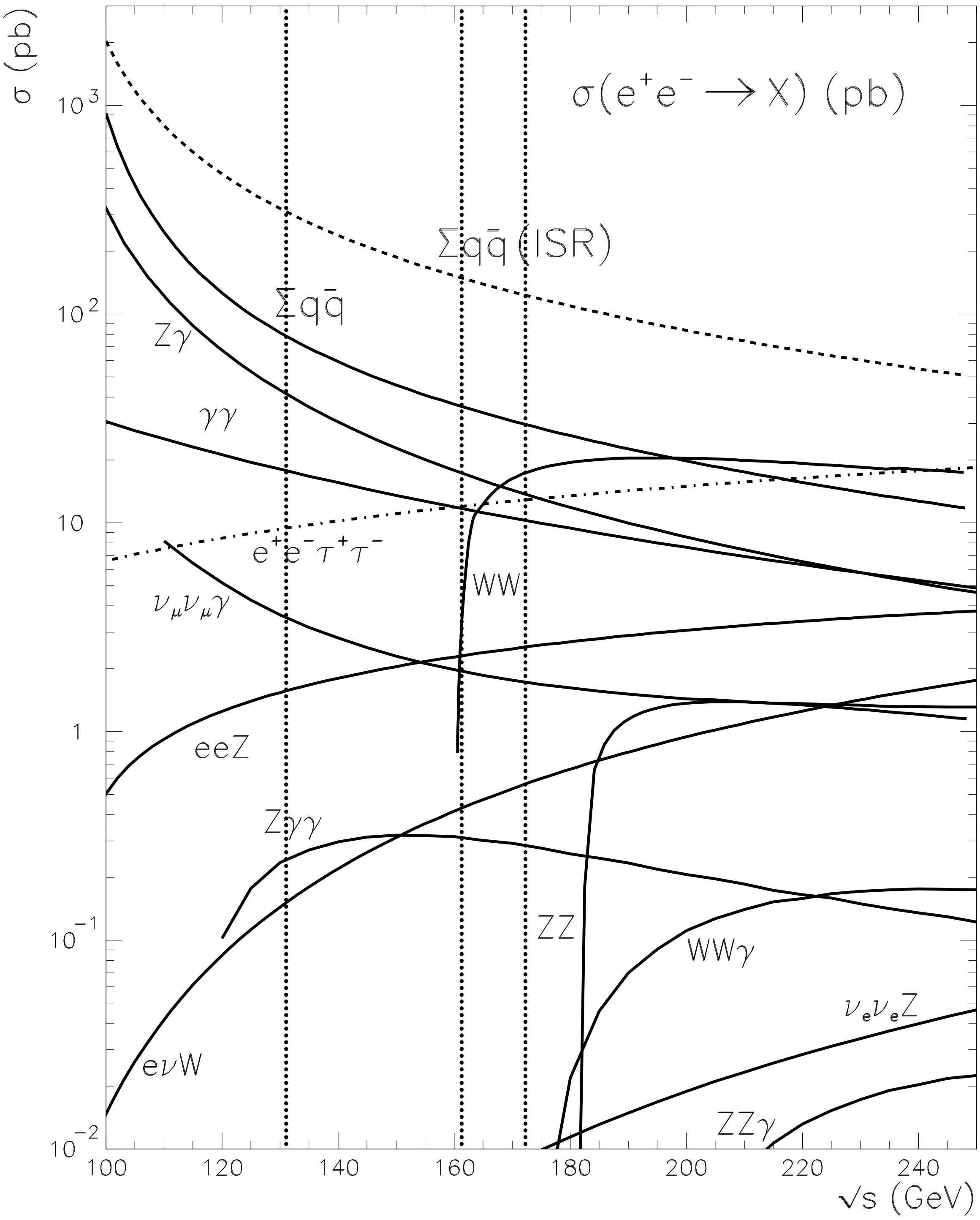

Figure 7.12: Cross sections for some typical Standard Model processes.
For $e^+e^- \rightarrow Zee$, $We\,\nu_e$, $Z\nu_e\bar{\nu}_e$ only the dominant t channel contribution is shown. The photons in $Z\gamma$ and $\gamma\gamma$ are such that $|\,cos\,\theta_{e\gamma}\,| < 0.9$. For $\nu_e\bar{\nu}_e\gamma$ there is the additional cut $E_\gamma > 10$ GeV. In $Z\gamma\gamma$, $W^+W^-\gamma$ and $Z\,Z\,\gamma$ the photon cut is $p_T^\gamma > 10$ GeV and all particles are separated with opening angles $\widehat{eV} > 15°$, $\widehat{VV'} > 10°$; V = W, Z, γ [98].

7.4 Selection Criteria and Efficiencies

There are mainly two sets of selection criteria that have been described here. The **first set** was used during the $\sqrt{s}$ = 130 - 136 GeV run. The set of variables was revised for the run at $\sqrt{s}$ = 161 – 172 GeV and the selection procedure has improved significantly with the addition of the new variables (**second set**). Results obtained from the two sets of selection at $\sqrt{s}$ = 130 - 136 GeV are compared in section 7.4.1. One can clearly see the improvement with the enlarged set of variables. Only the second set of selection criteria are used at $\sqrt{s}$ = 161 GeV and 172 GeV.

7.4.1 Selection Criteria at $\sqrt{s}$ = 130 - 136 GeV

Kinematic variables used at the time of LEP1.5 run (first set of variables) and their cut values are given in table 7.8 [99]. Selection efficiencies of $e^+e^- \to \tilde{e}^+\tilde{e}^-$, $e^+e^- \to \tilde{\mu}^+\tilde{\mu}^-$ and $e^+e^- \to \tilde{\tau}^+\tilde{\tau}^-$ are given in figure 7.13 (a). Standard Model background cross sections, after all selection cuts are shown in figure 7.14 (a). Here τ jets are reconstructed using Durham (k_T) algorithm [100].

	Variable	$\tilde{e}^+\tilde{e}^-$	$\tilde{\mu}^+\tilde{\mu}^-$	$\tilde{\tau}^+\tilde{\tau}^-$
Loose Cuts	$E_{Vis}/\sqrt{s}$	< 0.7	< 0.7	< 0.6
	$\mid E_{\parallel} \mid / E_{Vis}$	< 0.9	< 0.9	< 0.9
	$E_{\perp}/E_{Vis}$	> 0.01	> 0.01	> 0.05
	$E_{Lum}/\sqrt{s}$	< 0.1	< 0.1	< 0.1
	# Clusters	< 10	< 10	
	# Tracks			$1 - 6$
	# Leptons	≥ 1	≥ 1	$1 - 2$
	θ_{acop}	> 0.01	> 0.01	> 0.02
Tight Cuts	$E^{\perp}_{lept(1)}/E_{Vis}$	> 0.25	> 0.2	
	$\mid \theta_l - \pi/2 \mid$			< 0.95
	$E_{\perp}/E_{Vis}$	> 0.15	> 0.15	> 0.15
	# Leptons	$= 2$	$= 2$	$= 2$
	θ_{acop}	> 0.3	> 0.3	> 0.5
	E_{Lum} (GeV)	< 1	< 1	< 1
	$\mid T^{best}_{Scint} \mid$ (ns)		< 4	< 4
	DCA_{min} (mm)	< 1	< 1	< 1

Table 7.8: First set of cuts used for slepton pair selection at $\sqrt{s}$ = 130 - 136 GeV.

Loose selection cuts for the new set (second set) of variables are shown in table 7.6. Final selection cuts for $\tilde{e}^+\tilde{e}^-$ and $\tilde{\mu}^+\tilde{\mu}^-$ events, after the optimisation are given in table 7.9. Selection efficiencies of $e^+e^- \to \tilde{e}^+\tilde{e}^-$ and $e^+e^- \to \tilde{\mu}^+\tilde{\mu}^-$ are given in figure 7.13 (b). Standard Model background cross sections, after all selection cuts are shown in figure 7.14 (b).

With the improved selection criteria, efficiencies (ΔM $\geq$ 10 GeV) of selecting $\tilde{e}^+\tilde{e}^-$ process increases from $\sim$ 50 % to $\sim$ 70 % and for $\tilde{\mu}^+\tilde{\mu}^-$ process from $\sim$ 42 % to $\sim$ 60 %. Residual SM backgrounds cross sections are also reduced by a factor of $\sim$ 3.

$e + \mu = 1$					
$E_\perp$	$\geq$	1.01 GeV	$\not{E}^{b}_{60^\circ}$	$\leq$	4.63 GeV
$M_{Vis}/\sqrt{s}$	$\leq$	0.64	$[E_\perp^{\ell_1} + E_\perp^{\ell_2}]/E_{vis}$	$\geq$	0.54
$\sin\theta_{miss}$	$\geq$	0.30	$\not{E}^{\perp}_{25^\circ}$	$\leq$	2.05 GeV
ETTT	$\geq$	2.00 GeV	θ_{acop}	$\geq$	0.06 rad
E_{BGO}/E_{Vis}	$\geq$	0.45 (e=1)	E_{Much}/E_{Vis}	$\geq$	0.55 (μ = 1)
$E_{lepton(1)}/E_{beam}$	$\leq$	0.60	E_{30°/E_{vis}	$\leq$	0.74
$2 \leq (e + \mu) \leq 3$					
$E_\perp$	$\geq$	1.17 GeV	$\not{E}^{b}_{60^\circ}$	$\leq$	3.08 GeV
$M_{Vis}/\sqrt{s}$	$\leq$	0.70	$[E_\perp^{\ell_1} + E_\perp^{\ell_2}]/E_{vis}$	$\geq$	0.37
$\sin\theta_{miss}$	$\geq$	0.15	$\not{E}^{\perp}_{25^\circ}$	$\leq$	6.83 GeV
ETTT	$\geq$	2.06 GeV	θ_{acop}	$\geq$	0.05 rad
$E_{lepton(1)}/E_{beam}$	$\leq$	0.76	E_{30°/E_{vis}	$\leq$	0.89

Table 7.9: Improved slepton selection criteria at $\sqrt{s}$ = 136 GeV.

7.4.2 Selection Criteria at $\sqrt{s}$ = 161 GeV

Selection criteria of $e^+e^- \to \tilde{e}^+\tilde{e}^-$, $e^+e^- \to \tilde{\mu}^+\tilde{\mu}^-$ processes at $\sqrt{s}$ = 161 GeV are given in table 7.10. Similarly for $e^+e^- \to \tilde{\tau}^+\tilde{\tau}^-$ and $e^+e^- \to \tilde{\chi}_1^+\tilde{\chi}_1^-$ processes, cut values are given in table 7.11. Effect of individual selection variables can be seen by applying the selection cuts one by one. Residual cross section (selection efficiencies) of the SM backgrounds (signal events) are shown in table 7.12.

Selection, trigger and combined efficiencies are shown in figures 7.15, 7.16 and 7.17 respectively. Residual backgrounds from the SM processes are shown in figure 7.18.

7.4.3 Selection Criteria at $\sqrt{s}$ = 172 GeV

Selection criteria of $e^+e^- \to \tilde{e}^+\tilde{e}^-$ and $e^+e^- \to \tilde{\mu}^+\tilde{\mu}^-$ processes at $\sqrt{s}$ = 172 GeV are given in table 7.13. Similarly cut variables for $e^+e^- \to \tilde{\chi}_1^+\tilde{\chi}_1^-$ and $e^+e^- \to \tilde{\tau}^+\tilde{\tau}^-$ processes, are shown in table 7.14. Effect of individual selection cuts on the residual cross section of SM backgrounds and the selection efficiencies of SUSY signals are shown in table 7.15.

Selection efficiencies (combined with trigger efficiency) are shown in figure 7.19. Residual backgrounds from the SM processes are shown in figure 7.20.

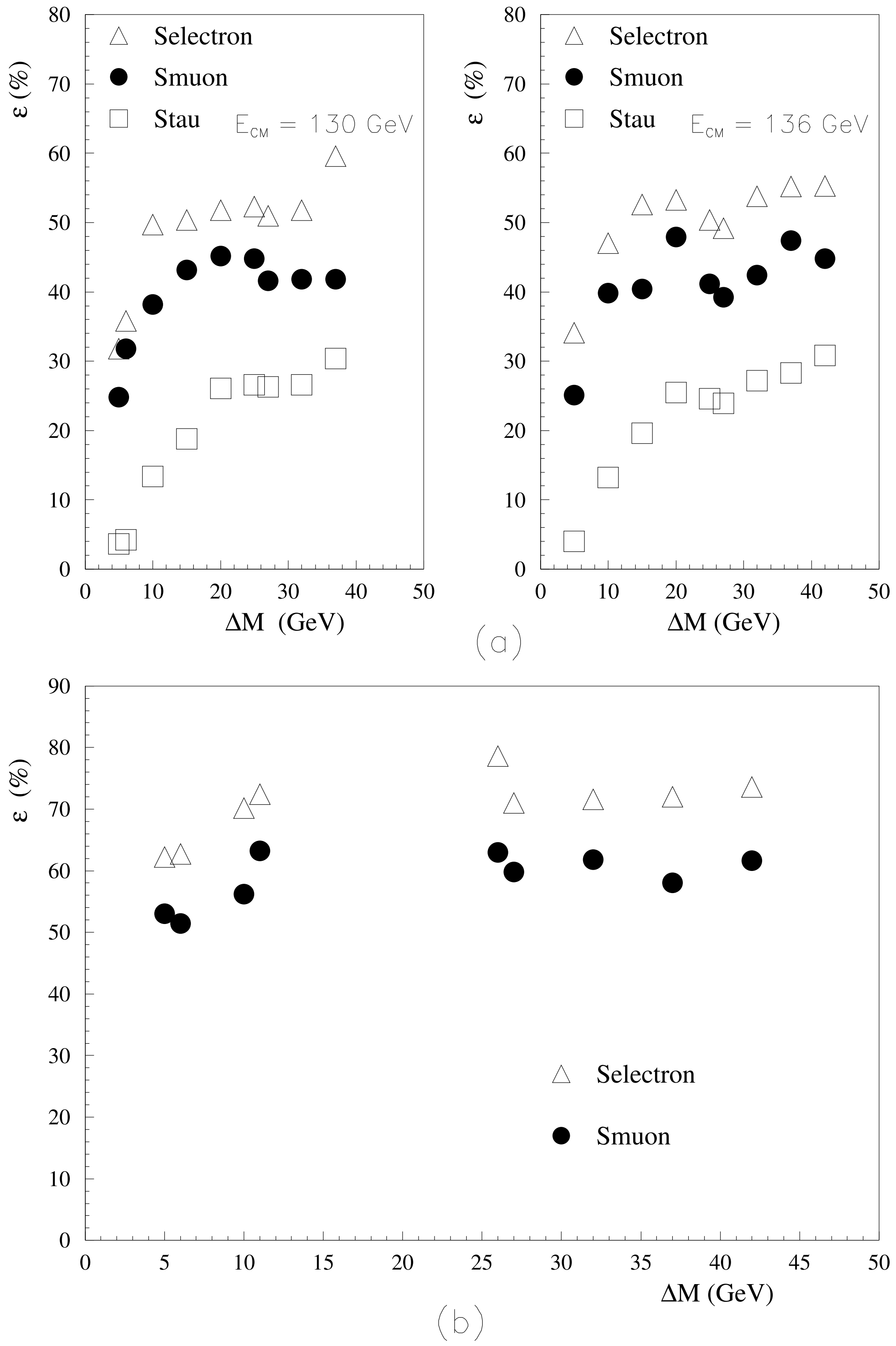

Figure 7.13: Slepton efficiencies at $\sqrt{s}$ = 130 - 136 GeV : (a) using first set of variables and (b) second set of variables.

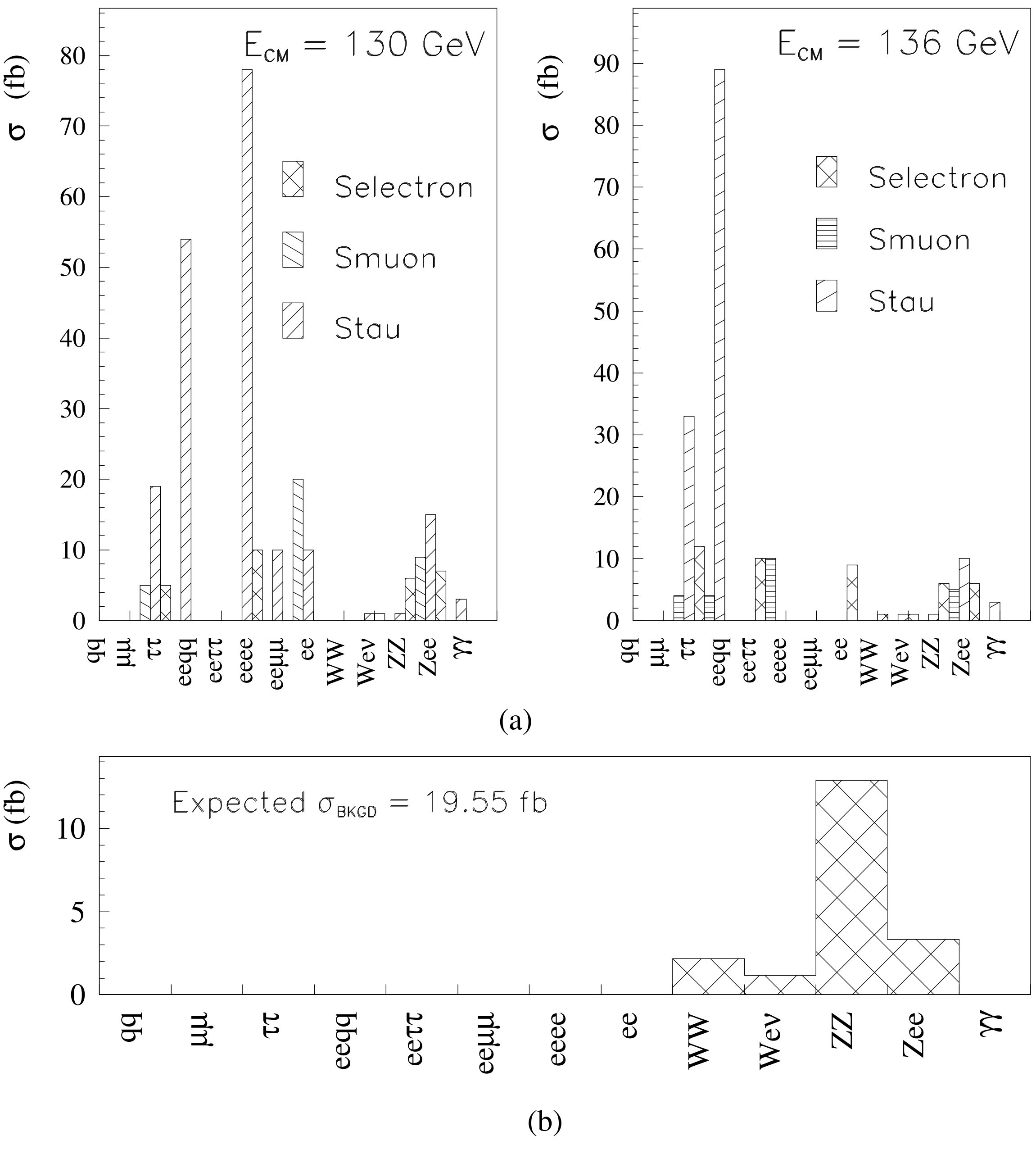

Figure 7.14: Residual SM backgrounds at $\sqrt{s}$ = 130 - 136 GeV : (a) using first set of variables ($\tilde{e}^+\tilde{e}^-$, $\tilde{\mu}^+\tilde{\mu}^-$ and $\tilde{\tau}^+\tilde{\tau}^-$ searches separately) and (b) second set of variables (combined from $\tilde{e}^+\tilde{e}^-$ and $\tilde{\mu}^+\tilde{\mu}^-$ searches).

		$e^+e^- \to \tilde{e}^+\tilde{e}^-$			$e^+e^- \to \tilde{\mu}^+\tilde{\mu}^-$		
$E_{lepton(1)}/E_{beam}$		≤ 0.22	0.22–0.48	0.48–0.70	≤ 0.14	0.14–0.44	0.44–0.70
$E_\perp$ (GeV)	$\geq$	0.67	3.63	4.97	0.55	0.58	2.16
$\not{E}^b_{60^\circ}$ (GeV)	$\leq$	13.8	14.9	7.83	11.8	9.10	13.9
$M_{Vis}/\sqrt{s}$	$\leq$	0.39	0.58	0.68	0.33	0.41	0.67
$[E^{\ell_1}_\perp + E^{\ell_2}_\perp]/E_{vis}$	$\geq$	0.50	0.50	0.65	0.50	0.50	0.54
$\sin\theta_{miss}$	$\geq$	0.15	0.15	0.15	0.16	0.15	0.49
$\not{E}^\perp_{25^\circ}$ (GeV)	$\leq$	4.35	9.97	9.69	7.27	4.54	2.01
ETTT (GeV)	$\geq$	2.89	2.77	2.55	3.03	2.05	6.08
θ_{acop} (rad)	$\geq$	0.09	0.05	0.07	0.14	0.05	0.06
E_{BGO}/E_{Vis} (e=1)	$\geq$	0.40	0.89	0.96	–	–	–
$\frac{(E_{Much}+E_{Hcal})}{E_{Vis}}(\mu = 1)$	$\geq$	–	–	–	0.40	0.62	0.99
E_{Lum} (GeV)	$\leq$	6.00	6.00	6.00	6.00	6.00	6.00
E_{30°/E_{vis}	$\leq$	0.87	0.89	0.80	0.83	0.87	0.86

Table 7.10: Cuts used for the selection of $e^+e^- \to \tilde{e}^+\tilde{e}^-$ and $e^+e^- \to \tilde{\mu}^+\tilde{\mu}^-$ events at $\sqrt{s}$ = 161 GeV. Three different sets corresponding to different ranges of $E_{lepton(1)}$ are shown.

		$e^+e^- \to \tilde{\chi}^+_1\tilde{\chi}^-_1$			$e^+e^- \to \tilde{\tau}^+\tilde{\tau}^-$		
$E_{lepton(1)}/E_{beam}$		≤ 0.09	0.09–0.26	0.26–0.38	≤ 0.07	0.07–0.20	0.20–0.45
$E_\perp$ (GeV)	$\geq$	1.62	4.94	2.62	4.71	1.50	1.96
$\not{E}^b_{60^\circ}$ (GeV)	$\leq$	8.79	6.86	5.54	6.89	6.09	3.54
$M_{Vis}/\sqrt{s}$	$\leq$	0.32	0.40	0.63	0.30	0.41	0.63
$[E^{\ell_1}_\perp + E^{\ell_2}_\perp]/E_{vis}$	$\geq$	0.50	0.50	0.51	0.51	0.50	0.50
$\sin\theta_{miss}$	$\geq$	0.17	0.20	0.31	0.48	0.55	0.36
$\not{E}^\perp_{25^\circ}$ (GeV)	$\leq$	2.31	2.95	3.11	3.18	2.21	2.07
ETTT (GeV)	$\geq$	3.04	3.78	2.34	2.51	2.51	2.00
θ_{acop} (rad)	$\geq$	0.48	0.08	0.17	0.08	0.10	0.05
$\frac{(E_{BGO}+E_{Hcal}+E_{Much})}{E_{Vis}}$	$\geq$	0.35	0.39	0.96	0.14	0.39	0.29
E_{Lum} (GeV)	$\leq$	6.00	6.00	6.00	6.00	6.00	6.00
E_{30°/E_{vis}	$\leq$	0.85	0.85	0.84	0.80	0.83	0.85
$(M_{Invis} - M_{Vis})/\sqrt{s}$	$\geq$	0.55	0.19	0.10	0.43	0.11	0.31

Table 7.11: Cuts used for the selection of $e^+e^- \to \tilde{\chi}^+_1\tilde{\chi}^-_1$ and $e^+e^- \to \tilde{\tau}^+\tilde{\tau}^-$ events at $\sqrt{s}$ = 161 GeV.

Cut Variables	Residual SM cross section (pb) Z/γ^*	$e^+e^-f\bar{f}$	$f\bar{f}f'\bar{f}'$	Total	Signal efficiencies (%) $\tilde{e}^+\tilde{e}^-$	$\tilde{\mu}^+\tilde{\mu}^-$	$\tilde{\chi}_1^+\tilde{\chi}_1^-$	$\tilde{\tau}^+\tilde{\tau}^-$
Preselection	.9178	4.5669	.3026	5.7872	81.20	70.21	73.90	47.90
$E_\perp$	.9152	2.7460	.3023	3.9635	80.40	70.21	71.20	47.60
$\not{E}^b_{60^\circ}$	.4564	2.7460	.2980	3.5004	80.40	70.21	71.20	47.60
$M_{Vis}/\sqrt{s}$	.4387	2.7460	.2968	3.4815	80.40	70.21	71.20	47.60
$[E_\perp^{\ell_1}+E_\perp^{\ell_2}]/E_{vis}$	.3107	1.9725	.2799	2.5632	79.90	69.63	69.70	44.60
$\sin\theta_{miss}$	.2786	1.9269	.2710	2.4764	79.90	69.19	69.20	43.30
$\not{E}^\perp_{25^\circ}$	.2420	1.9066	.2630	2.4116	79.90	69.12	68.70	42.60
ETTT	.1953	.1522	.2561	.6036	78.50	68.23	64.90	42.40
θ_{acop}	.1931	.1522	.2555	.6007	78.50	68.23	64.90	42.40
$\frac{(E_{BGO}+E_{Hcal}+E_{Much})}{E_{Vis}}$	.1754	.0556	.2495	.4805	70.90	66.94	62.30	42.10
E_{Lum}	.1724	.0303	.2480	.4506	70.90	66.94	62.30	42.10
E_{30°/E_{vis}	.1724	.0303	.2478	.4505	70.90	66.94	62.30	42.10
$E_{lepton(1)}/E_{beam}$	.0501	.0050	.1216	.1768	70.90	66.88	61.90	42.10
$(M_{Invis}-M_{Vis})/\sqrt{s}$	.0162	.0050	.1109	.1321	70.90	66.88	61.90	42.10

Table 7.12: Residual SM cross sections and selection efficiencies of different signal events ($\tilde{e}^+\tilde{e}^-$: $M_{\tilde{e}}$ = 80 GeV and $M_{\tilde{\chi}_1^0}$ = 50 GeV; $\tilde{\mu}^+\tilde{\mu}^-$: $M_{\tilde{\mu}}$ = 80 GeV and $M_{\tilde{\chi}_1^0}$ = 50 GeV; $\tilde{\tau}^+\tilde{\tau}^-$: $M_{\tilde{\tau}}$ = 80 GeV and $M_{\tilde{\chi}_1^0}$ = 50 GeV; $\tilde{\chi}_1^+\tilde{\chi}_1^-$: $M_{\tilde{\chi}_1^\pm}$ = 80 GeV and $M_{\tilde{\chi}_1^0}$ = 45 GeV) for successive cuts at $\sqrt{s}$ = 161 GeV.

		$e^+e^-\to\tilde{e}^+\tilde{e}^-$			$e^+e^-\to\tilde{\mu}^+\tilde{\mu}^-$		
$E_{lepton(1)}/E_{beam}$		$\leq$ 0.22	0.22–0.42	0.42–0.50	$\leq$ 0.16	0.16–0.34	0.34–0.54
$E_\perp$ (GeV)	$\geq$	0.56	0.70	6.97	0.53	0.70	1.07
$\not{E}^b_{60^\circ}$ (GeV)	$\leq$	14.6	6.03	14.9	14.9	8.68	4.67
$M_{Vis}/\sqrt{s}$	$\leq$	0.36	0.46	0.46	0.33	0.40	0.50
$[E_\perp^{\ell_1}+E_\perp^{\ell_2}]/E_{vis}$	$\geq$	0.50	0.50	0.52	0.50	0.50	0.57
$\sin\theta_{miss}$	$\geq$	0.14	0.14	0.66	0.15	0.15	0.15
$\not{E}^\perp_{25^\circ}$ (GeV)	$\leq$	3.84	4.30	3.46	7.29	4.35	4.23
ETTT (GeV)	$\geq$	2.50	2.00	9.00	2.00	2.00	2.00
θ_{acop} (rad)	$\geq$	0.07	0.05	0.23	0.08	0.05	0.05
E_{BGO}/E_{Vis} (e=1)	$\geq$	0.40	0.95	0.99	–	–	–
$\frac{(E_{Much}+E_{Hcal})}{E_{Vis}}(\mu=1)$	$\geq$	–	–	–	0.40	0.51	0.99
E_{Lum} (GeV)	$\leq$	6.00	6.00	6.00	6.00	6.00	6.00
E_{30°/E_{vis}	$\leq$	0.88	0.82	0.75	0.88	0.88	0.89

Table 7.13: Cuts used for the selection of $e^+e^-\to\tilde{e}^+\tilde{e}^-$ and $e^+e^-\to\tilde{\mu}^+\tilde{\mu}^-$ events at $\sqrt{s}$ = 172 GeV.

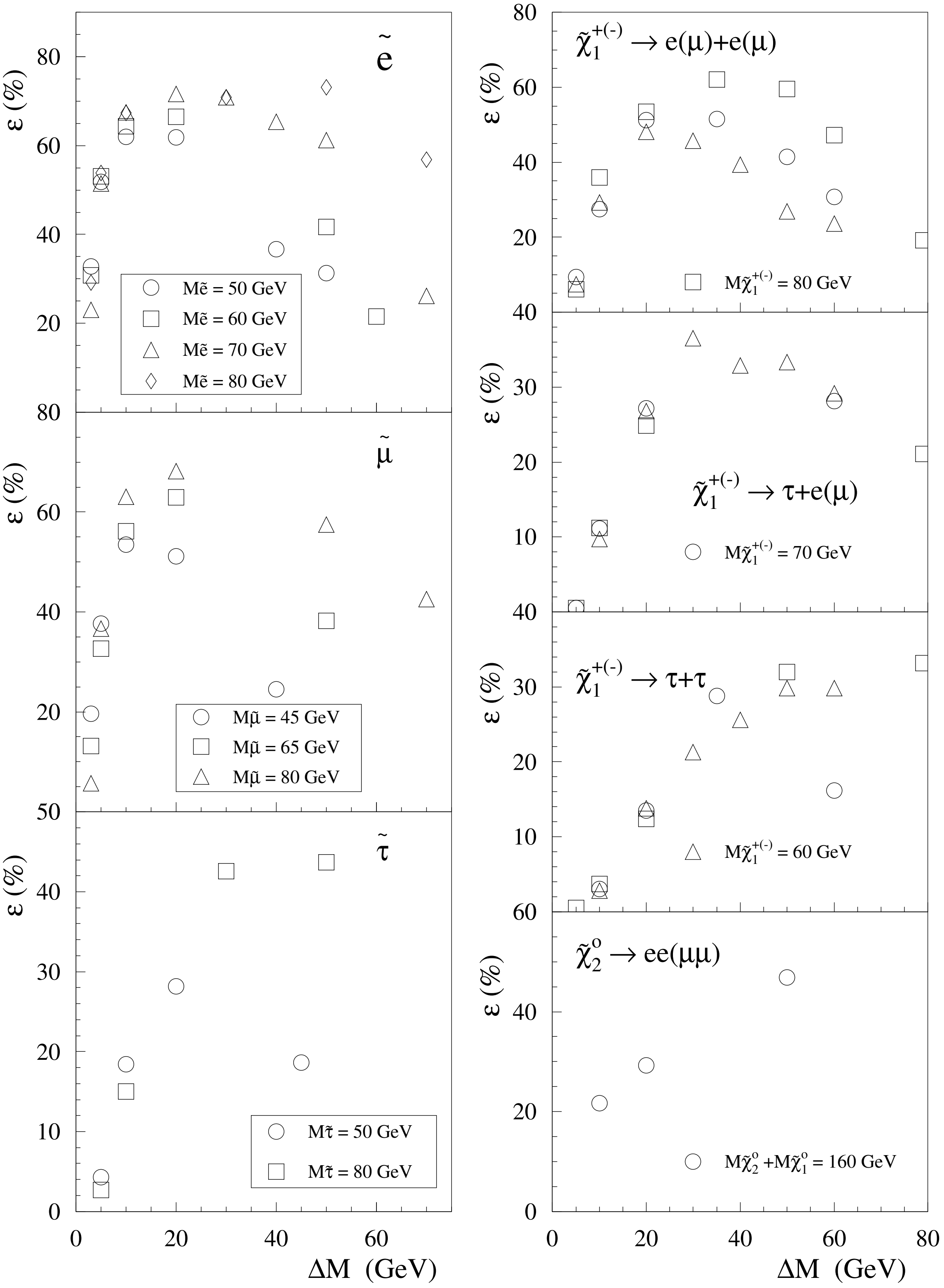

Figure 7.15: Selection efficiencies at $\sqrt{s} = 161$ GeV as a function of ΔM.

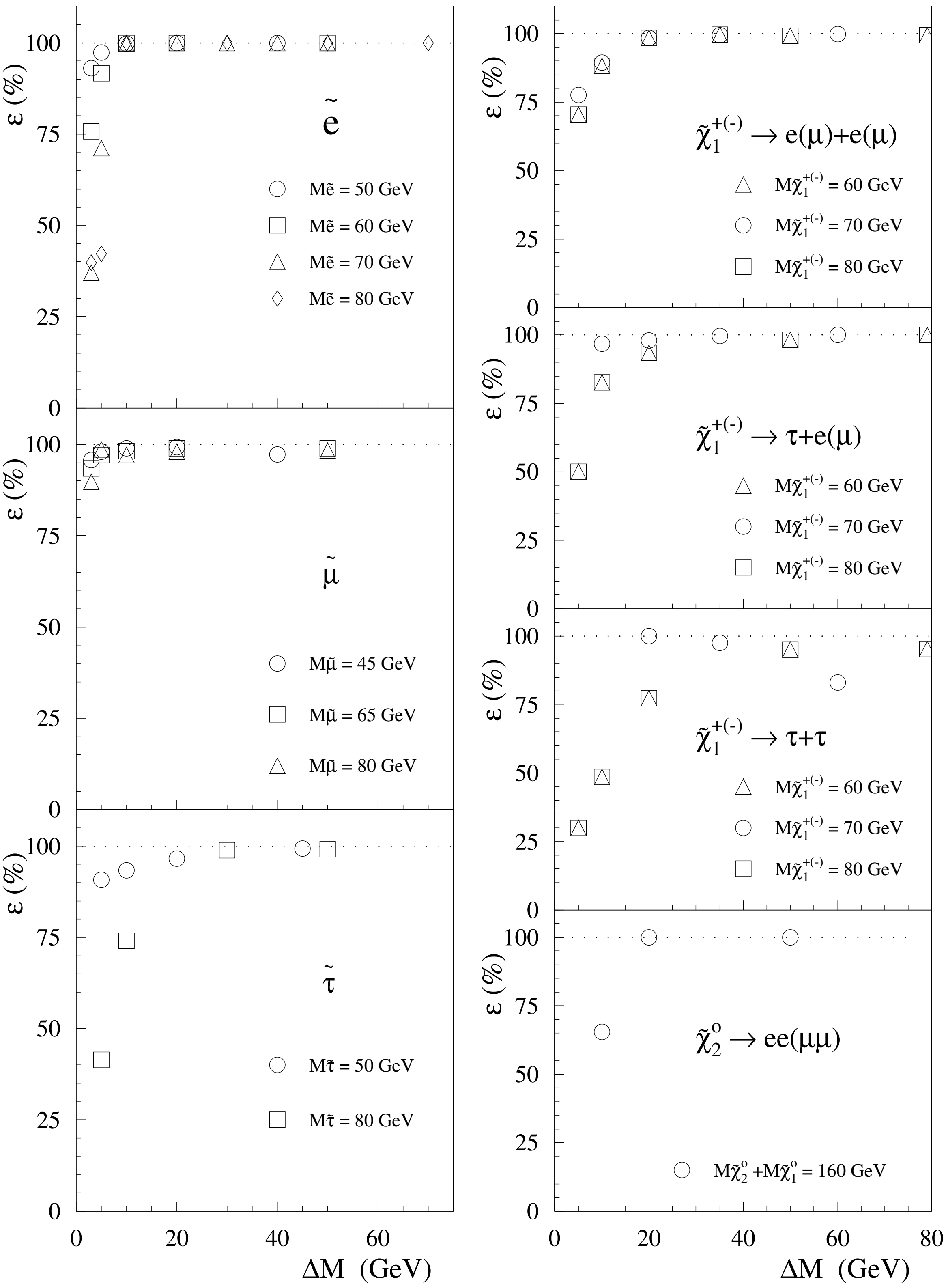

Figure 7.16: Trigger efficiencies at $\sqrt{s} = 161$ GeV as a function of ΔM.

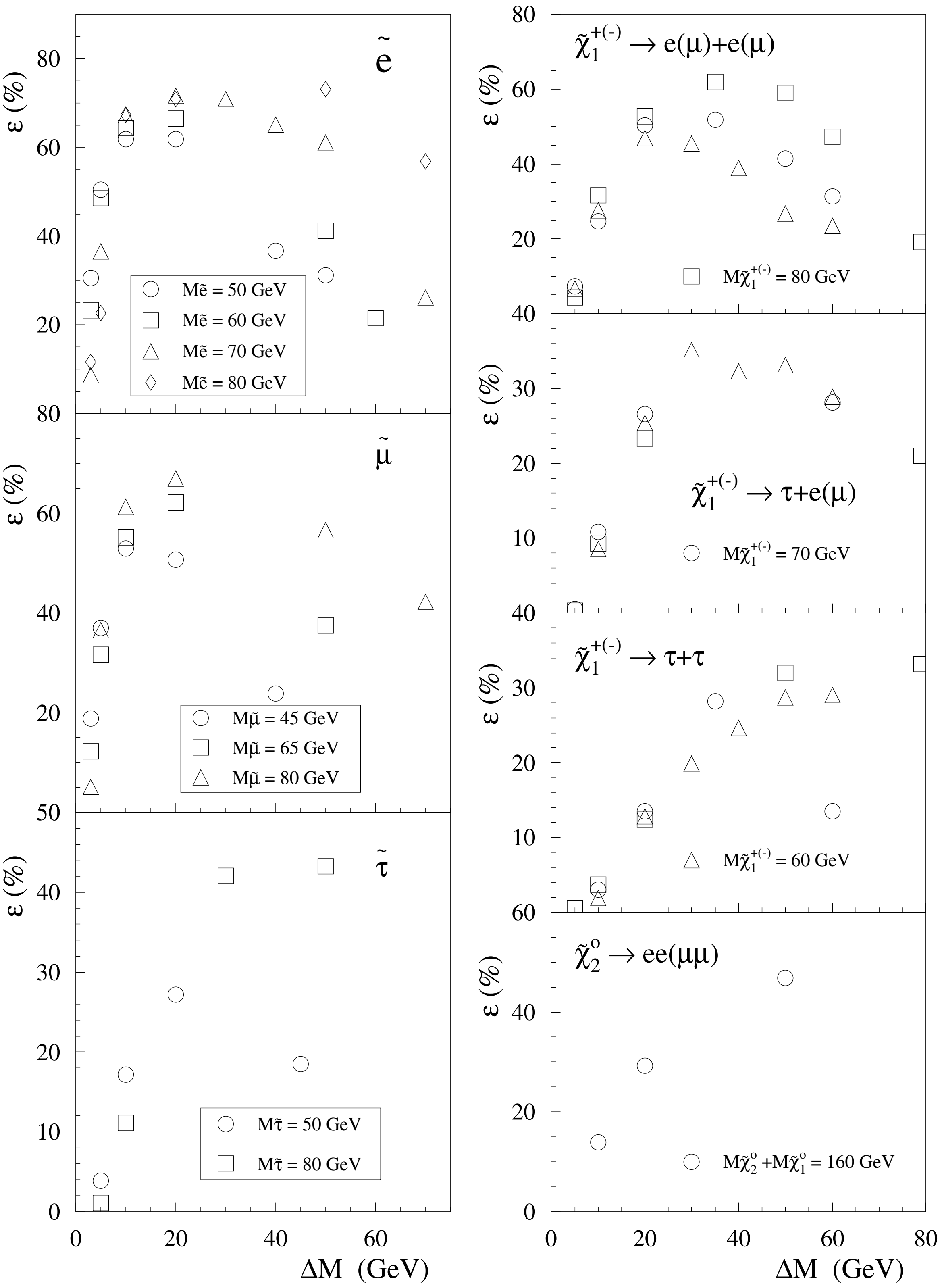

Figure 7.17: Overall efficiencies at $\sqrt{s} = 161$ GeV as a function of ΔM.

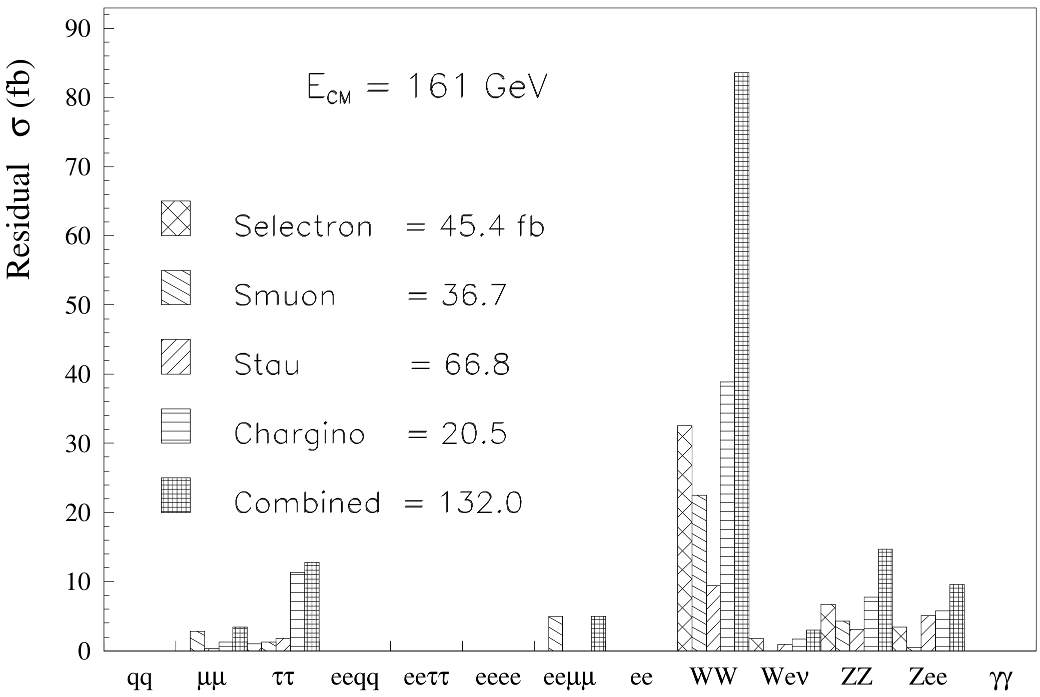

Figure 7.18: Residual SM backgrounds at $\sqrt{s} = 161$ GeV (combined implies events passing through one or more of the four event types indicated in figure).

		$e^+e^- \to \tilde{\chi}_1^+ \tilde{\chi}_1^-$			$e^+e^- \to \tilde{\tau}^+ \tilde{\tau}^-$		
$E_{lepton(1)}/E_{beam}$		≤ 0.08	0.08–0.20	0.20–0.34	≤ 0.06	0.06–0.22	0.22–0.30
$E_\perp$ (GeV)	$\geq$	1.08	1.15	1.95	3.43	1.67	1.62
$\not{E}^{b}_{60^\circ}$ (GeV)	$\leq$	7.44	5.91	4.91	6.87	3.40	2.74
$M_{Vis}/\sqrt{s}$	$\leq$	0.21	0.40	0.63	0.25	0.22	0.63
$[E_\perp^{\ell_1} + E_\perp^{\ell_2}]/E_{vis}$	$\geq$	0.50	0.50	0.50	0.60	0.53	0.54
$\sin\theta_{miss}$	$\geq$	0.16	0.14	0.14	0.53	0.22	0.50
$\not{E}^{\perp}_{25^\circ}$ (GeV)	$\leq$	2.33	3.05	3.34	2.72	2.27	2.88
ETTT (GeV)	$\geq$	2.50	2.51	2.00	2.60	2.58	2.93
θ_{acop} (rad)	$\geq$	0.40	0.08	0.08	0.35	0.24	0.07
$\frac{(E_{BGO}+E_{Hcal}+E_{Much})}{E_{Vis}}$	$\geq$	0.39	0.28	0.99	0.33	0.45	0.40
E_{Lum} (GeV)	$\leq$	6.00	6.00	6.00	6.00	6.00	6.00
E_{30°/E_{vis}	$\leq$	0.79	0.83	0.85	0.68	0.84	0.85
$(M_{Invis} - M_{Vis})/\sqrt{s}$	$\geq$	0.58	0.19	0.35	0.63	0.07	0.37

Table 7.14: Cuts used for the selection of $e^+e^- \to \tilde{\chi}_1^+ \tilde{\chi}_1^-$ and $e^+e^- \to \tilde{\tau}^+ \tilde{\tau}^-$ events at $\sqrt{s}$ = 172 GeV.

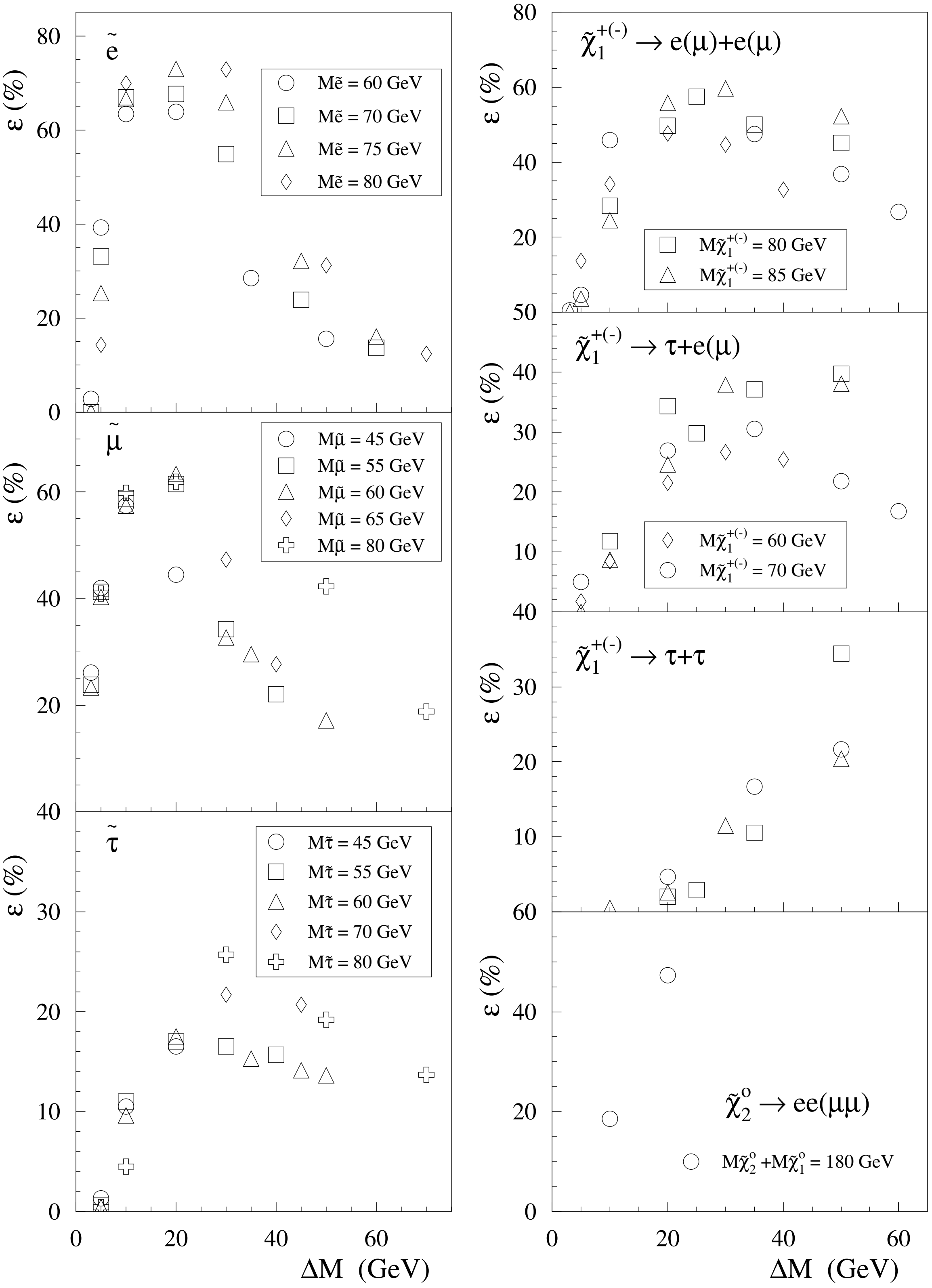

Figure 7.19: Combined efficiencies at $\sqrt{s} = 172$ GeV as a function of ΔM.

Cut Variables	Residual SM cross section (pb)				Signal efficiencies (%)			
	Z/γ^*	$e^+e^-f\bar{f}$	$f\bar{f}f'\bar{f}'$	Total	$\tilde{e}^+\tilde{e}^-$	$\tilde{\mu}^+\tilde{\mu}^-$	$\tilde{\chi}_1^+\tilde{\chi}_1^-$	$\tilde{\tau}^+\tilde{\tau}^-$
Preselection	.4853	.3934	1.0872	1.9659	83.47	68.40	66.15	28.37
$E_\perp$	.4818	.1649	1.0859	1.7326	83.47	68.40	65.98	27.53
$\not{E}^{b}_{60^\circ}$	.2151	.0873	1.0607	1.3631	83.47	68.40	65.98	27.24
$M_{Vis}/\sqrt{s}$	.1804	.0873	1.0348	1.3025	83.47	68.40	65.98	27.24
$[E_\perp^{\ell_1}+E_\perp^{\ell_2}]/E_{vis}$	.1526	.0556	.9946	1.2028	82.36	67.80	65.29	25.22
$\sin\theta_{miss}$	.1231	.0556	.9907	1.1694	82.26	67.70	65.29	25.05
$\not{E}^{\perp}_{25^\circ}$	.0908	.0476	.9744	1.1128	82.26	67.50	65.21	24.78
ETTT	.0668	.0000	.9610	1.0279	81.15	66.80	62.63	23.67
θ_{acop}	.0630	.0000	.9599	1.0229	81.15	66.80	62.63	23.67
$\frac{(E_{BGO}+E_{Hcal}+E_{Much})}{E_{Vis}}$	.0555	.0000	.9405	.9959	72.88	62.60	59.71	22.76
E_{Lum}	.0525	.0000	.9327	.9852	72.78	62.20	59.71	22.41
E_{30°/E_{vis}	.0525	.0000	.9324	.9849	72.78	62.20	59.71	22.41
$E_{lepton(1)}/E_{beam}$	.0056	.0000	.1421	.1478	72.78	61.90	59.71	13.77
$(M_{Invis}-M_{Vis})/\sqrt{s}$	.0052	.0000	.1411	.1463	72.78	61.90	59.71	13.77

Table 7.15: Reduction of remaining SM cross section and selection efficiencies of different types of signal ($\tilde{e}^+\tilde{e}^-$: $M_{\tilde{e}}$ = 80 GeV and $M_{\tilde{\chi}_1^\circ}$ = 50 GeV; $\tilde{\mu}^+\tilde{\mu}^-$: $M_{\tilde{\mu}}$ = 80 GeV and $M_{\tilde{\chi}_1^\circ}$ = 50 GeV; $\tilde{\tau}^+\tilde{\tau}^-$: all events with $M_{\tilde{\tau}}$ = 45-80 GeV and $M_{\tilde{\chi}_1^\circ}$ = 10-75 GeV; $\tilde{\chi}_1^+\tilde{\chi}_1^-$: $M_{\tilde{\chi}_1^\pm}$ = 85 GeV and $M_{\tilde{\chi}_1^\circ}$ = 55 GeV) for successive cuts at $\sqrt{s}$ = 172 GeV.

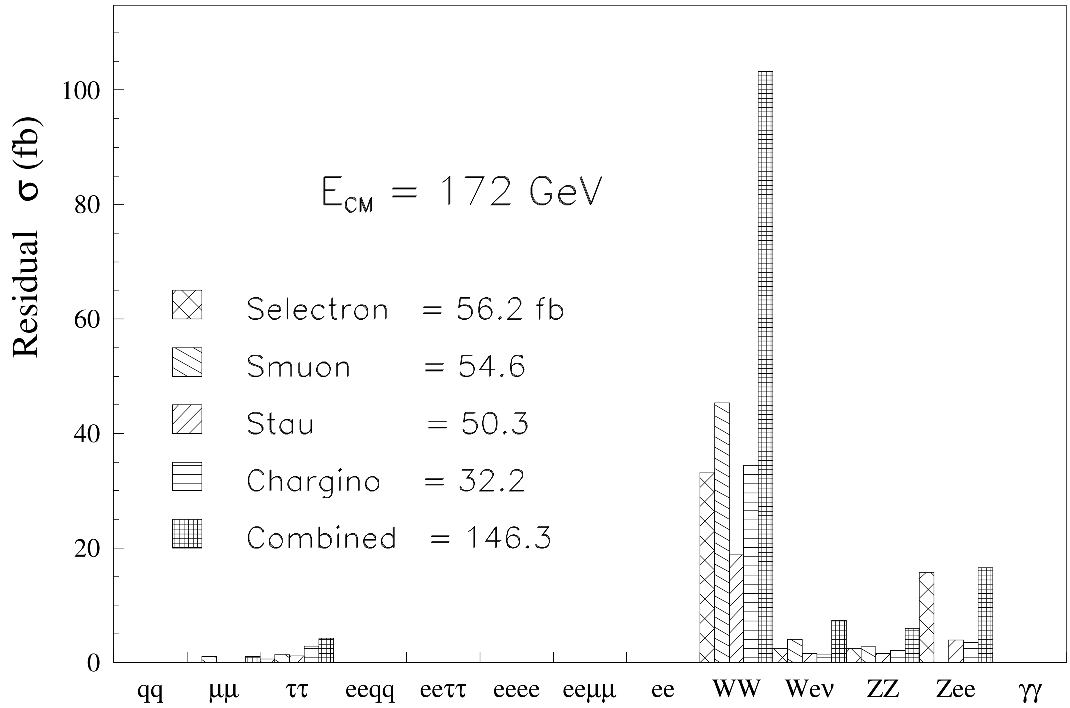

Figure 7.20: Residual SM backgrounds at $\sqrt{s} = 172$ GeV (Combined implies events passing through one or more of the four event types as indicated in figure).

7.5 Error Estimation

7.5.1 Statistical Error

Statistical error has been calculated for each individual point in the parameter space separately. It is calculated assuming the binomial distribution of the generated events. Let N be the number of event generated for a point (in SUSY parameter space) and N_s is the number of event passed through the selection criteria, then the efficiency of the sample file is $\varepsilon = N_s/N$. Error on the efficiency

$$\sigma_\varepsilon = \sqrt{\varepsilon \times (1. - \varepsilon)/N}$$

7.5.2 Systematic Uncertainties

Systematic errors are calculated for the following cases :

- **Detector uncertainty :**

  Systematic error on the efficiency due to finite resolution of the detector has been estimated by varying the cuts on the kinematic variables. The cut values are changed by one standard deviation in such a way that it always reduced the efficiencies. Corresponding uncertainties in the measured variables are calculated directly from data, or from Monte Carlo. Variables used in the systematics and the corresponding errors are given below :

  $\Delta\, E_\perp = 0.31$ GeV (0.51 GeV for μ)
  $\Delta\, \not{E}^{b}_{60^\circ} =$ as hadronic energy resolution
  $\Delta\, M_{Vis} = 0.23$
  $\Delta \sin\theta_{miss} = 0.007$
  $\Delta\, \not{E}^{\perp}_{25^\circ} =$ as hadronic energy resolution
  $\Delta\, ETTT = 0.03$ GeV (0.08 GeV for μ)
  $\Delta\, \theta_{acop} = 0.014$ rad (~ 0 for μ)
  $\Delta\, E_{lepton(1)}/E_b = 0.025$

  With these changes, average reduction in efficiencies of $\tilde{e}^+\tilde{e}^-$ and $\tilde{\mu}^+\tilde{\mu}^-$ signals are $\approx 1.3\,\%$ and $\approx 2.9\,\%$ respectively. A major fraction of the systematic error is due to the uncertainty in the measurement of transverse energy imbalance.

  The whole analysis has been carried out on the basis of two independent algorithms of energy calibration (section 4.9).

(i) Using New Particle Group (of L3) G-factor [101] : Energy of the events are calculated using track momentum in central tracking system and muon chamber and energy deposition in calorimeters. Here the whole detector is divided into 12 zones, but depending whether a track had an associated calorimetric cluster/muon or not, or a calorimetric cluster/muon has an associated track or not, two values of the G-factor are considered in each zone.

(ii) Using QCD group G-factor [102] : Here energy of the events are calculated using the localised energy deposited in ECAL and HCAL and track momentum in the MUCH. The whole detector are again divided into 12 zones, and each zone has an independent G-factor to get the true energy from the calibrated energy of that zone.

Fluctuation of SUSY signal efficiencies in these two independent analyses is $\approx 2.3\,\%$ for same background contamination.

This is an independent way to calculate the error on efficiency due to energy calibration factor. Conservatively the larger one from these two methods are quoted as the error in various channels.

- **Trigger efficiency :**

Trigger efficiency has been determined from the simulated events where trigger conditions are simulated with realistic thresholds and their fluctuations. Uncertainty in the estimation of trigger efficiency is calculated by comparing the simulated trigger condition with the real trigger condition in the data. The trigger efficiency quoted here refers to simulated events which pass the selection criteria. In data, statistics of such events would be extremely poor and consequently the statistical error will be overwhelming. On the other hand, bulk of data differ very much from SUSY signal events. So, as a compromise events have been selected using the loose SUSY event selection criteria to calculate the error on the trigger efficiency.

Trigger efficiency has been calculated by first dividing the event sample into two categories,

Type 1 : event with no muon
Type 2 : event containing at least one muon

Events in the type 1 category are selected mainly through *energy* and *TEC* trigger, whereas those from type 2 are selected mainly through *muon* and *TEC* trigger.

Let $\mathrm{N_{ET}}$, $\mathrm{N_E}$ and $\mathrm{N_T}$ are the number of events selected by both *energy* and *TEC* trigger, *energy* trigger and *TEC* trigger respectively in the events of type 1 category. If N, ε_{E}, and ε_{T} are the total number of events of type 1, *energy* trigger efficiency and *TEC* trigger efficiency respectively, then,

$$
\begin{aligned}
\mathrm{N_{ET}} &= \mathrm{N} \,.\, \varepsilon_{_E} \,.\, \varepsilon_{_T} \\
\mathrm{N_{E}} &= \mathrm{N} \,.\, \varepsilon_{_E} \\
\mathrm{N_{T}} &= \mathrm{N} \,.\, \varepsilon_{_T}
\end{aligned}
$$

which gives $\varepsilon_{_\mathrm{E}} = \mathrm{N_{ET}}/\mathrm{N_T}$, $\varepsilon_{_\mathrm{T}} = \mathrm{N_{ET}}/\mathrm{N_E}$ and the combined trigger efficiency is given by

$$\varepsilon = \varepsilon_{_E} + \varepsilon_{_T} - \varepsilon_{_E}\,\varepsilon_{_T}$$

Similarly trigger efficiencies are calculated for the type 2 events from the number of events selected by both *muon* and *TEC* trigger, *muon* trigger and *TEC* trigger respectively.

Trigger efficiency has been calculated from the same sample from the hardware (detector information) trigger pattern and the software (MC trigger simulation) trigger pattern. Half of the difference between the two estimation is taken as the error on trigger efficiency. Typical values vary between 0.25 % and 1.22 % for different types of loosely selected SUSY sample.

- **SUSY parameter space :**

  Systematic uncertainty due to different angular distributions (possible for selectron pair production via the t-channel) of produced selectrons and decay products has been estimated for seven different MSSM parameter sets ($tan\,\beta \in [1, 40]$, $\mu \in [-500., 500.]$), representing different neutralino field contents and coupling but keeping the masses of lowest neutralino ($\tilde{\chi}^\circ_1$) and right handed selectron ($\tilde{\mathrm{e}}_{_R}$) same. One finds that the efficiency depends on the mass of the selectron and the LSP and is rather independent of the other parameters of the SUSY model. The differences are less than or comparable to the error due to limited MC samples. So this uncertainty has been ignored during the exclusion of the SUSY parameter space.

- **Theoretical assumption** :

  The calculations on SUSY production cross sections and branching ratios have been carried out without any radiative correction except the ISR effect. The uncertainly due to this assumption has not been incorporated in the final results.

Chapter 8

Experimental Data

The first phase of LEP run (Z-physics) ended on 4th October 1995. Thereafter in 1995 and 1996 LEP operated at three successive higher energies. The first one started on 31st October '95 with $\sqrt{s}$ = 130 - 136 GeV. The second run at LEP took place during July-August of 1996 at the centre of mass energy of 161 GeV and the third one during October-November 1996 at $\sqrt{s} \approx 172$ GeV.

8.1 LEP Run and L3 Data Collection

Commissioning of high energy run began on October 27th, and within 4 days the world's first physics with colliding e^+e^- beams at $E_b = 65$ GeV took place corresponding to $\sqrt{s}$ = 130 GeV. The luminosities ($\mathcal{L}$) were of the order of 10^{31} cm^{-2} s^{-1}. The newly installed superconducting RF cavities imposed a maximum current limit of 4 mA for most of the period, and the operation was consequently with 4 positron against 4 electron bunches. LEP operated at 65 GeV as beam energy for e^-/e^+ for the first half of the four week period, with initial luminosities varying between (2.5 - 3.0)$\times 10^{31}$ cm^{-2} s^{-1}. Then followed by a short period of run at $E_b = 70$ GeV, which proved difficult as the RF system had no margin for safety and the energy was therefore reduced to 68 GeV for the final two weeks of running. Luminosities achieved during this run were $\approx 3.0\times 10^{31}$ cm^{-2} s^{-1}. These high performance levels were mostly due to very small vertical beam sizes, leading to values of the beam-beam parameter of 0.05. For the final run of the year, the current restrictions were relaxed and almost 6 mA, in 4 trains of 2 bunches per beam, was successfully used for physics. A record peak luminosity of 3.4 $\times 10^{31}$ cm^{-2} s^{-1} was achieved. LEP efficiency, defined as the time spent with stable physics beams divided by the total scheduled physics time, was lower (down to 39 %) than that of during Z runs (1990 : 42 %, 91 : 45 %, 92 : 51 %, 93 : 55 %, 94 : 59 % and 95 : 46 %), with around 70% of coasts lost with RF problems. 6.276 pb^{-1} integrated luminosity was delivered by LEP in this run (3.122 pb^{-1} at $\sqrt{s}$ = 130.3 GeV, 3.103 pb^{-1} at $\sqrt{s}$ = 136.3 GeV and 0.051 pb^{-1} at $\sqrt{s}$ = 140.2 GeV).

The LEP ran with high energy beam again on June 14th in the year 1996. On the ninth of July, the first collisions at 80.5 GeV were recorded by the LEP experiments. The physics run continued until August 16 except a weak of machine development. On August 16, a scheduled stop of several weeks for installation of more superconducting cavities began. The machine restarted on October 10, for a physics run at 86 GeV and it continued until November 25.

At the beginning of high energy runs, beams collided at the Z energy, when an integrated luminosity ($\int \mathcal{L}\, dt$) of 1.3 pb^{-1} was delivered. Together with 12.1 pb^{-1} at $\sqrt{s}$ = 80.5 GeV, 1.1 pb^{-1} at $\sqrt{s}$ = 170.3 GeV and 10.2 pb^{-1} at $\sqrt{s}$ = 172 GeV, the integrated luminosity for the year was nearly 25 pb^{-1}. The efficiency for physics was only 36% averaged over the year. This may be compared to 50 - 60 % obtained in previous years, when fewer changes were made and running conditions were much more stable.

8.2 Reconstruction of Data to the Search Level

The experimental data from e^+e^- interactions passed through the following procedures before going to the search level :

- Event reconstruction : L3 detector stores the information of e^+e^- interaction physics processes which pass the detector trigger criteria (chapter 5). Electronic signals of all subdetectors are passed through the L3 event reconstruction program REGEL3 (section 6.2) to get the details of the final state particles (section 7.1) of the e^+e^- interactions, energy deposited in various subdetectors and the kinematic variables of the events (few examples are shown in section 7.2).
- Event sample : Total events recorded by the L3 detector for these high energy runs are shown in table 8.1.

$\sqrt{s}$ (GeV)	Integrated luminosity (pb^{-1}) Delivered by LEP	Collected by L3	Good data [1]	Event recorded $\times 10^5$
130.26	3.122	2.737	2.694	
136.23	3.103	2.268	2.127	4.5
140.23	0.051	0.047	0.042	
161.35	12.1	11.115	10.102	7.7
170.27	1.1	1.029	0.981	
172.35	10.2	9.511	9.028	9.0

Table 8.1: Status of LEP run and L3 data taking at $\sqrt{s} = 130 - 172$ GeV.

[1] Good data implies that during the collection of data, all the subdetectors (LUMI, TEC, Scintillator, BGO, HCAL and MUCH), which are used in these analyses were in the stable running condition. Only good data are used in these analyses.

- Machine background rejection : L3 trigger system reject most of the machine background events (chapter 5). More strict cuts have been applied for these analyses, e.g., the best scintillation timing ($| T^{best}_{Scint} | \leq 5\ ns$) for the events with one or more muons, minimum distance of closest approach of the tracks in central tracking system in R-Φ plane ($DCA_{min} \leq 1$ mm), parallel energy imbalance ($| E_{||} | / E_{Vis} \leq 0.8$) etc.
- DATA vs Monte Carlo : From the data one intends to look for a small signal of SUSY over a huge background coming from the Standard Model processes. Thus one can assume that majority of the data collected by the detector must be coming from the SM processes. Plots of few variables, after a loose selection cuts (table 7.5) to avoid the beam-gas, beam-wall interaction processes, cosmic events etc., are shown in figures 8.1, 8.2, 8.3, 8.4, 8.5, 8.6 and 8.7. SM processes are properly normalised by their production cross sections and with the integrated luminosity collected by the L3 detector. Matching of the data and MC confirm that the kinematic variables are well measured and the detector effects as well as the knowledge of SM physics processes are well understood.

8.3 Searches for SUSY Signal in Data

8.3.1 Searches at $\sqrt{s}$ = 130 - 136 GeV

The selection criteria as mentioned in section 7.4.1 have been applied to the data sample collected at $\sqrt{s}$ = 130 GeV and 136 GeV. On the basis of the first selection procedure (section 7.4), no event survived the selection criteria for $e^+e^- \rightarrow \tilde{e}^+ \tilde{e}^-$ and $e^+e^- \rightarrow \tilde{\mu}^+ \tilde{\mu}^-$ channels, while one candidate was found for the $e^+e^- \rightarrow \tilde{\tau}^+ \tilde{\tau}^-$ channel at $\sqrt{s}$ = 136 GeV.

The characteristics of the candidate event are summarised in table 8.2 and figure 8.8 shows two views of the event. The candidate event has a μ^- of 16.3 GeV on one side (k_T algorithm gives a jet of energy 23.9 GeV which includes the muon and nearby calorimetric clusters) and two low energy tracks (only one of them satisfies a good track selection criteria) forming another jet of energy 3.4 GeV on the other side. It is characterised by a large transverse and longitudinal imbalances in momentum.

The number of observed events and expected background events are summarised in table 8.3. There was a candidate event in the $\tilde{\tau}^+\tilde{\tau}^-$ channel whereas one expects to find 0.8 events from known SM backgrounds.

With the second set of selection criteria (section 7.4.1) no candidate event was selected neither in $\tilde{e}^+\tilde{e}^-$ mode nor in $\tilde{\mu}^+\tilde{\mu}^-$ mode. There was no elaborate study of $\tilde{\tau}^+\tilde{\tau}^-$ channels with the second set of variables at $\sqrt{s}$ = 130 - 136 GeV, because even with the expected

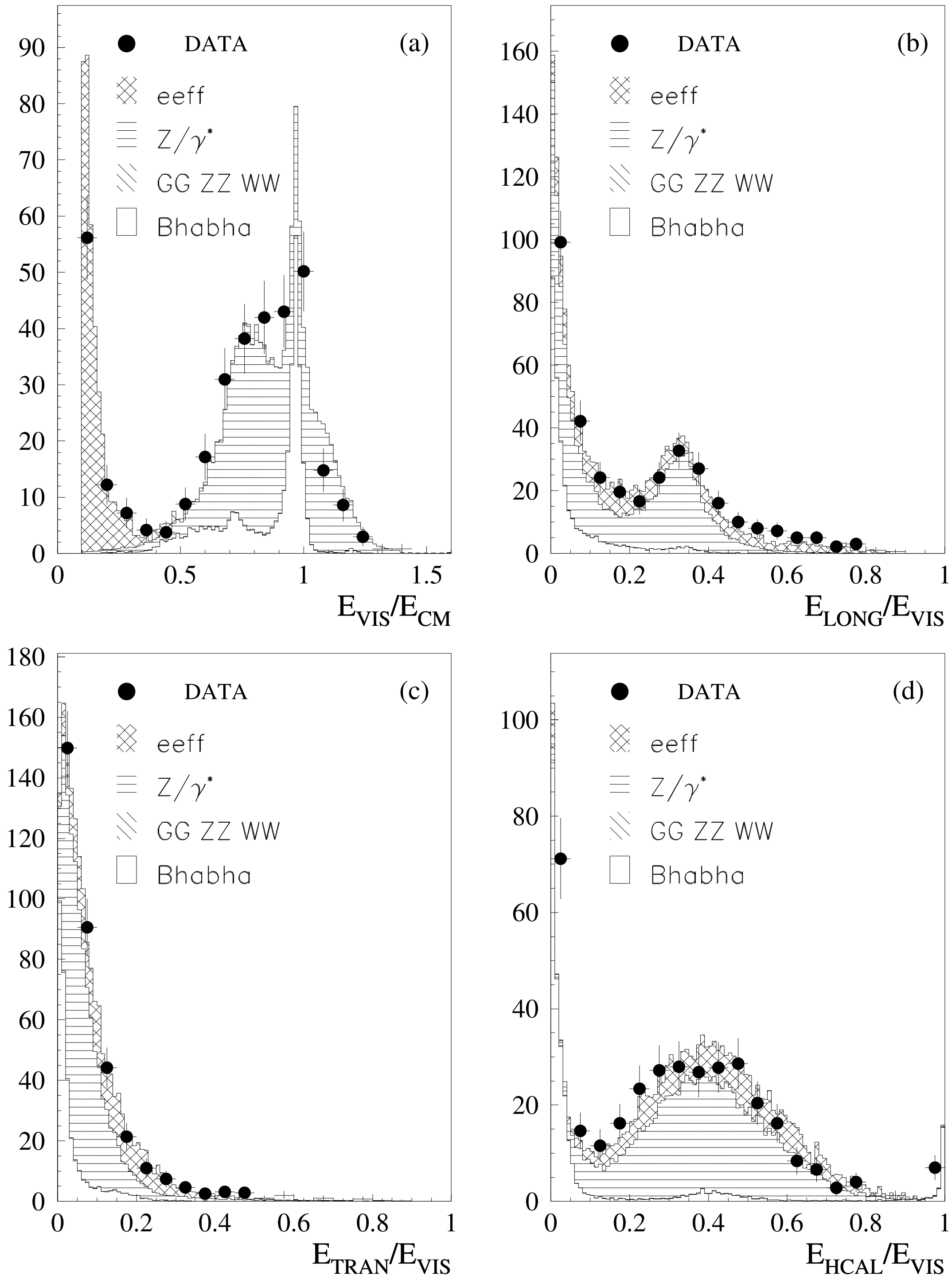

Figure 8.1: Comparison of data and SM Monte Carlo at $\sqrt{s} = 130$ GeV : (a) visible energy normalised to centre of mass energy, (b) longitudinal energy imbalance normalised to the visible energy (c) transverse energy imbalance normalised to the visible energy and (d) fraction of energy deposited in the hadron calorimeter.

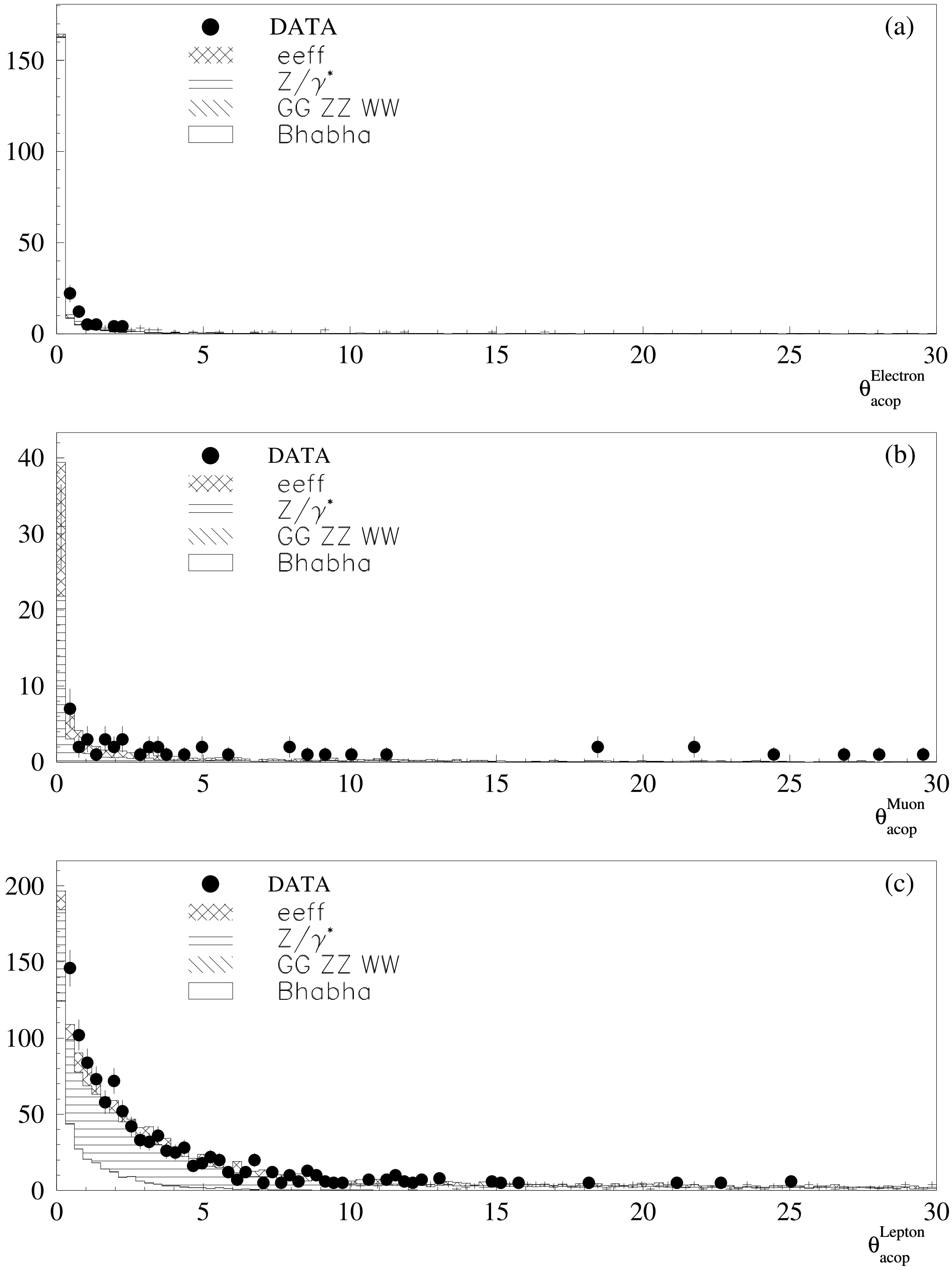

Figure 8.2: Comparison of data and SM Monte Carlo at $\sqrt{s} = 130$ GeV : acoplanarity angles (in degree) of (a) two most energetic electrons, (b) two most energetic muons and (c) two most energetic leptons.

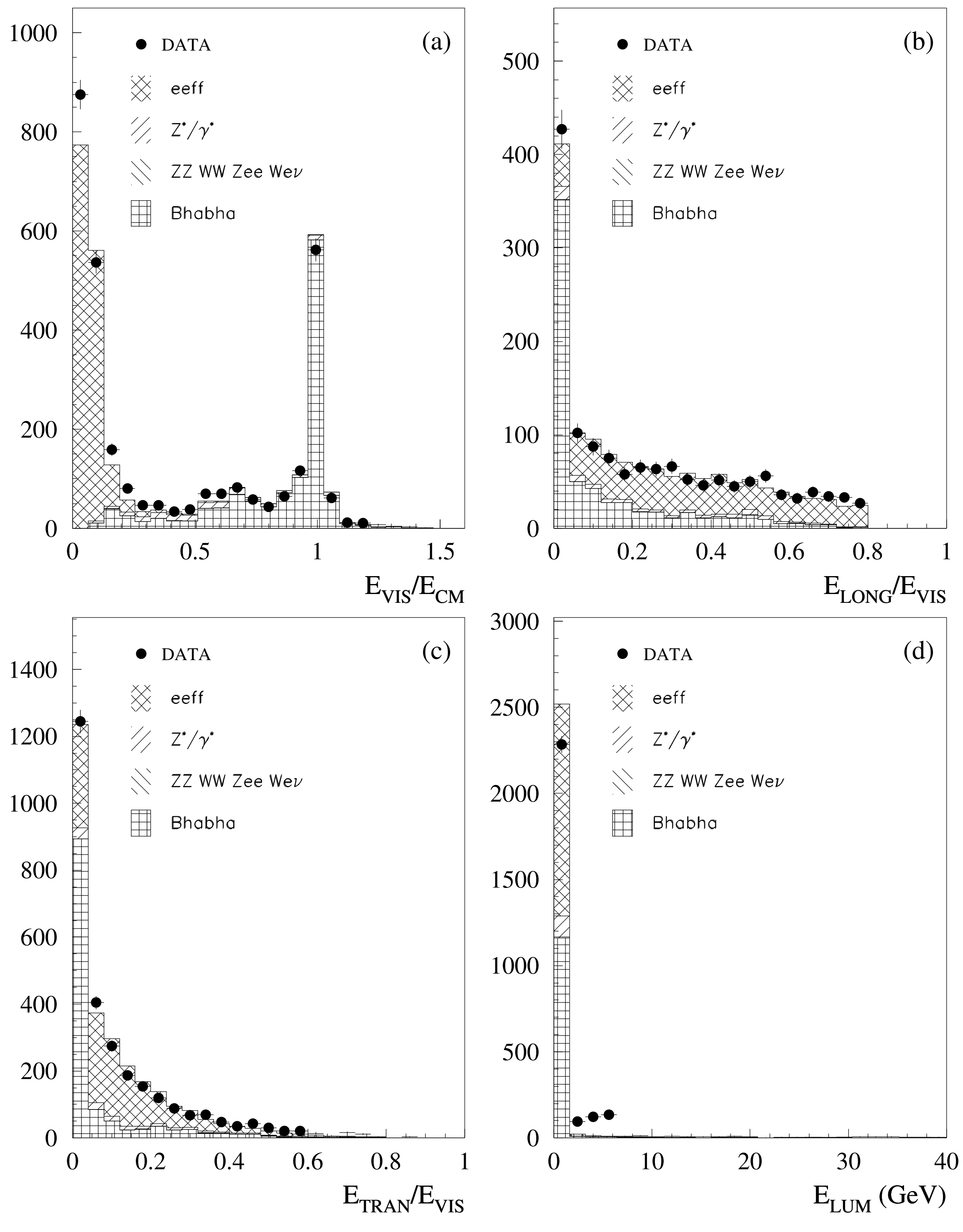

Figure 8.3: Comparison of data and SM Monte Carlo at $\sqrt{s} = 161$ GeV : (a) visible energy normalised to the centre of mass, (b) longitudinal energy imbalance normalised to the visible, (c) transverse energy imbalance normalised to the visible energy and (d) energy deposit in the luminosity monitors.

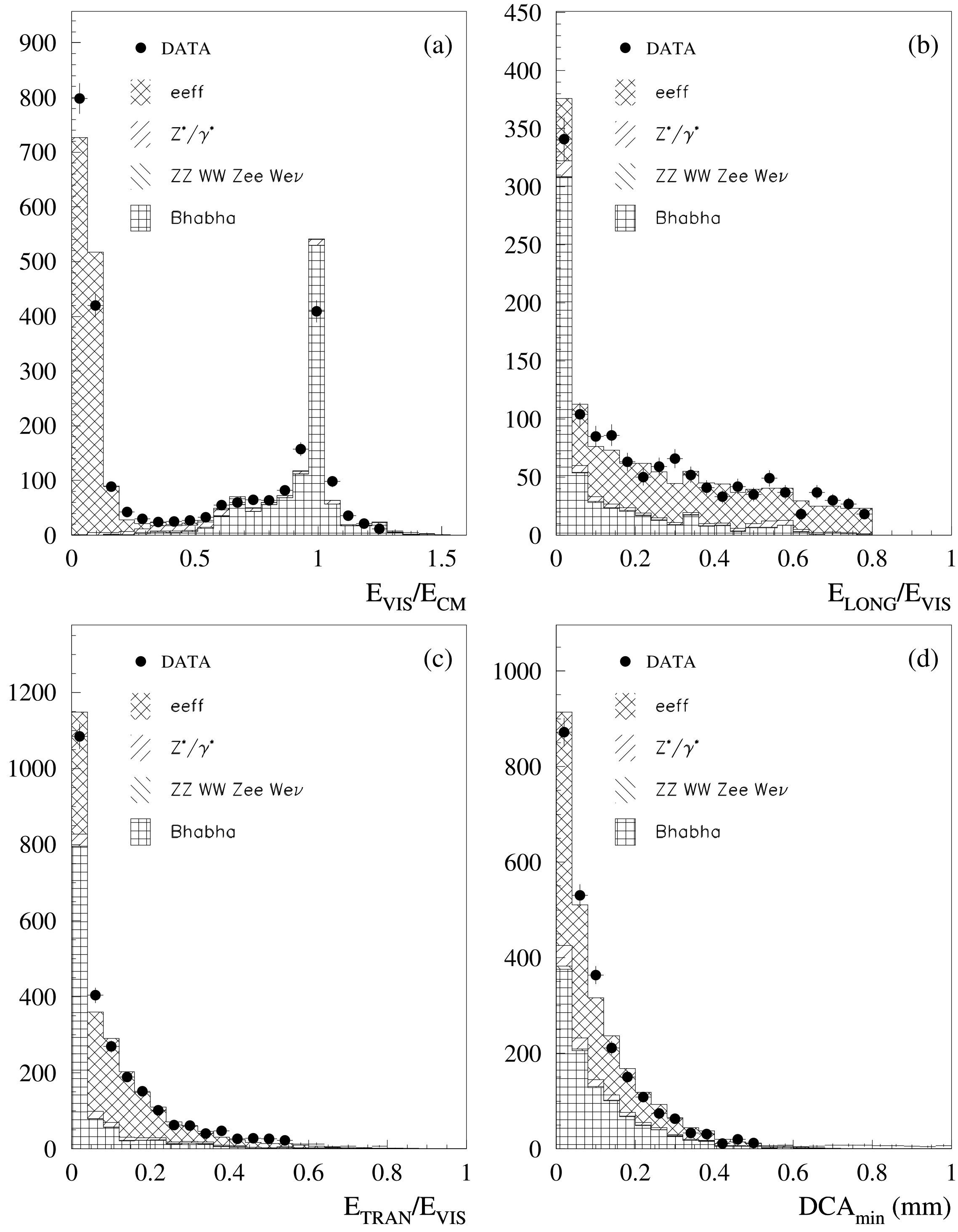

Figure 8.4: Comparison of data and SM Monte Carlo at $\sqrt{s} = 172$ GeV : (a) visible energy normalised to the centre of mass energy, (b) longitudinal energy imbalance normalised to the visible energy, (c) transverse energy imbalance normalised to the visible energy and (d) minimum distance of closest approach of the tracks in central tracking system.

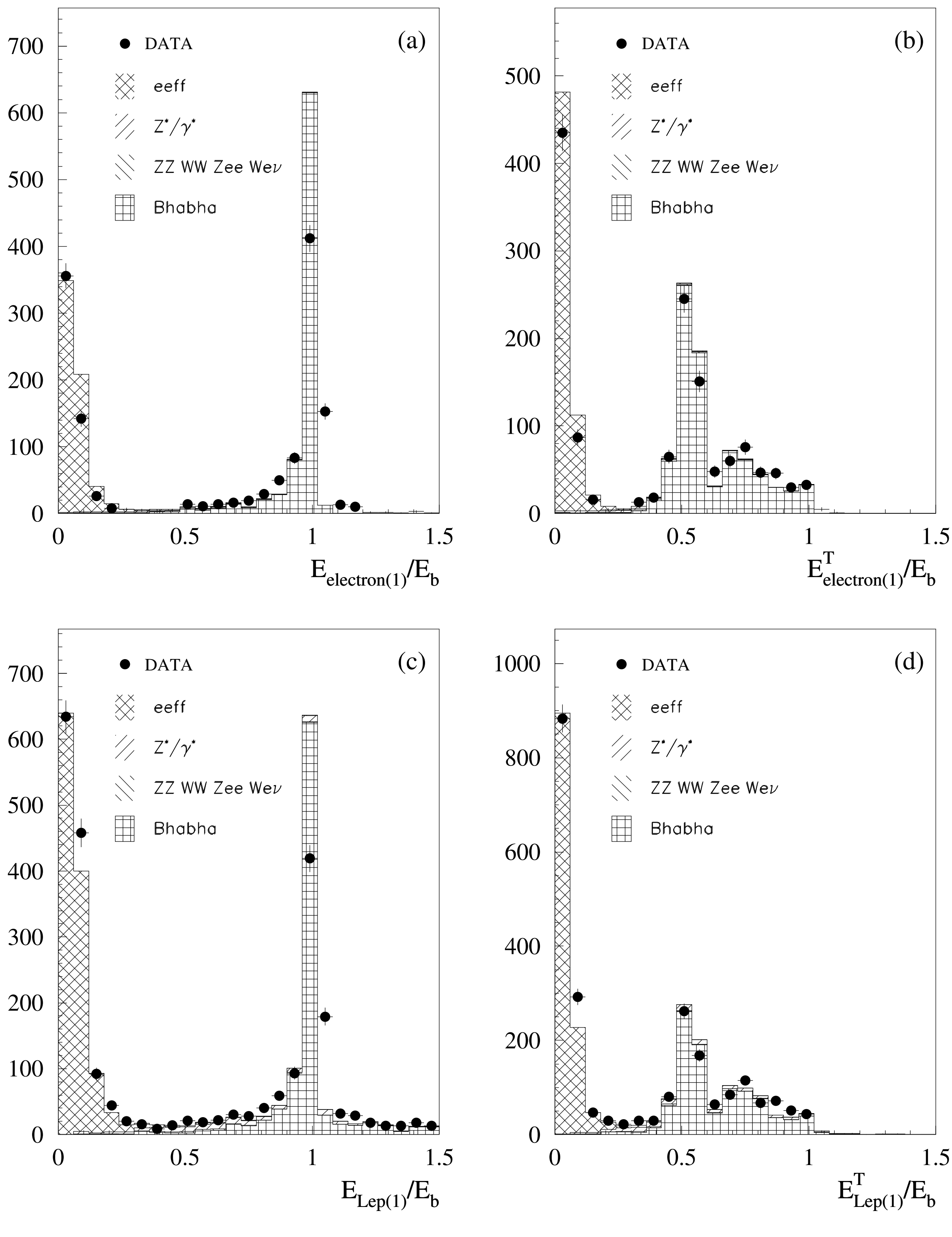

Figure 8.5: Comparison of data and SM Monte Carlo at $\sqrt{s} = 172$ GeV : (a) ratio of the energy of most energetic electron and beam energy, (b) ratio of the transverse energy of the most energetic electron and beam energy, (c) ratio of the energy of most energetic lepton and beam energy and (d) ratio of the transverse energy of the most energetic lepton and beam energy.

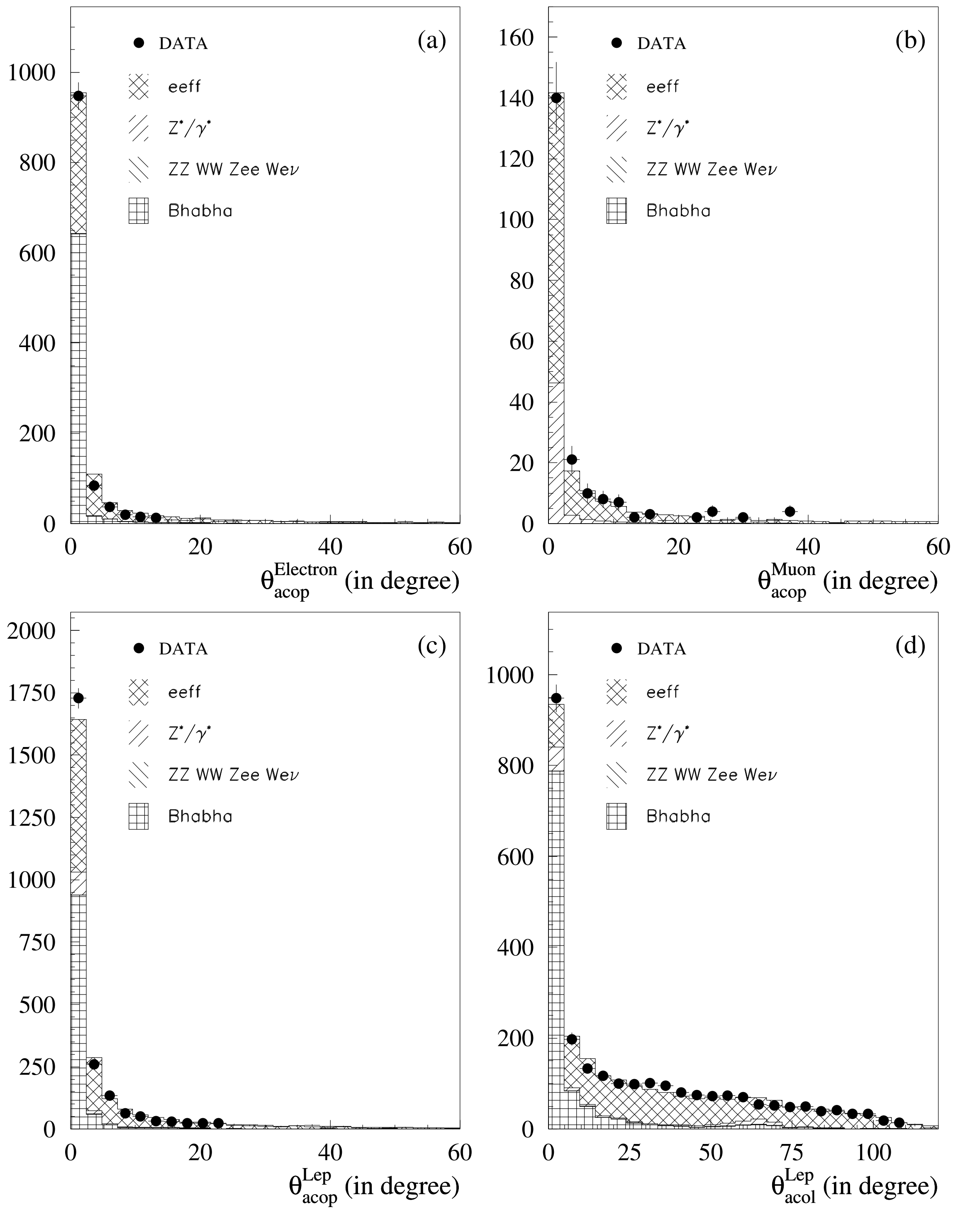

Figure 8.6: Comparison of data and SM Monte Carlo at $\sqrt{s} = 172$ GeV : the acoplanarity angles of (a) two most energetic electrons, (b) two most energetic muons and (c) two most energetic leptons and (d) acolinearity angles of two most energetic leptons.

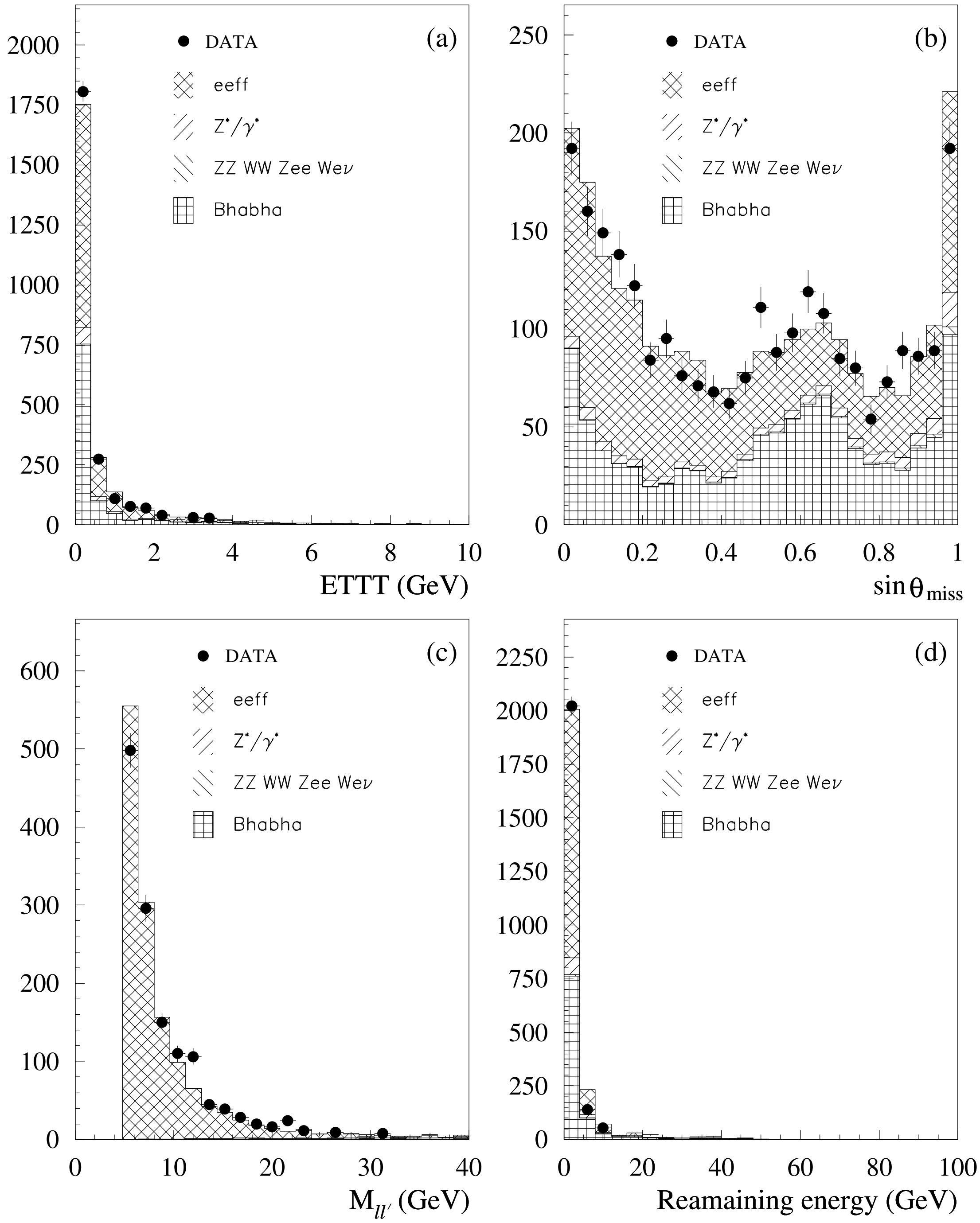

Figure 8.7: Comparison of data and SM Monte Carlo at $\sqrt{s} = 172$ GeV : (a) projected energy sum of two most energetic leptons in a direction perpendicular to their own thrust axis in R-Φ plane, (b) **sine** of the missing energy direction, (c) invariant mass of two most energetic leptons and (d) energy of the event without the two most energetic leptons ($E_{vis} - E_{\ell_1} - E_{\ell_2}$).

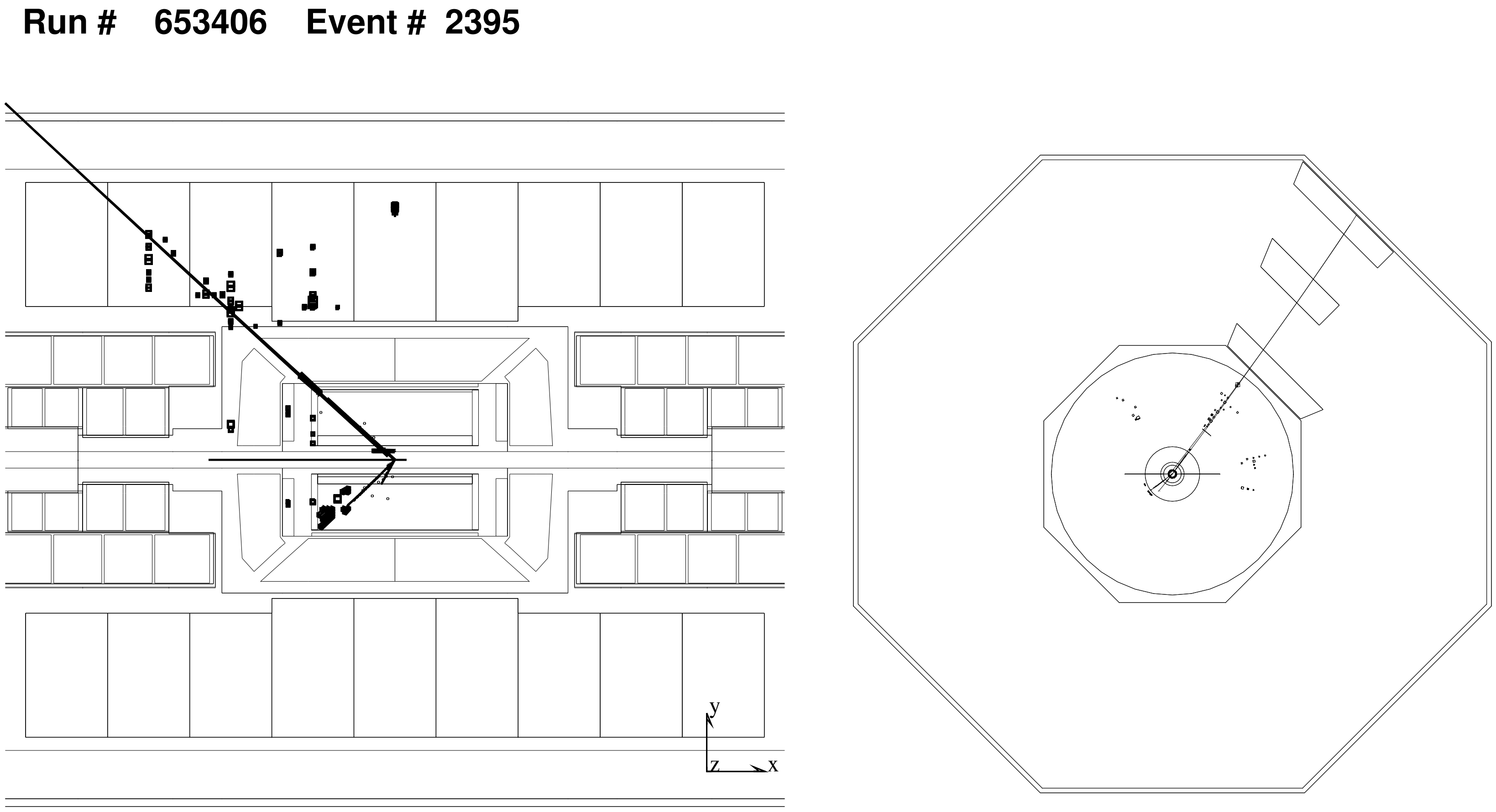

Figure 8.8: The candidate event in the $e^+e^- \rightarrow \tilde{\tau}^+ \tilde{\tau}^-$ channel at $\sqrt{s} = 136$ GeV.

E_{Vis}(GeV) = 24.7	$E_{\perp}/E_{Vis}$ = 0.64	$E_{\|}/E_{Vis}$ = 0.62
# Cluster = 8	# Track = 2	E_{Lum} (GeV) = 0.0
# jet = 2	# μ = 1	# electron = 0
Jet 1	E = 23.9 GeV; θ = 49.2°;	ϕ = 49.8°
Jet 2	E = 3.40 GeV; θ = 53.4°;	ϕ = 147.8°
θ_{acop} = 82.0°	$M_{J_1 J_2}$ (GeV) = 5.63	$\mid T^{best}_{Scint} \mid$ (ns) = −0.3

Table 8.2: Characteristics of the $e^+e^- \rightarrow \tilde{\tau}^+ \tilde{\tau}^-$ candidate event at $\sqrt{s}$ = 136 GeV.

$\sqrt{s}$	$\tilde{e}^+\tilde{e}^-$ Candidates		$\tilde{\mu}^+\tilde{\mu}^-$ Candidates		$\tilde{\tau}^+\tilde{\tau}^-$ Candidates	
(GeV)	Observed	Expected	Observed	Expected	Observed	Expected
130	0	0.04	0	0.01	0	0.36
136	0	0.03	0	0.01	1	0.43
Combined	0	0.07	0	0.02	1	0.79

Table 8.3: Observed and expected number of events from the Standard Model processes ($\sqrt{s}$ = 130 - 136 GeV).

higher efficiencies for $e^+e^- \rightarrow \tilde{\mu}^+ \tilde{\mu}^-$ process, one was unable to exclude any new parameter space (section 9.2). The event that passed the first selection procedure would not pass the second set of selection criteria, because the new jet algorithm fails to reconstruct the second jet in the event (the one with energy 3.4 GeV according to the first method). Thus no event was selected in the improved analyses, whereas from the known SM processes one expects $\sim$ 0.1 event for $e^+e^- \rightarrow \tilde{e}^+ \tilde{e}^-$ and $e^+e^- \rightarrow \tilde{\mu}^+ \tilde{\mu}^-$ channels.

8.3.2 Searches at $\sqrt{s} = 161 - 172$ GeV

The selection criteria as mentioned in section 7.4.2 have been applied to the data sample collected at $\sqrt{s}$ = 161 GeV and 172 GeV. Only two events survived these selection cuts. One event passed the criteria for the $e^+e^- \rightarrow \tilde{\tau}^+ \tilde{\tau}^-$ channel and the other passed the criteria for the $e^+e^- \rightarrow \tilde{\chi}_1^+ \tilde{\chi}_1^-$ process at $\sqrt{s}$ = 172.5 GeV.

The characteristics of the two candidate events are summarised in table 8.4 and figures 8.9 and 8.10 show diagrammatic views of the two events.

The candidate event for the chargino pair process has an electron of 9.45 GeV on one side and a μ of 5.37 GeV on the other side of the detector. It has 1.41 GeV energy deposited in the luminosity monitor.

The candidate event for the process $e^+e^- \rightarrow \tilde{\tau}^+ \tilde{\tau}^-$ has two good tracks, which are the seeds of the two narrow jets of energies 9.11 and 6.0 GeV. Except these two narrow jets, there is no other energy cluster in any part of the detector.

Interpretation of these events on the basis of SM processes: Though the main background (1.03 events expected in 10.1 pb^{-1} data) at $\sqrt{s}$ = 172 GeV is due to the process $e^+e^- \rightarrow W^+W^-$, the candidate event for $e^+e^- \rightarrow \tilde{\chi}_1^+ \tilde{\chi}_1^-$ channel is similar to the SM final state $e^+e^- \rightarrow e^+e^-\tau^+\tau^-$ process and the event $e^+e^- \rightarrow \tilde{\tau}^+\tilde{\tau}^-$ is similar to either $e^+e^- \rightarrow e^+e^-\tau^+\tau^-$ or $e^+e^- \rightarrow e^+e^- q\bar{q}$, whose contribution to SM background is negligible.

The number of observed and expected events (from Standard Model processes) are summarised in table 8.5.

$e^+e^- \rightarrow \tilde{\chi}_1^+ \tilde{\chi}_1^-$ candidate

E_{Vis}(GeV) = 14.81 # Cluster = 2 # Narrow jet = 0	$E_\perp/E_{Vis}$ = 0.46 # Track = 2 # μ = 1	$E_{\|\|}/E_{Vis}$ = -0.80 E_{Lum} (GeV) = 1.41 # electron = 1
e	E = 9.45 GeV; θ = 22.7°;	ϕ = 42.7°
μ	E = 5.37 GeV; θ = 54.0°;	ϕ = 340.3°
θ_{acop} = 117.6° DCA_{min} (mm) = 0.25	$M_{e\mu}$ (GeV) = 5.63 $\|T^{best}_{Scint}\|$ (ns) = −0.7	ETTT (GeV) = 4.09 $\sin\theta_{miss}$ = 0.5

$e^+e^- \rightarrow \tilde{\tau}^+\tilde{\tau}^-$ candidate

E_{Vis}(GeV) = 15.11 # Cluster = 6 # Narrow jet = 2	$E_\perp/E_{Vis}$ = 0.89 # Track = 2 # μ = 0	$E_{\|\|}/E_{Vis}$ = 0.35 E_{Lum} (GeV) = 0.0 # electron = 0
Jet1	E = 9.11 GeV; θ = 122.9°;	ϕ = 327.3°
Jet2	E = 6.00 GeV; θ = 95.01°;	ϕ = 342.3°
θ_{acop} = 165.0° DCA_{min} (mm) = 0.09	$M_{\tau_1\tau_2}$ (GeV) = 4.20 $\|T^{best}_{Scint}\|$ (ns) = 0.58	ETTT (GeV) = 13.5 $\sin\theta_{miss}$ = 0.93

Table 8.4: Characteristics of the candidate events at $\sqrt{s}$ = 172 GeV.

Channel	$\sqrt{s}$ = 161 GeV		$\sqrt{s}$ = 172 GeV		Combined	
	Exp BG	DATA	Exp BG	DATA	Exp BG	DATA
$e^+e^- \rightarrow \tilde{e}^+\tilde{e}^-$	0.46	0	0.57	0	1.03	0
$e^+e^- \rightarrow \tilde{\mu}^+\tilde{\mu}^-$	0.37	0	0.51	0	0.88	0
$e^+e^- \rightarrow \tilde{\chi}_1^+ \tilde{\chi}_1^-$	0.21	0	0.32	1	0.53	1
$e^+e^- \rightarrow \tilde{\tau}^+\tilde{\tau}^-$	0.67	0	0.51	1	1.18	1
All	1.33	0	1.48	2	2.81	2

Table 8.5: Observed and expected number of events from the Standard Model processes ($\sqrt{s}$ = 161 – 172 GeV).

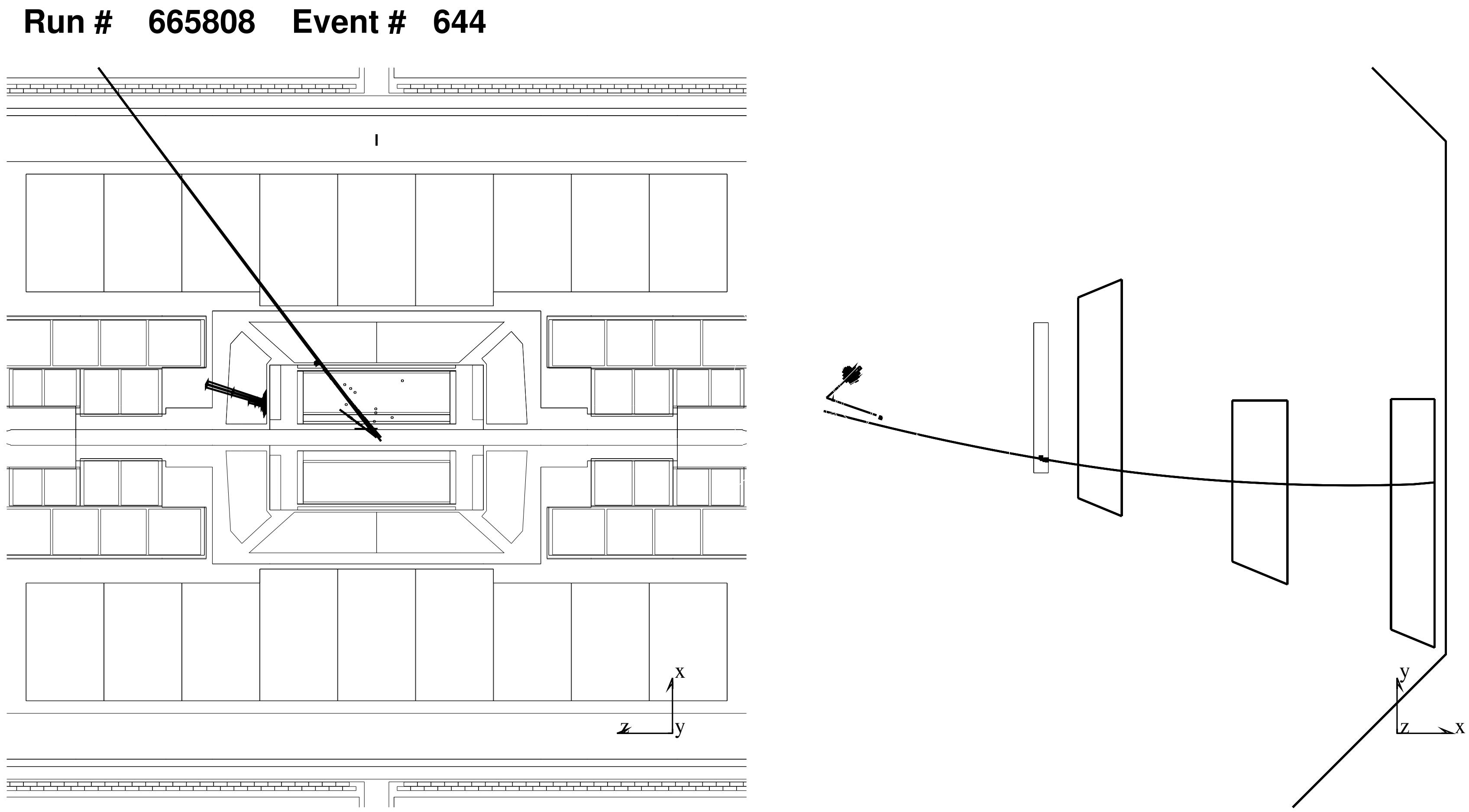

Figure 8.9: The candidate event in the $e^+e^- \to \tilde{\chi}_1^+ \tilde{\chi}_1^-$ channel at $\sqrt{s} = 172$ GeV.

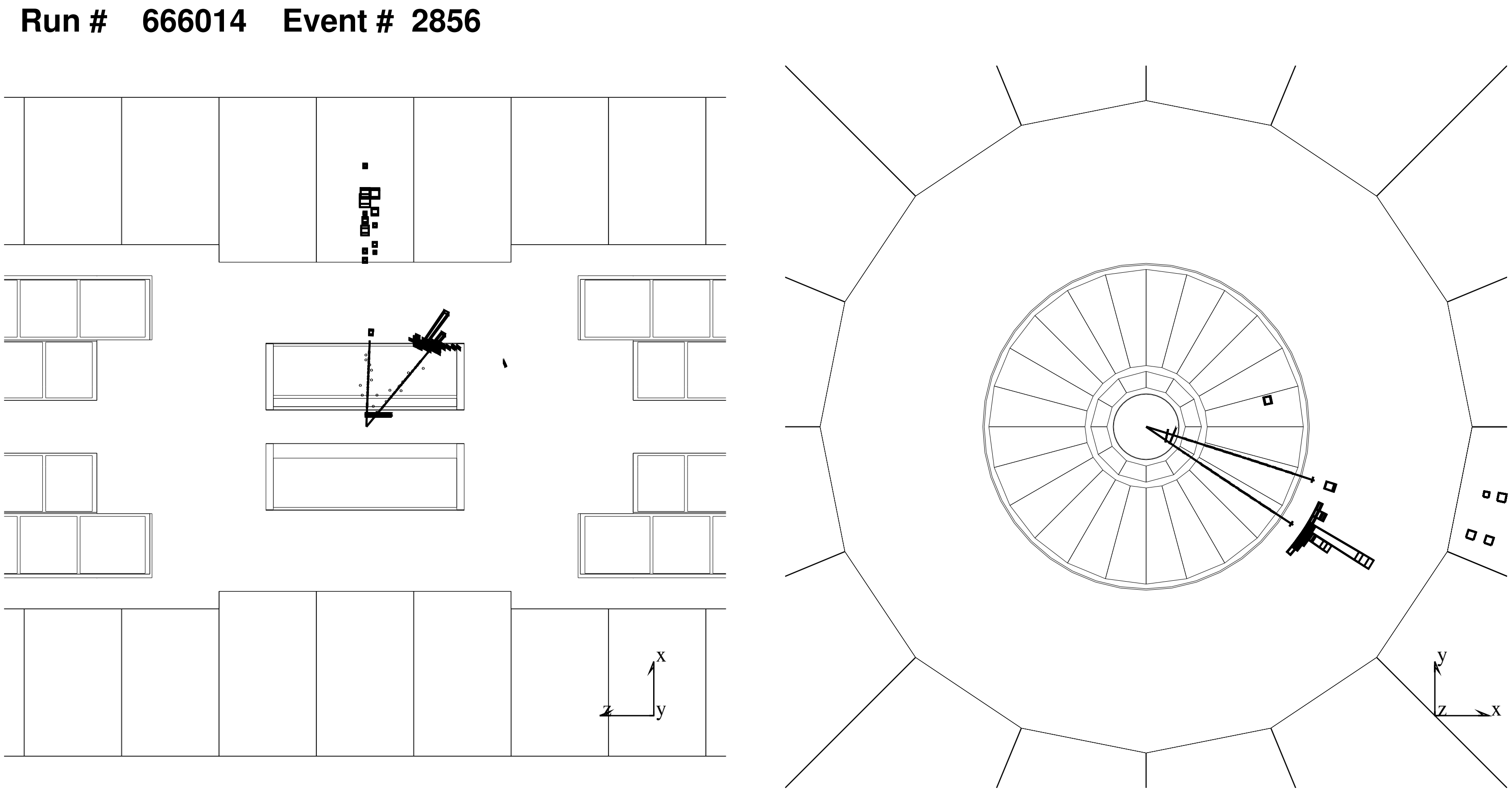

Figure 8.10: The candidate event in the $e^+e^- \rightarrow \tilde{\tau}^+\tilde{\tau}^-$ channel at $\sqrt{s} = 172$ GeV.

8.4 Conclusion

Data collected by the L3 detector during the high energy runs ($\sqrt{s} = 130 - 172$ GeV) of the LEP collider is consistent with expectations from SM processes. There is no excess in the signals due to physics processes beyond the SM.

Chapter 9

Interpretation of Search Results in the MSSM Framework

Since October 1995 to November 1996, the L3 detector have been collected data from e^+e^- interactions of three different LEP runs with centre of mass energies as 130-136 GeV, 161 GeV and 172 GeV. After reconstruction of the events and subjecting the data through selection criteria to search for SUSY particles, no excess of events is seen above the background due to the Standard Model processes (tables 8.3 and 8.5 of section 8.3). This chapter describes the calculation of upper bounds on production cross sections of scalar leptons and exclusion plots in the framework of the Minimal Supersymmetric Standard Model (MSSM).

9.1 Upper Bounds on Production Cross Sections

Upper bounds on production cross section (σ_{UP}) times branching ratios are calculated for individual channels from the number of observed and expected background events using Poisson statistics. This is done by folding in the selection and trigger efficiencies and the integrated luminosity, using the following formula :

$$\sigma_{UP} \times Br = \frac{N}{\varepsilon \int \mathcal{L}\, dt} \tag{9.1}$$

where ε is the product of selection and trigger efficiencies ($\varepsilon = \varepsilon_{selection} \times \varepsilon_{trigger}$).
$\int \mathcal{L}\, dt$ is the integrated luminosity at a given $\sqrt{s}$.
$N \equiv$ Upper limit on the average number of signal events with an expected background of μ_B, such that random repetition of the experiment has a probability ϵ to observe more than $n_\circ$ observed events. N is calculated from the compound Poisson distribution using the formula [94] (details are given in appendix B),

$$\epsilon = 1.0 - \frac{e^{-(\mu_B + N)} \sum_{n=0}^{n_\circ} \frac{(\mu_B + N)^n}{n!}}{e^{-\mu_B} \sum_{n=0}^{n_\circ} \frac{\mu_B^n}{n!}} \tag{9.2}$$

To obtain 95 % CL upper limit, one needs to compute N corresponding to $\epsilon = 0.95$. 95 % CL upper limits on the production cross section times branching ratio have been calculated and these results are also used to make the exclusion plots in SUSY particles mass plane and the MSSM parameter space.

9.2 Exclusion Plots using Data of $\sqrt{s}$ = 130 - 136 GeV

Production cross section limits :

At $\sqrt{s} = 130$ - 136 GeV, the selection efficiencies depend on ΔM which is the difference between the SUSY particle mass (M_{SUSY}) and the mass of the lowest neutralino ($M_{\tilde{\chi}_1^\circ}$) as shown in figure 7.13. Since there is no candidate event ($n_\circ = 0$) at these centre of mass energies for $e^+e^- \to \tilde{e}^+\tilde{e}^-$ and $e^+e^- \to \tilde{\mu}^+\tilde{\mu}^-$ channels (as shown in table 8.3), the 95 % CL upper limit on the cross section of these processes are 0.86 pb and 1.01 pb respectively [1], provided $\Delta M \geq 10$ GeV. For the ΔM values < 10 GeV, the limits go up almost inversely with ΔM because selection efficiencies decrease rapidly with ΔM. For large ΔM, the limit on $e^+e^- \to \tilde{\tau}^+\tilde{\tau}^-$ production cross section limit is about 3.1 pb [2].

Exclusion plots :

The upper limits on production cross sections (σ_{UP}) for slepton searches can be interpreted in the framework of the MSSM by comparing them with the expected production cross sections (σ_{th}) for different sets of parameter values [3]. Upper limit on production cross sections for the processes $e^+e^- \to \tilde{\mu}^+\tilde{\mu}^-$ and $e^+e^- \to \tilde{\tau}^+\tilde{\tau}^-$ cannot add to the exclusion of parameter space, because σ_{UP} of these channels are larger than the largest cross section expected in MSSM for $\tilde{\ell}$-pair production in the unexplored region of mass plane. But for the process $e^+e^- \to \tilde{e}^+\tilde{e}^-$, the combined data from 130 and 136 GeV can exclude

[1] Upper limit of production cross sections for all decay modes (i.e. Br = 1) are calculated using the equation 9.2 with the following informations :

$e^+e^- \to \tilde{e}^+\tilde{e}^-$: $\varepsilon = 71.5\,\%$ from figure 7.13(b), $\int \mathcal{L}\,dt = 4.86\,\mathrm{pb}^{-1}$ from table 8.1 and N = 3 corresponding to $n_\circ = 0$.

$e^+e^- \to \tilde{\mu}^+\tilde{\mu}^-$: $\varepsilon = 60.5\,\%$ from figure 7.13(b) and the other two variables are same as above.

[2] $e^+e^- \to \tilde{\tau}^+\tilde{\tau}^-$: $\varepsilon = 27\,\%$ from figure 7.13(a), $\int \mathcal{L}\,dt = 5.05\,\mathrm{pb}^{-1}$ from table 8.1 and N = 4.2 corresponding to $n_\circ = 1$ and $\mu_B = 0.79$. As mentioned in section 8.3.1, that with the expected higher efficiencies for $e^+e^- \to \tilde{\mu}^+\tilde{\mu}^-$ process, while one was unable to exclude any new parameter space, no elaborate study was done of $\tilde{\tau}^+\tilde{\tau}^-$ channels with the second sets of variables at $\sqrt{s} = 130$ - 136 GeV. In the first results, integrated luminosities collected by L3 detector were taken as $\int \mathcal{L}\,dt$.

[3] $\sigma_{th} > \sigma_{UP}$ implies exclusion of that point of the parameter space.

the parameter space where the theoretical $\tilde{e}^+\tilde{e}^-$ production cross section is more than $\sigma_{UP}(=0.86$ pb) and for a large range of parameter space, the theoretical cross section is more than 0.86 pb for $\tilde{e}_R$ mass upto 58 GeV depending on $M_{\tilde{\chi}_1^\circ}$. As an example, figure 9.1 shows the 95 % CL exclusion regions in the SUSY parameter space of M_2 ($m_{1/2}$ at GUT scale $= \alpha_G\, m_2 \sin^2\theta_W/\alpha_{em} \sim 1.22 \times M_2$) and $m_\circ$ plane and mass plane of $\tilde{e}_R$ and $\tilde{\chi}_1^\circ$ for the other MSSM parameters at $\mu = -200$ GeV, tan $\beta = 1.2$ and A = 0.

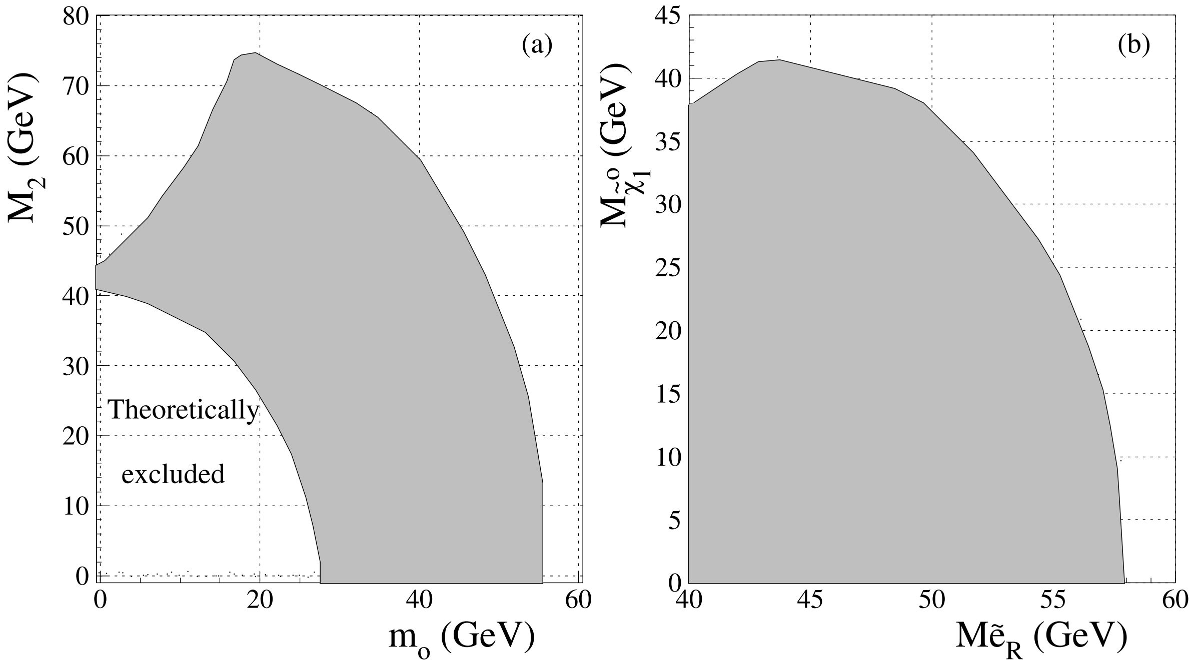

Figure 9.1: 95 % CL exclusion regions in (a) M_2 and $m_\circ$ plane and (b) $\tilde{e}_R$ and $\tilde{\chi}_1^\circ$ mass plane from $\tilde{e}_R$ search for $\mu = -200$ GeV, tan $\beta = 1.2$ GeV, and A = 0. In the theoretically excluded region $m_{\tilde{\nu}} \leq m_{\tilde{\chi}_1^\circ}$.

9.3 Exclusion Plots using Data of $\sqrt{s}$ = 161 – 172 GeV

At $\sqrt{s} = 161 - 172$ GeV, selection efficiencies in different channels are functions of not only ΔM, but also of the SUSY particle mass, M_{SUSY}. These are shown in figures 9.2 (a), (b), (c) and 9.3 (a), (b), (c) for final states $\tilde{e}^+\tilde{e}^-$, $\tilde{\mu}^+\tilde{\mu}^-$ and $\tilde{\tau}^+\tilde{\tau}^-$ at $\sqrt{s} = 161$ GeV and 172 GeV respectively as a function of ΔM for various M_{SUSY}. Typical errors due to limited Monte Carlo sample and systematics are in the range 2-5 % and these are not shown in the figures.

9.3.1 Parametrisation of Selection Efficiencies

In order to extract selection efficiencies for different values of ΔM and M_{SUSY}, it was found that by plotting $\varepsilon/\sqrt{M}$ vs ΔM/M, all points for the final states $\tilde{e}^+\tilde{e}^-$ and $\tilde{\mu}^+\tilde{\mu}^-$ lie on a single curve within error bars as shown in figures 9.2 (d), (e) and 9.3 (d), (e). For the final state $\tilde{\tau}^+\tilde{\tau}^-$ the points lie on a single curve within error bars when plotted as ε/M vs ΔM/M and these are shown in figures 9.2 (f) and 9.3 (f). The errors on the efficiencies shown in the plots are due to limited MC statistics with the systematic uncertainties added in quadrature.

These points are fitted with one of the following combinations of polynomials and exponentials (types of fit and the values of the fitted parameters for different channels at two $\sqrt{s}$ values are shown in table C.1 of appendix C),

$$\frac{\varepsilon}{\sqrt{M}} \left(or\ \frac{\varepsilon}{M}\right) = P_1 \left(\left(\frac{\Delta M}{M}\right) - P_2 \right)^{P_3} \exp\left(P_4 \left(\frac{\Delta M}{M}\right) + P_5 \left(\frac{\Delta M}{M}\right)^2 + \cdots \right) \tag{9.3}$$

$$\frac{\varepsilon}{\sqrt{M}} \left(or\ \frac{\varepsilon}{M}\right) = \exp\left(P_1 \left(\frac{\Delta M}{M}\right) + P_2 \left(\frac{\Delta M}{M}\right)^2 \right) \left(P_3 + P_4 \left(\frac{\Delta M}{M}\right) + P_5 \left(\frac{\Delta M}{M}\right)^2 + \cdots \right) \tag{9.4}$$

In these fits, statistical errors have been taken as uncorrelated and the systematic errors as fully correlated. Acceptable fits have been obtained in all cases with confidence level above a few percent. The results of the fit are used in deriving the efficiencies at various points of mass plane to make the exclusion plots. To take care of the uncertainties, the fitted efficiencies are reduced by one standard deviation in calculating the final limits. The parametrisation of selection efficiencies are also carried out for $e^+e^- \rightarrow \tilde{\chi}_1^+ \tilde{\chi}_1^-$.

9.3.2 Upper Bound on Production Cross Sections at $\sqrt{s}$ = 161 – 172 GeV

Upper bounds on production cross section at 95 % CL are calculated as described in sections 9.1 and 9.2. The following quantities are used for this calculation :

(i) selection efficiencies are calculated from the parametrisation as described above,

(ii) Observed events ($n_\circ$) in different channels are taken from table 8.5 and

(iii) Integrated luminosities are taken from table 8.1.

Figures 9.4(a)-(c) show contour plots corresponding to the 95 % CL upper bounds of the cross section (σ_{UP}) for slepton pair production at $\sqrt{s}$ = 161 GeV in the mass plane of $\tilde{\ell}$ and $\tilde{\chi}_1^\circ$. All the decay modes of $\tilde{\ell}$ have been taken into account to calculate the selection efficiencies and consequently for the exclusion plots. The results from the two centre of mass energies ($\sqrt{s}$) are combined to get better limits on production cross section

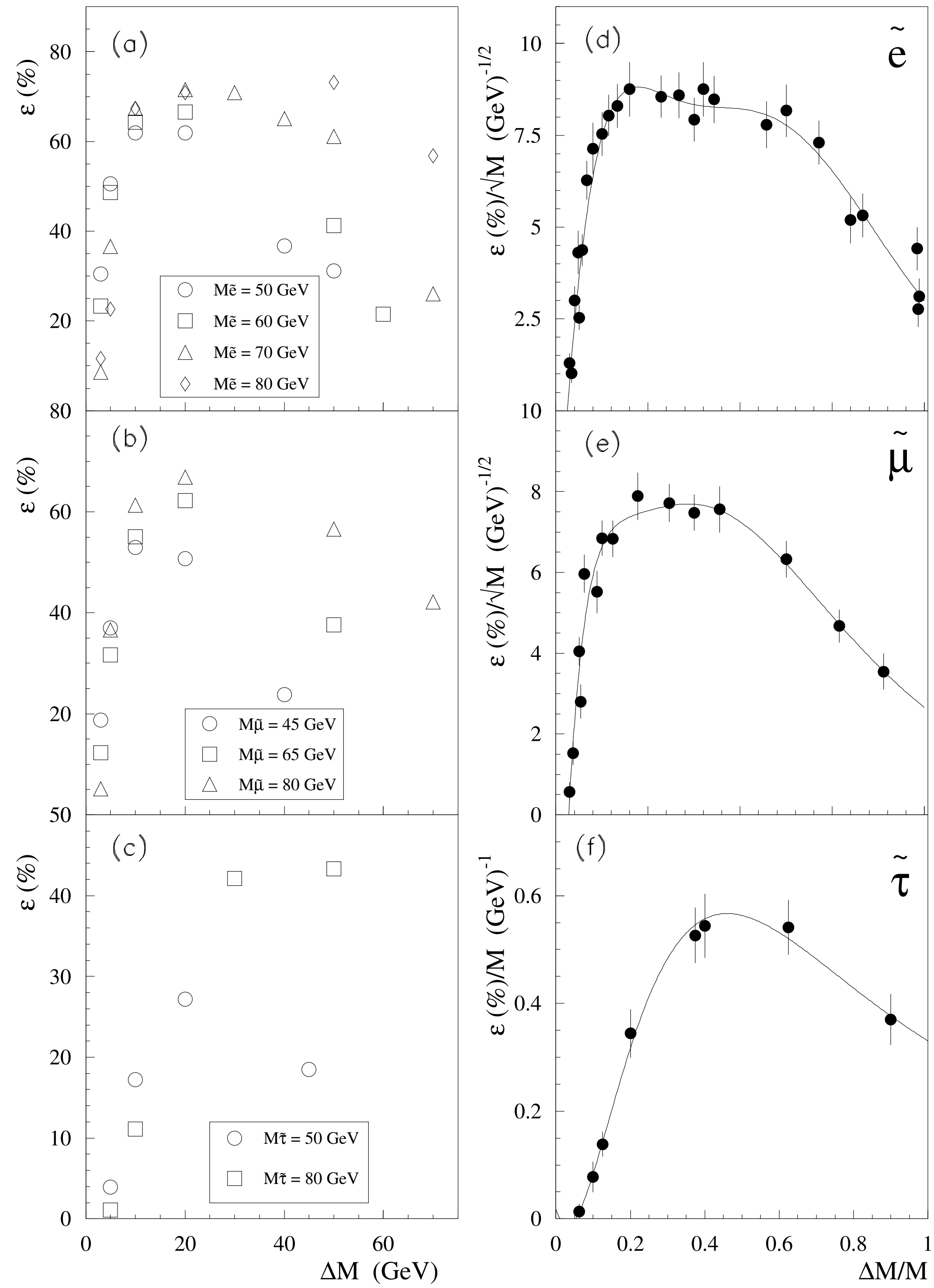

Figure 9.2: The combined efficiencies of (a) $\tilde{e}^+\tilde{e}^-$, (b) $\tilde{\mu}^+\tilde{\mu}^-$ and (c) $\tilde{\tau}^+\tilde{\tau}^-$ processes as a function of ΔM for different values of M_{SUSY} at $\sqrt{s} = 161$ GeV. Universal parametrisation, as a function of ΔM and M_{SUSY} can be obtained by using $\varepsilon/\sqrt{M}$ for (d) $\tilde{e}^+\tilde{e}^-$ and (e) $\tilde{\mu}^+\tilde{\mu}^-$ and ε/M for (f) $\tilde{\tau}^+\tilde{\tau}^-$. All points in the figures (d–f) can be fitted by a smooth function of $\Delta M/M$ as explained in text.

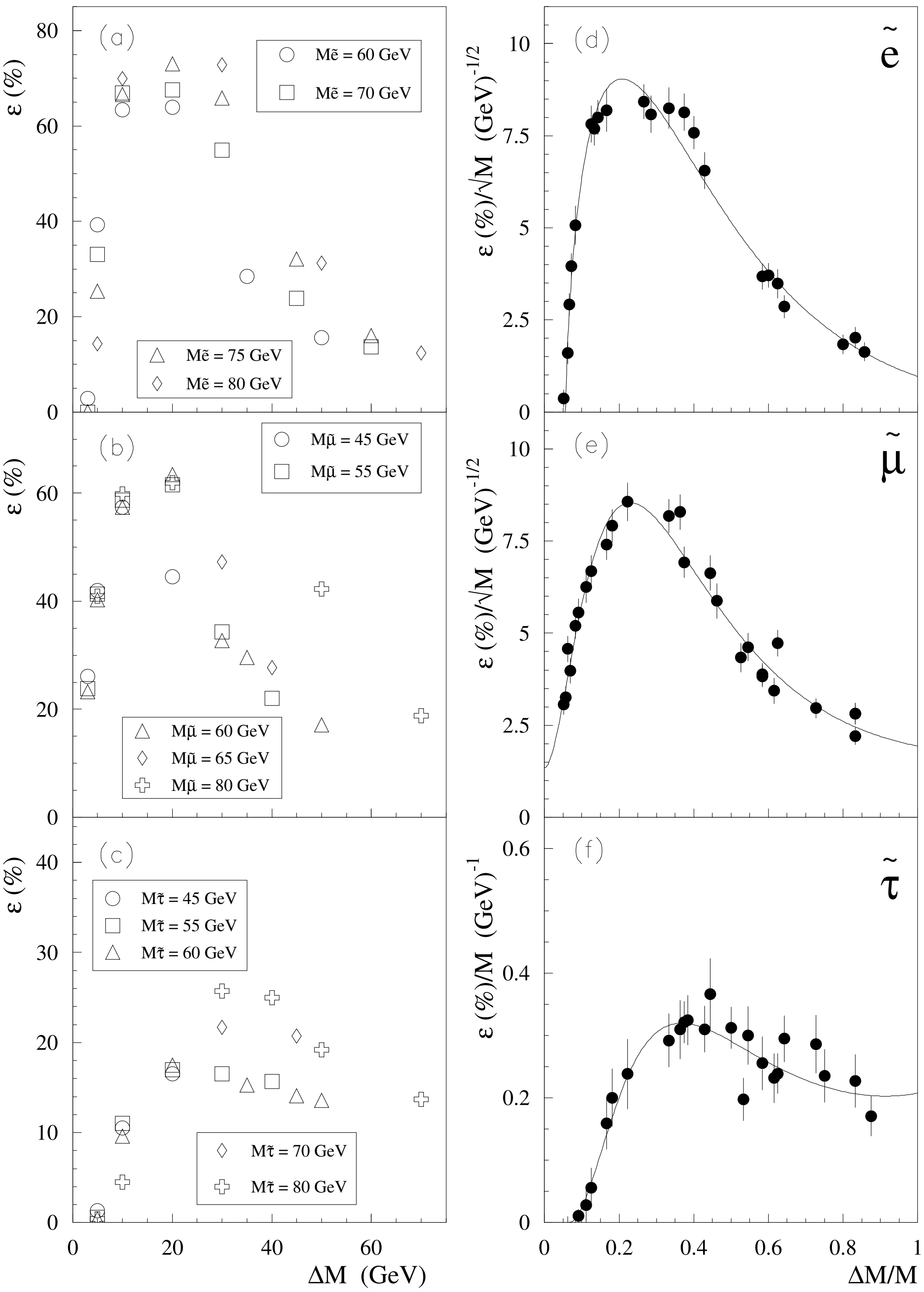

Figure 9.3: The combined efficiencies of (a) $\tilde{e}^+\tilde{e}^-$, (b) $\tilde{\mu}^+\tilde{\mu}^-$ and (c) $\tilde{\tau}^+\tilde{\tau}^-$ processes as a function of ΔM for different values of M_{SUSY} at $\sqrt{s} = 172$ GeV. Universal parametrisation, as a function of ΔM and M_{SUSY} can be obtained by using $\varepsilon/\sqrt{M}$ for (d) $\tilde{e}^+\tilde{e}^-$ and (e) $\tilde{\mu}^+\tilde{\mu}^-$ and ε/M for (f) $\tilde{\tau}^+\tilde{\tau}^-$. All points in the figures (d–f) can be fitted by a smooth function of $\Delta M/M$ as explained in text.

and better exclusion plots. Two integrated luminosities are combined with a weighting factor obtained from the cross section ratios for slepton pair production at these energies (details are given in appendix D). Selectron mass ($M_{\tilde{e}_R}$) is excluded almost over the entire kinematic limit except for very low ΔM region for a production cross section at $\sqrt{s}$ = 161 GeV greater than 2 pb. One finds almost similar limits for $M_{\tilde{\mu}_R}$. $M_{\tilde{\tau}_1}$ is excluded for production cross section (at $\sqrt{s}$ = 161 GeV) larger than 5 pb for ΔM greater than 8 GeV.

Figure 9.4(d) shows contour plots corresponding to the 95 % CL upper bound of cross section times Br^2 ($\tilde{\chi}_1^{\pm} \rightarrow e/\mu$) of the process $e^+e^- \rightarrow \tilde{\chi}_1^+ \tilde{\chi}_1^-$ as a function of the masses of the chargino and neutralino at $\sqrt{s}$ = 161 GeV (combined with the $\sqrt{s}$ = 172 GeV data by adding the luminosities linearly).

9.3.3 Exclusion of Parameter Space and SUSY Particle Mass Plane

The excluded cross sections for the slepton searches can be interpreted in the framework of the MSSM by comparing them with the expected cross sections at different sets of parameter values. The excluded cross section for the process $e^+e^- \rightarrow \tilde{\tau}^+ \tilde{\tau}^-$ is larger than the cross section provided by the MSSM model in the unexplored region. So, it does not provide any additional exclusion of the parameter space than the earlier one from LEP 1. But the searches for $\tilde{e}^+\tilde{e}^-$ and $\tilde{\mu}^+\tilde{\mu}^-$ separately exclude some new parameter space. Using the combined data at $\sqrt{s}$ = 161 GeV and 172 GeV, one can probe $M_{\tilde{e}_R}$ upto 74 GeV and $M_{\tilde{\mu}_R}$ mass upto 64 GeV for a limited mass range of $M_{\tilde{\chi}_1^\circ}$ ($M_{\tilde{\chi}_1^\circ}$ $\approx$ 30-40 GeV). $M_{\tilde{e}_R}$ is completely excluded upto 69 GeV. Figure 9.5 shows the 95 % CL exclusion region in the mass plane of $M_{\tilde{\ell}_R} - M_{\tilde{\chi}_1^\circ}$ and $M_2 - m_\circ$ from $\tilde{e}_R$ and $\tilde{\mu}_R$ searches corresponding to $\tan\beta$ = 1.2, μ = -200 GeV and A = 0. Exclusion plots in the mass plane of $M_{\tilde{e}_R}$ and $M_{\tilde{\chi}_1^\circ}$ are also shown in figure 9.6 for various sets of μ and $tan\,\beta$. Same plots are also shown in figure 9.7 for the plane of M_2 and $m_\circ$.

9.4 Summary

In the search of scalar leptons, $M_{\tilde{e}_R}$ are excluded upto 69 GeV for almost all the parameter space, except in a very low ΔM region. It can be probed upto 74 GeV for the $M_{\tilde{\chi}_1^\circ}$ $\approx$ 35 GeV. There is also an improvement in the exclusion region of the mass plane of $M_{\tilde{\mu}_R}$ and $M_{\tilde{\chi}_1^\circ}$.

Searches for chargino and neutralino production are used for the combined limits of SUSY parameter space from the L3 analyses using the search results of L3 collaboration in other decay modes.

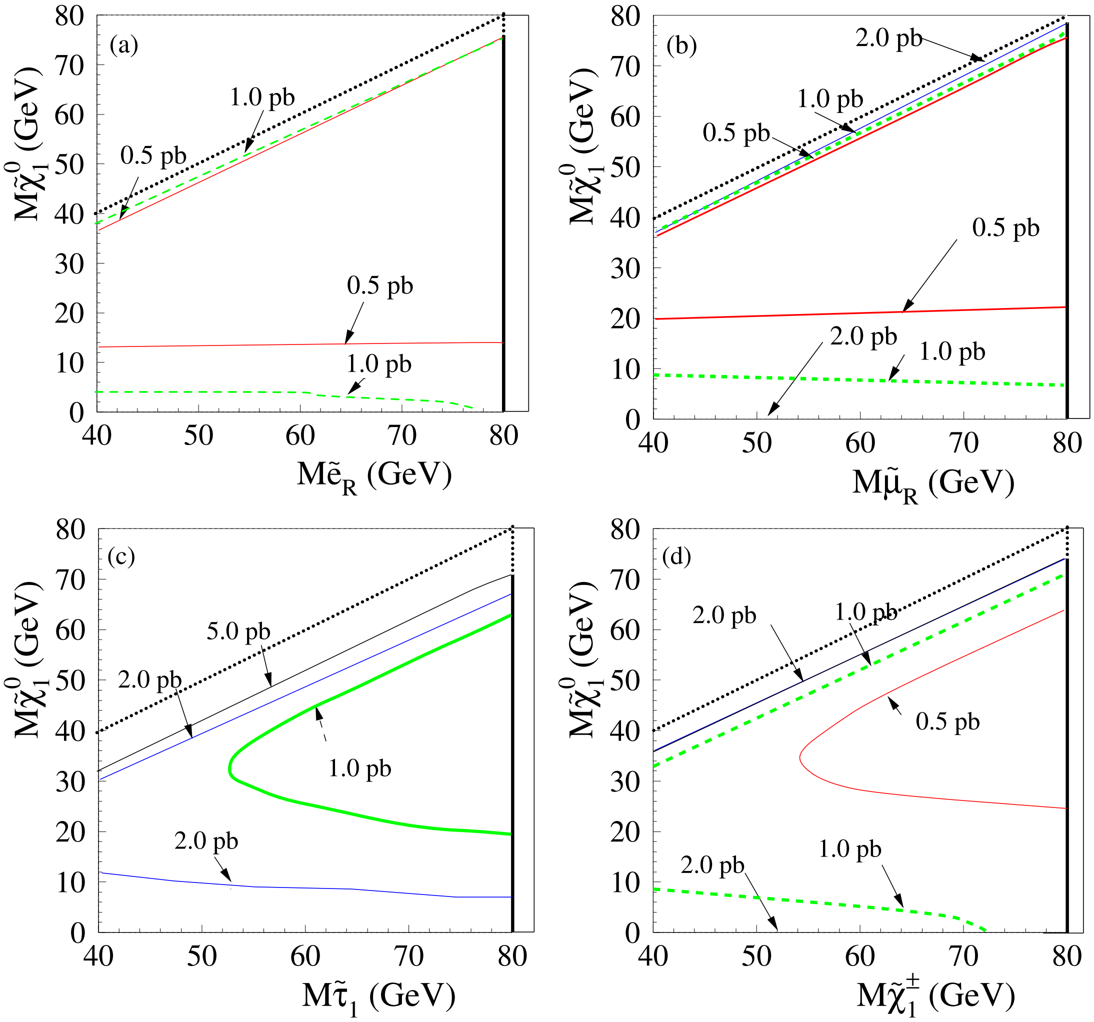

Figure 9.4: Contours corresponding to 95 % upper bounds on cross sections (at $\sqrt{s} = 161$ GeV) for the processes (a) $e^+e^- \to \tilde{e}^+\tilde{e}^-$, (b) $e^+e^- \to \tilde{\mu}^+\tilde{\mu}^-$ and (c) $e^+e^- \to \tilde{\tau}^+\tilde{\tau}^-$ as functions of slepton and neutralino masses. (d) Contours corresponding to 95 % upper bounds on cross section times branching ratio for the process $e^+e^- \to \tilde{\chi}_1^+\tilde{\chi}_1^-$ at $\sqrt{s} = 161$ GeV as a function of the chargino, neutralino masses.

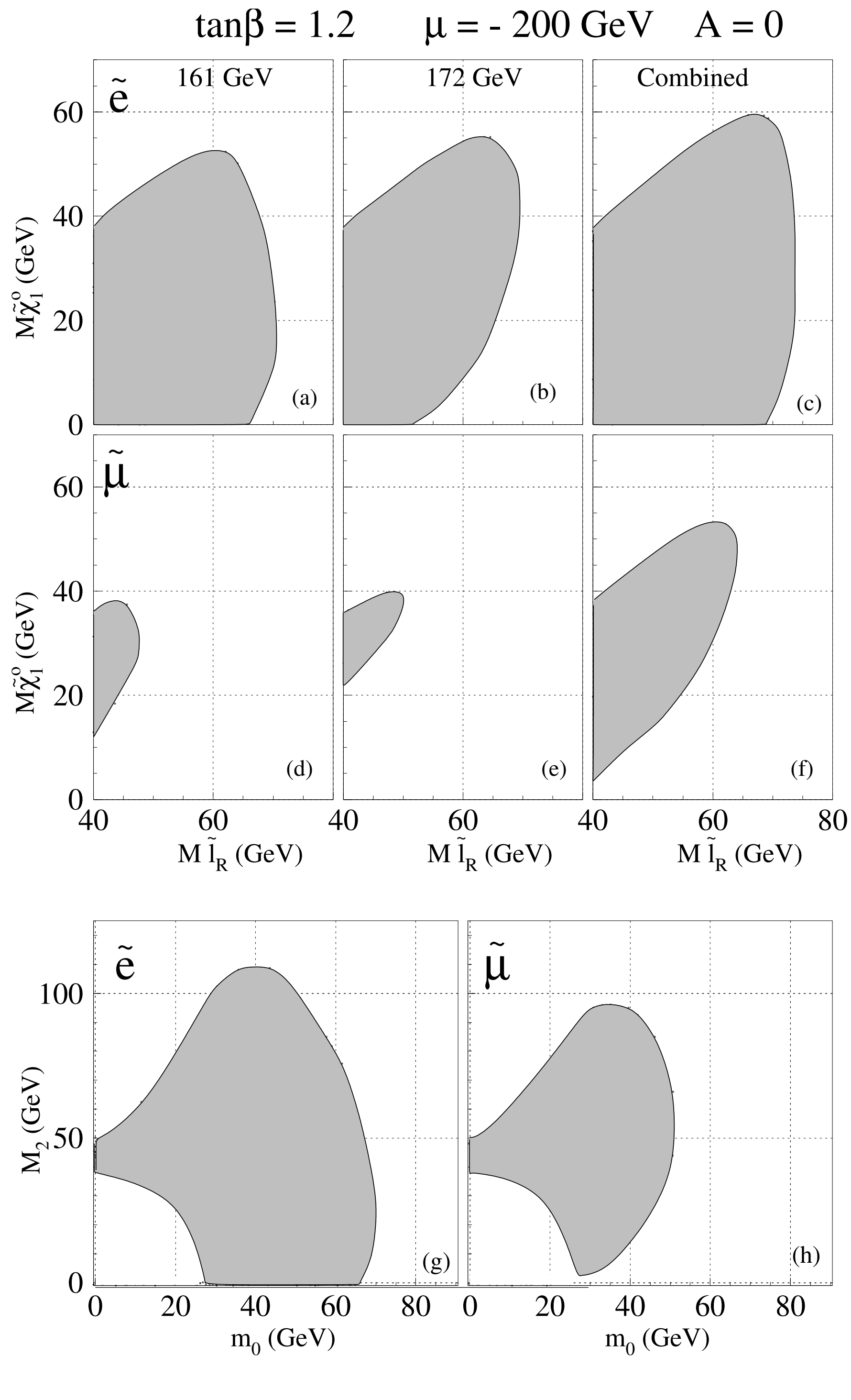

Figure 9.5: 95% CL exclusion regions in $M_{\tilde{\ell}_R} - M_{\tilde{\chi}_1^\circ}$ plane using the data at $\sqrt{s}$ 161 GeV, 172 GeV and combined data for the processes $e^+e^- \rightarrow \tilde{e}^+ \tilde{e}^-$ are shown in plots (a)–(c). Similar plots for the process $e^+e^- \rightarrow \tilde{\mu}^+ \tilde{\mu}^-$ are shown in (d)–(f). Exclusion plots from the combined analyses in the $M_2 - m_\circ$ plane from $\tilde{e}^+\tilde{e}^-$ and $\tilde{\mu}^+\tilde{\mu}^-$ searches are shown in (g) and (h) respectively.

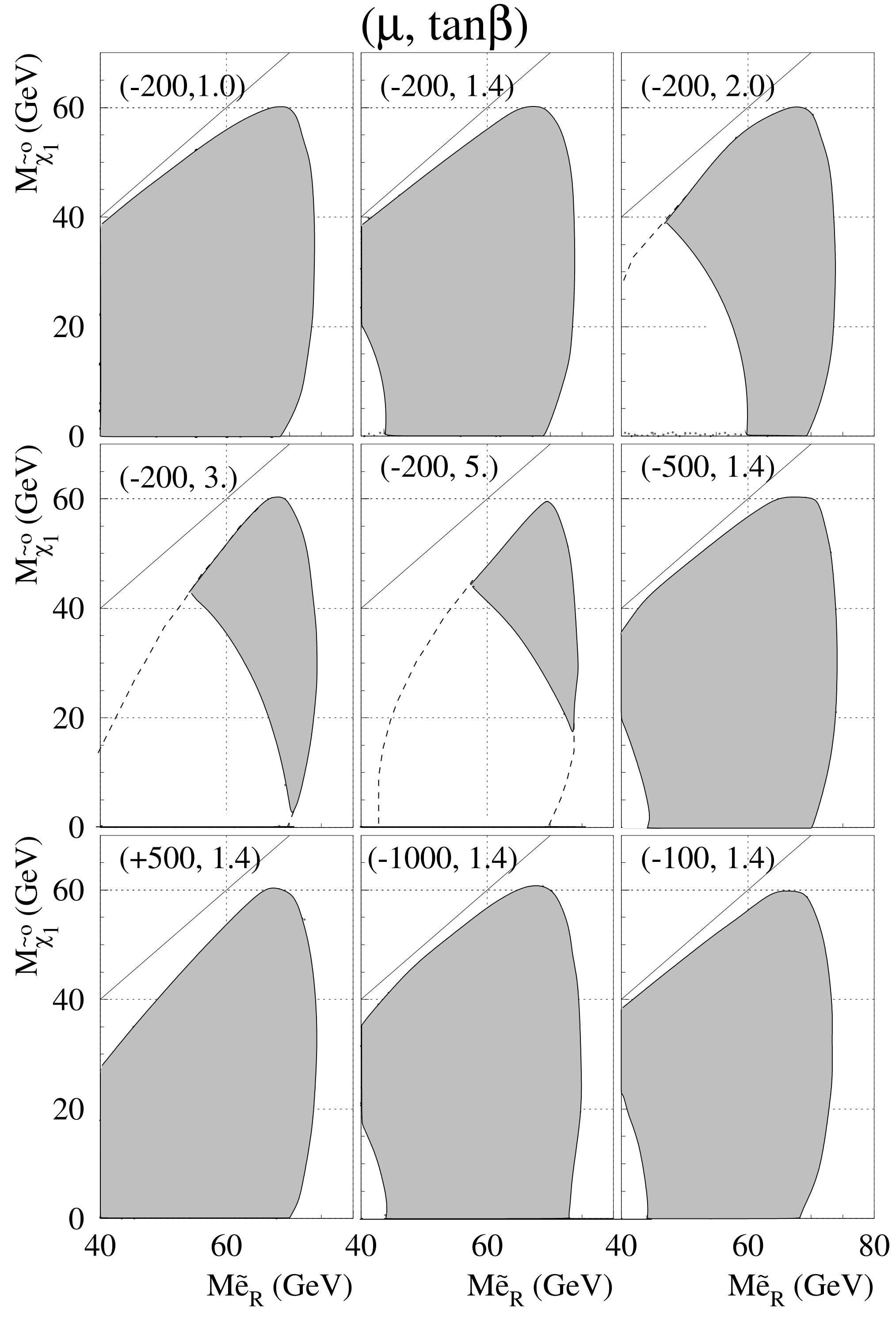

Figure 9.6: 95% CL exclusion region in $M_{\tilde{\ell}_R} - M_{\tilde{\chi}^\circ_1}$ plane using the combined data for the processes $e^+e^- \rightarrow \tilde{e}^+\tilde{e}^-$. Numbers in the plots are the value of μ and $tan\,\beta$. Common trilinear coupling $A = 0$. Area inside the dashed line are theoretically disfavoured because $m_{\tilde{\nu}} < m_{\tilde{\chi}^\circ_1}$ in these regions.

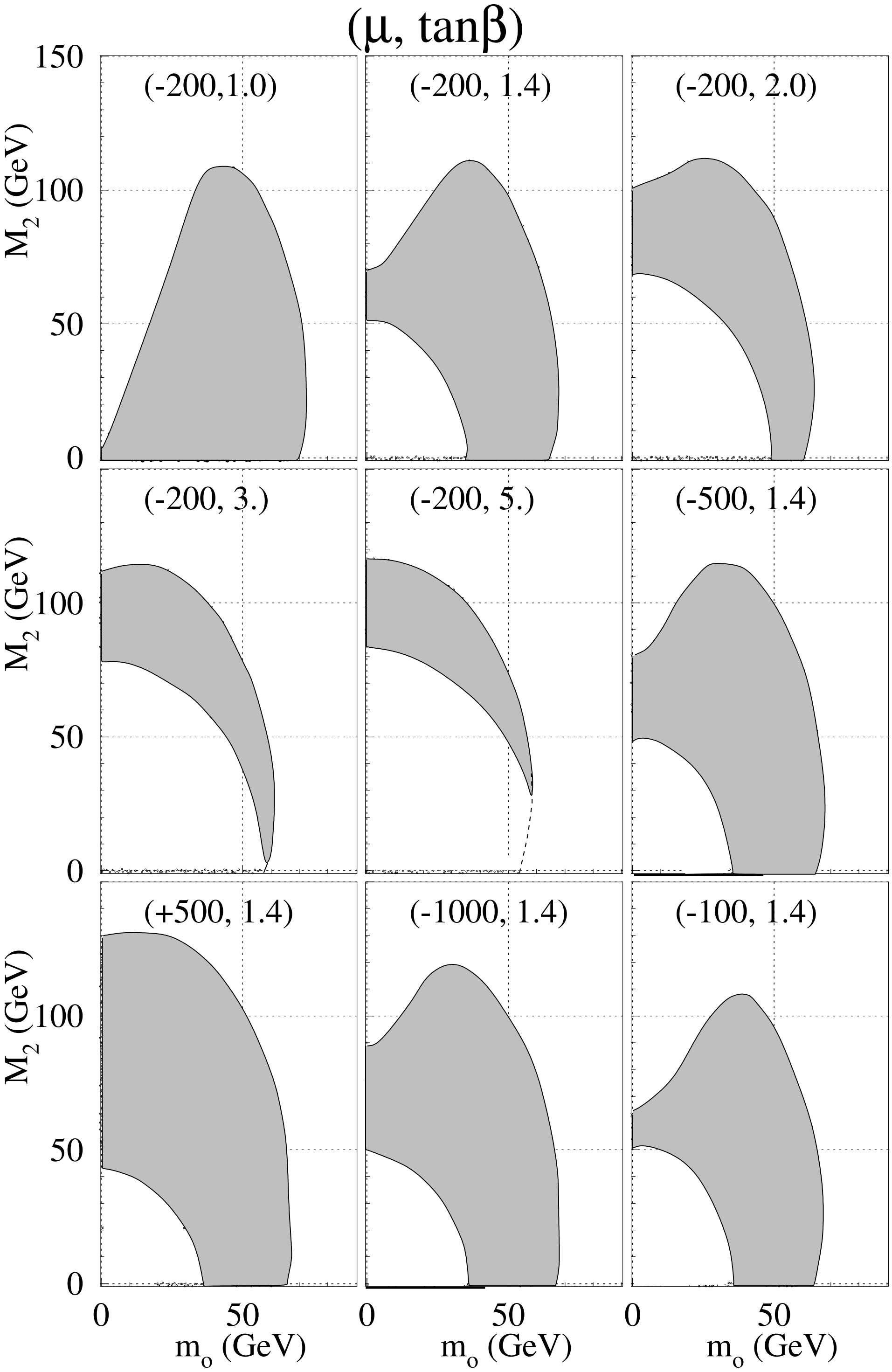

Figure 9.7: 95% CL exclusion region in $M_2 - m_\circ$ plane using the combined data for the processes $e^+e^- \rightarrow \tilde{e}^+ \tilde{e}^-$. Numbers in the plots are the value of μ and $tan\,\beta$. Common trilinear coupling $A = 0$. Blanc space in lower mass regions are theoretically disfavoured because $m_{\tilde{\nu}} < m_{\tilde{\chi}^\circ_1}$.

Chapter 10

Summary and Outlook

Events with acoplanar lepton pairs and large missing energy and large transverse momentum imbalance has been looked for in e^+e^- interactions at the center of mass energies ($\sqrt{s}$) ranging from 130 to 172 GeV. Such events are signatures of slepton pair ($\tilde{\ell}^+\tilde{\ell}^-$) production or chargino pair ($\tilde{\chi}_1^+\tilde{\chi}_1^-$) production where both the charginos decay leptonically or neutralino pair ($\tilde{\chi}_1^\circ\tilde{\chi}_2^\circ$) production where the second lightest neutralino ($\tilde{\chi}_2^\circ$) decays to a lepton pair and lightest neutralino ($\tilde{\chi}_1^\circ$). Searches for these channels have been conducted in the framework of Grand Unified Theory motivated Minimal Supersymmetric Standard Model. The good data collected by the L3 detector corresponding to integrated luminosity $\sim$ 25 pb^{-1} from the high energy LEP runs (delivered luminosity $\sim$ 31 pb^{-1}) in the years 1995 and 1996 at the center of mass energies ($\sqrt{s}$) ranging from 130 to 172 GeV have been used for these analyses.

Optimisation of the search technique has resulted in a very high efficiency for selecting slepton pairs events ($\sim$70 % for $e^+e^- \to \tilde{e}^+\tilde{e}^-$ processes) with a very low residual SM backgrounds (suppressed by five orders of magnitude). Results of these searches very much depend on the Monte Carlo simulation. By comparing kinematic variables from data and the SM Monte Carlo processes one can conclude that these variables are well measured and the SM physics processes as well as the detector effects are well understood.

No candidate for $\tilde{e}$-pair or $\tilde{\mu}$-pair events has been observed at the $\sqrt{s}$ ranging from 130 to 172 GeV. One candidate for $\tilde{\tau}$-pair event was observed at $\sqrt{s}$ = 136 GeV and two candidates at $\sqrt{s}$ = 172 GeV, one for $\tilde{\tau}$-pair event and another for $\tilde{\chi}_1^+\tilde{\chi}_1^-$ event. The observed number of candidate events is compatible with the expectation from the standard model processes. So one can conclude that **no** new physics beyond the SM has been found in these searches of acoplanar leptonic events.

From the search results, one may obtain upper bounds on the production cross sections for the three types of sleptons and also on the production cross section times the branching ratio ($\tilde{\chi}_1^\pm \to e/\mu$) for the process $e^+e^- \to \tilde{\chi}_1^+\tilde{\chi}_1^-$.

The excluded cross sections for the slepton searches can be interpreted in the framework of the MSSM by comparing them with the expected cross sections for different sets of parameter values. Only using the data from $\sqrt{s}$ = 130-136 GeV one can exclude a new region of $M_{\tilde{e}_R}$-$M_{\tilde{\chi}_1^0}$ plane. Search for ẽ-pair and $\tilde{\mu}$-pair at $\sqrt{s} = 161-172$ GeV separately exclude part of the mass plane as well as SUSY parameter space, but the exclusion cross section for the process $e^+e^- \rightarrow \tilde{\tau}^+ \tilde{\tau}^-$ could not improve the LEP 1 exclusion plots.

With these results one can probe $\tilde{\ell}$ masses up to 74 GeV and 64 GeV for ẽ and $\tilde{\mu}$ respectively. The mass of $\tilde{e}_R$ is excluded upto 69 GeV for all values of $|\mu| <$ 200 GeV.

CERN-SL division is planing to deliver high energy data equivalent to luminosity $\approx$ 500 pb^{-1} to each of the four detectors in the next four years including the year 1997, where LEP is running at $\sqrt{s}$ = 183 GeV. In the next years it will run at $\sqrt{s}$ = 192 GeV and higher energies. Integrated data from the four experiments will be able to probe the SUSY particles upto the kinematic limit of production.

Appendix A

Production and Decay Formulae of Selectron

Mass eignestates of selectron are defined as :

$$\tilde{\mathrm{e}}_1 = \tilde{\mathrm{e}}_L \, cos\phi + \tilde{\mathrm{e}}_R \, sin\phi$$
$$\tilde{\mathrm{e}}_2 = \tilde{\mathrm{e}}_L \, sin\phi + \tilde{\mathrm{e}}_R \, cos\phi$$

A.1 $e^+ + e^- \longrightarrow \tilde{\mathrm{e}}_i^+ + \tilde{\mathrm{e}}_j^-$

Differential cross-sections for different processes are described below :

(i) $e^+ + e^- \rightarrow \tilde{\mathrm{e}}_1^+ + \tilde{\mathrm{e}}_1^-$

$$\begin{aligned}
\frac{d\sigma}{dt} &= \left.\frac{d\sigma}{dt}\right|_\gamma + \left.\frac{d\sigma}{dt}\right|_Z + \left.\frac{d\sigma}{dt}\right|_{\tilde{\chi}^\circ} + \left.\frac{d\sigma}{dt}\right|_{\gamma Z} + \left.\frac{d\sigma}{dt}\right|_{\gamma \tilde{\chi}^\circ} + \left.\frac{d\sigma}{dt}\right|_{Z \tilde{\chi}^\circ} \\
\left.\frac{d\sigma}{dt}\right|_\gamma &= \frac{e^4}{8\,\pi\, s^4}\left(u.t - \tilde{m}_1^4\right), \\
\left.\frac{d\sigma}{dt}\right|_Z &= \frac{1}{16\,\pi\, s^2}\frac{g^4}{\cos^4\theta_{\mathrm{W}}}\left(u.t - \tilde{m}_1^4\right) \\
&\quad |\, D_Z(s)\,|^2 \left(L_e\, cos^2\phi + R_e\, sin^2\phi\right)^2 \left((L_e)^2 + (R_e)^2\right) \\
\left.\frac{d\sigma}{dt}\right|_{\tilde{\chi}^\circ} &= \frac{g^4}{64\,\pi\, s^2}\left\{\left(u.t - \tilde{m}_1^4\right)\left(A cos^4\phi + B sin^4\phi\right) + C cos^2\phi sin^2\phi\right\} \\
\left.\frac{d\sigma}{dt}\right|_{\gamma Z} &= \frac{1}{8\,\pi\, s^3}\frac{e^2 g^2}{cos^2\theta_{\mathrm{W}}}\left(u.t - \tilde{m}_1^4\right) \\
&\quad \left(L_e\, cos^2\phi + R_e\, sin^2\phi\right)(L_e + R_e)\, Re\,(D_z(s))
\end{aligned} \tag{A.1}$$

$$\left.\frac{d\sigma}{dt}\right|_{\gamma\tilde{\chi}^\circ} = \frac{e^2 g^2}{16\,\pi\, s^3}\left(u.t - \tilde{m}_1^4\right)\sum_{k=1}^{4} D_k(t)\left(cos^2\phi \mid f_{ek}^L \mid^2 + in^2\phi \mid f_{ek}^R \mid^2\right)$$

$$\left.\frac{d\sigma}{dt}\right|_{Z\tilde{\chi}^\circ} = \frac{1}{16\,\pi\, s^2}\frac{g^4}{cos^2\theta_{\mathrm{W}}}\left(u.t - \tilde{m}_1^4\right)\left(L_e\, cos^2\phi + R_e\, sin^2\phi\right) Re\left(D_Z(s)\right)$$
$$\sum_{k=1}^{4} D_k(t)\left(L_e \mid f_{ek}^L \mid^2\ cos^2\phi + R_e \mid f_{ek}^R \mid^2\ sin^2\phi\right)$$

where,

$$A = \left(\sum_{k=1}^{4} D_k(t) \mid f_{ek}^L \mid^2\right)^2$$
$$B = \left(\sum_{k=1}^{4} D_k(t) \mid f_{ek}^R \mid^2\right)^2$$
$$C = 2\,s \sum_{k,\,l=1}^{4} m_k\, m_l\, \eta_k\, \eta_l\, D_k(t)\, D_l(t)\, f_{ek}^R\, f_{ek}^L\, f_{el}^R\, f_{el}^L$$

(ii) $e^+ + e^- \longrightarrow \tilde{e}_2^+ + \tilde{e}_2^-$

The cross section for $e^+ + e^- \longrightarrow \tilde{e}_2^+ + \tilde{e}_2^-$ is obtained by substituting $cos\phi \leftrightarrow sin\phi$ and $\tilde{m}_1 \rightarrow \tilde{m}_2$.

(iii) $e^+ + e^- \longrightarrow \tilde{e}_1^+ + \tilde{e}_2^-$

$$\left.\frac{d\sigma}{dt}\right|_{\gamma} = \left.\frac{d\sigma}{dt}\right|_{\gamma Z} = \left.\frac{d\sigma}{dt}\right|_{\gamma\tilde{\chi}^\circ} = 0,$$

$$\left.\frac{d\sigma}{dt}\right|_{Z} = \frac{1}{16\,\pi\, s^2}\frac{g^4}{\cos^4\theta_{\mathrm{W}}} sin^2\phi\, cos^2\phi$$
$$\mid D_Z(s)\mid^2 (L_e - R_e)^2\left((L_e)^2 + (R_e)^2\right)\left(u.t - \tilde{m}_1^2\tilde{m}_2^2\right)$$
$$\left.\frac{d\sigma}{dt}\right|_{\tilde{\chi}^\circ} = \frac{g^4}{64\,\pi\, s^2}\left\{F(sin^2\phi + cos^2\phi) + G(cos^4\phi + sin^4\phi)\right\}$$
$$\left.\frac{d\sigma}{dt}\right|_{Z\tilde{\chi}^\circ} = \frac{1}{16\,\pi\, s^2}\frac{g^4}{cos^2\theta_{\mathrm{W}}}\left(u.t - \tilde{m}_1^2\tilde{m}_2^2\right)\ sin^2\phi\, cos^2\phi \tag{A.2}$$
$$(L_e - R_e) Re\left(D_Z(s)\right)\sum_{k=1}^{4} D_k(t)\left(L_e \mid f_{ek}^L \mid^2 - R_e \mid f_{ek}^R \mid^2\right)$$

where

$$F = \left(u.t - \tilde{m}_1^2\tilde{m}_2^2\right)\left[\left(\sum_{k=1}^{4} D_k(t) \mid f_{ek}^L \mid^2\right)^2 + \left(\sum_{k=1}^{4} D_k(t) \mid f_{ek}^R \mid^2\right)^2\right]$$
$$G = s \sum_{k,\,l=1}^{4} m_k\, m_l\, \eta_k\, \eta_l\, D_k(t)\, D_l(t)\, f_{ek}^R\, f_{ek}^L\, f_{el}^R\, f_{el}^L$$

The cross section for $e^+ e^- \to \tilde{e}_2^+ \tilde{e}_1^-$ is given by the same formula (A.2). In the formulae above, m_i, denotes the mass of the selectron $\tilde{e}_i$ (i = 1,2); $s,\ t,\ u$ are the usual Mandelsum variables, and $D_Z(s) = ((s - m_Z^2) + i\, m_Z \Gamma_Z)^{-1}$, $D_k(t) = (t - m_k^2)^{-1}$, m_k being the (positive value) mass of the neutralino $\tilde{\chi}_k^\circ$ (k = 1,..,4). Furthermore, $e = g\, sin\, \theta_W$, $L_e = -1/2 + \sin^2\theta_W$, $R_e = \sin^2\theta_W$, and $f_{ek}^L = \sqrt{2}\left[sec\,\theta_W(1/2 - \sin^2\theta_W)\,N_{k2} + \sin^2\theta_W\, N_{k1}\right]$, $f_{ek}^R = \sqrt{2}\sin^2\theta_W(tan\theta_W\, N_{k2} - N_{k1})$. Here N_{kl} being the 4×4 unitary matrix which diagonalizes the gauge fermion-higgsino mass matrix (in the $\tilde{\gamma}$, $\tilde{Z}$, $\tilde{H}_1^\circ$, $\tilde{H}_2^\circ$) and η_k, $\eta_l = \pm 1$ is the sign of the corresponding eigenvalue of the mass matrix.

A.2 $\tilde{e}_i^\pm \to e^\pm + \tilde{\chi}_k^\circ$

The width for the decay $\tilde{e}_1^\pm \to e^\pm + \tilde{\chi}_k^\circ$ is given by

$$\Gamma(\tilde{e}_1^\pm \to e^\pm + \tilde{\chi}_k^\circ) = \frac{g^2}{16\,\pi\,\tilde{m}_1^3}\left(\tilde{m}_1^2 - \tilde{m}_k^2\right)^2\left[|\,f_{ek}^L\,|^2\ cos^2\phi + |\,f_{ek}^R\,|^2\ sin^2\phi\right] \tag{A.3}$$

The width for $\tilde{e}_2^\pm \to e^\pm + \tilde{\chi}_k^\circ$ is obtained from equation (A.3) by replacing $cos\phi \leftrightarrow sin\phi$ and $\tilde{m}_1 \to \tilde{m}_2$.

The angular distribution of the decay electron with respect to the beam axis is calculated to be

$$\frac{d\sigma}{d\cos\theta_e} = \frac{1}{4\,\pi}\int d\,cos\theta_e\, d\phi_e \frac{d\,\sigma}{d\cos\theta_{\tilde{e}}}\frac{\tilde{m}_1^2}{(E_1 - q cos\,\bar{\theta})^2} \tag{A.4}$$

with $\bar{\theta} = sin\,\theta_{\tilde{e}}\ sin\,\theta_e\ cos\,\phi_e + cos\,\theta_{\tilde{e}}\ cos\,\theta_e$, $\frac{d\,\sigma}{d\,cos\,\theta_{\tilde{e}}} = q\sqrt{s}\,\frac{d\sigma}{dt}$, θ_e and ϕ_e are respectively the polar and azimuthal angles of the decay electron, $\theta_{\tilde{e}}$ is the polar angle of produced selectron in the e^+e^- centre of mass frame.

Appendix B

Upper Limits of Signal Events

Observed events ($n_\circ$) has two components, signal (μ_S) and backgrounds (μ_B), where the latter one is known very accurately. Let N be the desired upper limit on μ_s with a confidence level ϵ (95 %). One has to set the value of N such that random repetition of the experiment with μ_S = N and the same μ_B has a probability ϵ to observe more than $n_\circ$ events. The argument is illustrated in figure B.1 (a) and correlation between μ_B and $n_\circ$ with N of 95 % CL is shown in figure B.1 (b).

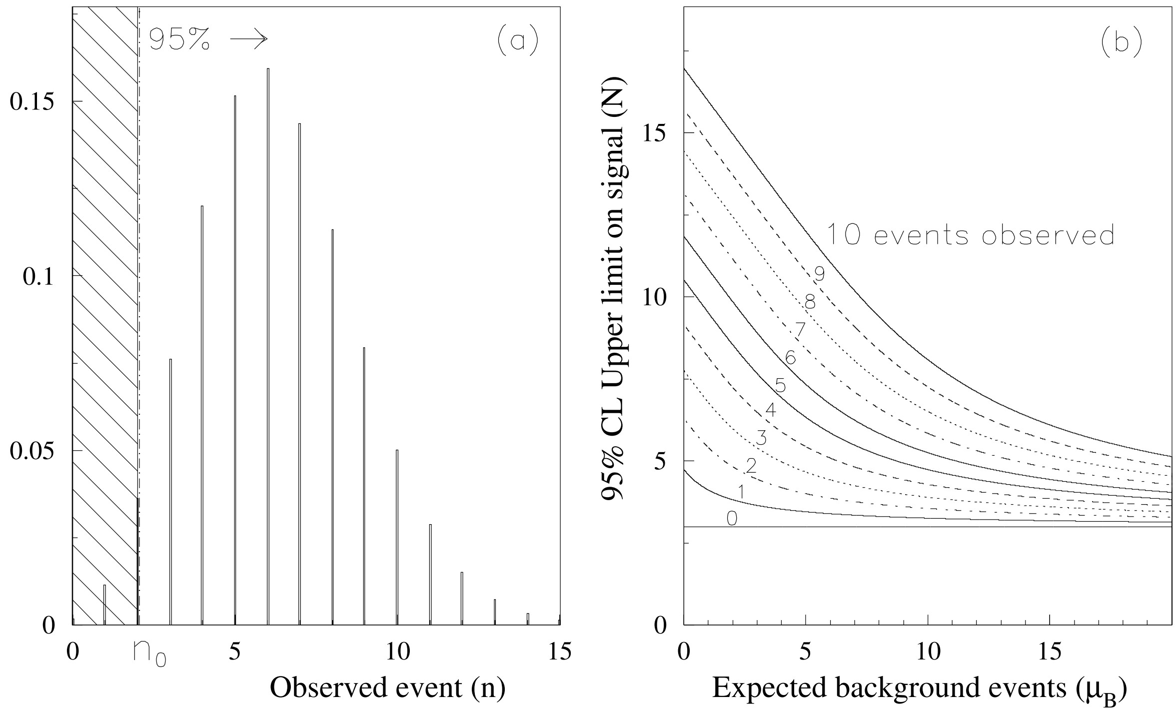

Figure B.1: Poisson upper limit on signal events : (a) Calculation of 95 % CL upper limit of signal event N (= 5.91) corresponding to μ_B = 0.4 and $n_\circ$ = 2 and (b) correlations between μ_B and $n_\circ$ with N of 95 % CL.

Appendix C

Fitted Values of the Parametrisation of Selection Efficiencies

(i) $\sqrt{s} = 161$ GeV

final states	variable	fit type	# of parameters	values of parameters
$\tilde{e}^+\tilde{e}^-$	$\varepsilon/\sqrt{M}$	eqn 9.4	6	$P_1 = -2.447,\ P_2 = -2.603,\ P_3 = -5.079,$ $P_4 = +179.97,\ P_5 = -542.93,\ P_6 = +835.13$
$\tilde{\mu}^+\tilde{\mu}^-$	$\varepsilon/\sqrt{M}$	eqn 9.3	6	$P_1 = -7.552,\ P_2 = +0.829,\ P_3 = -8.335,$ $P_4 = +269.65,\ P_5 = -902.80,\ P_6 = +2851.4$
$\tilde{\tau}^+\tilde{\tau}^-$	ε/M	eqn 9.4	5	$P_1 = -5.782,\ P_2 = +1.205,\ P_3 = +0.018,$ $P_4 = -2.1364,\ P_5 = +34.222$
$\tilde{\chi}_1^+\tilde{\chi}_1^-$	ε/M	eqn 9.4	5	$P_1 = -1.882,\ P_2 = +0.560,\ P_3 = -0.345,$ $P_4 = +6.8758, P_5 = -5.5188$

(ii) $\sqrt{s} = 172$ GeV

final states	variable	fit type	# of parameters	values of parameters
$\tilde{e}^+\tilde{e}^-$	$\varepsilon/\sqrt{M}$	eqn 9.4	4	$P_1 = +59.84,\ P_2 = +0.057,\ P_3 = +0.653,$ $P_4 = -4.3347$
$\tilde{\mu}^+\tilde{\mu}^-$	$\varepsilon/\sqrt{M}$	eqn 9.4	5	$P_1 = -9.938,\ P_2 = +3.465,\ P_3 = +1.341,$ $P_4 = +13.266,\ P_5 = +1238.7$
$\tilde{\tau}^+\tilde{\tau}^-$	ε/M	eqn 9.3	5	$P_1 = +99.39,\ P_2 = +0.063,\ P_3 = +2.423,$ $P_4 = -10.810,\ P_5 = +4.6906$
$\tilde{\chi}_1^+\tilde{\chi}_1^-$	$\varepsilon/\sqrt{M}$	eqn 9.3	5	$P_1 = +235.6,\ P_2 = +0.035,\ P_3 = +1.582,$ $P_4 = -6.1718,\ P_5 = +1.6584$

Table C.1: Co-efficients of parametrisation of selection efficiencies for three leptons and charginos (e/μ decay mode) at $\sqrt{s} = 161$ GeV and 172 GeV.

Appendix D

Combination of two Luminosities for $\tilde{\ell}^+\tilde{\ell}^-$ Limits

Though the production cross section of $\tilde{\ell}^+\tilde{\ell}^-$ depends on the value of $\tan\beta$ and μ i.e., on $M_{\tilde{\chi}^\circ_i}$, the ratio as obtained in MSSM framework has been found to be dependent on the mass of the slepton and rather insensitive to other parameter values i.e., $\frac{\sigma_{161}(e^+e^-\to\tilde{\ell}^+\tilde{\ell}^-)}{\sigma_{172}(e^+e^-\to\tilde{\ell}^+\tilde{\ell}^-)}$ depends only on $m_{\tilde{\ell}}$ as shown in figure D.1.

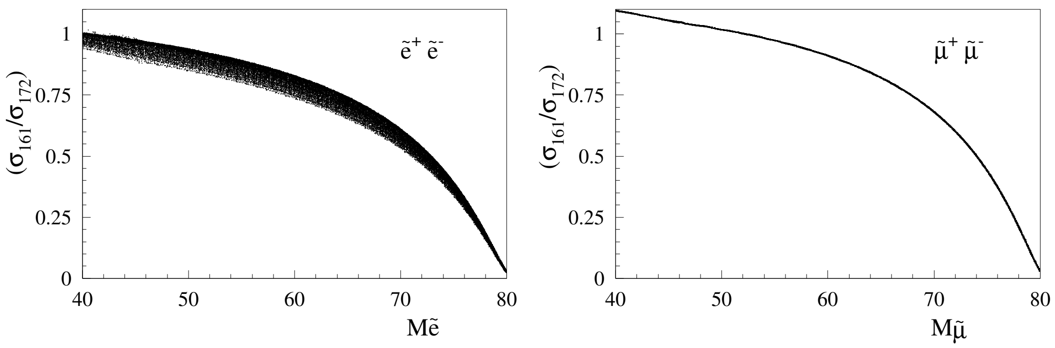

Figure D.1: Ratio of $\tilde{\ell}^+\tilde{\ell}^-$ production at $\sqrt{s}$ = 161 GeV and 172 GeV, (left) $\tilde{e}^+\tilde{e}^-$ production and (right) $\tilde{\mu}^+\tilde{\mu}^-$ production.

To be conservative the parameter space has been scanned for $\tan\beta \in [1., 40.]$ and $|\mu| \in [100., 1000.]$ and the minimum value of σ at $\sqrt{s}$ = 172 GeV has been chosen for a given mass point. All the points are shown in the plots. The upper limit on the production cross section at $\sqrt{s}$ = 161 is calculated from the expression,

$$N = \mathcal{L}_{161}\,\sigma_{161}\,\varepsilon_{161} + \mathcal{L}_{172}\,\sigma_{172}\,\varepsilon_{172} = \sigma_{161}\,(\mathcal{L}_{161}\,\varepsilon_{161} + \mathcal{L}_{172}\,\frac{\varepsilon_{172}}{f(m_{\tilde{\ell}})})$$

where the upper limit on signal event (N) is calculated using equation 9.2 with the combined values of expected backgrounds (μ_b) and the observed events ($n_\circ$) are taken from table 8.5 and integrated luminosities ($\int \mathcal{L}\,dt$) are taken from table 8.1. Fitted parameters of the plot $\frac{\sigma_{161}(e^+e^-\to\tilde{\ell}^+\tilde{\ell}^-)}{\sigma_{172}(e^+e^-\to\tilde{\ell}^+\tilde{\ell}^-)}$ vs $m_{\tilde{\ell}}$ gives $f(m_{\tilde{\ell}})$ and the efficiencies (ε) are calculated as described in section 9.3.1.

References

[1] S. L. Glashow, Nuclear Physics **22** (1961) 579;
S. Weinberg, Physical Review Letters **19** (1967) 1264;
A. Salam, in Proceedings of the 8th Nobel Symposium, ed. N. Svartholm, (Almquist and Wiksell, Slockholm, 1968).

[2] *Search for the Standard Model Higgs Boson in* e^+e^- *Collisions at* $\sqrt{s}$ *= 161, 170 and 172 GeV*
ALEPH Collaboration, D. Abbaneo *et al.*, CERN-PPE-97-070.

[3] SLD Collaboration, E. Torrence, *Determination of Electroweak Parameters at the SLC*, talk presented at ICHEP96, Warsaw, 25-31 July 1996;
K. Abe *et al.*, Physical Review Letters **70** (1993) 2515;
K. Abe *et al.*, Physical Review Letters **73** (1994) 25.

[4] *A Combination of Preliminary Electroweak Measurements and Constraints on the Standard Model*
LEP collaboration, CERN PPE/96-183.

[5] *The Current Status of the Super-Kamiokande Experiment*
K.Martens, Talk given at the 25th International INS Symposium, Tokyo, Dec 1996.

[6] H1 Collaboration, C. Adolff *et al.*, Zeitschrift für Physik **C 74** (1997) 191;
ZEUS Collaboration, G. Abbiendi *et al.*, Zeitschrift für Physik **C 74** (1997) 207.

[7] *An introduction to Supersymmetry*, Manual Drees, KEP-TH-501.

[8] D. A. Dicus and V. S. Mathur, Physical Review **D 7** (1973) 3111;
B. W. Lee, C. Quigg and H. Thacker, Physical Review **D 16** (1977) 1519.

[9] Y. Gollfand and E. Likhrman, JETP Lett. **13** (1971) 323;
D. Volkov and V. Akulov Physics Letters **B 46** (1973) 109;
J. Wess and B. Zumino, Nuclear Physics **B 70** (1974) 39.

[10] A. Bertl, H. Fraas and W. Majerotto, Zeitschrift für Physik **C 30** (1986) 441;
A. Bertl, H. Fraas, W. Majerotto, and B. Mösslacher, Zeitschrift für Physik **C 55** (1992) 257.

[11] J. Ellis, *et al.*, Nuclear Physics **B** 238 (1984) 453.

[12] A. Bertl, H. Fraas and W. Majerotto, Nuclear Physics **B 278** (1986) 1.

[13] A. Bertl, H. Fraas and W. Majerotto, Zeitschrift für Physik **C 34** (1987) 411.

[14] H. Haber and G. Kane, Physics Reports **117** (1985) 75;
S. Dawson, SUSY and SUCH, hep-ph/9612229.

[15] J. Wess and J. Bagger, *Supersymmetry and Supergravity*, (Princeton University Press, Princeton, N.J. 1983;
P. Fayet ans S. Ferrara, Physics Reports **32** (1977) 249.

[16] L. Girardello and M. Grisaru, Nuclear Physics **B 194**, (1982) 65.

[17] H. Haber, G. Kane and T. Sterling, Nuclear Physics **B 161** (1979) 493.

[18] J. Gunion H. Haber, G. Kane and S. Dawson, *The Higgs Hunter Guide* (Addison Wesley, Menlo Park, CA) 1990.

[19] H. Murayama, H. Suzuki, T. Yanagida and J. Yokoyama, Physical Review Letters **70** (1993) 1912.

[20] S. Dimapoulos and H. Georgi, Nuclear Physics **B 193** (1981) 150;
N. Sakai, Zeitschrift für Physik **C 11** (1981) 153;
P. Fayet, Physics Letters **B 69** (1977) 489 and **B 84** (1979) 416.

[21] M. Dine, A. Nelson and Y. Shirman, Physical Review **D 51** (1995) 1362;
M. Dine, A. Nelson, Y. Nir and Y. Shirman, Physical Review **D 53** (1996) 2658;
S. Weinberg, Physical Review **D 26** (1982) 287;
N. Sakai and T. Yanagida, Nuclear Physics **B 197** (1982) 533;
S. Dimapoulos, S. Raby and F. Wilczek, Physics Letters **B 112** (1982) 133;
J. Ellis, D. Nanopoulos and S. Rudaz, Nuclear Physics **B 202** (1982) 43.

[22] C. Carlson, P. Ray and M. Sher, Physics Letters **B 357** (1995) 99;
G. Bhattacharyya, hep-ph/9608415, 1996.

[23] H. Haber and G. Kane, Physics Reports **117** (1985) 75;
A. B. Lahanas and D. V. Nanopoulos, Physics Reports 145 (1987) 1.

[24] H. P. Nilles, Physics Reports **110**, (1984) 1;
X. Tata, in *The Standard Model and Beyond*, p. 304, edited by J. E. Kim, World Scientific (1991);
R. Arnowitt and P. Nath, *Lectures presented at the VII J. A. Swieca Summer School, Campos do Jordo, Brazil, 1993* CTP-TAMU-52/93;
Properties of SUSY Particles, L. Cifarelli and V. Khoze, Editors, World Scientific (1993).

[25] K. Inoue, A. Kakuto, H. Komtsu and H. Takeshita, Prog. Theor. Phys. **68** (1982) 927 and **71** (1984) 413.

[26] W. de Boer, R. Ehret and D.I. Kazakov, Zeitschrift für Physik **C 67** (1995) 647.

[27] H1 collaboration, S. Aid *et al.*, Physics Letters **B 380** (1996) 461.

[28] K. De, for the D∅ Collaboration, *11th Topical Workshop on Proton-Antiproton Collider Physics*, Padova, Italy, 1996;
F. Abe *et al.*, CDF Collaboration, Physical Review Letters **96**, (1996) 4307.

[29] ALEPH Collaboration, D. Decamp *et al.*, Physics Letters **B 236** (1990) 86;
ALEPH Collaboration, D. Decamp *et al.*, Physics Letters **B 244** (1990) 541;
ALEPH Collaboration, D. Decamp *et al.*, Physics Reports **216** (1992) 253;
DELPHI Collaboration, P, Abreu *et al.*, Physics Letters **B 247** (1990) 157;
OPAL Collaboration, K. Ahmet *et al.*, Physics Letters **B 240** (1990) 261;
OPAL Collaboration, K. Ahmet *et al.*, Physics Letters **B 248** (1990) 211;
L3 Collaboration, B. Aveda *et al.*, Physics Letters **B 233** (1989) 530;
L3 Collaboration, M. Acciarri *et al.*, Physics Letters **B 350** (1995) 109.

[30] J. Bailey *et al.*, Nuclear Physics **B 150** (1979) 1.

[31] M. Misiak *et al.*, hep-ph/9703442, 1997.

[32] CLEO collaboration, M. Alam *et al.*, Physical Review Letters **74** (1995) 2885.

[33] H. Baer and M. Brhlik, hep-ph/9610224, 1996.

[34] ALEPH Collaboration, D. Decamp *et al.*, Nuclear Instruments & Methods **A 294** (1990) 127.

[35] DELPHI Collaboration, P. Aarnio *et al.*, Nuclear Instruments & Methods **A 303** (1991) 233.

[36] L3 Collaboration, B. Adeva *et al.*, Nuclear Instruments & Methods **A 289** (1990) 35.

[37] OPAL Collaboration, K. Ahmet *et al.*, Nuclear Instruments & Methods **A 305** (1991) 275.

[38] R. Bailey, (World Scientific, Singapore, 1993), volume International Journal of Modern Physics A, Proc. Suppl., p. 401;
J. Jowett, *The 8-bunch pretzel scheme, Proceedings of the first workshop on LEP performance*, Chamonix 1991, CERN-SL-91-23 (1991).

[39] J. Billan, J.P. Gourber, K.N. Henrichsen and L.W. Walckiers, *XIV Int. Con. on High Energy Accelerators*, Tsukuba, Japan (1989) and Part. Accel. 29 (1990) 215.

[40] J. billan, J.P. Gourber and K.N. Henrichsen, *1991 Particle Accelerator Consf.*, San Francisco, CA (1991) and CERN-AT-MA-91-03.

[41] R. Bailey *et al.*, *2nd European Particle Accelerator Conf.*, Nice, France (1990) and CERN-SL 90-95.

[42] R. Assmann *et al.*, *Energy Calibration with Resonant Depolarization at LEP in 1993*, CERN-SL 94-61-AP.

[43] L. Arnaudon *et al.*, *Accurate Determination of the LEP Beam Energy by Resonant Depolarization*, CERN-SL 94-71-BI.

[44] C. Bovet *et al.*, *Final Report of the 1994 Bunch Train Study Group*, Preprint CERN-SL-94-95-AP, CERN, 1994.

[45] W. herr, *Bunch train without crossing angle*, CERN-SL/94-06-DI 1994 323.

[46] *LEP design report, vol I, The LEP Injector Chain*, CERN/SPS/83-26.

[47] B. Dhning *et al.*, *A Study of the Magnetic Dipole Field of LEP during the 1995 Energy Scan*, CERN-SL 96-54-BI.

[48] P. Galumian *et al.*, Nuclear Instruments & Methods **A 327** (1993) 269.

[49] O. Adriani *et al.*, Physics Reports **236** (1993) 1.

[50] M. Chemarin *et al.*, Nuclear Instruments & Methods **A 349** (1994) 345;
M. Bourquin *et al.*, L3 Internal note **2138**, 1997.

[51] B. Basti *et al.*, Nuclear Instruments & Methods **A 374** (1996) 293.

[52] The L3 F/B Muon Group, A. Adam *et al.*, Nuclear Instruments & Methods **A 383** (1996) 342.

[53] G. Carlino *et al.*, L3 Internal note **1811**, 1995.

[54] M. Caccia *et al.*, Nuclear Instruments & Methods **A 315** (1992) 197;
G. Ambrosi *et al.*, Nuclear Instruments & Methods **A 344** (1994) 133;
O. Adriani *et al.*, Nuclear Instruments & Methods **A 348** (1994) 431;
A. Adam *et al.*, Nuclear Instruments & Methods **A 348** (1994) 436;
The L3 SMD collaboration, M. Acciarri *et al.*, Nuclear Instruments & Methods **A 351** (1994) 300;
M. Acciarri *et al.*, Nuclear Instruments & Methods **A 360** (1995) 103.

[55] H. Akbari *et al.*, Nuclear Instruments & Methods **A 315** (1992) 161;
G.M. Viertel, Nuclear Instruments & Methods **A 323** (1992) 399;
F. Beissel *et al.*, Nuclear Instruments & Methods **A 332** (1993) 33.

[56] A. Böhm *et al.*, Nuclear Instruments & Methods **A 273** (1988) 471.

[57] H. Ma *et al.*, Nuclear Instruments & Methods **A 274** (1989) 113.

[58] J.A. Bakken *et al.*, Nuclear Instruments & Methods **A 275** (1989) 81.

[59] A. Bay *et al.*, Nuclear Instruments & Methods **A 321** (1992) 119.

[60] H. Bergstein *et al.*, SC-N project, Vol I-III, Internal Report, I. Phys. Inst., RWTH-Aachen, Aachen -1995.

[61] Ulrich Uwer, L3 Internal note **2003**, 1996.

[62] A. Arefiev *et al.*, Nuclear Instruments & Methods **A 275** (1989) 71;
A. Arefiev *et al.*, Nuclear Instruments & Methods **A 285** (1989) 403.

[63] R. D'Alessandro, Nuclear Instruments & Methods **A 289** (1990) 103;
O. Adriani *et al.*, Nuclear Instruments & Methods **A 300** (1991) 493.

[64] B. Adeva *et al.*, Nuclear Instruments & Methods **A 277** (1989) 187;
B. Adeva *et al.*, Nuclear Instruments & Methods **A 323** (1992) 109.

[65] R. Santonico and R. Cardarelli, Nucl. Instr. and Meth. **187** (1981) 377.

[66] I.C. Brock *et al.*, Nuclear Instruments & Methods **A 381** (1996) 236.

[67] T. Van Rhee *et al.*, L3 internal note **2117**, 1997.

[68] J. Simkin and C.W. Towbridge, Int. Jour. Num. Math. Eng., **14** (1979).

[69] A. Kunin *et al.*, L3 Internal note **1840**, 1995.

[70] R. Bizzarri *et al.*, Nuclear Instruments & Methods **A 283** (1989) 799;
R. Bizzarri *et al.*, Nuclear Instruments & Methods **A 317** (1992) 463;
P. Bagnaia *et al.*, Nuclear Instruments & Methods **A 323** (1992) 528;
P. Bagnaia *et al.*, Nuclear Instruments & Methods **A 324** (1993) 101;
P. Bagnaia *et al.*, Nuclear Instruments & Methods **A 344** (1994) 212.

[71] M. Fukushima, L3 Internal note **515**, (1987);
T.S. Dai and M. Fukushima, L3 Internal note **668**, (1989);
G. Carlino *et al.*, L3 Internal note **1951**, (1997).

[72] P. Béné *et al.*, Nuclear Instruments & Methods **A 306** (1991) 150.

[73] U. Uwer, L3 Internal note **1400**, (1993).

[74] S. P. Beingessner *et al.*, Nuclear Instruments & Methods **A 340** (1994) 322.

[75] C. Diobisi *et al.*, Nuclear Instruments & Methods **A 336** (1993) 78.

[76] S. Katsanevas, in the LEP200 workshop report, CERN 96/01 (1996).

[77] J.H. Field and T. Reimann, Computer Physics Communications **94** (1996) 53.

[78] S. Jadach, J.H. Kühn and Z. Wąs, Computer Physics Communications **64** (1991) 275;

S. Jadach, M. Jeżabak, J.H. Kühn and Z. Wąs, Computer Physics Communications **70** (1992) 69;
R. Decker, S. Jadach, J.H. Kühn and Z. Wąs, Computer Physics Communications **76** (1993) 361;
S. Jadach, B. F. L. Ward and Z. Wąs, Computer Physics Communications **79** (1994) 503.

[79] E. Barberio B. Eijk and Z. Wąs, Computer Physics Communications **66** (1991) 115;
E. Barberio Z. Wąs Computer Physics Communications **79** (1994) 291.

[80] M. Skrzypek, S. Jadach, W. Placzek and Z. Wąs, Computer Physics Communications **94** (1996) 216.

[81] T. Sjöstrand, Computer Physics Communications **82** (1994) 74.

[82] E. Boudinov, *et al.*, *$\gamma\gamma$ event generators*, hep-ph/9512371, 1995.

[83] F.A. Berends, R. Pittau and R. Kleiss, Computer Physics Communications **85** (1995) 437.

[84] F.A. Berends and R. Kleiss, Nuclear Physics **B 186** (1981) 22.

[85] T. Sjöstrand, Computer Physics Communications **39** (1986) 347;
T. Sjöstrand and M. Bengtsson, Computer Physics Communications **43** (1987) 367.

[86] S. Jadach and Z. Wąs, Computer Physics Communications **64** (1991) 267.

[87] D.R. Yennie, S. Frautschi and H. Suura, Ann. Phys. (NY) **13** (1961) 379.

[88] A. Capella, *et al.*, Physics Reports **236** (1994) 227.

[89] R. Burn *et al.*, GEANT3 *User Guide*, CERN DD/EE/84-1.

[90] H. Fesefeldt, *The Simulation of Hadronic Showers: Physics and applications* RWTH, Aachen, PITHA 85/02 (1985).

[91] B. Adeva, *et al.*, Nuclear Instruments & Methods **A 289** (1990) 335.

[92] B. Adeva, *et al.*, Nuclear Instruments & Methods **A 309** (1991) 318.

[93] S. Banerjee and F. Bruyant, L3 Internal note **748**, 1989.

[94] Physical Review **D 54** (1996) 21.

[95] S. Banerjee *et al.*, L3 Internal note **2111**, 1997.

[96] L3 Collaboration, M. Acciarri *et al.*, Physics Letters **B 377** (1996) 289.

[97] F. James *et al.*, CERN Program Library Long writeup D506.

[98] Standard Model Process, hep-ph/9601224.

[99] S. Banerjee *et al.*, L3 Internal note **1885**, 1995.

[100] Y.L. Dokshitzer, *Contribution to the Workshop on Jets at LEP and HERA*
N. Brown and W.J. Stirling, Rutherford Preprint RAL-91-049;
S. Catani *et al.*, Nuclear Physics **B 269** (1991) 432;
S. Bethke *et al.*, Nuclear Physics **B 370** (1992) 310.

[101] A. Favara *et al.*, L3 Internal note **1728**, 1995.

[102] S. Banerjee *et al.*, L3 Internal note **1939**, 1996.

List of Publications

[1] Measurement of eta Production in Two and Three-Jet Events from Hadronic Z Decays at LEP.
L3 Collab., M. Acciarri *et al.* : G. Majumder + 468 other authors
Phys. Lett. **B 371** (1996) 126.

[2] Measurement of Hadron and Lepton-Pair Production at 130 GeV $< \sqrt{s} <$ 140 GeV at LEP.
L3 Collab., M. Acciarri *et al.* : G. Majumder + 470 other authors
Phys. Lett. **B 370** (1996) 195.

[3] Studies of Hadronic Event Structure and α_s Determination at $\sqrt{s}$ = 130, 136 GeV.
L3 Collab., M. Acciarri *et al.* : G. Majumder + 470 other authors
Phys. Lett. **B 371** (1996) 137.

[4] Search for Excited Leptons in e^+e^- Annihilation at $\sqrt{s}$ = 130–140 GeV.
L3 Collab., M. Acciarri *et al.* : G. Majumder + 470 other authors
Phys. Lett. **B 370** (1996) 211.

[5] Measurement of Muon Pair Production at $50 < \sqrt{s} < 86$ GeV at LEP.
L3 Collab., M. Acciarri *et al.* : G. Majumder + 456 other authors
Phys. Lett. **B 374** (1996) 331.

[6] Combining Heavy Flavour Electroweak Measurements at LEP.
The LEP Experiments: ALEPH, DELPHI, L3 and OPAL Nucl. Inst. and Meth. **A 378** (1996) 101.

[7] Search for Supersymmetric Particles at 130 GeV $< \sqrt{s} <$ 140 GeV at LEP.
L3 Collab., M. Acciarri *et al.* : G. Majumder + 456 other authors
Phys. Lett. **B 377** (1996) 289.

[8] Search for Unstable Sequential Neutral and Charged Heavy Leptons in e^+e^- Annihilation at $\sqrt{s}$ = 130 and 136 GeV.
L3 Collab., M. Acciarri *et al.* : G. Majumder + 454 other authors
Phys. Lett. **B 377** (1996) 304.

[9] Measurement of the Michel Parameters and the average tau neutrino helicity from tau decays in $e^+e^- \rightarrow \tau^+\tau^-$.
L3 Collab., M. Acciarri *et al.* : G. Majumder + 454 other authors
Phys. Lett. **B 377** (1996) 313.

[10] Observation of Multiple Hard Photon Final States at $\sqrt{s}$ = 130–140 GeV at LEP.
L3 Collab., M. Acciarri *et al.* : G. Majumder + 454 other authors
Phys. Lett. **B 384** (1996) 323.

[11] Measurement of the Branching Ratios $b \longrightarrow e\nu X$, $\mu\nu X$, $\tau\nu X$ and νX.
L3 Collab., M. Acciarri *et al.* : G. Majumder + 454 other authors
Z. Phys. **C71** (1996) 379.

[12] Search for New Particles in Hadronic Events with Isolated Photons.
L3 Collab., M.Acciarri *et al.* : G. Majumder + 450 other authors
Phys. Lett. **B 388** (1996) 409

[13] Measurement of the $\bar{d}$ Meson Oscillation Frequency.
L3 Collab., M. Acciarri *et al.* : G. Majumder + about 450 other authors
Phys. Lett. **B 383** (1996) 487.

[14] Search For Neutral Higgs Boson Production Through the Process
$e^+e^- \rightarrow Z^*H^\circ$.
L3 Collab., M. Acciarri *et al.* : G. Majumder + 450 other authors
Phys. Lett. **B 385** (1996) 454.

[15] Measurement of the Lifetime of the Tau Lepton.
L3 Collab., M. Acciarri *et al.* : G. Majumder + 448 other authors
Phys. Lett. **B 389** (1996) 187.

[16] Search for Neutral B Meson Decays to Two Charged Leptons.
L3 Collab., M. Acciarri *et al.* : G. Majumder + 449 other authors
Phys. Lett. **B 391** (1997) 474.

[17] Search for Exclusive B Decays to J and η or π^0 with the L3 Detector.
L3 Collab., M. Acciarri *et al.* : G. Majumder + 449 other authors
Phys. Lett. **B 391** (1997) 481.

[18] Measurement of Inclusive Ω and η' Production in Hadronic Z Decays.
L3 Collab., M. Acciarri *et al.* : G. Majumder + 449 other authors
Phys. Lett. **B 393** (1997) 465.

[19] Study of the Weak Charged Hadronic Current in b Decays.
L3 Collab., M. Acciarri *et al.* : G. Majumder + 449 other authors
Phys. Lett. **B 393** (1997) 477.

[20] A Combination of Preliminary Electroweak Measurements and Constraints on the Standard Model.
The LEP Experiments: ALEPH, DELPHI, L3 and OPAL, the LEP Electroweak Working Group and the SLD Heavy Flavour Group.
CERN preprint CERN-PPE/96-183

[21] Measurement of $\mathrm{D_s^-} \to \tau^-\bar{\nu_\tau}$ and a new limit for $\mathrm{B}^- \to \tau^-\bar{\nu_\tau}$.
L3 Collab., M. Acciarri *et al.* : G. Majumder + 449 other authors
Phys. Lett. **B 396** (1997) 327.

[22] Search for Excited Leptons in $\mathrm{e^+e^-}$ Annihilation at $\sqrt{\mathrm{s}} = 161$ GeV.
L3 Collab., M. Acciarri *et al.* : G. Majumder + 452 other authors
Phys. Lett. **B 401** (1997) 139.

[23] Pair-Production of W Bosons in $\mathrm{e^+e^-}$ Interactions at $\sqrt{\mathrm{s}} = 161$ GeV.
L3 Collab., M. Acciarri *et al.* : G. Majumder + 452 other authors
Phys. Lett. **B 398** (1997) 223.

[24] Production of Single W Bosons at LEP.
L3 Collab., M. Acciarri *et al.* : G. Majumder + 449 other authors
Phys. Lett. **B 403** (1997) 168.

[25] Production of e, μ and τ Pairs in Untagged Two-Photon Collisions at LEP.
L3 Collab., M. Acciarri *et al.*, : G. Majumder + 453 other authors
Phys. Lett. **B 407** (1997) 341.

[26] Inclusive J/ψ and χ_c Production in Hadronic Z Decays.
L3 Collab., M. Acciarri *et al.*, : G. Majumder + 453 other authors
Phys. Lett. **B 407** (1997) 351.

[27] QCD Studies and Determination of α_s in $\mathrm{e^+e^-}$ collisions at $\sqrt{\mathrm{s}} = 161$ GeV and 172 GeV.
L3 Collab., M. Acciarri *et al.*, : G. Majumder + 453 other authors
Phys. Lett. **B 404** (1997) 390.

[28] Cross section of hadron production in gamma gamma collisions at LEP.
L3 Collab., M. Acciarri *et al.*, : G. Majumder + 453 other authors
Phys. Lett. **B 408** (1997) 450.

[29] Measurement of Hadron and Lepton-Pair Production at 161 GeV $< \sqrt{\mathrm{s}} <$ 172 GeV at LEP.
L3 Collab., M. Acciarri *et al.*, : G. Majumder + 453 other authors
Phys. Lett. **B 407** (1997) 361.

[30] K°_s and Λ Production in Quark and Gluon Jets at LEP.
L3 Collab., M. Acciarri *et al.*, : G. Majumder + 453 other authors
Phys. Lett. **B 407** (1997) 389.

[31] Search for anomalous four-jet events in e^+e^- annihilation at $\sqrt{s}$ = 130-172 GeV.
L3 Collab., M. Acciarri *et al.*, : G. Majumder + 453 other authors
Phys. Lett. **B** accepted.

[32] Measurement of W-Pair Cross Sections in e^+e^- Interactions at $\sqrt{s} = 172\,\mathrm{GeV}$ and W-Decay Branching Fractions.
L3 Collab., M. Acciarri *et al.*, : G. Majumder + 453 other authors
Phys. Lett. **B 407** (1997) 419.

[33] Resonance Formation in the $\pi^+\pi^-\pi^\circ$ Final State in Two-Photon Collisions.
L3 Collab., M. Acciarri *et al.*, : G. Majumder + 453 other authors
Phys. Lett. **B** accepted.

[34] Study of Hadronic Events and Measurements of α_s between 30 and 91 GeV.
L3 Collab., M. Acciarri *et al.*, : G. Majumder + 453 other authors
Phys. Lett. **B** accepted.

[35] Search for Heavy Neutral and Charged Leptons in e^+e^- Annihilation at $\sqrt{s} = 161$ and $\sqrt{s} = 172$ GeV.
L3 Collab., M. Acciarri *et al.*, : G. Majumder + 453 other authors
Phys. Lett. **B** accepted.

[36] Single and Multi-Photon Events with Missing Energy in e^+e^- Collisions at 161 GeV $< \sqrt{s} <$ 172 GeV.
L3 Collab., M. Acciarri *et al.*, : G. Majumder + 453 other authors
Phys. Lett. **B** accepted.

[37] Hard-photon production at $\sqrt{s}$ = 161 GeV and 172 GeV at LEP.
L3 Collab., M. Acciarri *et al.*, : G. Majumder + 453 other authors
Phys. Lett. **B** accepted.

[38] Upsilon Production in Z Decays.
L3 Collab., M. Acciarri *et al.*, : G. Majumder + 453 other authors
Phys. Lett. **B** accepted.

[39] Search for the Standard Model Higgs Boson in e^+e^- Interactions at 161 GeV $< \sqrt{s} <$ 172 GeV.
L3 Collab., M. Acciarri *et al.*, : G. Majumder + 450 other authors
Phys. Lett. **B** accepted.

[40] Search for new physics in energetic single photon production in e^+e^- annihilation at the Z resonance.
L3 Collab., M. Acciarri *et al.*, : G. Majumder + 450 other authors
Phys. Lett. **B** accepted.

[41] Missing mass spectra in hadronic events from e^+e^- collisions at $\sqrt{s}$ = 161-172 GeV and limits on invisible Higgs decays L3 Collab., M. Acciarri *et al.*, : G. Majumder + 451 other authors
Phys. Lett. **B** accepted.

[42] Measurements of Mass, Width and Gauge Couplings of the W Boson at LEP.
L3 Collab., M. Acciarri *et al.*, : G. Majumder + 451 other authors
Phys. Lett. **B** accepted.

[43] Search for R-Parity Breaking Sneutrino Exchange at LEP.
L3 Collab., M. Acciarri *et al.*, : G. Majumder + 451 other authors
Phys. Lett. **B** accepted.

[44] Neutral-Current Four-Fermion Production in e^+e^- Interactions at 130 GeV $\leq \sqrt{s} \leq$ 172 GeV.
L3 Collab., M. Acciarri *et al.*, : G. Majumder + 451 other authors
Phys. Lett. **B** accepted.

[45] Measurement of $\eta'(958)$ Formation in Two-Photon Collisions at LEP1.
L3 Collab., M. Acciarri *et al.*, : G. Majumder + 451 other authors
Phys. Lett. **B** accepted.

[46] Measurement of the Average Lifetime of b-Hadrons in Z Decays.
L3 Collab., M. Acciarri *et al.*, : G. Majumder + 445 other authors
Phys. Lett. **B** submitted.

[47] Search for Scalar Leptons, Charginos and Neutralinos in e^+e^- collisions at $\sqrt{s}$ = 161 - 172 GeV.
L3 Collab., M. Acciarri *et al.*, : G. Majumder + 445 other authors
Phys. Lett. **B** submitted.